Design, Modelling and Control of Electrical Machines - With Applications to Iron-powder Machines and Acoustic Noise

Martinez, David

2005

Design, Modelling and Control of Electrical Machines

With Applications to Iron-powder Machines and Acoustic Noise

David Martínez Muñoz

LUND UNIVERSITY

Doctoral Dissertation in Industrial Electrical Engineering
Department of Industrial Electrical Engineering
and Automation

Department of
Industrial Electrical Engineering and Automation
Lund Institute of Technology
Lund University
P.O. Box 118
SE-221 00 LUND
SWEDEN

http://www.iea.lth.se

ISBN 91-88934-35-7
CODEN:LUTEDX/(TEIE-1043)/1-338/(2004)

Printed in Sweden by Media-Tryck
Lund University
Lund 2004

To my parents:

Manuel and Josefa

Abstract

This thesis consists of two parts, the first dealing with the design of iron-powder synchronous machines, and the second with the analysis and prediction of the acoustic noise in electrical machines.

In Part I, a 1.6 kW electrically magnetized claw-pole machine with magnetically conducting end-plates has been analyzed and a prototype tested. The machine is built from soft magnetic composite material (SMC), also known as iron-powder. The magnetic isotropy of SMC gives enormous flexibility in electrical machine design, enabling new topologies exploiting three dimensional flux paths. This is the main advantage compared to conventional machines using laminations, where the flux is constrained into two dimensions. The novelty of the machine presented lies in that the slip-rings in the rotor are no longer needed, since the field coils are removed from the rotor and placed in magnetically conducting end-plates attached to both sides of the stator. This also improves the cooling capability of the copper losses from the field winding, allowing an increased electric loading. The rotor is of the claw-pole type, and the end-plates close the magnetic circuit between the stator and the rotor. The machine has been optimized using a magnetic equivalent circuit model allowing rotation, where non-linearities have been included using an iterative approach based on the linearisation of the BH curve. The traditional leakage paths in claw-pole machines are modified because of the magnetically conducting end-plates, and alternatives are proposed to reduce them. The machine has also been compared to two alternative topologies with electrical magnetization and another with permanent magnets. The comparison has been carried out for a similar temperature rise in the windings, and thermal models have been developed for every machine to determine their maximum electric loading. The rotational and alternating components of the iron losses are calculated using the finite element method (FEM). The results from the measurements indi-

cate that the average torque is 14% lower than predicted. This is probably due to a leakage path between the end-plates through the shaft, which carries the homopolar flux, and that was not considered in the predictions. The concept of *series magnetization* has also been tested. This consists of feeding the field winding directly from the rectified three phase armature currents at the neutral point, therefore eliminating the need for the d.c. power source.

Electrical machines are finding application in new environments where lower noise levels are demanded. The main focus of Part II is the measurement and prediction of the noise emissions from induction motors using the vector control technique as well as the analysis of some structural changes to reduce these emissions. A digital drive system has been developed for a 2.2 kW induction motor, and its dynamic capabilities demonstrated for a wide range of the frequency spectrum. This tool has been used for the experimental evaluation of the noise emissions when the flux and/or the torque are modulated with high frequency noise signals. The results showed that the noise emissions were higher when the flux was modulated compared to the torque, although the differences were considerably reduced when the machine was loaded. It was also observed that the noise emissions were decreased importantly at load. Sound pressure and sound intensity measurements have been conducted with the rotor stationary and rotating at low speed, showing that the most proper way to quantify the noise emissions from electric machinery is to measure the sound power. A method for the prediction of the noise emissions has been proposed, based on the interactive use of commercial packages for mechanical, electromagnetic and acoustic analyses based in the finite and boundary element methods. The results show that the accuracy of the noise prediction depends on the proper calculation of the modes of vibration in the structural analysis, as well as a suitable selection of the material damping. Skewing also needs to be modelled in order to account for the rotor harmonics. A study has been conducted to assess the effectiveness of introducing peripheral air gap layers around the stator core to reduce the noise emissions. It was observed that the acoustic behaviour was not improved, since the reduction of the stiffness in the outer part of the core actually increased its sensitivity to the vibrations.

Preface

This thesis constitutes the work I have carried out in my pursuit of a PhD in Industrial Electrical Engineering at the Department of Industrial Electrical Engineering and Automation (IEA), Lund University, Sweden. During the course of my PhD studies I also had the opportunity to spend almost one year as a guest research fellow at the Acoustics and Vibration Unit (AVU), University College, The University of New South Wales, at the Australian Defence Force Academy, in Canberra, Australia.

The thesis addresses two topics in electrical machines. The first is concerned with the design of iron-powder machines. The second is about modelling acoustic noise in electrical machines. The thesis is divided into two parts accordingly, both written as a monograph. For the sake of clarity, each part has been organized in a series of chapters followed by the bibliography and the appendices related to that part.

During the years of PhD studies, part of the material in the thesis has been published at other occasions. The research on iron-powder machines has been published in the following articles:

- Martínez-Muñoz, D. and Alaküla, M. (2003). "Comparison between a novel claw-pole electrically magnetized synchronous machine without slip-rings and a permanent magnet machine". *IEEE International Electrical Machines and Drives Conference, IEMDC'03 Conf. Proc.*, Madison, WI, USA, June 2003, pp. 1351-1356.

- Martínez-Muñoz, D. and Alaküla, M. (2004a). "Alternatives for leakage reduction in a novel claw-pole electrically magnetized synchronous machine". *IEE International Conference on Power Electronics, Machines and Drives, PEMD 2004 Conf. Proc.*, Edinburgh, UK, April 2004, pp. 386-391.

- Martínez-Muñoz, D. and Alaküla, M. (2004b). "A MEC network method based on the BH curve linearisation: study of a claw-pole machine". *International Conference on Electrical Machines, ICEM'04 Conf. Proc.*, Cracow, Poland, Sept. 2004, 6 pp.

- Martínez-Muñoz, D., Reinap, A. and Alaküla, M. (2004a). "Comparison between three iron-powder topologies of electrically magnetized synchronous machines". *International Conference on Electrical Machines, ICEM'04 Conf. Proc.*, Cracow, Poland, Sept. 2004, 6 pp.

- Martínez-Muñoz, D., Reinap, A. and Alaküla, M. (2004b). "Comparison between four topologies of synchronous machines using SMC", invited paper, The UK Magnetics Society, *Seminar on SMC and their use in electrical machines*, Newcastle, UK, Nov. 2004, 7 pp.

The thesis author has also co-authored the following publication in the same field. The contribution made by the thesis author in this paper is minor:

- Reinap, A., Martínez-Muñoz, D. and Alaküla, M. (2004). "Iron loss calculation in a claw-pole structure". *IEEE Nordic Workshop on Power and Industrial Electronics, NORPIE'04 Workshop Proc.*, Trondheim, Norway, June 2004, 5 pp.

The research on acoustic noise in electrical machines is reported in the following articles:

- Martínez-Muñoz, D., Pulle, D. W. J., Alaküla, M. and Weibull, H. (1999). "A drive system for acoustical analysis". *IEE International Conference on Electrical Machines and Drives, EMD'99 Conf. Proc.*, Canterbury, UK, Sept. 1999, pp. 147-150.

- Martínez-Muñoz, D. and Lai, J. C. S. (2003). "Acoustic noise prediction in a vector controlled induction machine". *IEEE International Electrical Machines and Drives Conference, IEMDC'03 Conf. Proc.*, Madison, WI, USA, June 2003, pp. 104-110.

- Martínez-Muñoz, D., Lai, J. C. S. and Pulle, D. W. J. (2003). "Acoustic noise radiated from vector controlled induction motor drives". *European Conference on Power Electronics and Applications, EPE'03 Conf. Proc.*, Toulouse, France, Sept. 2003, 10 pp.

- Martínez-Muñoz, D., Lai, J. C. S. and Alaküla, M. (2003). "A study of the acoustical properties of stators with an outer-surface layer of air gaps". *European Conference on Power Electronics and Applications, EPE'03 Conf. Proc.*, Toulouse, France, Sept. 2003, 10 pp.

Acknowledgements

Along the years of PhD studies I have had the privilege to work with different supervisors. I would like to express my sincere gratitude to Prof. Mats Alaküla, who welcomed me at the department already as an exchange student and gave me the opportunity to continue with the PhD studies. Mats is very encouraging and really enjoys exploring unconventional ideas. I am very grateful to Prof. Joseph C. S. Lai (AVU) who was my advisor for the research on acoustic noise and invited me to work at the AVU. Joseph is very friendly and helpful and without his support the acoustic experiments and simulations would not have been possible. I am also thankful to Prof. Duco W. J. Pulle for his advice in the first stages of my PhD studies.

I would like to especially thank my colleague and friend Avo Reinap, who has been an extraordinary working companion. Avo is always willing to discuss any topic and to fill the white board in our office.

A number of people earn my gratitude for their support during the experimental work. Dr Thomas Rundqvist (ProEngCo Permedyn) and Ludvig Wadsten (Motor & Bilelektra) have been very helpful with the construction of the prototype machine in Part I. Andrew Roberts, Glenn Torr and Dr Andrew Dombek at the AVU helped with practical aspects related to the acoustic noise experiments in Part II. At the AVU I also would like to thank Antti Pappiniemi for enjoyable discussions.

The structural models of the test motor included in Part II were created by Dr Chong Wang during his PhD studies at the AVU, and their availability is acknowledged. Dr Alex Michaelides at the VectorFields support in Oxford has been a good help in the initial stages of the electromagnetic finite element modelling. I would also like to thank my former colleague Tech. Lic. Svante Andersson for interesting discussions.

I would like to express my gratitude to the staff at IEA. Even if all the people at the department are helpful and friendly there are those that I owe a special thank. Getachew Darge has provided very valuable help with practical issues for

the experiments. Dr Morten Hemmingsson takes care of the LaTeX package in UNIX, which I use for most of the writing. Dr Gunnar Lindstedt helps to keep my PC healthy and also allowed me to "occupy" the computers in the lab with my simulations. I am also grateful to Prof. Gustaf Olsson, who I believe played an important role in my admission as a PhD student at the department.

Apart from my supervisors, a number of people earn my gratitude for proof reading parts of the thesis. Part I has been reviewed by Prof. Sture Eriksson and Tech. Lic. Svante Andersson. Part II has been reviewed by Prof. Lars Gertmar, Dr Kelvin Maliti, and Tech. Lic. Anders Daneryd in a seminar. Their comments have certainly contributed to improve the quality of the thesis.

I would also like to thank Dr Ola Stenlåås, Dr Rolf Egnell and Dr Olof Erlandsson from the joined project for Part I. Together with the members of the steering committee, Prof. Sture Eriksson (EME/KTH), Göran Masus (Finnveden Powertrain), Dr Göran Johansson (Volvo), and Tech. Lic. Joachim Lindström (Volvo) they are acknowledged for fruitful comments and discussions.

The projects in Part I and Part II have been financially supported by STEM (The Swedish Energy Agency), and NUTEK (The Swedish Business Development Agency), respectively. This support is gratefully acknowledged.

Finally, I would like to thank my parents Manuel and Josefa, and my two brothers Manuel and José Andrés, in Spain, for all their love, trust and support over the years. I would like to pay tribute to my parents, who always have supported my projects and have encouraged me to travel. Their wisdom, understanding and care has enabled me and my brothers to attain graduate education. This thesis is dedicated to them.

Lund, November 20, 2004,

David Martínez Muñoz

Contents

Part I

Design of Iron-powder Synchronous Machines

Chapter 1

Introduction

1.1 Background and Motivation

There is a broad consensus among leading climate scientists that emissions from human activities are enhancing the natural greenhouse effect, that this is already having a discernible effect on climate, and that the ultimate effect will be much larger. This fact was a conclusion from The Royal Commission on Environmental Pollution's 22nd Report (2000), where it was stated that in the 20th century the global mean temperature of the Earth's surface rose by about 0.6^oC, and it was predicted that it would rise at a rate of up to 3^oC by the end of the 21th century. A direct consequence of the global warming is the raise in the sea level, which was estimated to increase the number of people in the world affected by coastal flooding from today's 13 million per year to 94 million each year by the 2080's, unless there were to be large-scale migration away from threatened areas. Four fifths of the people affected would be in south and south-east Asia.

Carbon dioxide is an important greenhouse gas, and the most important in terms of human impact on the atmosphere. Its concentration in the atmosphere can vary naturally, and Figure 1.1 shows the variations in the carbon cycle that have occurred over the last 400.000 years (upper curve) and how these related to changes in the temperature (lower curve). During relatively warm periods (similar to the climate over the last 10.000 years) the concentration of carbon dioxide in the atmosphere was, as in the pre-industrial period, about 270-280 parts per million by volume (ppmv); during the coldest parts of glacial periods it was significantly lower, about 180-190 ppmv. However, over the last 250 years, as industrialization has taken place, the concentration has risen to about 370

ppmv. It is now increasing by 0.4% a year on average. Two-thirds of the current enhancement in the greenhouse effect is estimated to be due to this increased concentration of carbon dioxide. Nearly four-fifths of the extra carbon dioxide entering the atmosphere since 1750 is estimated to have come from burning fossil fuels.

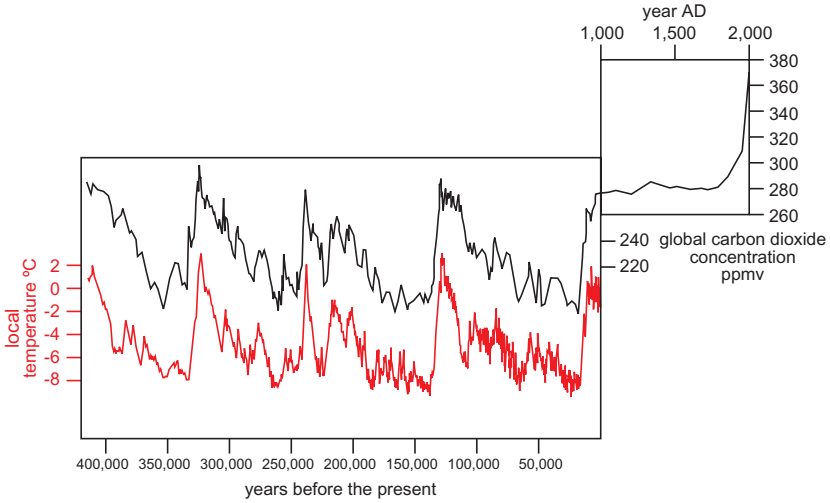

Figure 1.1: Carbon dioxide concentration and temperature: evidence from ice cores. (The Royal Commission on Environmental Pollution's 22nd Report, 2000)

The world energy supply is dominated by fossil fuels, which account for about 80% of the total. Oil is the most important energy source, meeting 37% of the demand, followed by coal at 22% and natural gas at 21%. Only in Sweden, with a population of 9 million people, the annual oil consumption (petrol and diesel fuel) in the transport sector is equivalent to around 80 TWh, which corresponds to more than 19% of the total final energy use in the country (The Swedish Energy Agency, 2003). The transport sector in Sweden is responsible for 40% of the total carbon dioxide emissions. In the rest of the world, as in Sweden, the trend is increasing both in a short and long term perspective, and it is therefore important to use fuels more effectively in vehicles to reduce their consumption.

Fuel cell and hybrid vehicles

Technology advances both through improvements in existing technology and in the form of completely new technologies. Of the latter, looking further ahead than ten years, the automotive industry is pinning considerable hopes on fuel cell vehicles (FCV). Fuel cells convert energy stored in chemical form in the fuel directly into electricity and heat. The working principle is comparable to that of a battery, with the difference that the fuel cell produces electricity and heat as long as it is supplied with fuel. The electrical efficiency of fuel cells can be as high as 60-70%. The waste product is the burnt fuel. Normally the fuel is hydrogen, and mixed with the oxygen in the atmosphere produces water. The operating temperature is too low to produce NOx. Therefore, apart from efficient, fuel cells have the advantage of being non-polluting and silent. The drawbacks of FCV are twofold: first, there is presently no refueling infrastructure; second, there are substantial differences in cost, complexity and safety concerns between a gas station and a liquefied hydrogen refueling station. Technological improvements are needed to address these challenges, which leads to yet another drawback what regards the cost of the technology, both in the vehicle itself and in the fueling infrastructure. An alternative to FCV are ethanol-fueled vehicles or even flexible fuel vehicles (FFV), which use different fuels simultaneously, i.e. ethanol and petrol. Although these vehicles use more or less conventional combustion engine technology, they share the problem with fuel cells in that there is no refueling infrastructure for ethanol nowadays.

The alternative that is likely to achieve a commercial breakthrough in the next ten years is the hybrid electric vehicle (HEV). Hybrid vehicles have two combined systems, i.e. both an electric motor and a combustion engine. A definition of the concept of hybrid vehicle from one of the biggest automotive manufacturers says: “A Hybrid vehicle is a conventionally fueled and operated vehicle that has been equipped with a power train capable of implementing at least the first three of the following four hybrid functions:

- Engine shut-down when power demand is zero or negative.
- Engine down-size for improved thermal efficiency.
- Regenerative braking for recovery and re-use of braking energy.
- Engine-off propulsion at low power (when the engine is inefficient).”

The most important feature of a hybrid vehicle is the possibility of choosing a working point for the internal combustion engine (ICE) independent, or almost independent, of the drivers choice of driving power. The balance between the installed power of the ICE and the electrical machines determines the effectiveness in reduced fuel consumption and emissions, keeping similar driving characteristics as a traditional ICE vehicle of the same type.

There are different types of hybrid vehicles, namely *mild hybrids*, *power hybrids* and *energy hybrids*. Mild hybrids have only 5-15 kW installed electric power, mainly intended for energy generation for electrically driven loads onboard, and for driving at low speeds. Power hybrids have 20-40 kW installed electric power and can therefore contribute significantly to acceleration at any speed, but they still have too low battery capacity (a few km pure electric driving). Finally, energy hybrids have 70-100 kW installed electric power and have therefore energy for long distance driving. The battery is still the weakest point in hybrid vehicles, with low energy density and high price, and therefore the trend to minimize its size. This is the reason for the car industry to focus on mild and power hybrids with relatively small batteries.

The trend in the automotive industry is to use permanent magnet synchronous machines (PMSM) for traction in hybrid vehicles (Kazuaki et al., 2000), due to their high torque to weight ratio. However, the price and the availability of magnet material is an issue that needs to be considered, especially if these machines have to satisfy mass production demands from the car industry in the future. Regarding thermal performance, operation of permanent magnet machines in the field weakening region requires better cooling since the electrical loading in the stator winding is increased. There are also concerns about using an additional current to counteract the magnetic field at high speeds. If this current disappears, due to a control failure or power electronics malfunction, the sudden increase in the back e.m.f. could destroy the power electronics and cause a breakdown in the machine. This risk of over voltage is prevented in an electrically magnetized synchronous machine (EMSM), where the field is provided by a separate coil and the current is in fact decreased in order to weaken the field. A lower current is also advantageous from the cooling point of view. However, there are drawbacks using electrical magnetization in a conventional synchronous machine, such as the need of slip-rings to feed the current into the rotor, and the extra power electronics to control this current. This part of the thesis focuses on the study of an alternative design to eliminate the slip-rings.

1.2 Basic design principle

The structure of the electrically magnetized synchronous machine analyzed more in detail in this part of the thesis is shown in Figure 1.2(a). The novelty of the machine lies in that the slip-rings are removed by placing the field coils in magnetically conducting end-plates attached to both sides of the stator. The iron plates close the magnetic circuit between the stator and the claw-pole rotor. The field coils are wound around the salient part of these plates, remaining therefore stationary. The stator coils are wound around a single tooth, forming a three phase concentrated winding. This has advantages from the manufacturing point of view since the coils can be pressed in order to increase the filling factor (Jack et al., 2000). The teeth have rounded edges in order to decrease the length of the end-windings and improve the heat transfer from the coils through a better fit. A simplified plot of the machine with the flux flow is shown in Figure 1.2(b). The magnetizing flux flows from one of the rotor claw-poles towards the stator and then back to the same claw-pole through the corresponding iron plate, as indicated in the figure. The flux crosses two air-gaps in a complete loop, the radial between the rotor claw-pole and the stator teeth, and the axial between the iron plate and the rotor claw-pole. When the a.c. coils are excited, a flux flows between the teeth in the tangential direction, and perpendicular to the magnetization path in Figure 1.2(b). Therefore, the current loading imposes a three-dimensional flux flow, and the machine is an optimal application for iron-powder technology.

Soft Magnetic Composites

Soft magnetic composite (SMC) materials consist of iron powder particles where the surface of every particle is insulated using a continuous oxide layer (Skarrie, 2001). The particles are compacted, together with a lubricant and possibly a binder, at high pressure into a bulk material. The lubricant eases compaction and the ejection of the components after compaction, while the binder increases the strength of the material. The lubricant and the binder also provide the insulation between particles. During compaction, internal stresses are generated in the material, which can be relieved with a heat treatment process (curing). This treatment also increases the strength of the material. Conventional uniaxial pressing at ambient temperatures with lubricant additives is readily available for mass production.

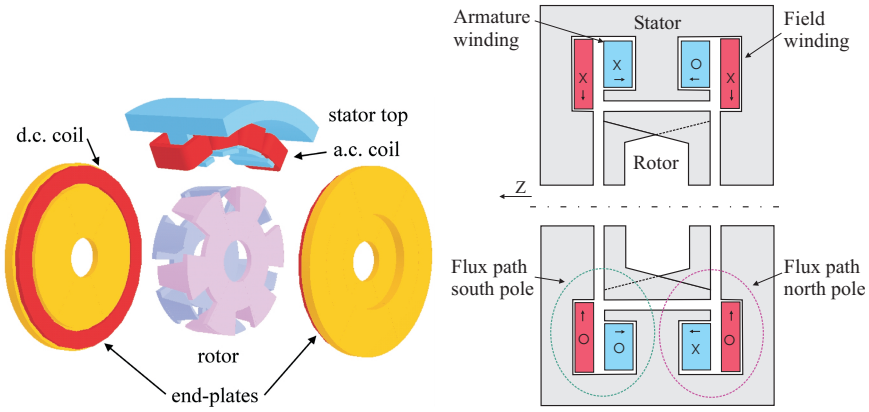

(a) 3-D view. (b) Axial plot.

Figure 1.2: Structure of the EMSM.

Iron powder materials can be considered as magnetically, thermally and mechanically isotropic in their behaviour. Due to the small insulated powder particles the properties are uniform in the bulk material. The magnetic isotropy gives enormous flexibility in electrical machine design, enabling new topologies exploiting 3-D flux paths rather than being constrained to the 2-D flux flow in laminated machines. The main drawbacks of SMC compared to laminations are the smaller permeability (maximum 800 vs. >3000) and the higher iron losses at practical frequencies. This is illustrated in Figure 1.3, which shows a plot with the BH curve for a typical laminated material and for the iron powder used in this thesis, Somaloy^{TM} 500 + 0.6% LB1. There are also practical limits on shapes that can be pressed, e.g. 6:1 aspect ratio (Jack, 2003). Simply replacing an existing design using laminations by SMC is bound to be worse in performance and probably more expensive. In general, SMC materials are more conveniently used in machines with separate excitation, since the demands on the permeability of the magnetic material is lower compared to machines without separate field provision. Apart from building complex 3-D structures, such as claw-poles, SMC can also be used to improve the tooth shapes, decreasing the amount of copper by decreasing the length of the end-windings. The bet-

ter fitting between the coil and the teeth allows increased copper filling factor and heat transfer to the core, which can be further increased by pressing the coils. The smoother tooth surface also makes possible to reduce the slot wall insulation. All this allows to change the shape of the machine to improve the overall product, e.g. smaller and easier to make. The material can also be tailored for a specific application by changing the composition of the powder and adapting the fabrication process. Looking at environmental aspects the material waste can be minimized because of the pressing. The brittleness of the material (strength around 50-100 MPa TRS) simplifies the separation of the core from the winding when recycling.

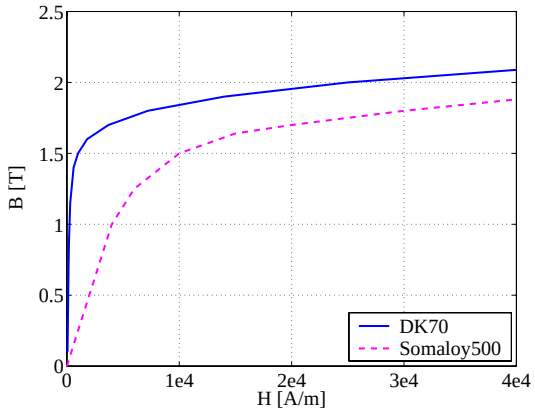

Figure 1.3: Comparison between the BH curve in laminated material (DK70) and SMC (Somaloy 500 + 0.6% LB1).

1.3 A novel HEV application

Today's ICE descends from the end of the 19th century. Since then, its development has been characterized by stepwise improvements and increasing fine-tuning of the basic principle. A subsystem that during this long evolution has been kept more or less unchanged is the crankshaft movement. The reason for this is that this way of controlling the movement of the pistons has been simply the best. For direct driven vehicles, the transmission of the forward and backwards movement of the pistons to a rotating shaft has been a simple and natural mechanism. When the ICE is used as a primary energy converter, i.e.

fuel into electricity in a hybrid system, it is no longer obvious that the classical crankshaft movement and flywheel are the best alternatives. There might be other waveforms that give better engine performance (Blarigan et. al, 1998).

The basic thought behind the novel HEV application was to analyze what improvements could be done in the efficiency and emissions in todays vehicles if the piston movement could be controlled freely by electrical means. The efficiency of the combustion process and the emissions are affected by the pressure and the temperature profiles in the combustion chamber, which in turn are determined by the trajectory that the piston describes. A free piston movement can be realized in practice for example by using the electro-mechanical system presented in Figure 1.4(a). The piston is connected to two plates, one of them mounted on the shaft of the electrical machine and the other represents the crankshaft itself. The piston can move freely along the cylinder by rotating both shafts independently in any direction at any speed. An example is shown in Figure 1.4(b), where the stroke is plotted as a function of the crankshaft angle (CAD). The wave referred to as the 'equal speed' curve corresponds to a rotation of both shafts in the same direction and with the same speed. This gives a waveform similar to the one obtained from a conventional combustion engine. The wave referred to as the 'double speed' curve is obtained by rotating both shafts in the same direction but one with double the speed as the other. It is thus illustrated how the degrees of freedom in the ICE can be increased with this configuration.

Alvar motor

In order to explore the idea of the free piston movement, it is cost-effective to try the idea using a known mechanical solution, rather than constructing a completely new system. The Alvar motor shown in Figure 1.5 was found very appropriate. This motor is a Swedish invention of Alvar Gustavsson, from Skärblacka, Östergötland. The idea behind this combustion engine was to achieve a variable compression ratio, which is a way of increasing the efficiency in the Otto motor at partial load. The main difference compared to a conventional ICE lies in the cylinder head, where there is room for an extra crankcase, crankshaft and cylinders. These cylinders are connected to the combustion chamber, and the space required is obtained compromising in the size and location of the valves. Typically, the top cylinder has half the bore and stroke as the base engine. The compression volume in the motor can be changed by adjusting the synchroniza-

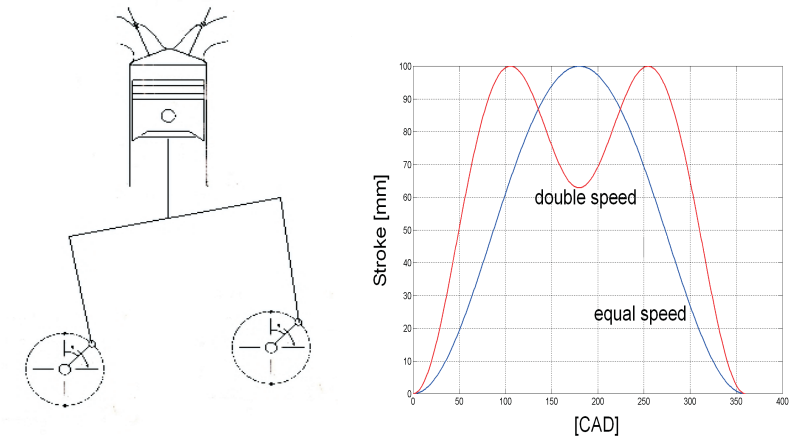

(a) Electro-mechanical system (b) Comparison of piston movements

Figure 1.4: Alternative piston movement.

tion between the two crankshafts, which in turn affects the compression ratio. The unique feature in the Alvar motor is that the extra crankshaft (secondary shaft) rotates with half the speed than the primary shaft, which allows to control the emissions and provides a higher expansion and compression ratio. Previous studies have demonstrated the potential of the Alvar motor as a machine with variable compression ratio (Stewart, 1997), (Erlandsson, 1998), (Wong et. al, 1998), (Erlandsson et. al, 1998).

The secondary shaft of the Alvar motor can be coupled to an electrical machine, which can be controlled to achieve the desired piston movement, as it was done with the system in Figure 1.4(a). The Alvar motor available was based in a Volvo B5254 FS motor. Four of the five cylinders in the engine block were deactivated, using only one for the experiments. The displaced volume is around 0.5 liters per cylinder, and the compression could be changed from 6:1 to 15:1. The study of the optimized combustion cycle and the experiments were carried out by Stenlåås (2004). Simulations were performed in order to find the torque requirements for the electrical machine to adapt the piston cycle, and the results are shown in Figure 1.6. This figure shows the torque as a function of a

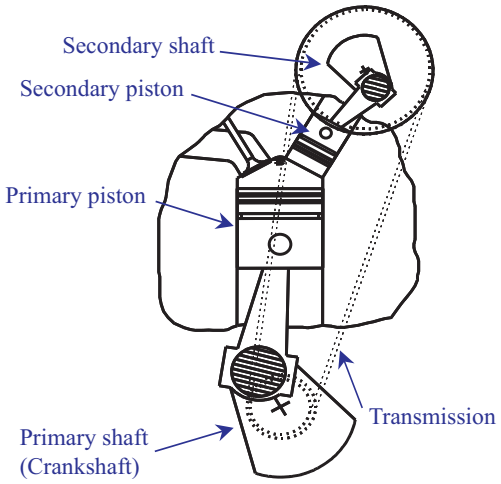

Figure 1.5: Alvar motor plot.

normalized mechanical angle for one revolution of the electrical machine, and a speed of 500 r.p.m. It can be observed that the peak torque is quite high, 108 Nm, while the continuous torque calculated using (1.1) is much lower, 24.5 Nm. These calculations assumed that the inertia of the electrical machine was $0.6{\cdot}10^{-3}$ kg·m^2. It is important to have a low inertia in the secondary shaft and in the electric motor to allow quick changes of the volume of the combustion chamber during the short period when the combustion takes place.

$$T_{rms} = \sqrt{\frac{1}{t_{cycle}} \int_0^{t_{cycle}} T^2(t)dt} \tag{1.1}$$

It was realized that the requirements for the Alvar motor application could not be fulfilled with the electrical machine presented in section 1.2. The principle of having magnetically conducting end-plates implies that the machine should be short, in order to minimize the magnetization path and thus the leakage. In a short machine, the rotor diameter needs to be high in order to increase the torque output, which also increases its inertia. It was therefore decided that a commercial servo motor should be used instead to implement the modified

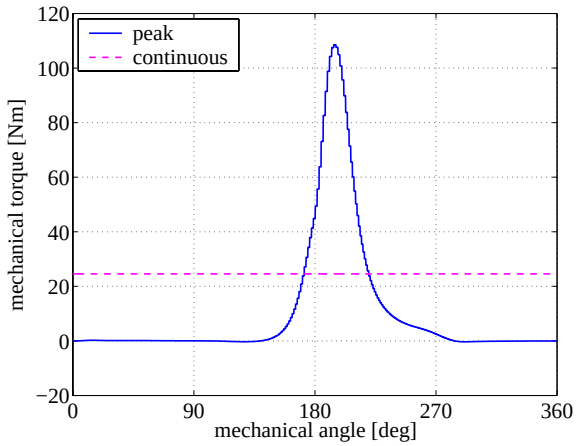

Figure 1.6: Torque requirements for the Alvar application.

combustion cycle using the Alvar motor principle. The study and development of the electrical machine presented in this thesis was carried out independently, and the machine was down-scaled so that it could be easily tested with the available equipment and laboratory facilities.

The commercial machine used for the Alvar application had an inertia of $2.2{\cdot}10^{-3}$ kg·m^2, and the total inertia including the secondary shaft and other parts became $4.2{\cdot}10^{-3}$ kg·m^2, almost double the value used in the simulations. This higher inertia limited the dynamic characteristics, i.e. how fast the compression or volume ratio can be changed during combustion. Nevertheless, experimental and simulation results showed that the possibility of affecting the emissions by adjusting the piston movement are limited, without compromising the efficiency, and not cost-effective. The reader is referred to (Stenlåås, 2004) for a detailed and extensive description of the theory, simulations, experiments and conclusions of the study.

1.4 Objectives and contributions

The main objective of this part of the thesis is to explore the possibilities of using SMC to modify the conventional design of electrically magnetized synchronous machines by removing the coils from the rotor, and therefore also the slip-rings.

A prototype has been built based on this idea and tested.

A magnetic equivalent circuit (MEC) model has been developed for the optimization of the prototype design, and it allows backwards and forward rotation of the rotor mesh. Non-linearities have been included in the model using an iterative approach based on the linearisation of the BH curve, which proves to be very fast and accurate.

The traditional leakage paths in claw-pole machines are modified in the prototype design because of the magnetically conducting end-plates. A sensitivity study has been carried out in FEM to assess how different permanent magnet materials can be used to minimize the leakage from the rotor claw-poles. The study considers machines with 12, 16, 20 and 24 poles.

The prototype design has been compared by simulation to three alternative machines, an outer rotor EMSM, a conventional EMSM, and a surface mounted PMSM. The comparison has been carried out for the same temperature rise in the windings, and thermal models were developed for each machine to determine the maximum current loading. The performance of the machines was evaluated using the 3-D computational finite element method (FEM). This method has also been used to calculate the iron losses in the machines using a detailed formulation that includes both alternating and rotational field components.

Finally, an idea consisting of feeding the field winding from the rectified three phase armature currents at the neutral point (series magnetization) has been tested with the prototype machine. In this way the d.c. power source for the field winding can be removed.

1.5 Outline

The material in Part I is divided in eight chapters. In the first Chapter the structure of the machine has been described, as well as the application where the machine was initially meant to be used. The rest of the chapters are focused on different aspects related to the design, modelling and testing of the electrical machine.

In Chapter 2, the MEC model of the machine is described, together with the method to include non-linearities in the model. This model is used to optimize the machine and to assess the shape of the torque response. The results are validated with FEM calculations.

In Chapter 3, the FEM model is presented. The calculation of the iron

losses in FEM considering alternating and rotational field components is also described. The losses are calculated at load and no load in the stator and in the rotor as a function of the harmonic number.

In Chapter 4, the thermal model is presented, together with the electrical calculations. Heat transfer theory is used to calculate the heat transfer coefficient in the water-cooled machine, as a function of the properties of the flow and the geometry.

In Chapter 5, alternatives to reduce the high leakage in the machine are studied. A sensitivity analysis is carried out for machines with different number of poles.

In Chapter 6, three alternative machine topologies are studied. Basically, a similar analysis to that described in Chapter 3 and Chapter 4 is now carried out with the new topologies, and their performance is compared to the original machine by simulation.

In Chapter 7, the construction of the prototype is described. Measurements are carried out in order to assess the characteristics of the machine and validate the electromagnetic and thermal models. The concept of series magnetization is also tested.

Finally, Chapter 8 presents a summary of the most important results and conclusions of this part of the thesis, together with some suggestions for future work in this area.

Chapter 2

Magnetic-Equivalent-Circuit model

2.1 Introduction

One of the numerical methods employed for electrical machine analysis is the magnetic equivalent circuit (MEC) approach. This method is well described by Ostović (1989). Basically, the complex magnetic circuit of the machine is transformed into a simple, resistive electrical network, which is solved using electric circuit theory. The fewer number of elements compared to the finite element method (FEM) decreases considerably the computation time, although the accuracy of the solution is also compromised. For highly saturated devices, the number of elements in the MEC model may need to be increased (Moallem and Dawson, 1998). The advances in computing technology during the last decade have contributed to extend the use of FEM for the analysis of electromagnetic devices, specially what regards two-dimensional problems. However, the CPU time needed to solve three-dimensional problems is still prohibitive, which jeopardizes the use of FEM for 3D optimization (Ostović et al., 1999).

In this chapter, a 3D MEC model has been developed for the electrically magnetized machine presented in Chapter 1. This model is used for the optimization of the machine using a non-linear iterative method based on the linearisation of the BH curve. This method allows very fast convergence. The MEC model has been extended to accomplish forward and backward rotation, which is used for the assessment of the torque response. Results compared to FEM simulations demonstrate the feasibility of the MEC model for predicting

the performance of the machine.

Due to the initial specifications on the electrical machine for the Alvar motor application, the study and the optimization was carried out for a machine with an outer diameter of 400 mm and an axial length of 152 mm. However, the final design that is analyzed in the next chapters was down-scaled to half the size in the axial and radial directions, maintaining exactly the same proportions.

2.2 MEC model of the EMSM

The MEC model of the machine is shown in Figure 2.1. The machine has 12 poles and 18 teeth, and the MEC model represents one pole pair at the position of maximum torque along the negative pole period. Iron and air reluctances are coloured in grey and white respectively. Each reluctance is identified with a number which represents the main mesh that the reluctance belongs to. There are three main meshes, associated with the three stator teeth. The reluctances linking the main meshes are identified with their respective numbers. The following iron reluctances were considered: the tip of the stator tooth (Rsc), the body of the stator tooth (Rps), the yoke in the axial direction (Ryx) and in the tangential direction (Ryp), the end-plates at the level of the stator teeth (Rss) and at the level of the rotor (Rsra, Rsrb), the rotor plates attached to the claw-poles (Rcra1), and the claw-poles (Rcra2). There are four airgap reluctances (Rgr), and 'Rgr1' and 'Rgr4' are connected together since the first stator tooth is located exactly between the two claw-poles. They also have double the value than the rest of the airgap reluctances. The leakage reluctances are identified with the symbol 'σ'. The following leakage reluctances were considered: between the stator tooth tips (Rcs_σ), between the stator tooth tips and the end-plates (Rsf_σ), between the sides of the claw-poles (Rcr_σ), between the tips of the claw-poles and the end-plates (Rsr_σ), and the reluctance for the zig-zag leakage through the claw-poles (Rlea). The equations used to calculate the reluctances are included in Appendix A. The m.m.f. of the armature coils wound around the stator teeth is referred to as 'Fph'. They contribute to drive the flux through the four meshes adjacent to one stator tooth, and therefore a source with one quarter of the total m.m.f. in the corresponding coil was placed in each one of these meshes. The m.m.f. of the field coils wound around the end-plates is referred to as 'Fex'. They contribute to drive the magnetizing flux in the axial direction and they are located between the axial core and end-plate reluctances.

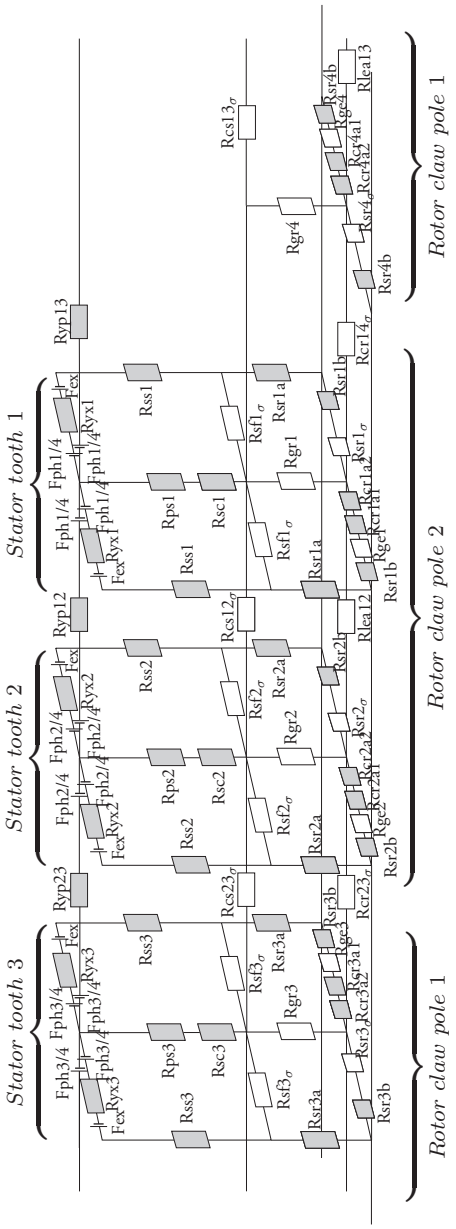

Figure 2.1: MEC model of the EMSM.

2.3 Mesh rotation

The dynamic characteristics of the machine can be studied by rotating the rotor mesh with respect to the stator. When the rotor is rotated, the radial and axial airgap reluctances, together with the axial leakage paths between the claw-poles and the end-plates, are modified at each step. The position of maximum torque along the negative pole represented in Figure 2.1 will be referred to as *position zero*. From this position, it was desired that the rotor could rotate 90 electrical degrees forward and backward in steps of 15 electrical degrees. Forward rotation will be linked to counter-clockwise rotation, i.e. from right to left in Figure 2.1, and the opposite is true for backward rotation. The arrangement used for forward rotation is shown in Figure 2.2, and for backward rotation in Figure 2.3. The rotor mesh below the first stator tooth has been modified grouping together 'Rsr1b' and 'Rsr4b' from Figure 2.1 into 'Rsr1b' in Figures 2.2 and 2.3.

In general, the principle for rotating the rotor mesh is that each one of the radial and axial air reluctances linking the stator and the rotor are by-passed by another reluctance from the same origin in the stator side but ending at the point in the rotor mesh which approaches with the rotation. The original reluctances linking the stator and the rotor at position zero will be referred to as *direct reluctances* and their value as *nominal reluctance value*. The new reluctances added to accomplish rotation will be referred to as *by-pass reluctances*. The by-pass reluctances for the radial airgap are 'Rgr21', 'Rgr32', and 'Rgr13' for forward rotation, and the same names but swapping the numbers for backward rotation. The rest of the new reluctances above the rotor mesh are by-pass reluctances for the axial airgaps, including leakage. These reluctances have the same name as the direct reluctances that they by-pass, followed by a number which indicates the part of the stator mesh (first number) that is linked to the part of the rotor mesh (second number) that is approaching.

For convenience, it is important to note that each stator tooth will see exactly the same rotor part as the adjacent tooth after eight steps in any direction. This ratio is easily obtained from the step angle and considering that the stator is divided in three parts, each one associated with one tooth, spanning 120 electrical degrees. Therefore, the direct and by-pass reluctances will be increased and decreased respectively by one eighth of the nominal reluctance value after each rotation step. At position zero, the direct reluctances will have the nominal value and the by-pass reluctances will be infinite. From the first step to the seventh, the direct reluctances will be increased from 8/7 to 8/1 the nominal

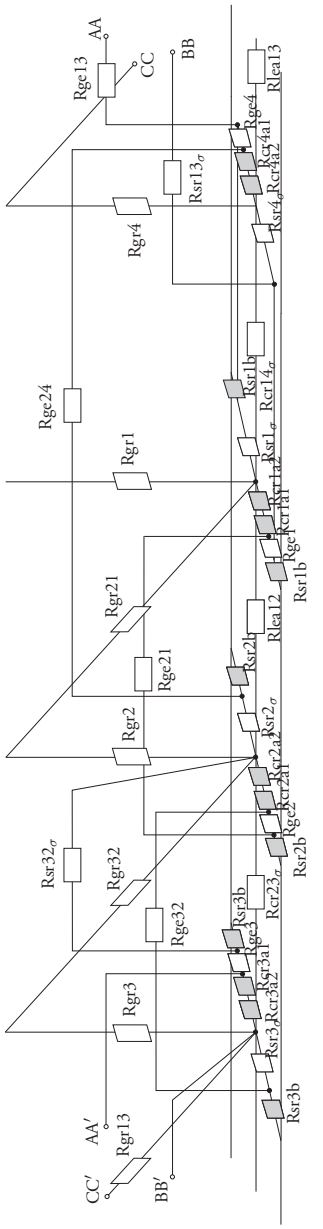

Figure 2.2: Arrangement for forward rotation.

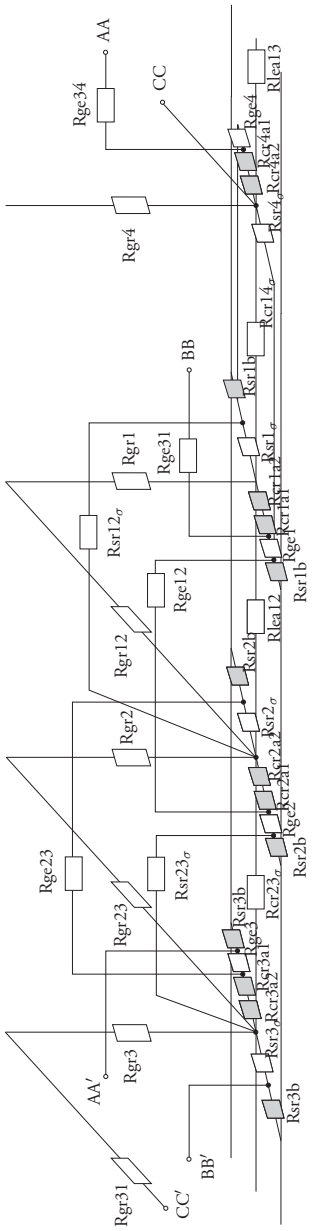

Figure 2.3: Arrangement for backward rotation.

value, and the by-pass reluctances will be decreased from 8/1 to 8/7 the nominal value. After eight steps, the direct reluctances will be infinite and the by-pass reluctances equal to the nominal values.

2.4 Non-linear iterative method

The flux density in the iron reluctances is a non-linear function of the field strength. The BH curve of the composite material (or any iron material) can be divided in a series of linear intervals, as shown in Figure 2.4(a). Each one of these intervals is linearly extrapolated until they intersect with the B-axis at a certain level, depending on their slope. The intersection level and the slope will be referred to as B_{0fe} and μ_{fe} respectively. For simplicity, let us assume a magnetic circuit with a yoke and an airgap, excited with a magnet and a coil, as shown in Figure 2.4(b). The iron, the magnet and the airgap in this structure are considered to form a single reluctance element each. The flux density in the iron at any interval can be expressed as in (2.1). The flux density in the permanent magnet is given by (2.2). Assuming a linear characteristic for the magnet, B_{0pm} represents the remanence of the material. Otherwise, the BH curve of the magnet could be linearised in a similar way as it is done for the iron. The flux density in the air is given by (2.3). These flux densities can also be expressed as a function of the flux through their respective area, as in (2.4).

$$B_{fe} = B_{0fe} + \mu_0 \cdot \mu_{fe} \cdot H_{fe} \tag{2.1}$$

$$B_{pm} = B_{0pm} + \mu_0 \cdot \mu_{pm} \cdot H_{pm} \tag{2.2}$$

$$B_{\delta} = \mu_{\delta} \cdot H_{\delta} \tag{2.3}$$

$$B_{fe} = \frac{\phi_{fe}}{A_{fe}} \qquad B_{pm} = \frac{\phi_{pm}}{A_{pm}} \qquad B_{\delta} = \frac{\phi_{\delta}}{A_{\delta}} \tag{2.4}$$

Applying Ampere's law to the circuit yields (2.5). Including H_{fe} from (2.1), H_{pm} from (2.2), and H_{δ} from (2.3) into (2.5), and using the equivalence from (2.4) yields (2.6). Assuming that there is no leakage flux, then the flux flowing through the iron, the permanent magnet and the airgap is the same, denoted by ϕ. No fringing flux is assumed in the airgap. Equation (2.6) can be re-written as in (2.7). Leaving ϕ alone yields (2.8), where R_{fe}, R_{pm} and R_{δ} are the iron, magnet and air reluctances respectively, given in (2.9). Equation (2.8) shows that both the iron and the permanent magnet have an 'internal m.m.f.' source.

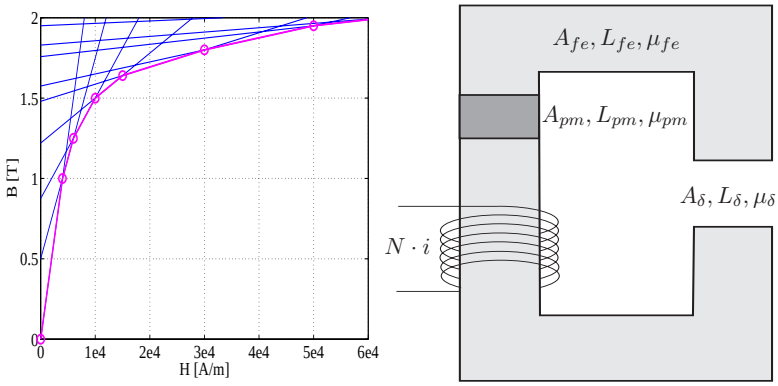

(a) Linearised BH curve (b) Yoke with coil and magnet

Figure 2.4: Linearised BH curve (Somaloy500) and yoke structure.

For the non-linear iron, this m.m.f. is a function of the values of $B0_{fe}$ and μ_{fe} in the interval where its flux density is located.

$$N \cdot i = H_{fe} \cdot l_{fe} + H_{pm} \cdot l_{pm} + H_\delta \cdot l_\delta \tag{2.5}$$

$$N \cdot i = \frac{\frac{\phi}{A_{fe}} - B_{0fe}}{\mu_0 \cdot \mu_{fe}} \cdot l_{fe} + \frac{\frac{\phi}{A_{pm}} - B_{0pm}}{\mu_0 \cdot \mu_{pm}} \cdot l_{pm} + \frac{\frac{\phi}{A_\delta}}{\mu_0} \cdot l_\delta \tag{2.6}$$

$$N \cdot i = \frac{\phi}{\mu_0}\left(\frac{l_{fe}}{A_{fe} \cdot \mu_{fe}} + \frac{l_{pm}}{A_{pm} \cdot \mu_{pm}} + \frac{l_\delta}{A_\delta}\right) - \frac{B_{0fe}}{\mu_0 \cdot \mu_{fe}} \cdot l_{fe} - \frac{B_{0pm}}{\mu_0 \cdot \mu_{pm}} \cdot l_{pm} \tag{2.7}$$

$$\phi = \frac{N \cdot i + \frac{B_{0fe}}{\mu_0 \cdot \mu_{fe}} \cdot l_{fe} + \frac{B_{0pm}}{\mu_0 \cdot \mu_{pm}} \cdot l_{pm}}{R_{fe} + R_{pm} + R_\delta} \tag{2.8}$$

$$R_{fe} = \frac{l_{fe}}{\mu_0 \cdot \mu_{fe} \cdot A_{fe}} \quad R_{pm} = \frac{l_{pm}}{\mu_0 \cdot \mu_{pm} \cdot A_{pm}} \quad R_\delta = \frac{l_\delta}{\mu_0 \cdot A_\delta} \tag{2.9}$$

This formulation can be easily extrapolated to the MEC model of the machine. At position zero, the MEC model contains 43 iron reluctances and 25

air reluctances, and a number of 27 fluxes need to be calculated. When the rotor mesh is rotated, the MEC model contains 9 additional air reluctances, and 36 fluxes need to be calculated. The flux density in one iron reluctance *k* at any interval can be expressed as in (2.10). Applying Ampere's law to the mesh containing that reluctance yields (2.11), where 'w', 'n' and 'r' are the number of winding m.m.f.'s, iron and air reluctances included in that mesh respectively. Following the same procedure explained above, the flux in a mesh 'x' can be expressed as in (2.12).

$$B_{fe}(k) = B_{0fe}(k) + \mu_0 \cdot \mu_{fe} \cdot H_{fe}(k) \tag{2.10}$$

$$\sum_{h=1}^{w} N(h) \cdot i(h) = \sum_{k=1}^{n} H_{fe}(k) \cdot l_{fe}(k) + \sum_{p=1}^{r} H_{\delta}(p) \cdot l_{\delta}(p) \tag{2.11}$$

$$\phi(x) = \frac{\sum_{h=1}^{w} N(h) \cdot i(h) + \sum_{k=1}^{n} \frac{B0_{fe}(k)}{\mu_0 \mu_{fe}} l_{fe}(k)}{\sum_{k=1}^{n} R_{fe}(k) + \sum_{p=1}^{r} R_{\delta}(p)} \tag{2.12}$$

Equation (2.12) is solved iteratively for all the meshes using MATLAB, and the procedure is described in the flowchart shown in Figure 2.5. In the definition stage, the BH curve is linearised, and the limits for the intervals are calculated together with their slopes and the extrapolation at $H_{fe} = 0$. In the initialization stage, all the reluctances are set to be within the first interval (linear solution), and thereafter the iteration process is started. The reluctance (R) and the m.m.f. (F) for each element are calculated using the updated value of μ_{fe} and $B0_{fe}$ after each iteration. The total m.m.f. matrix (F_{total}) is obtained by adding the internal m.m.f. of each element within a mesh to the m.m.f. value of the coils that are included in that mesh. The flux matrix is calculated dividing the total m.m.f. matrix by the reluctance matrix using the back-slash operator in MATLAB. The flux densities are then calculated at each element and compared to the limits of the corresponding interval. If they are located within these limits, the proper H_{fe} and μ_{fe} are calculated using the non-linearised BH curve ($BH_{material}$). If the value is higher than the upper limit or lower than the lower limit, the values of $B0_{fe}$ and μ_{fe} are updated to the corresponding values of the next or the previous interval respectively, and the program moves to the next iteration. It was observed that the process converged after less than 20 iterations (N), taking less than 2 seconds in computer equipped with a 1.2

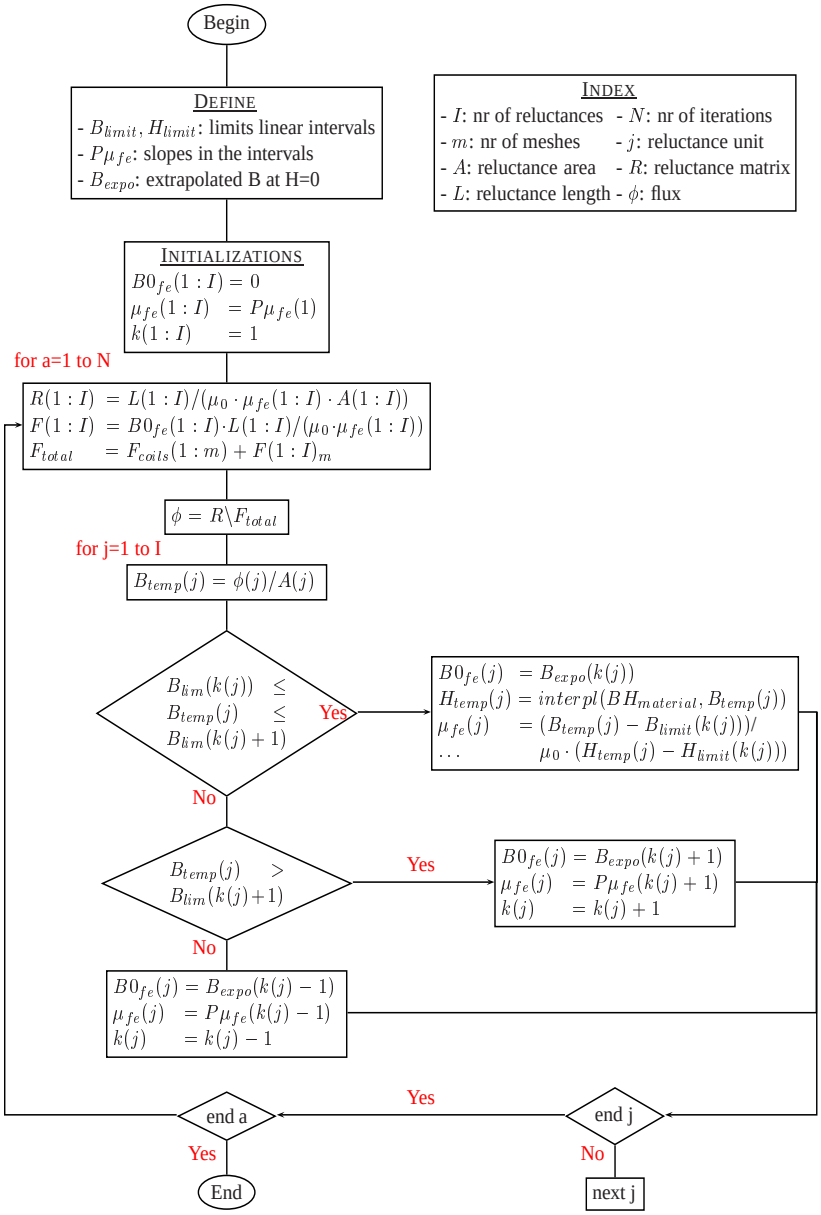

Figure 2.5: Flowchart for the non-linear iteration process.

GHz Pentium III processor and 1 Gb RAM. The results of the flux densities obtained at the elements of the MEC model (Figure 2.1) are shown in Figure 2.6, at no load and load. The limits of the linearised intervals are also indicated in the figures. It can be observed that most of the reluctances are located in the first (linear) interval.

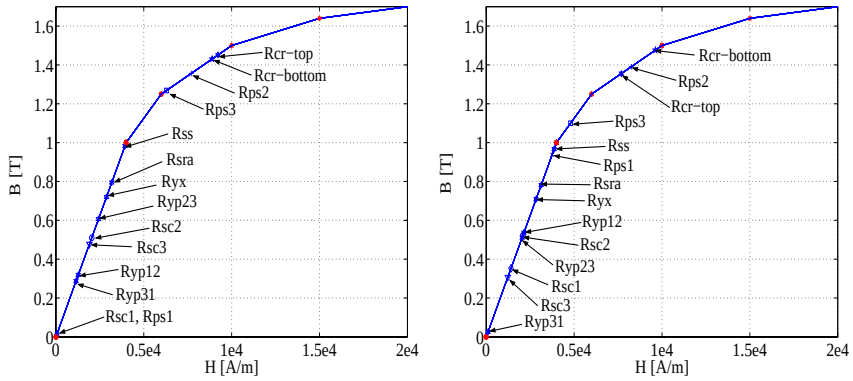

(a) No load (b) Load

Figure 2.6: Flux densities at the elements in the MEC model.

2.5 FEM and MEC results

The machine was simulated using finite element (FE) analysis. The details about the FE model set-up will be described in Chapter 3, but some results will be included in this section for comparison. The FE model reproduced the same part of the machine as the MEC model, and it was solved applying symmetric boundary conditions at the edges. The number of elements was 451248. The rotor mesh could be rotated in steps of 2.5 degrees, comprising 12 steps per pole. One simulation at a fixed rotor position required 1.5 hours CPU time using the same computer equipment described above for the MEC model implementation.

Flux distribution

The flux flow through the teeth and the end-plates was evaluated for the FEM and MEC simulations at position zero, both at no load and load. The results are summarized in Table 2.1. The sign indicates the direction of the flux, which was considered positive in the radial direction outwards. In the table, the linking flux is obtained adding the absolute value of the flux flowing through the three teeth, and the total flux is obtained adding the flux through both end-plates. The leakage is calculated as the percentage of the total flux that does not contribute to the linking flux. The results show a very good agreement at no load. At load there are more discrepancies in the values at the teeth. This may be due to the assumption that the m.m.f. from the armature coils contributes equally to the flux flow in the four meshes adjacent to one tooth. Nevertheless, the results are acceptable especially comparing the total, linking and leakage fluxes. In both cases the difference in the leakage predicted from the FEM and MEC simulations is less than 2%.

Torque response

It was desired to assess the shape of the torque response, and this could be achieved by rotating the mesh. The points 90 electrical degrees before and after position zero will be referred to as *position minus six* and *position six* respectively, indicating the number of steps that the rotor mesh needs to be rotated until that position. The change of torque between two positions was calculated using (2.13), where θ is the angle rotated. In this equation, as a first approximation, W_{mag} was calculated from the magnetic energy in the system, when in fact it should be the co-energy. However, in a first stage the effects of magnetic saturation in the torque production were neglected. This is not too unreasonable since most of the reluctances in Figure 2.6 are located in the first interval, indicating that the machine is not too saturated. Under these circumstances the magnetic energy and co-energy were assumed to be similar. The energy after each step was calculated using (2.14), which is derived from the equivalence between the equations for the magnetic energy density w_{mag} in (2.15). In these equations, B represents the flux density in the selected reluctance element, and V its volume.

Table 2.1: Flux results [wb] from the FEM and MEC simulations

	No Load		**Load**	
Part	FEM	MEC	FEM	MEC
Tooth 1	-4.37e-7	-1.88e-5	-8.97e-4	-6.93e-4
Tooth 2	9.61e-4	10.02e-4	11.81e-4	10.28e-4
Tooth 3	-9.62e-4	-9.37e-4	-1.86e-4	-6.02e-4
Plate1	32.37e-4	31.85e-4	29.02e-4	32.90e-4
Plate2	-32.36e-4	-32.31e-4	-29.51e-4	-30.23e-4
Linking	19.24e-4	19.58e-4	22.64e-4	23.23e-4
Total	64.74e-4	64.16e-4	58.51e-4	63.13e-4
Leakage	70.27%	69.47%	61.30%	63.20%

$$\Delta T = \frac{\Delta W_{mag}}{\Delta \theta} \tag{2.13}$$

$$W_{mag} = \frac{1}{2}\frac{1}{\mu_0}\sum_{i=1}^{N_{gap}} B_i^2 \cdot V_i \tag{2.14}$$

$$w_{mag} = \frac{1}{2}\frac{1}{\mu_0}B^2 \qquad w_{mag} = \frac{W_{mag}}{V} \tag{2.15}$$

It can be shown that the torque does not depend on the state in the iron and/or leakage paths, but on the conditions in the airgap only (Ostović, 1989). Furthermore, the energy stored in the axial airgaps does not contribute to the torque production in the direction of rotation. Therefore, equation (2.14) was only evaluated in the direct and by-pass reluctances along the radial airgap (N_{gap}). It should be noted that the torque expression obtained combining (2.13) and (2.14) is equivalent to (2.16) (Miller, 1993), where i is the current, and L the inductance at a particular position.

$$\Delta T = \frac{1}{2} i^2 \frac{\Delta L}{\Delta \theta} \tag{2.16}$$

A value of zero torque was assigned to positions six and minus six. The MEC model for backward rotation was used to calculate the torque change

between positions zero and minus six, starting from position minus six. The model for forward rotation was used between positions zero and six, starting from position six. The results from the FEM and MEC simulations are shown in Figure 2.7. In this figure, the response from MEC has been scaled to fit the amplitude of the FEM response, since it was observed that the method described above was quite sensitive to the dimensions of the radial airgap reluctances. In fact, a change in this area affected significantly the amplitude of the torque response, while the overall shape was little affected. In order to fit the amplitude of the FEM response, the area of the radial airgap reluctances was increased by 45% with respect to their original value. The airgap reluctances affect directly the values of the magnetic energy in (2.14) or the inductance in (2.16). An acceptable error in reluctance approximation can produce too high an error when it is differentiated, thus giving an inaccurate result for torque. Overall, it can be observed that the shape of the torque response is reasonably predicted. It should be pointed also that the area of the radial airgap reluctances in the MEC model corresponds to that below the tip of the teeth, and their length is the airgap length. Having a slot opening of 33% the tooth pitch, the fringing effects in the airgap region may not be negligible, which in turn would increase the effective reluctance area.

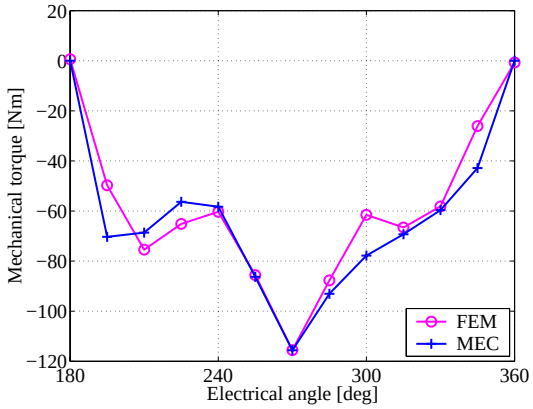

Figure 2.7: Torque response from FEM and scaled from MEC.

2.6 Optimization

The results presented in the previous section were calculated for a geometry obtained from an optimization process. The optimization criteria was to achieve the maximum possible torque for a given volume, and within the specified thermal constrains. Simple cut and try was used first in FEM to set the approximate dimensions of the different components. Thereafter, an optimization routine was implemented in MATLAB using the MEC model in Figure 2.1. Although the torque could not be calculated directly from this model, the goal was to maximize the linking flux and the armature current for a given copper filling factor in the coils (0.75 assuming pressed windings). For optimization, the iron losses were calculated using Steinmetz formulation (2.17), in W/m^3, where f is the frequency and B the flux density. The parameters k_h and k_{dyn} account for the hysteresis and dynamic losses. The dynamic losses consist of eddy current and anomalous losses. These parameters together with n, n_B and n_f have been empirically calculated by Skarrie (2001) for the iron powder used in the machine ($k_h = 1160$, $n = 1.6$, $k_{dyn} = 57$, $n_B = 1.85$, $n_f = 1.40$).

$$P_{fe} = k_h \hat{B}^n f + k_{dyn} \hat{B}^{n_B} f^{n_f} \tag{2.17}$$

The calculation was carried out at no load and only for the fundamental frequency component, so the losses in the rotor were neglected. It was assumed that the flux variation anywhere else in the machine followed a sinusoidal shape with that frequency. This is clearly not true, but predicting analytically the real flux change pattern at different parts of the machine is difficult and time-consuming. Instead, this will be done using FEM in Chapter 3. It was assumed that the heat could be removed from all the external surfaces of the machine with a rate of 5000 W/m^2. In fact, this factor depends of course on the temperature gradient between the surface and the coolant, the speed of flow and the geometry of the cooling surface, among others. A detailed formulation for the calculation of the heat transfer coefficient from the different surfaces will be described in Chapter 4. Finally, it was assumed that the iron losses in the teeth and the back core, together with the a.c. copper losses, were cooled through the external cylindrical surface. The iron losses in the end-plates together with the d.c. copper losses were cooled through the surface area of the end-plates.

The volume of the machine was kept constant during the optimization process. The rest of the design variables were optimized in groups. The first group

included the stator yoke, the axial length of the stator teeth body, the thickness of the end-plates at the yoke connection, and the thickness of their salient part, where the magnetizing coils are resting. Changing this last dimension modified the magnitude of the magnetizing current, since the available space for the coil was affected. The axial length of the stator teeth also determined the magnitude of the load current, since it affected the space available for the accommodation of the end-windings. An iteration process was set-up for each geometry to find the current loading in the coils corresponding to the maximum copper and iron losses that could be dissipated. For a given current, the iron losses were calculated from the flux density at each reluctance element in the MEC model, which was obtained using the non-linear iterative method presented in section 2.4.

The second group of variables included the thickness of the rotor body and the shape of the claw-pole. This shape was defined by the thickness and the angle span of both the base and the tip of the claw-pole. Finally, the thickness of the tooth tip, the slot opening, the axial and radial airgap lengths, and the shaft diameter were optimized individually. The length of the radial and axial airgaps was 0.6 mm and 0.5 mm respectively. The radial airgap diameter was 270 mm. The slot opening was 33% of the tooth pitch to reduce the leakage between the teeth. This will of course increase the ripple in the machine, and it was expected that it could be compensated electronically introducing a suitable harmonic in the currents from the control system. It was observed that some material could be removed from the surface of the end-plates closer to the shaft. The weight of the active parts of the machine was 102 kg, distributed in 77.7 kg of iron, and 24.3 kg of copper (14.9 kg for the armature coils and 9.4 kg for the field coils).

2.7 Conclusions

In this chapter, a method to include non-linearities in MEC models has been presented. The method is based on the linearisation of the BH curve, and it has been applied to calculate the leakage and the torque response in a three-dimensional electrically magnetized synchronous machine. The method provides very fast and accurate results for the flux distribution in the machine at load and no load, predicting the leakage with an error lower than 2% in a few seconds. Modifications to accomplish forward and backward rotation were incorporated in the model. A simplified method was used to assess the shape of

the torque response. It was observed that a change in the area of the airgap reluctances affected significantly the amplitude of the torque response, while the shape was reasonably predicted. Finally, the optimization process has been presented, and the results will be used for the down-scaled prototype, maintaining exactly the same proportions.

Chapter 3

Finite Element model

3.1 Introduction

MEC models are useful during the optimization process of an electrical machine, but more advanced methods are needed to assess more accurately the final characteristics of the design. Today, numerical methods are increasingly used for the solution of electromagnetic fields. There is a variety of commercial computer programs based on the finite element method (FEM) used for this purpose. In this chapter the finite element (FE) model of the machine will be presented, after a short introduction to FEM. Thereafter, the FE model will be used to predict the iron losses in the machine. As it will be shown in Chapter 5, the output torque of the machine is most optimal for a 16 pole design, which will be the configuration used for the final prototype. Therefore, the machine studied in this and next chapters is not only down-scaled compared to the design in Chapter 2 but it also has a higher pole number. The inner and outer radius are 19 mm and 100 mm, and the total length of the machine is 76 mm.

3.2 FEM

The method of the finite elements is a numerical approach by which the general differential equations describing a certain physical phenomena in a structure can be solved in an approximate manner. These equations are assumed to hold over a certain region of the structure, which can be one-, two- or three-dimensional. In fact, the region is divided into smaller parts, so-called *finite elements*, and the approximation is then carried out over each element. This approximation, usu-

ally a polynomial, is actually some kind of interpolation over the element, and it is assumed that the variable is known at certain points within the element, called *nodal points*. The precise manner in which the variable changes between its values at the nodal points is expressed by the specific approximation, which may be linear, quadratic, cubic, etc. The coefficients of the polynomials are chosen in such a way that a variational principle is approximately satisfied. Having determined the behaviour of all elements, they are then patched together, using some specific rules, to form the entire region. The collection of all elements is called a *finite element mesh*. More information about the basic formulation used in FEM can be found for example in (Ottosen and Petersson, 1992).

The emergence of FEM took place in the early 1960's and since then its use has spread to virtually all fields of engineering. The first applications on electrical machine problems were presented in the early 1970's. In the 1980's, the research on numerical field computation methods expanded rapidly, and there are nowadays several commercial program packages available for the computation of two- and three-dimensional magnetic fields and eddy currents. In general, the electromagnetic field is defined by Maxwell's equations, which are a rather simple formulation of the field problem but they are difficult to solve, especially in electrical machines. This is due to the complicated geometry, the time-dependency of the magnetic field, and the non-linearities because of the magnetic saturation of the iron. Furthermore, the equations of the magnetic field are coupled with the electric circuit equations of the windings and the motion of the rotor.

The variable that is solved in electromagnetic FEM is the magnetic potential at the nodes. The solution algorithm is often based on the minimisation of a mathematical function that is related to the stored potential energy in the field. From the node potentials, the parameters of the machine are obtained using different formulations. Surely the most difficult quantity to calculate is the torque, and better formulations are still being developed. The virtual work method is normally approximated evaluating the rate of change of the magnetic coenergy between two positions with respect to the step angle. If the distance is short, the coenergy values at the two positions differs only slightly. Therefore, the accuracy of the result obtained by subtraction may be low, if the errors of the two coenergy values are not similar. A more common method is based on the Maxwell stress tensor, defined in (3.1). It allows to calculate the force acting on all parts within a volume (the rotor) by evaluating a surface integral around the volume (Γ_j). The volume should be totally enclosed by the

surface and the surface itself should span through a nonferromagnetic region (the airgap). The flux density vector $\vec{B}$ is given by (3.2), where B_n is the normal component, B_t is the tangential component, $\vec{n}$ is the unit normal vector and $\vec{t}$ is the unit vector in the direction of the projection of $\vec{B}$ on the tangential plane Γ_j. The calculations using this method may be inaccurate since the error in the direction of the flux density vector is amplified in the force calculation by the multiplication of the flux density components. However, the accuracy can be improved by using higher-order finite elements. A more detailed explanation of the application of the FE method to electric machine analysis can be found in the specialised literature (Hamdi, 1994), (Luomi, 1993), (Zhou, 1993).

$$\begin{aligned}\vec{F} &= \oint_{\Gamma_j} \left(\frac{1}{\mu_0} B_n \vec{B} - \frac{1}{2\mu_0} B^2 \, \vec{n} \right) d\Gamma = \\ &= \oint_{\Gamma_j} \left(\frac{1}{2\mu_0} (B_n^2 - B_t^2) \, \vec{n} + \frac{1}{\mu_0} B_n B_t \, \vec{t} \right) d\Gamma \qquad (3.1) \\ \vec{B} &= B_n \, \vec{n} + B_t \, \vec{t} \qquad (3.2)\end{aligned}$$

3.3 FE model of the EMSM

The FE model was implemented in a commercial package, OPERA 3D. The design procedure was automated in MATLAB using a set of libraries already available to generate the OPERA code for the different steps in the definition of a FE model. To automate the process for a specific design is time-consuming, but once it is completed a new FE model with changes in the original geometry, or in the formulation of the model, can be obtained in a matter of seconds. This is of course very useful for fine-tuning of the design.

The FE model of the claw-pole machine was divided in two meshes, corresponding to the part of the machine above and below the airgap. To reduce the size of the model, symmetry was exploited and only one pole pair was modelled. For each mesh a grid of macroelements (facets) was built from a set of circumferential lines of constant radius, corresponding to the radius of the different parts of the machine, and a set of radial lines separated by a constant angle. This angle defined the minimum step of rotation, and it was selected for a resolution of 24 steps per pole-pair. The sides of the facets were then divided into smaller parts, which formed the finite elements. Thereafter the grid was

extruded in a number of steps in the axial direction, forming hexaedral volumes. This shape of the elements was mandatory using the pre-processor module of the program. The material properties were assigned to the facets at the extrusions, which implied that all the finite elements within the volume between two extrusions on one side of the facet shared the same material properties. The model was solved using a magnetostatic analysis, where no eddy currents are induced in the iron, and a total scalar potential was defined for the iron, and a reduced scalar potential for all the air. The conductors were built adapting pre-defined geometries available in the software and incorporated in the mesh. Positive periodic boundary conditions were defined at the facets located in the symmetry planes, with the condition that the normal derivative vanishes at the boundary (Neumann condition). A thin (5 mm) layer of air was defined around the rest of the external surfaces, and the condition that the flux density has only tangential component (Dirichlet condition) was imposed on the air external surface. Finally, the coordinates of the nodes in the grid at each extrusion were modified in the radial, axial and circumferential directions to fit the desired geometry of the machine. A plot of the final 3D grid is shown in Figure 3.1. The finite element mesh of the model will be shown in next sections where the iron losses are analyzed.

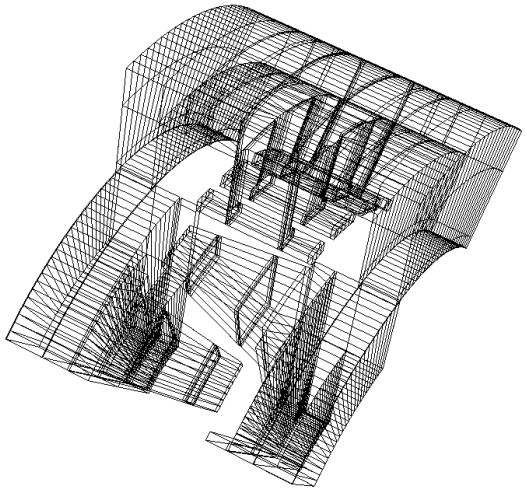

Figure 3.1: Plot of the 3D grid of the FE model.

The mesh continuity has to be ensured over the whole model. Dividing the grids of the two meshes in the same number of divisions in the circumferential direction facilitated the coupling between them through the radial airgap. This airgap was divided into four layer of elements, two located in each mesh. This is recommended since the torque calculations are jeopardized if they are carried out through elements linking materials with very different permeability. The four meshes also allow to compare two alternative paths of integration, through the middle of the second and third layers. The axial airgaps were also divided into four layer of elements. Quadratic elements, with an extra node on each side, were used in the airgaps in order to further increase the accuracy of the fields in these critical regions, while the potential variation in the rest of the elements was assumed to be linear. The non-linearities in the iron were defined with a table containing the values of the BH curve of the material provided by the manufacturer. The total number of elements in the model was 154224, requiring 33 minutes to solve one simulation at load for a certain rotor position. Triplicating the number of elements changed the torque response less than 1%. The post-processing module of the software had in-built functions to perform calculations over a specified path. The torque density was calculated applying the Maxwell stress tensor in Cartesian coordinates using (3.3)-(3.7), where H represents the magnetic field intensity. The calculations were performed over a grid of 50x400 points in the axial and circumferential directions through the middle of the third airgap layer all around the rotor. The total torque was obtained by integrating Tq_z along the grid surface. The action point for the torque was located at the geometrical center of the machine (x_0, y_0, z_0).

$$H_n = H_x n_x + H_y n_y + H_z n_z \tag{3.3}$$

$$H_m = B_x H_x + B_y H_y + B_z H_z \tag{3.4}$$

$$F_x = B_x H_n - n_x \frac{H_m}{2} \tag{3.5}$$

$$F_y = B_y H_n - n_y \frac{H_m}{2} \tag{3.6}$$

$$Tq_z = (x - x_0) F_y - (y - y_0) F_x \tag{3.7}$$

3.4 Iron losses

After copper losses, core losses are generally the second largest component of power loss or inefficiency in electrical machines. They arise from the variation

of the magnetic flux density through the core. In general, the iron losses can be divided into three types depending on the physical background of the loss: hysteresis, eddy current, and anomalous loss. Hysteresis loss is a static loss that is due to the hysteresis of the material. It is the part of the applied energy used to move the microscopic domain walls when they are magnetised, and it is converted into heat instead of being stored in the material. Eddy current and anomalous losses are dynamic losses, both depending on eddy currents in the material, but in different scales. The macroscopic eddy current loss, sometimes referred to as the classical eddy current loss, origins from currents in the material set up by an applied varying magnetic field, while the microscopic eddy current loss, often called anomalous or excess loss, is due to eddy currents generated by domain wall motion. This is caused by the inhomogeneity in the magnetisation between adjacent domains, or domain groups depending on their size, which gives rise to eddy currents at the walls surrounding them (Skarrie, 2001).

The lower permeability of SMC compared to laminations implies that the hysteresis losses are higher at most relevant frequencies (a few hundreds hertz) (Höganäs AB, 2001). However, the dynamic losses are lower in SMC, since the material is built up by small particles electrically isolated from each other. If the insulation was perfect, there would be only eddy currents circling inside the iron particles but no currents in-between them. This implies that the eddy current loss in iron powder would be independent of the geometry of the specimen but dependent on the size and shape of the particles. However, this assumption is in most cases not true since the insulation between particles is not perfect and currents between particles exist. Nevertheless, the dynamic losses are in general lower in SMC compared to laminations.

Iron loss prediction

Iron loss prediction is an important issue in both design and analysis of electrical machines. It is a difficult task, due to the complexity of the machine, flux distribution and rotational variation of flux. It has long been realized that a considerable amount of the total iron loss in the stator core of a rotating electrical machine is caused by the rotating magnetic field. However, the lack of data and proper models for rotational core losses has traditionally led to the use of the Steinmetz equation for alternating core loss instead. This trend has changed in the last years, when important advances have been made regarding the modelling of rotational losses.

Zhu and Ramsden (1998) reported novel formulations of rotational losses for electrical sheet steels, and they were applied to electrical machines. Useful values of the empirical coefficients used in the formulations were provided. A similar study was performed later by Guo et al. (2003) using SMC material. Ma et al. (2003) studied the effects of the iron loss caused by flux harmonics. In all these contributions the method was evaluated following a procedure where the finite element problem was solved first, and then the hysteresis effects were inserted at the post-processing level. Bottauscio et al. (2002) made an assessment about how the results are affected if the hysteresis effects are included directly inside the solution process. A comparison with the previous procedure, or even with a direct calculation based on the specific loss data-sheet provided by the manufacturer, showed very little difference in the iron loss results.

The empirical coefficients in the formulation described by Guo et al. (2003) are calculated for the same iron powder material used in this thesis, but using a different lubricant (Somaloy 500 + 0.5% Kenolube). However, this is the most similar measured data available for the iron powder, and is therefore used for the iron loss calculations in this chapter. In general, the iron losses in a rotating electrical machine consist of an alternating and a rotating component, and can be expressed as in (3.8). For pure alternation and rotation the trajectory of the flux density loci describes a line and a circle respectively. But generally, alternating and rotating effects interact yielding an elliptical trajectory, and B_{major} and B_{minor} represent the major and minor axis of the ellipse. Their ratio $R_B = B_{minor}/B_{major}$ determines the contribution of the alternating and rotating components to the total core losses. When R_B is 0 or 1 the losses are purely alternating or rotational respectively.

$$P_{tot} = R_B P_{rot} + (1 - R_B)^2 P_{alt} \tag{3.8}$$

The specific alternating and rotational components in (3.8) are calculated according to the procedure presented by Guo et al. (2003). The alternating losses were separated into hysteresis, eddy current and anomalous losses using (3.9), where $\hat{B}$ is the peak value of flux density and f the frequency. Similarly, the specific circular core loss was also separated into three parts using (3.10), where P_{hr} is the rotational hysteresis loss, and C_{er} and C_{ar} are the coefficients for the rotational eddy current and anomalous losses. The rotational hysteresis loss per cycle was expressed in terms of four parameters a_1, a_2, a_3 and B_s (3.11). The value of s was calculated from (3.12). The loss coefficients were determined experimentally and they are summarized in Table 3.1. It was pointed

out that the rotational excess loss is generally a function of the flux density and eventually reduces to zero when the material is saturated and all domain walls disappear.

$$P_{alt} = C_{ha} \cdot f \cdot \hat{B}^h + C_{ea}(f \cdot \hat{B})^2 + C_{aa}(f \cdot \hat{B})^{1.5} \quad (3.9)$$

$$P_{rot} = P_{hr} + C_{er}(f \cdot \hat{B})^2 + C_{ar}(f \cdot \hat{B})^{1.5} \quad (3.10)$$

$$P_{hr} = f \cdot a_1 \left[\frac{\frac{1}{s}}{\left(a_2 + \frac{1}{s}\right)^2 + a_3^2} - \frac{\frac{1}{2-s}}{\left[a_2 + \frac{1}{2-s}\right]^2 + a_3^2} \right] \quad (3.11)$$

$$s = 1 - \frac{\hat{B}}{B_s}\sqrt{1 - \frac{1}{a_2^2 + a_3^2}} \quad (3.12)$$

3.5 Iron losses in the EMSM

The model described in the previous section was adapted to calculate the iron losses in the EMSM, both in the stator and the rotor. The FE model was solved at no load at 24 positions along one electrical period. This implied that the losses could be calculated up to the 11^{th} harmonic. A table was created with the field values calculated in the center of all the elements in the model. This procedure was jeopardized by the fact that the element numbering was automatically modified in all the model after each rotor rotation. Therefore, a table with the coordinates of the elements at the first position was created, and the field values were evaluated at these coordinates in the rest of the steps. Although this procedure was effective in the stator, the problem in the rotor is that the coordinates of the elements change after each step. The only way of identifying the rotor elements was to rotate back the whole model so that the rotor mesh coincided with its first position. At the same time the stator will be displaced and the field in its elements corrupted, and this is the reason why the stator and rotor losses were calculated separately.

The field tables were processed in MATLAB. The flux density values were transformed from Cartesian to polar coordinates, and the FFT of the radial, circumferential and axial components was calculated. The ratio R_B was computed at each element and harmonic using (3.13). The major and minor axis of the ellipse were obtained from the maximum and minimum between the modulus of the radial and axial components of the flux density together, and the tangential component. Inherent with this procedure is the approximation that

Table 3.1: Loss coefficients for Somaloy 500 (Guo et al., 2003)

Coefficient	Value	Coefficient	Value
C_{ha}	0.1402	C_{er}	$2.303 \cdot 10^{-4}$
C_{ea}	$1.233 \cdot 10^{-5}$	a_1	6.814
C_{aa}	$3.645 \cdot 10^{-4}$	a_2	1.054
h	1.548	a_3	1.445
C_{ar}	0	B_s	2.134 T

either the maximum or the minimum radius of the ellipse are located exactly along the plane defined by the axial and radial components, or in the tangential direction. This is not necessarily true, but it is reasonable since the pattern of flux flow in the machine occurs mainly in these two directions. Actually, in most parts of the machine one component or the other will be negligible. When the machine rotates, the change in magnetization will give rise to an increased tangential component, especially in the teeth tips and the back core right above the teeth, and probably also in the end-plates at the level of the rotor, but in a smaller scale.

$$R_B = \frac{\min\left(\sqrt{B_{rad}^2 + B_{ax}^2}\,, B_{tan}\right)}{\max\left(\sqrt{B_{rad}^2 + B_{ax}^2}\,, B_{tan}\right)} \tag{3.13}$$

Finally, tables were created with the harmonic components of the flux density in each element, and the index R_B. These tables were imported into the FE post-processor, where (3.8) was implemented for each element and harmonic, and the losses were calculated performing a volume integral and multiplying by the density of the material. The total loss at each element was approximated simply by adding the fundamental and all its harmonic components. Finally, the losses from the elements corresponding to the same region in the thermal model (analysed in next chapter) were added together. It should be noted that P_{hr} in (3.11) becomes negative for values of $\hat{B} > B_s$. Although the total flux density in some local heavily saturated part of the machine passed this limit, it was observed that this condition was never satisfied for the fundamental or the harmonic components on their own.

Results

Simulations were carried out to assess the losses in the machine at load and no load with a current loading calculated for the thermal limit in the windings, which will be treated in next chapter. Figure 3.2(a) shows the distribution of the alternating and rotational losses in the stator of the machine for the fundamental flux density at no load. The R_B distribution shows that the alternating losses are concentrated in the body of the teeth, while the losses in the tips are dominated by the rotational component. In the back core, rotational losses appear around the regions where the teeth are connected to the core, while alternating losses are more important in the regions between the teeth. The rotational losses are clearly dominating in the regions of the end-plates close to the rotor. However, although R_B provides information about the ratio of change of the components of the flux density vector at each element, the total losses due to these components depends directly on the level of the flux density. Figure 3.2(b) shows the flux density distribution in the stator for the same conditions as Figure 3.2(a). It can be observed that the flux density variation is concentrated mainly on the teeth body and tips (around 1.4 T), while the values in the back-core and in the end-plates are much lower. The flux density in the back-core is maximum right above the teeth (1 T), and 0.35 T in the surface of the end-plates closest to the rotor. Therefore it can be concluded that the iron losses in the stator at the fundamental frequency is dominated by the alternating component in the body of the teeth.

The distribution of R_B and the flux density in the rotor for the third harmonic are shown in Figure 3.2(c) and Figure 3.2(d) respectively. It can be observed how the rotational components are concentrated in the upper surface of the claw-poles and to a lower extent in the sides closest to the end-plates. However, the maximum flux density is mainly located in the upper surface of the claw-poles. It can be therefore concluded that the losses in the rotor at this frequency are due to the rotating component in their surface below the radial airgap.

A summary of the losses in the stator and in the rotor at load and no load including the harmonics is presented in Figure 3.3(a) and Figure 3.3(b) respectively. The load simulations where performed rotating the current vector in the stator together with the rotor for one cycle, in order to obtain the maximum torque at each position. Above each plot the total loss is referred to as 'Tot', and the losses in the stator and the rotor are referred to as 'St' and 'Rt' respectively.

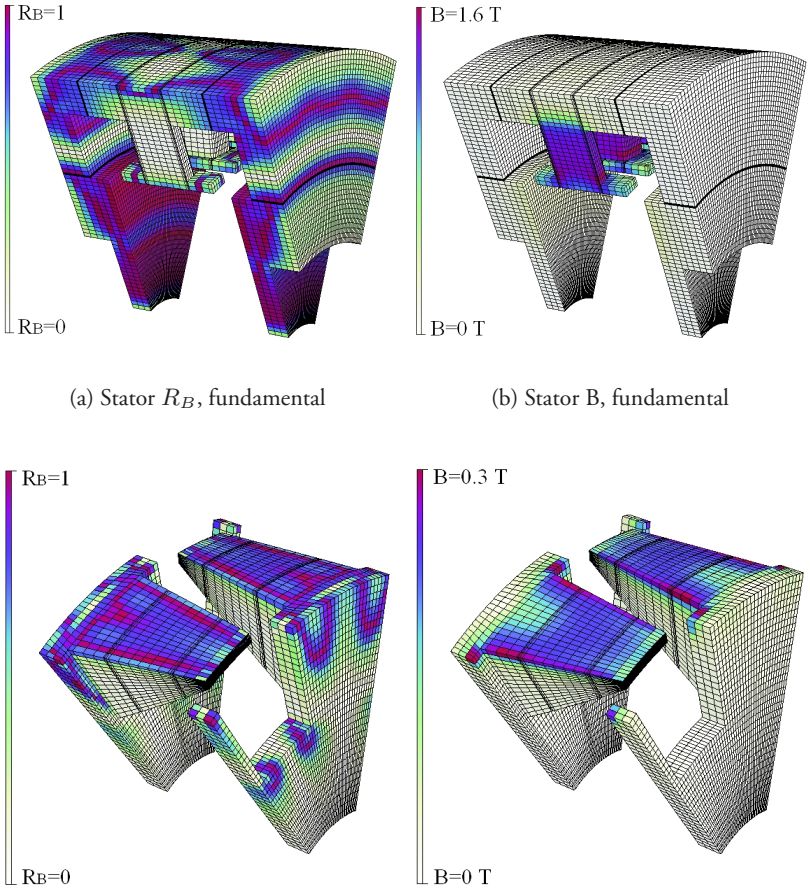

(a) Stator R_B, fundamental

(b) Stator B, fundamental

(c) Rotor R_B, 3rd harmonic

(d) Rotor B, 3rd harmonic

Figure 3.2: R_B and flux density distribution for the fundamental in the stator and the third harmonic in the rotor, no load.

It can be observed that the highest losses are due to the fundamental component in the stator. At load, the losses at this frequency are also increased by 30% compared to the no load case. The rotor losses appear only at harmonics multiple of 3, which is due to the slotting harmonics. The losses in the rotor at load due to the third harmonic are considerably bigger than at other frequencies, and together with the stator losses at that harmonic account for 23% of the total losses at load. In general, comparing the load and no load case, the total losses are increased at load by 40%, the stator losses by 38% and the rotor losses by 55%. It is also clear from the plots the rapid decay of the losses with the frequency. Therefore neglecting the harmonics above the 11^{th} component has little effect in the total predicted iron losses.

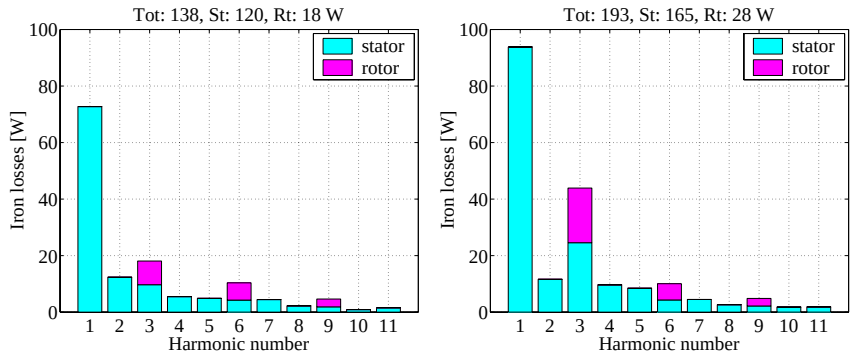

(a) No load (b) Load

Figure 3.3: Distribution of the iron losses in the machine as a function of the harmonic number.

Table 3.2 shows a summary of the alternating and rotating loss components calculated at different parts of the machine, both at load and no load. The values are obtained from the sum of all the harmonics for the respective component at each part. In general, it can be observed that the losses are dominated by the rotating component, which represents 78% of the total losses at no load and 71% at load. The only place in the machine where the alternating losses are more important is in the body of the teeth, which represents 75% of the total alternating losses at no load, and 70% at load. At no load, the contribution to the total rotating losses is biggest at the end-plates, followed by the back-

Table 3.2: Summary of the predicted iron losses in the machine [W]

	No Load		Load	
Part	Alternation	Rotation	Alternation	Rotation
back-core	3.8	27.1	8.2	43.4
teeth body	22.8	5.6	38.5	5.6
teeth tip	2.2	23.1	4.0	29.3
end-plates	0.9	34.7	3.2	32.8
rotor sides	0.1	3.0	0.5	3.5
claw-poles	0.5	13.7	1.2	22.7
Total	30.3	107.2	55.6	137.3

core, the teeth tips and to a lower extent the claw-poles. However, at load the contribution from the back-core is the most important, increasing about 60%, although the other parts also experience an increase, except in the case of the end-plates. Nevertheless, the back-core stands alone for 54% of the increase in the rotational losses between no load and load. The alternating losses in the teeth body are increased by almost 70% at load. The other parts also experience an increase in the alternating losses, but their effect in the final value is more modest. The teeth body stand alone for 62% of the increase in the alternating losses between no load and load. The losses at load will be used for the thermal model presented in next chapter.

3.6 Conclusions

In this chapter it has been shown how 3D FE analysis can be used to calculate the iron losses in the machine using a method to separate the losses in alternating and rotational components. It has been shown that the rotational losses represent around 70% of the total losses in the machine, and that these losses dominate everywhere except in the body of the teeth. Although this method to calculate the losses may be accurate, it is not practical for optimization. To the time of approximately 13 hours needed to simulate the 23 rotor positions for given load conditions, around 6 hours more need to be added for the loss calculation. However, once the design is quasi-optimized, this method allows to

calculate precisely where the losses are located, their components, and how they behave with the frequency. The losses at different parts of the machine can then be imported into the thermal model to assess how they affect the temperature distribution in the machine.

Chapter 4

Thermal model

4.1 Introduction

The thermal characteristics of an electrical machine are important since the temperature rise in the windings usually defines the power that can be obtained from the machine. The lumped parameter thermal model has been used for a long time for calculating the temperature rise in electrical machines. Advanced models for machines of TEFC design, mainly induction motors, have been reported in the literature (Mellor et al., 1991), (Jokinen and Saari, 1997), (Kylander, 1995), (Boglietti et al., 2004). In recent years there has been also a trend to use computer FEM models to calculate the thermal characteristics of machines, where the magnetic and thermal simulations are usually coupled (Driesen et al., 2001), (Vong and Rodger, 2003). In this chapter, a lumped parameter thermal network model will be presented for calculating the temperature distribution in the machine at steady state operation. The thermal resistances are directly calculated as a function of the geometry details, which are defined in Appendix B.

In general, the most important source of heat in electrical machines are the copper losses from the windings. Therefore the electrical calculations are described first, which will serve to predict these losses. The thermal network with the path for the losses through different parts of the machine is described before introducing a more detailed formulation of the heat transfer problem. The machine is water cooled, and it is assumed that the coolant flows directly along the external surface of the back-core and the end-plates.

4.2 Electrical calculations

The d.c. link voltage U_{link} in the converter was selected as 275 V, around 10% below the maximum of 300 V available in the laboratory equipment. The machine will be driven using vector control, and it can be shown that the peak phase voltage can be increased by 15% using third harmonic injection (symmetrization) compared to the case with sinusoidal modulation (Alaküla, 2002). The peak phase voltage $\hat{U}f_{ac}$ is then $U_{link}/\sqrt{3}$. The number of conductors in the a.c. winding was calculated using (4.1). The value of ω_s corresponds to the fundamental electrical frequency f in rad/sec, and $\hat{\phi}$ is the fundamental peak flux-linkage of one phase. This value was preliminary taken from the MEC model at no load. For the prototype, $\hat{\phi}$ was calculated by doing the FFT of the flux linkage of one phase at the 24 FEM solutions along one electrical cycle. The number of turns in the d.c. winding were calculated using (4.2). This equation is deduced making equal (4.3) and (4.4), which are two different expressions to calculate the d.c. coil resistance from an electrical and a geometrical point of view respectively. In these equations, Uf_{dc} is the voltage, A_{dc} the slot area, k_{fill} the copper fill factor, It_{dc} the Ampere turns in the slot, and $\bar{r}_{dc}$ the average radius of the coil. The voltage was selected as 12 V per field coil (24 V connected in series).

$$Nc_{ac} = \frac{\hat{U}f_{ac}}{\omega_s \cdot \hat{\phi} \cdot p} \tag{4.1}$$

$$Nc_{dc} = \frac{Uf_{dc} \cdot A_{dc} \cdot k_{fill}}{\rho \cdot 2\pi \cdot It_{dc} \cdot \bar{r}_{dc}} \tag{4.2}$$

$$Rcoil_{dc} = \frac{Uf_{dc}}{if_{dc}} = \frac{Nc_{dc} \cdot Uf_{dc}}{It_{dc}} \tag{4.3}$$

$$Rcoil_{dc} = \rho \frac{2\pi \cdot \bar{r}_{dc} \cdot Nc_{dc}}{A_{dc} \cdot k_{fill}/Nc_{dc}} \tag{4.4}$$

The diameter of the copper conductors was calculated from (4.5). F_s is the slot fill factor, including the insulation, and normal values for non-pressed windings range from 0.6 to 0.7. N_c is the number of conductors in one coil, and A_{slot} the slot area. N_{p1} and N_{p2} are the number of parallel strands with diameter d_{is1} and d_{is2}, where $d_{is} = d_{cu} \cdot k_{is}$. The factor k_{is} accounts for the coating, and it was selected in order to increase the diameter of the copper strand by 7% (Sadarangani, 2000). Equation (4.5) can be simplified into (4.6)

considering single diameter conductors in the coils and no parallel strands. In the a.c. winding there are two coils sharing one slot, so Nc was twice the number of conductors in one coil.

$$F_s = Nc\left(0.25\pi\left(N_{p1}\cdot d_{is1}^2 + N_{p2}\cdot d_{is2}^2\right)\right)/A_{slot} \tag{4.5}$$

$$d_{cu} = \sqrt{\frac{F_s\cdot A_{slot}}{0.25\pi\cdot Nc\cdot k_{is}^2}} \tag{4.6}$$

Although the distribution of the three phases in the teeth is straightforward, it is instructive to determine it following the more general procedure for concentrated windings described by Cros and Viarouge (2002). The number of slots N_s per pole N_p and per phase N_{ph} is defined as S_{pp} in (4.7) and has to be reduced to a fraction of two non divisible integers b and c. For our distribution of three phases accommodated in three slots per pole pair the values are b=1 and c=2. A repeatable sequence of 0 and 1 specific to the winding can be derived from this relation. The number of 1 is equal to b and the number of 0 is equal to $c-b$. The 1 and 0 have to be distributed as evenly as possible in the sequence, which is then repeated three times. In our case this is straightforward and the sequence becomes 101010. To this sequence it is associated the usual phase sequence AC'BA'CB'. Then the conductors associated with the number 1 are extracted to form the first layer of the winding. The second layer of the winding is obtained reproducing and shifting the initial layer by a tooth. From this simple procedure, the distribution of the windings in the machine is obtained, as shown in Figure 4.1.

$$S_{pp} = \frac{N_s}{N_p\cdot N_{ph}} = \frac{b}{c} \tag{4.7}$$

The coating material was bonding epoxy, with a temperature class of 180^o C (class H). For the slot wall insulation, a 0.5 mm thick layer of Kapton material was used. The thermal conductivity of the materials is listed in Table 4.1. The equivalent thermal conductivity in the a.c. and d.c. coils was calculated using (4.8). This expression was deduced by Arkkio (2002), for a squared slot and round conductors. The value of κ_i is the conductivity of the coating, d_1 is the diameter of the copper strand, d_2 is the diameter of the copper strand and coating together, and δ_i is the shortest distance between the surface of two

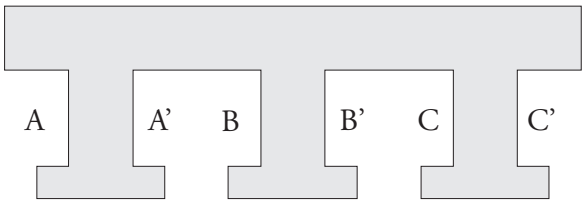

Figure 4.1: Sequence of the winding distribution.

Table 4.1: Thermal conductivity κ of the materials

Material	κ [W/mK]
Somaloy500	13
Copper	360
Bonding epoxy	0.64
Kapton	0.12

copper strands, which was approximated as two times the thickness of the coating. Jack et al. (2000) stated that the thermal resistance of the pressed windings (78% copper fill factor) was reduced by 46%. Assuming that this thermal resistance would be similar in our machine with a 75% copper fill factor, then the value calculated from (4.8) for the d.c. and a.c. windings was increased by 92%, and κ_{coil}=17.6 W/mK.

$$\kappa_{coil} = \kappa_i \left(\frac{d_1}{\delta_i} + \frac{\delta_i}{d_2} \right) \tag{4.8}$$

Copper losses

The total copper losses in the d.c. and the a.c. windings are calculated as in (4.9) and (4.10). The currents in the a.c. coils are $I_a = It_{ac}, I_b = -It_{ac}/2$, and $I_c = -It_{ac}/2$, where It_{ac} is the maximum peak Ampere turns in one coil. The losses in all the a.c. coils in the machine are calculated by multiplying with the number of pole pairs p. It should be noted that this way of calculating the losses for the a.c. winding is equivalent to the more familiar expression

$P = 3 \cdot I^2 \cdot R$, where the effective current is $I = It_{ac}/(\sqrt{2} \cdot Nc_{ac})$ and $R = \rho \cdot Nc_{ac} \cdot L_{ac}/(A_{ac}/Nc_{ac})$. The resistance of the d.c. coil (4.11) is calculated at the average radius $\bar{r}_{dc}$ (4.12). The value of $insl$ in the coil cross sectional area A_{dc} (4.13) corresponds to the thickness of the wall insulation. The resistance of the a.c. coil is calculated as in (4.14), where L_{ac} (4.15) is simply obtained by adding the average length of the two axial sides (4.16) and the two tangential sides (4.17). In these equations, the coil thickness $cwth_{ac}$ is calculated as in (4.18), at the average radius given in (4.19). The cross sectional area of one a.c. coil A_{ac} (4.20) was calculated as the minimum between the area available in the axial (4.21) and the tangential (4.22) directions. The weight of the conductors was calculated as in (4.23) and (4.24) for the a.c. and d.c. windings, where δ_{cu} is the density of the copper (8900 kg/m^3). It should be noted that the resistivity of the copper ρ_{cu} is calculated at a temperature of 140^{o}C, using the equivalence $\rho_{cu} = \rho_{cu0}(1 + \alpha_{cu}(T_{cu} - 20))$, where ρ_{cu0} is the resistivity at 20^{o}C ($1.673 \cdot 10^{-8}$ Ω m) and α_{cu} is the temperature coefficient ($3.93 \cdot 10^{-3}$ /^{o}C).

$$
\begin{aligned}
Pcu_{dc} &= 2 \cdot It_{dc}^2 \cdot R_{dc} && (4.9)\\
Pcu_{ac} &= (I_a^2 + I_b^2 + I_c^2) \cdot R_{ac} \cdot p && (4.10)\\
R_{dc} &= \rho_{cu} \frac{2\pi \cdot \bar{r}_{dc}}{A_{dc} \cdot k_{fill}} && (4.11)\\
\bar{r}_{dc} &= \frac{ros - dy + ris}{2} && (4.12)\\
A_{dc} &= (ros - dy - ror - 2 \cdot insl) \cdot \\
&\quad \cdot (zdy + g2 - 2 \cdot insl) && (4.13)\\
R_{ac} &= \rho_{cu} \frac{L_{ac}}{A_{ac} \cdot k_{fill}} && (4.14)\\
L_{ac} &= 2 \cdot Laxi_{ac} + 2 \cdot Ltan_{ac} && (4.15)\\
Laxi_{ac} &= zts + cwth_{ac} && (4.16)\\
Ltan_{ac} &= wt + cwth_{ac} && (4.17)\\
cwth_{ac} &= \frac{1}{2}(2\pi \bar{r}_{ac}/N_s - wt - 2 \cdot insl) && (4.18)\\
\bar{r}_{ac} &= \frac{1}{2}(ros - dy + ris + dos) && (4.19)\\
A_{ac} &= \min(Aaxi_{ac}, Atan_{ac}) && (4.20)
\end{aligned}
$$

$$
\begin{aligned}
Aaxi_{ac} &= \frac{1}{2}\Big(\frac{2\pi/N_s}{2}\left((ros-dy-insl)^2-(ris+dos+insl)^2\right)- \\
&\quad -2(\frac{wt}{2}+insl)((ros-dy-insl)- \\
&\quad -(ris+dos+insl))\Big) \qquad (4.21)\\
Atan_{ac} &= (\frac{1}{2}(ztps-zts)-insl)((ros-dy-insl)- \\
&\quad -(ris+dos+insl)) \qquad (4.22)\\
W_{ac} &= A_{ac}\cdot 2(Ltan_{ac}+Laxi_{ac})\cdot N_s\cdot \delta_{cu} \qquad (4.23)\\
W_{dc} &= 2\cdot A_{dc}\cdot 2\pi\bar{r}_{dc}\cdot \delta_{cu} \qquad (4.24)
\end{aligned}
$$

4.3 Thermal network

The losses considered to contribute to the heat production in the machine are the iron and copper losses. Friction and stray losses are not included at this point, but they will certainly appear in the measurements in Chapter 7. Two paths were defined for the dissipation of the losses from the stator, and they are shown in Figure 4.2. The copper losses of the a.c. winding ('Pcu1') and the iron losses of the stator teeth and the stator yoke are referred to as 'Pac'. These losses are dissipated in the radial direction through the outer cylindrical surface of the yoke. The whole surface area of the end-plates is used to cool the copper losses of the d.c. winding ('Pcu2') and the iron losses of the end-plates, and they are referred to as 'Pdc'.

It was assumed that 20% of the copper losses in the a.c. winding was transferred directly to the back core through the top of the coil and that the other 80% was transferred through the teeth, following the path shown in Figure 4.2. This is not unreasonable since the contact area between the coil and the back core is 60% of the contact area between the coil and the teeth, which implies that in principle 38% of the copper losses would be dissipated directly to the back core. However, in practice it is more complicated to fit the coil with the surface of the core than with the teeth, especially with the type of modular winding used. Therefore the heat transfer to the core was reduced to almost half the theoretical value. The iron losses calculated for the FE model at load (Chapter 3) were grouped into the macro-elements in the thermal model, namely the tooth tip, the tooth body, the stator core, the end-plates, the rotor claw-poles and the rotor sides attached to these claw-poles. Since the rotor is completely enclosed by the surrounding stator parts, it is reasonable to assume that its losses

will be transferred to the stator through the closest path. Therefore, the losses from the rotor claw-poles were added to 'Pac', whereas the losses from the rotor sides were added to 'Pdc'.

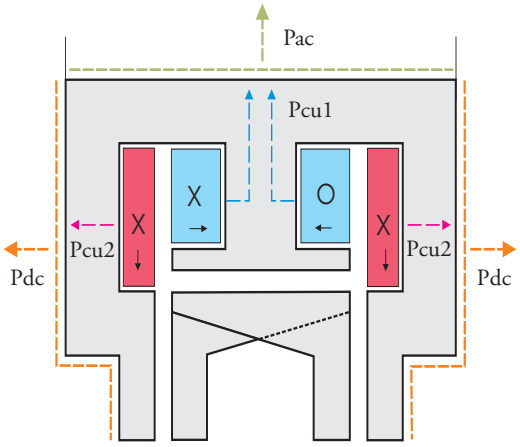

Figure 4.2: Thermal dissipation in the EMSM.

The study of the thermal circuit for the dissipation of the 'Pac' losses is simplified considering a pole pair, where three teeth are allocated, as shown in Figure 4.3. The copper losses in the armature coils transferred to the teeth are referred to as 'Pcua^{1}', 'Pcub^{1}' and 'Pcuc^{1}', while those transferred directly to the back core are referred to as 'Pcua^{2}', 'Pcub^{2}' and 'Pcuc^{2}'. In these labels the superscript '^{2}' should be read as a label, not as a square symbol. The thermal resistance in the coils and the wall insulation around the teeth is referred to as 'Rcw'. This resistance was not included in the path for the losses directly transferred to the core. This is because the temperature in the coils was calculated for the most critical conditions, i.e. following the path through the teeth. Most of the losses are dissipated through this way, which is also the longest. The iron losses in the three teeth are referred to as 'Pfea', 'Pfeb' and 'Pfec' respectively, and the thermal resistances of the teeth are referred to as 'Rfea', 'Rfeb' and 'Rfec'. The iron losses in the core and its thermal resistance are referred to as 'Pfe2$_{ac}$' and 'Rfe2' respectively. The thermal resistance from the surface of the machine to the coolant is 'Rv'. There are a series of assumptions that can be made in this circuit:

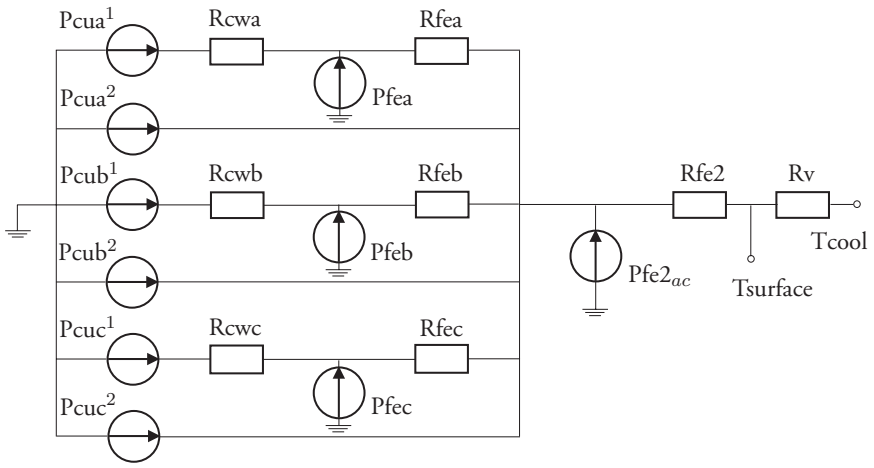

Figure 4.3: Thermal circuit for 'Pac' losses in one pole pair.

- the copper losses in the three windings during one a.c. cycle are the same ($Pcua^{1,2} = Pcub^{1,2} = Pcuc^{1,2}$).
- the iron losses in the three teeth during one a.c. cycle are the same (Pfea = Pfeb = Pfec).
- the thermal resistances in the coils and wall insulation around the three teeth is the same (Rcwa = Rcwb = Rcwc).
- the thermal resistance in the body of the three teeth is the same (Rfea = Rfeb = Rfec).

Then the circuit in Figure 4.3 can be simplified into the circuit in Figure 4.4, where the copper losses are $Pcu^1_{ac} = Pcua^1 + Pcub^1 + Pcuc^1$, and $Pcu^2_{ac} = Pcua^2 + Pcub^2 + Pcuc^2$. The iron losses in the teeth are $Pfe1_{ac}$ = Pfea + Pfeb + Pfec, and the thermal resistances are Rcwt = Rcwa||Rcwb||Rcwc, and Rfe1 = Rfea||Rfeb||Rfec, in parallel.

The thermal model for 'Pdc' in one end-plate is represented in a similar way, see Figure 4.5. The copper losses of one d.c. coil are $Pcu_{dc}/2$ and the iron losses in the plate are Pfe_{dc}. The thermal resistance in the coil and wall insulation is Rcwp and the resistance in the end-plate is Rfep.

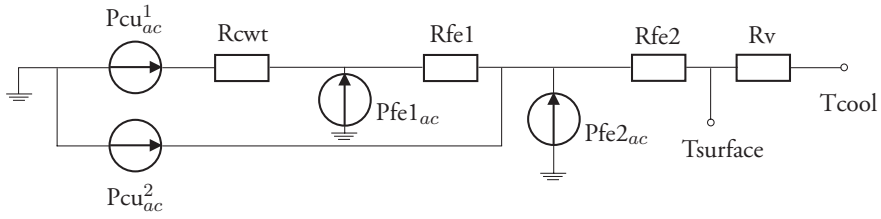

Figure 4.4: Simplified thermal circuit for 'Pac' losses in one pole pair.

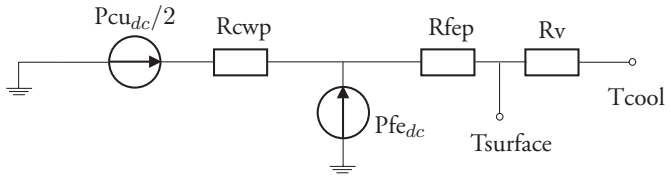

Figure 4.5: Simplified thermal circuit for 'Pdc' losses in one end-plate.

4.4 Heat transfer

The two mechanisms governing the heat transmission in electrical machines are conduction and convection. In conduction, the heat is transmitted from one part to another without relative movement between these parts. The equation for conduction takes the form in (4.25), where q is the heat transmitted through the surface A along a material with thermal conductivity κ, between two parts separated by Δx and with a temperature difference ΔT. In convection, a fluid moves relative to the cooled part, removing the heat, and (4.26) describes this process. The parameter $hconv$ is the heat transfer coefficient, which depends on the properties of the fluid, the pattern of movement, and the geometry of the cooled surface. It therefore needs to be calculated for each case depending on the conditions.

$$q_{cond} = A\frac{\Delta T}{\Delta x/\kappa} \tag{4.25}$$

$$q_{conv} = A \cdot hconv \cdot \Delta T \tag{4.26}$$

The cooling system was first adapted to the one available for the Alvar motor application. The total water flow $\dot{Q}$ was limited to 1.2 liter/minute with a

temperature of 27^{o}C, between the heat exchanger and the engine. At this stage, it was assumed that half of the coolant flow is used to cool the armature winding, and the other half the field winding through separate circuits. The maximum temperature rise allowed in the coils was 100^{o}C above an ambient temperature of 40^{o}C. It was assumed that the coolant would flow through a duct of exactly the same shape as the cooled surface and a thickness of 3 mm. With these conditions, the heat transfer coefficient from the surfaces of the machine was calculated from the known formulas for simple geometries given in the basic heat transfer theory (Wong, 1977), (Holman, 1992).

Heat transfer coefficient

In principle, the heat transfer coefficient for the cylindrical surface used to cool 'Pac' could be calculated using the formulation for forced convection in a circular cylinder with normal flux, as shown in Figure 4.6. In the machine, the flux flow would hit perpendicularly the surface from the top (Figure 4.6 rotated clockwise 90^o), and then split into two paths parallel to the end-plates. However, the fact that the fluid is contained in a duct does not allow to reproduce the behaviour associated with this formulation in the textbooks, where the fluid is not constrained into a tight surface around the cylinder. In this case, as the flow progresses along the front side of the cylinder, the pressure would decrease and then increase along the back side of the cylinder, resulting in an increase of free-stream velocity on the front side and a decrease on the back side. This could eventually cause reverse flow in the back if a phenomenon called boundary-layer separation occurs. If the fluid is contained inside a narrow duct, the velocity profile could be assumed to be similar in the front and in the back, and the heat transfer behaviour could then be approximated as that of a fluid flowing along a plane surface.

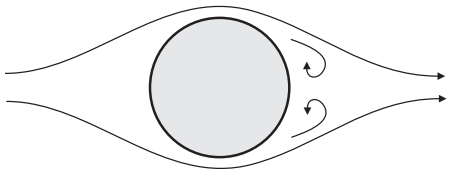

Figure 4.6: Cylinder with normal flux

The heat transfer coefficient from the surface of the cylinder was therefore approximated using the formulation for forced convection over a plate, which assumes that the flow is parallel to a plane surface. Due to symmetry, this formulation is applied to only one of the two paths around the cylinder. The properties of the coolant were evaluated at the so-called *film temperature*, defined as the arithmetic mean between the surface (T_{sf}) and free-stream (T_∞) temperatures (4.27). The value of T_∞ was calculated as the average between the inlet (27^{o}C) and outlet temperatures (4.28). The increase in temperature in the fluid at the output can be calculated using (4.29), where P_{ac} are the copper and iron losses dissipated through this path, $\dot{q}_{ac}$ the coolant volumetric flow ($\dot{Q}/4$), ρ_w the density and cp_w the specific heat. These properties were calculated at the inlet water temperature.

$$T_m = \frac{1}{2}(T_{sf} + T_\infty) \tag{4.27}$$

$$T_\infty = \frac{1}{2}(T_{in} + T_{out}) \tag{4.28}$$

$$\Delta T_w = \frac{P_{ac}}{\dot{q}_{ac} \cdot \rho_w \cdot cp_w} \tag{4.29}$$

The determination of the film temperature involves an iteration process, since the temperature in the surface is a priori unknown. A table was created with the physical properties of water between 273 K and 375 K in steps of 5 degrees. The values for the specific heat, density, viscosity (μ), and thermal conductivity (κ) were then extrapolated automatically depending on the calculated surface temperature. The speed of flow is obtained from (4.30), where zdy is the axial length of the core and w_{dct} is the thickness of the cooling duct. A so-called Reynolds number (Re) appears in forced convection, and it gives information about the characteristics of the flow, laminar or turbulent. In general, this number is calculated as in (4.31), where x is the geometric characteristic of the problem. In our case, this corresponds to the length of the plane ($L_{cyl} = \pi \cdot ros$), in order to calculate the average Reynolds number in the surface. The Prandlt number (Pr) appears in any heat transfer process and relates the velocity and temperature fields. It can be expressed as in (4.32). Finally, the Nusselt number (Nu) also appears in any heat transfer process and relates the heat transfer coefficient $hconv$ in the solid surface with the thermal conductivity of the fluid per unit length (4.33). In our specific problem it takes also the form given in (4.34). The coefficients A, m and n are taken depending on

the value of the Reynolds and Prandlt numbers. Combining (4.33) and (4.34) allows to calculate the heat transfer coefficient from the cylinder.

$$U_{ac} = \frac{\dot{q}_{ac}}{zyc \cdot w_{dct}} \tag{4.30}$$

$$Re = \frac{\rho \cdot U \cdot x}{\mu} \tag{4.31}$$

$$Pr = \frac{\mu \cdot cp}{\kappa} \tag{4.32}$$

$$Nu = \frac{hconv \cdot x}{\kappa} \tag{4.33}$$

$$Nu = A \cdot Re_L^m \cdot Pr^n \tag{4.34}$$

A similar formulation was used to calculate the heat transfer coefficient from the surface of the end-plates. The length L_{plt} is approximated as the dashed line shown in Figure 4.7 (4.35), and the area A_{plt} corresponded to half the end-plate surface. The properties of the water were calculated at the film temperature, where T_{sf} is now the temperature at the surface of the end-plate. The increase in the cooling water temperature was calculated as in (4.29), updating the coefficients. The speed of the flow is calculated as in (4.36), where $\dot{q}_{dc} = \dot{Q}/8$. The Reynolds, Prandlt and Nusselt numbers were calculated as above, using L_{plt} as the geometric characteristic. A summary of the values obtained applying these formulas to the cylinder and the plate is shown in Table 4.2.

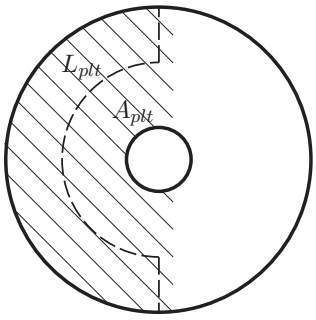

Figure 4.7: Length and cooling area in the end-plate

Table 4.2: Parameters for the heat transfer coefficient calculation

Coefficient	Cylinder	End-plate
Tm [^{o}C]	48	47
Δ T$_w$ [^{o}C]	9	10
U [m/s]	0.022	0.014
Re	12076	6663
Pr	3.7	3.8
Nu	112	84
A	0.664	0.664
m	0.50	0.50
n	0.33	0.33
hconv [W/mK]	229	193

$$L_{plt} = (ros - rir) + zdx + \frac{1}{4}2\pi(ros + rir) \tag{4.35}$$

$$U_{dc} = \frac{\dot{q}_{dc}}{A_{plt}/L_{plt} \cdot w_{dct}} \tag{4.36}$$

Heat transfer model

In this section, the heat transfer between the different parts of the model will be described. The thermal resistances are a function of the area and the length of the transmission path. The explicit derivation of these components are included in Appendix C. The calculations for the path following 'Pac' in Figure 4.2 will include all the a.c. copper losses and all the iron losses in the back core and in the teeth. Therefore, the whole cylindrical surface of the core will be used for cooling. The path for the heat dissipation from the two d.c. coils is identical, and therefore the calculations will be done only for one of them. The temperatures are calculated starting from the heat exchange between the surface of the motor and the coolant. The temperature in the surface of the core is given by (4.37), where the iron losses from all the rotor claw-poles (Pfe_{rC}) have been

included in the power dissipated. The temperature in the surface of the end-plates is given by (4.38), which includes the iron losses in the corresponding side of the rotor attached to the claw-poles (Pfe_{rT}). The areas Asf_{ac} and Asf_{dc} correspond to the cooling surface area of the back core and one end-plate respectively.

$$Tsf_{ac} = \frac{Pcu_{ac} + p \cdot (Pfe1_{ac} + Pfe2_{ac}) + Pfe_{rC}}{Asf_{ac} \cdot hconv_{ac}} + T_{\infty 1} \quad (4.37)$$

$$Tsf_{dc} = \frac{Pcu_{dc}/2 + Pfe_{dc} + Pfe_{rT}}{Asf_{dc} \cdot hconv_{dc}} + T_{\infty 2} \quad (4.38)$$

The temperature in the inner surface of the core was calculated as in (4.39), where Lsc_{ac} is the thickness of the yoke, and Asc_{ac} is the area around the cylinder through the middle of the yoke. The temperature in the surface of the wall insulation in contact with the iron is calculated using (4.40) and (4.41) for the a.c. and d.c. circuits respectively. For the calculation of the temperature in the teeth walls, the copper losses are reduced by 20% and only the iron losses in the teeth and in the claw-poles are considered. The length Lcw_{ac} is half the distance between the teeth tips (at the width of the body) and the center of the connection with the core, as shown in Figure 4.8(a). The equivalent distance is the arithmetic average between half Lt_1 and half Lt_2. At each side, the area for the transmission was selected as the average between the wall area (At_1) and the corresponding triangle at the top (Ac_1). The total area Acw_{ac} was calculated adding the value for the four sides and multiplying by the number of teeth. The area in one tooth is actually equivalent to the arithmetic average between the area in the four walls together and the connection area with the core. For the d.c. circuit Lsw_{dc} is calculated as the average distance from the surfaces of the iron in contact with the wall insulation to the surface of the machine, as shown in Figure 4.8(b) ($Lp_1, \ldots, Lp_4$). The area Asw_{dc} was calculated between the wall insulation and the surface at the level indicated by the dotted line in the figure.

$$Tcr_{ac} = \frac{(Pcu_{ac} + p \cdot (Pfe1_{ac} + Pfe2_{ac}) + Pfe_{rC}) Lsc_{ac}}{Asc_{ac} \cdot \kappa_{fe}} + \\ + Tsf_{ac} \quad (4.39)$$

$$Twl_{ac} = \frac{(p \cdot (Pcu^1_{ac} + Pfe1_{ac}) + Pfe_{rC}) Lcw_{ac}}{Acw_{ac} \cdot \kappa_{fe}} + Tcr_{ac} \quad (4.40)$$

$$Twl_{dc} = \frac{(Pcu_{dc}/2 + Pfe_{dc} + Pfe_{rT})Lsw_{dc}}{Asw_{dc} \cdot \kappa_{fe}} + Tsf_{dc} \quad (4.41)$$

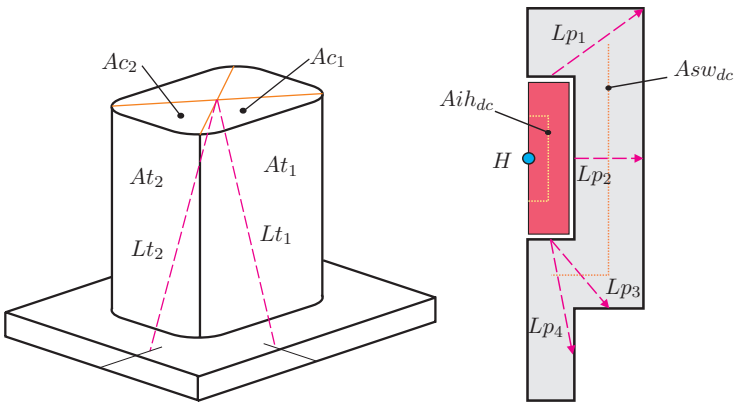

(a) Tooth element (b) Plate element

Figure 4.8: Parametrization of the tooth and plate thermal elements.

The temperature in the surface of the a.c. and d.c. windings closest to the iron is calculated using (4.42) and (4.43). The length of the path is the insulation thickness. For the a.c. winding the area Awi_{ac} is similar to Acw_{ac}, but now through the middle of the insulation. In the same way, for the d.c. winding the area Awi_{dc} is proportional to Asw_{dc} through the middle of the insulation, but now it also includes the insulation area between the top of the coil and the core. Only the copper losses are transferred through these paths.

$$Tis_{ac} = \frac{p \cdot Pcu_{ac}^{1} \cdot insl}{Awi_{ac} \cdot \kappa_{kapton}} + Twl_{ac} \quad (4.42)$$

$$Tis_{dc} = \frac{Pcu_{dc}/2 \cdot insl}{Awi_{dc} \cdot \kappa_{kapton}} + Twl_{dc} \quad (4.43)$$

The hot spot of the a.c. winding is located at the midpoint along the the external surface of the coil which is located in the center of the slot. The temperature at this point was calculated using (4.44), where Lih_{ac} is the geometrical distance and Aih_{ac} corresponds to half the surface area of the coil at the level

Table 4.3: Estimated temperature distribution [^{o}C]

Part	a.c. path	d.c. path
Tsf	65	63
Tcr	72	
Twl	100	82
Tis	133	126
Thp	140	140

of the main insulation, multiplied by the number of teeth. The hot spot of the d.c. winding is located at the midpoint along its interior surface, as shown in Figure 4.8(b) (H). The temperature is calculated using (4.45), where Lih_{dc} is the arithmetic average between the axial and half the radial lengths of the coil, and Aih_{dc} is the area through the middle of the coil as shown in Figure 4.8(b).

$$Thp_{ac} = \frac{Pcu_{ac}^{1} \cdot Lih_{ac}}{Aih_{ac} \cdot \kappa_{coil}} + Tis_{ac} \tag{4.44}$$

$$Thp_{dc} = \frac{Pcu_{dc}/2 \cdot Lih_{dc}}{Aih_{dc} \cdot \kappa_{coil}} + Tis_{dc} \tag{4.45}$$

The results at the different parts of the machine at the thermal limit are summarized in Table 4.3. The Ampere turns in one a.c. coil were 839 A, and in one d.c. coil 1195 A. A proposed method to cool the machine in practice is shown in Figure 4.9. The parts are attached on top of the stator core and the end-plates. The water flow is similar to the pattern explained in this chapter, although now the fluid is constrained into tubes rather than flowing through a continuous surface. The calculated heat transfer coefficient is not applicable for this case since a different formulation should be used, namely forced convection inside a tube. The number of ducts and their diameter can be optimized at will. This system may not be straight forward to manufacture, and practical measures should be taken to ensure that the water flow is evenly distributed through all the ducts. However, it can provide an acceptable cooling with reasonable robustness.

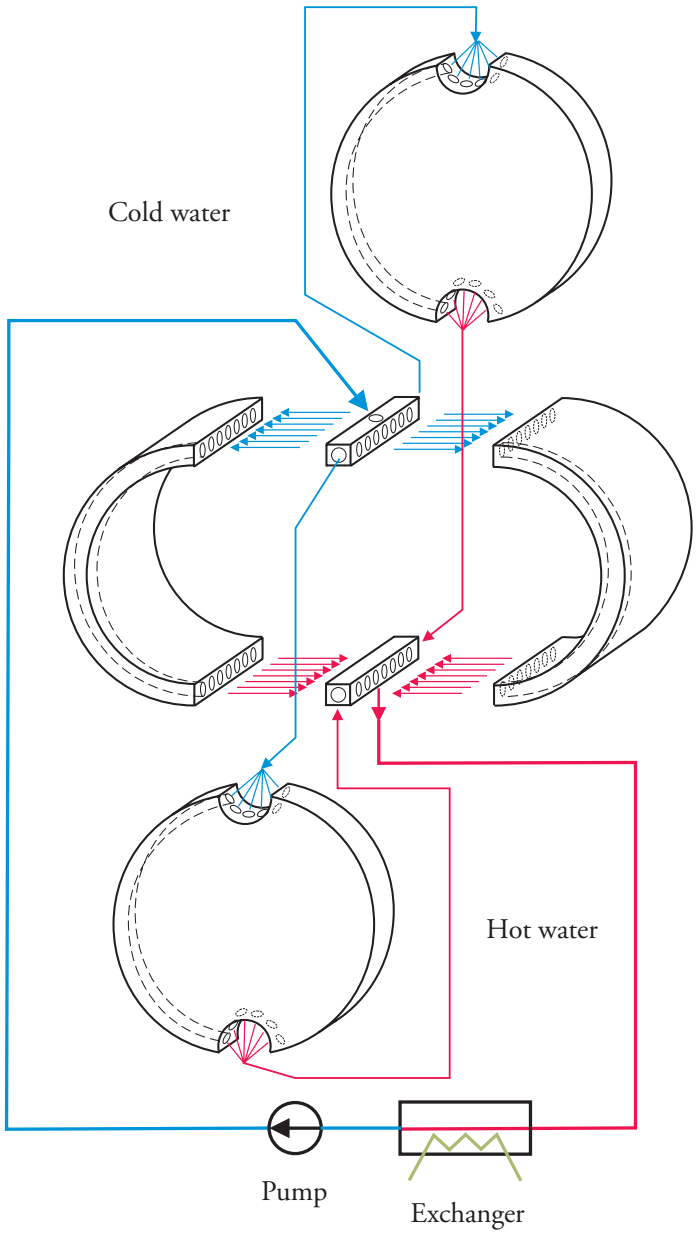

Figure 4.9: An alternative cooling system.

4.5 Conclusions

A thermal network model for the machine has been described together with the formulations for the heat transfer between the different parts of the machine. The total copper losses are 568 W (209 W a.c. and 358 W d.c.) while the iron losses calculated in the previous chapter at load were 193 W. For a peak torque of 15.4 Nm, the efficiency of the machine at 1500 r.p.m. is then 76%. This low efficiency is mainly due to the high copper losses, which account for 75% of the total losses in the active parts of the machine. Mechanical and stray losses have not been included in the calculations since they are very difficult to predict, but they will further decrease the value of the efficiency.

Chapter 5

Alternatives for leakage reduction

5.1 Introduction

In claw-pole structures the flux has a tendency to flow between the lateral faces of adjacent poles. One way of reducing the leakage is to introduce permanent magnets between the claw-poles with opposite polarization to the direction of the leakage, and this idea has already been presented by Taniguchi (2000), and Henneberger et al. (1996). However, this solution assumes that the leakage from the tip of the claw-pole to the end-plate is negligible, which is not true in the case of having magnetically conducting end-plates. The purpose of this chapter is to analyse how this principle can be applied to our electrically magnetized claw-pole machine, based on an in-depth study of the leakage paths in this novel structure by means of FEM simulations. The study compares machines with 12, 16, 20 and 24 poles.

5.2 Leakage paths in the rotor

The flux balance is evaluated in a claw-pole as indicated in Figure 5.1(a). This is a north pole according to the convention that the flux lines leave a north pole and enter a south pole. The paths considered for the flux flow are represented by arrows. The flux entering the pole is referred to as 'Fluxin'. The area through which this flux is measured comprises not only the surface spanned the same angle as the main claw-pole, but also the surface below and next to the adjacent cavity. The flux from the claw-pole crossing the radial airgap is referred to as 'Fluxout'. There are three leakage paths, referred to as 'Fluxbtw1' and

'Fluxbtw2' for the leakage between the claw-poles, and 'Fluxtip' for the leakage from the tip of the claw-pole to the opposite end-plate and rotor side. The areas used for the measurement of the flux through the different paths are shown in Figure 5.1(b).

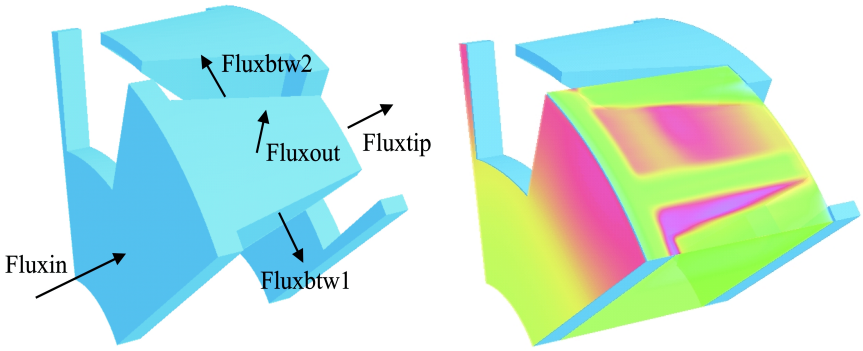

(a) Flux paths (b) Measurement surfaces

Figure 5.1: Flux paths and measurement surfaces in the rotor.

The leakage in the machine is expressed as the percentage of the flux flowing through the end-plates which does not enter the main body of the stator teeth. These quantities are measured at the radius corresponding to the middle of the teeth. It should be pointed out that the leakage cannot be directly calculated as the ratio between Fluxout and Fluxin, since a part of Fluxout will be driven through the leakage between the teeth. In order to reduce the leakage, ferrite and/or neodium-iron-boron (NdFeB) magnets will be incorporated in the original design. The ferrite magnet has a remanence of 386 mT, and a coercivity of 191 kA/m. The NdFeB magnet has a remanence of 1.12 T and a coercivity of 781 kA/m. Their BH curve is shown in Figure 5.2.

5.3 Topologies for leakage reduction

The analysis of the leakage flux flow in the original machine without magnets indicated that the main leakage path is from the tips of the claw-poles to the opposite end-plate (Fluxtip). Although perhaps unexpected, this fact is not sur-

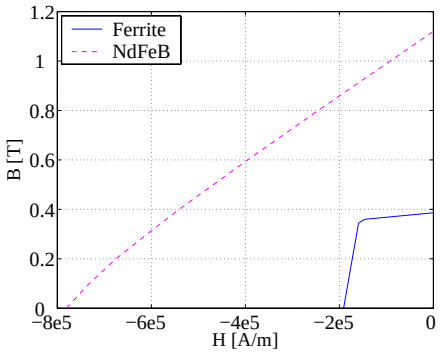

Figure 5.2: Magnet BH curves.

prising due to the proximity of the magnetically conducting end-plate. In order to decrease the leakage, seven designs with different alternatives for the location of the magnets around the claw-poles have been studied. The configurations are referred to with a number: number 1 is the original design without magnets (Figure 5.3(a)); number 2 is the design with only ferrite magnets in the cavities opposite the tips of the claw-poles (Figure 5.3(b)); number 3 is the design with only ferrite magnets between the claw-poles (Figure 5.3(c)); number 4 is the design with ferrite magnets in the tips and between the claw-poles (Figure 5.3(d)); number 5 is the design with only NdFeB magnets in the tips; number 6 is the design with NdFeB magnets in the tips and ferrite magnets between the claw-poles; and number 7 is the design with NdFeB magnets both in the tips and between the claw-poles. The arrows in the magnets indicate the direction of magnetization, which is opposite to the direction of the leakage in the original design.

5.4 Flux distribution results

The topologies presented in the previous section have been implemented in machines with different number of poles. It would be expected that the torque response increases with the pole number. However, as the number of poles increases, the claw-poles are closer to each other, which in turn increases the leakage between them. The ratio of three stator teeth per pole pair was maintained, independent of the number of poles. The angular measures were adapted in

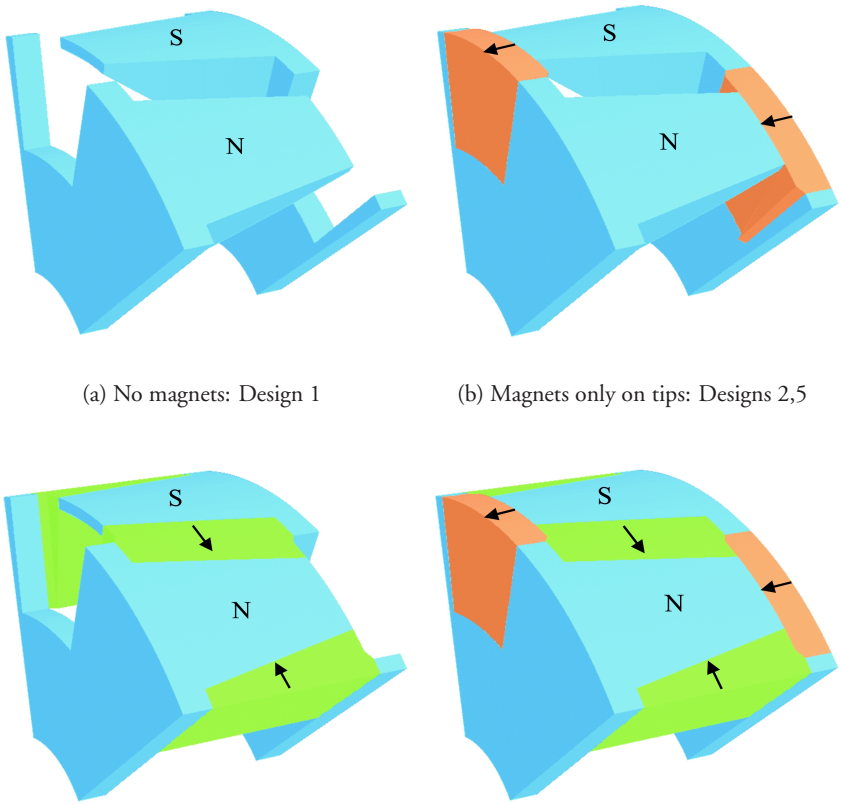

(a) No magnets: Design 1

(b) Magnets only on tips: Designs 2,5

(c) Magnets only in-between: Design 3

(d) Magnets overall: Designs 4,6,7

Figure 5.3: Topologies for leakage reduction.

proportion to the change in the pole angle, while the radial and axial measures were kept constant. The study of the flux distribution was performed at no load.

Design with 12 poles

The results for the flux flow in the 12-pole design are summarized in Table 5.1. It can be observed that in the original design without magnets, Fluxtip is about twice Fluxbtw1 and Fluxbtw2 together. When ferrite magnets are included in the tips, Fluxtip decreases by 14% while Fluxbtw1 and Fluxbtw2 are increased by 10%. The leakage is marginally reduced by 2%. Introducing only ferrite magnets between the claw-poles changes the direction of Fluxbtw1 and Fluxbtw2, which now contribute to increase Fluxout, and the leakage is decreased by 10%. The change in direction in the fluxes is represented with a negative sign in front of its value in the table. The differences between Design 3 and Design 4, with ferrite magnets both in the tips and between the claw-poles, are small. When only NdFeB magnets are included in the tips, the leakage is considerably improved compared to Design 2, since Fluxin is little changed whereas Fluxout is increased by 18%. However, although Fluxtip is decreased by 33%, the leakage between the claw-poles increases by 60%. This is probably due to the fact that the stator teeth are already saturated (1.4 T), what makes them a more difficult path to follow than the way to the adjacent claw-pole.

With ferrite magnets between the claw-poles and NdFeB in the tips, Fluxbtw1 and Fluxbtw2 shift direction and contribute to increase Fluxout by 40% compared to Design 1. Fluxtip is almost unchanged, and the leakage is reduced to less than half. Finally, including NdFeB magnets overall increases enormously the contribution of Fluxbtw1 and Fluxbtw2 to Fluxout, which is now 63% bigger than in Design 1. Fluxin is however decreased by 62%. These results indicate that the NdFeB magnets between the claw-poles are more effectively increasing the total flux in the machine, and driving it in the tangential direction. In fact, the leakage calculated as the percentage of the flux entering the teeth compared to the flux flowing in the end-plates is now negative, which implies that there is a source which drives the flux through an alternative path. Design 7 is basically a permanent magnet machine where the field coils can be used to adjust the level of magnetization.

Table 5.1: Summary of flux flow [wb]· 10^{-4} for the 12 pole design

Design	Fluxin	Fluxtip	Fluxbtw1	Fluxbtw2	Fluxout	leakage
1	7.53	2.24	0.55	0.59	4.44	71.6%
2	8.22	1.93	0.61	0.65	4.60	69.5%
3	6.20	3.50	-1.71	-1.66	5.54	62.0%
4	6.79	3.23	-1.66	-1.61	5.60	60.1%
5	8.41	1.28	0.90	1.10	5.45	48.3%
6	6.90	2.20	-1.00	-0.91	6.24	27.1%
7	2.84	3.51	-4.70	-4.57	7.22	$<$0%

Designs with higher pole number

The results for the flux flow in the designs with 16, 20 and 24 poles are summarized in Table 5.2, Table 5.3, and Table 5.4 respectively. It can be observed how the leakage increases with the number of poles. For a given pole number, the leakage decreases continuously from Design 1 to 7. In Design 1, the difference between the flux leaking between the poles and Fluxtip decreases with the pole number. In the machine with 24 poles, Fluxtip, Fluxbtw1 and Fluxbtw2 are quite similar. This means that as the pole number increases, the leakage between the claw-poles is becoming more important than the leakage from the tips. This is reasonable, since the angular distance between the poles decreases while the distance from the tip to the opposite end-plate is constant.

When ferrite magnets are included in the tips (Design 2), Fluxtip decreases by up to 24%, but Fluxout increases less than 7% in all the machines. However, Fluxbtw1 and Fluxbtw2 also increase by up to 20%. Therefore, part of the contribution from the magnet is lost through the leakage between the claw-poles. As indicated above, this is probably due to the saturation in the teeth combined with the low strength of the ferrite magnet. The decrease in the leakage with this solution is around 2% for all the machines.

Introducing only ferrite magnets between the claw-poles (Design 3) changes the direction of Fluxbtw1 and Fluxbtw2 in all the machines. Fluxtip is now increased from 56% in the 12-pole machine to 87% in the 24-pole machine. However, Fluxout is also increased by around 30%, and the leakage is decreased

Table 5.2: Summary of flux flow [wb]· 10^{-4} for the 16 pole design

Design	Fluxin	Fluxtip	Fluxbtw1	Fluxbtw2	Fluxout	leakage
1	5.88	1.53	0.63	0.65	3.26	74.8%
2	6.42	1.28	0.72	0.75	3.40	72.6%
3	5.07	2.60	-1.16	-1.12	4.31	65.9%
4	5.56	2.35	-1.07	-1.03	4.36	64.2%
5	6.79	0.77	1.04	1.21	4.11	56.2%
6	6.05	1.42	-0.25	-0.16	4.76	45.2%
7	2.08	2.70	-4.04	-3.92	5.95	<0%

Table 5.3: Summary of flux flow [wb]· 10^{-4} for the 20 pole design

Design	Fluxin	Fluxtip	Fluxbtw1	Fluxbtw2	Fluxout	leakage
1	4.86	1.13	0.68	0.71	2.48	77.5%
2	5.33	0.91	0.78	0.89	2.63	75.0%
3	4.40	2.01	-0.69	-0.65	3.41	69.5%
4	4.88	1.76	-0.58	-0.53	3.46	68.0%
5	5.72	0.46	1.08	1.12	3.20	61.5%
6	5.40	0.94	0.16	0.25	3.74	55.0%
7	1.74	2.12	-3.62	-3.51	5.14	<0%

Table 5.4: Summary of flux flow [wb]$\cdot 10^{-4}$ for the 24 pole design

Design	Fluxin	Fluxtip	Fluxbtw1	Fluxbtw2	Fluxout	leakage
1	4.10	0.86	0.72	0.74	1.93	80.4%
2	4.49	0.65	0.82	0.84	2.07	77.7%
3	3.87	1.61	-0.41	-0.37	2.74	73.2%
4	4.25	1.33	-0.30	-0.25	2.78	71.7%
5	4.91	0.26	1.11	1.14	2.54	66.6%
6	4.78	0.64	0.41	0.49	2.99	62.1%
7	1.55	1.70	-3.18	-3.07	4.54	$<$0 %

by around 8% in all the machines. The differences between Design 3 and Design 4, with ferrite magnets both in the tips and between the claw-poles, are small for all the machines. Fluxout is indeed very similar, and the difference in leakage between these two designs is less than 2%.

When NdFeB magnets are included in the tips (Design 5), Fluxtip decreases by up to 50%, and Fluxout increases between 22% and 32%. These values are clearly better than in Design 2, using ferrite magnets. However, the leakage between the claw-poles increases now between 55% and 75% compared to Design 1, due to the higher strength of the magnet. The benefits of including NdFeB magnets in the tips to reduce the leakage decreases with the pole number, from 23% for 12 poles, to 14% for 24 poles. In fact, the magnitude of the increase in Fluxout is four times the increase in Fluxin for the 12-pole design, while it is almost the same for the 24-pole design.

With ferrite magnets between the claw-poles and NdFeB in the tips (Design 6), Fluxbtw1 and Fluxbtw2 do not shift direction in the designs with 20 and 24 poles. The magnet capability to drive the flux in a certain direction is directly proportional to its thickness. When the pole number is increased, the space available for the magnet in its axial direction is considerably reduced between the claw-poles, while it is unaffected in the cavities. Therefore, in this case the contribution from the NdFeB magnets in the tips is stronger than that from the ferrite magnets on both sides of the claw-poles. The effectiveness of Design 6 to improve the leakage decreases with the pole number, from 45% in the 12-pole design, to 18% in the 24-pole design. While the increase in Fluxin between

Design 1 and 6 is more or less constant in all the machines, the increase in Fluxout is reduced with higher pole numbers, up to half in the 24-pole machine compared to the machine with 12 poles.

Finally, when NdFeB magnets are included overall (Design 7), the effect of the magnets between the claw-poles prevails over the magnets in the tips. It can be observed that the directions of Fluxbtw1 and Fluxbtw2 are opposite to the original direction of the leakage in all the machines. The increase in Fluxout between Design 1 and 7 is almost the same for all the machines, while the decrease in Fluxin is almost half in the 24-pole design compared to the design with 12 poles. This trend could be interpreted as a lower capability of the magnets between the claw-poles to drive the flux in the tangential direction, as the pole number increases, due to the reduction of their thickness.

It can be observed that the leakage in Design 7 is negative in all the machines. Indeed, the NdFeB magnets between the claw-poles open an important path to the linking flux along the circumferential direction, as an alternative to the axial path. This new linking flux is not accounted for in the total flux, which is measured through the stator end-plates. Therefore the leakage results for Design 7 are not really representative of the leakage of the machine and cannot be compared to the rest of the designs under the same conditions. However, it is clear that the linking flux is importantly increased in Design 7, and this will eventually lead to a considerable increase in the output torque of the machine.

5.5 Torque response

The torque response is calculated at the thermal limit, and the iron losses were obtained from the MEC model, as explained in Chapter 2. As the pole number increases, there is less cooling surface per tooth, and the resistance in the a.c. coils increases. This is due to the less space available in the slots if the insulation thickness in the wall and between the coils is kept constant. This implied that the total a.c. current for the machines with 16, 20 and 24 poles was reduced by 14%, 26% and 34% respectively, compared to the design with 12 poles. To achieve thermal equilibrium, the d.c. currents also had to be adjusted, although the decrease was less than 5%.

The static torque response through the positive electrical pole for the machines with different pole numbers is shown in Figure 5.4. The results for Design 5 have been omitted in order to provide a clearer plot. This response is indeed very close to the response from Design 4, with a slightly higher peak.

However, this peak is always below the peak in Design 6 and usually half the way between Design 4 and 6. The responses from Designs 1 and 2, and Designs 3 and 4, have been assigned the same curve, since they are almost literally on top of each other.

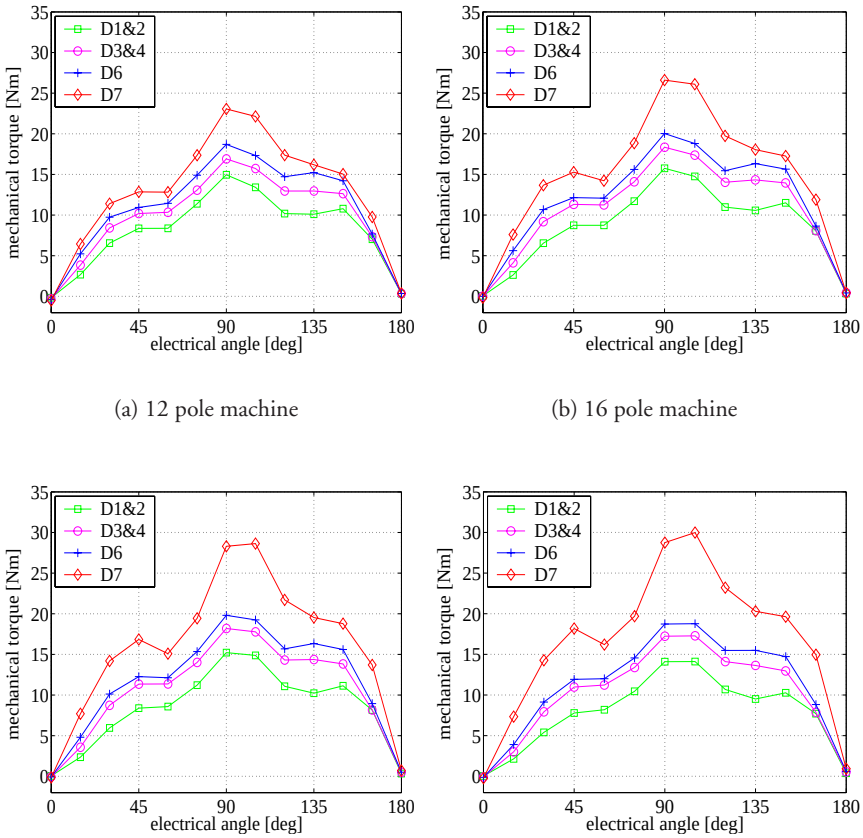

(a) 12 pole machine

(b) 16 pole machine

(c) 20 pole machine

(d) 24 pole machine

Figure 5.4: Static torque response.

It can be observed from the figures that, for a given pole number, the peak torque increases continuously from Design 1 to 7. This agrees with the flux flow results presented in the previous section, which indicate that Fluxout in-

creases in the same manner. The peak torque in the original design without magnets is very similar for all the machines, around 15 Nm, although it slightly decreases for the 24-pole case. The torque delivered by Design 3&4 increases by 13%, 16%, 20% and 22% for the machines with 12, 16, 20 and 24 poles respectively, compared to the original design with no magnets. When implementing Design 6, the torque increase reaches 25%, 27%, 30% and 33% in the same pole number order. Finally, when implementing Design 7 the peak torque increases by 53%, 69%, 88% and 113% respectively. The configuration delivering the maximum torque is Design 7 with 24 poles, which gives 30 Nm. For all machines, it can be observed that the difference is very significant when NdFeB magnets are used overall, compared to the rest of the designs.

Economical considerations

The solutions presented in this chapter to reduce the leakage are based in the use of permanent magnet material, which is considerably more expensive than iron or copper. Therefore, the improvement in the performance of the machine needs to be compared to the cost of the solution. Another implication is that the inertia of the rotor will be increased due to the mass added when the magnets are incorporated. Table 5.5 presents a summary of the amount of each magnet material which is needed for the different configurations, the change in the inertia of the rotor and the cost.

The mass calculation was performed as a function of the volume, with a density of 7500 kg/m^3 for NdFeB magnets and 4800 kg/m^3 for the ferrite material. The mass of magnet material and iron is independent of the number of poles. The mass of iron in the machine is 9.73 kg. This is distributed in 1.42 kg in the rotor, 4.35 kg in the stator core and teeth, and 3.96 kg in the end-plates. The mass of copper in the d.c. coils is constant for all the machines, 1.12 kg. However, the mass of copper in the a.c. coils decreases with the pole number, 1.71 kg for 12 poles, 1.39 kg for 16 poles, 1.20 kg for 20 poles, and 1.07 kg for 24 poles.

The per unit material cost was calculated as a function of the mass of the active parts of the machine. The iron was assigned 1 p.u., the copper 5 p.u., the ferrite magnet 10 p.u., and the NdFeB magnet 50 p.u. The cost due to the difference in the weight of the a.c. coils for different pole numbers was not considered. The values in the table correspond to the 12-pole design, but the ratio of change between different designs will be similar independently of the

Table 5.5: Summary of the properties of the designs

Design	ferrite [kg]	NdFeB [kg]	inertia [kg · m^2]	cost [p.u.]
1	0	0	$4.0 \cdot 10^{-3}$	23.9
2	0.185	0	$4.6 \cdot 10^{-3}$	25.7
3	0.377	0	$5.3 \cdot 10^{-3}$	27.7
4	0.563	0	$5.9 \cdot 10^{-3}$	29.5
5	0	0.290	$5.0 \cdot 10^{-3}$	38.4
6	0.377	0.290	$6.2 \cdot 10^{-3}$	42.2
7	0	0.880	$6.9 \cdot 10^{-3}$	67.9

pole number. In general, an average increase in the torque by 18% (Design 3&4), 29% (Design 6) and 81% (Design 7) implies an approximate increase in the cost of the machine by 20%, 77% and 284% respectively. The maximum torque increase (Design 7, 24 poles) corresponds to a increase in the cost around 19% per extra Newton-meter.

5.6 Conclusions

In this chapter, it has been shown how permanent magnets can be used to enhance the performance of a claw-pole machine. Although the main leakage path in our particular machine is through the tip of the claw-poles to the opposite end-plate, placing ferrite magnets between the claw-poles proves to be more effective than using them in the tips. This is mainly due to the higher space available on both sides of the poles compared to the cavity in front of the tip, which allows to use thicker magnets. However, if high density NdFeB magnets are used only in the tips, the leakage is considerably reduced, although the peak torque only increases with less than 6% compared to the case with only ferrite magnets in-between. Combining NdFeB magnets in the tips and ferrite magnets in-between further improves the leakage and torque response, although not as much as using NdFeB magnets overall. In this case, the pattern of magnetization of the machine is significantly altered, since it is basically shifted from the axial to the tangential direction. The torque response increases between 53% for the machine with 12 poles up to 113% for the 24-pole case.

However, in this design the mass of NdFeB reaches 7% of the total mass of the active components in the machine, which in turn would increase its cost significantly. Finally it should be pointed out that the possibilities of achieving field weakening by reducing the current in the d.c. coils are reduced when stronger magnets are incorporated.

Chapter 6

Comparison with three alternative machines

6.1 Introduction

The purpose of this chapter is to compare the performance of the machine treated so far with other topologies. The designs considered are an outer rotor claw-pole machine, and two more conventional designs of synchronous machines with electrical and permanent magnet magnetization. The machines are compared for similar cooling conditions. Therefore, a similar calculation of the iron losses and the thermal properties will be carried out as in Chapter 3 and Chapter 4. The a.c. coils form a similar concentrated winding in all the designs, and the thermal calculations will emphasize the new considerations specific for each design. The losses at load are higher in all the designs compared with the no load case, and they are used in the thermal models. All the machines have 12 poles, and the characteristics of the 12-pole version of the EMSM analyzed so far are included for comparison. The new machines have been directly optimized in FEM, refining the original measures from the EMSM for each particular case. In principle it was desired to keep constant the total volume for comparison. However, it was observed that a considerable amount of material could be removed from certain topologies in the axial direction. The constrain was then chosen to be a constant outer and inner diameter only. With these specifications, and for the given cooling system, the aim was to achieve the best possible design for each topology in order to make a fair comparison. The dimensions of the machines are included in Appendix D.

6.2 EMSM

The characteristics of the 12-pole version of the machine analyzed so far are summarized in this section, and the design will be referred to as 'Design 1'. The iron losses in the stator and in the rotor at no load and load are shown in Figure 6.1(a) and Figure 6.1(b) respectively. The losses at load are around 30% higher than in the no load case. Compared to the 16-pole machine, the losses at no load are only slightly reduced (3%). At load the losses are decreased by around 10% in the 12-pole design, mainly due to the reduced stator losses. Table 6.1 shows the distribution of the alternating and rotating losses through the different parts in the machine. The same trends as in the 16-pole design are observed, although a considerable reduction in the alternating losses can be appreciated in the teeth body.

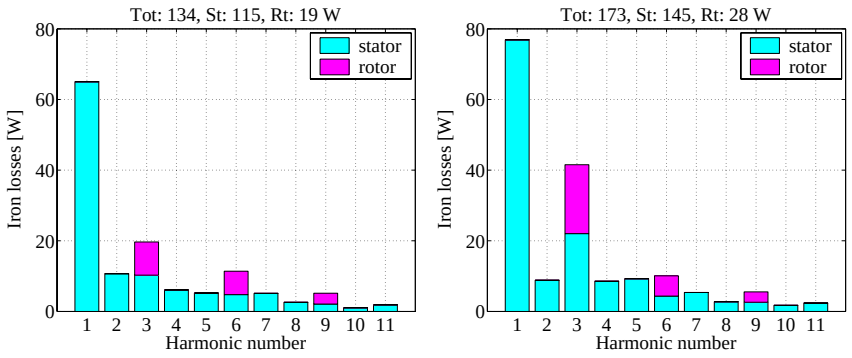

(a) No load (b) Load

Figure 6.1: Distribution of the iron losses in Design 1 as a function of the harmonic number.

The thermal model is exactly the same as the one presented in Chapter 4, now adapted to the new dimensions of the machine. The parameters obtained for the heat transfer calculation are shown in Table 6.2, and they are very similar to the design with 16 poles. In particular, the heat transfer coefficient is identical for the end-plate, and only reduced by two units in the cylinder. This is mainly due to the 2^oC decrease in the film temperature, which affects slightly the properties of the coolant.

Table 6.1: Summary of the predicted iron losses in Design 1. [W]

	No Load		**Load**	
Part	Alternation	Rotation	Alternation	Rotation
back-core	4.3	27.4	7.6	40.8
teeth body	18.4	6.7	28.4	5.8
teeth tip	1.7	23.0	3.2	26.1
end-plates	1.0	32.2	2.7	30.0
rotor sides	0.1	3.3	0.4	4.2
claw-poles	0.5	15.2	1.1	22.6
Total	26.0	107.8	43.4	129.5

Table 6.2: Parameters for heat transfer calculation in Design 1

Coefficient	**Cylinder**	**End-plate**
Tm [^{o}C]	46	46
Δ T$_w$ [^{o}C]	8	10
U [m/s]	0.022	0.014
Re	11697	6605
Pr	3.8	3.8
Nu	112	84
A	0.664	0.664
m	0.50	0.50
n	0.33	0.33
hconv [W/mK]	227	193

Table 6.3: Temperature distribution in Design 1 [^{o}C]

Part	a.c. path	d.c. path
Tsf	61	62
Tcr	67	
Twl	96	81
Tis	130	126
Thp	140	140

The temperatures in the different regions of the machine are summarized in Table 6.3. The temperatures in the d.c. circuit are practically identical as in the 16-pole design, while in the a.c. circuit they are reduced by around 4^{o}C for the same temperature rise in the coils. This can be explained considering the lower losses in the teeth and core, together with the fact that the total current loading is reduced by 15% in the 12-pole machine. Adding the a.c. Ampere turns in all the slots around the machine, a figure of $6.4{\cdot}10^4$ A/m is obtained for the 16-pole machine, and $5.6{\cdot}10^4$ A/m for the 12-pole machine, expressed as a function of the circumferential length along the surface of the machine.

The static and dynamic torque response at the thermal limit are shown in Figure 6.2. The maximum torque is 14.4 Nm. and the ripple is 33% of the peak torque. The Ampere turns in one a.c. and d.c. coil are 969 A and 1199 A respectively. The copper losses are 545 W (184 W a.c. and 361 W d.c.). The efficiency at 1500 r.p.m. is 76%. The copper losses account for 76% of the total losses in the active parts of the machine.

6.3 Outer rotor EMSM

The second topology studied is shown in Figure 6.3, and it will be referred to as 'Design 2'. This design is an outer rotor variant of Design 1, and the claw-pole rotor is now sandwiched between the stator core and the stator ring, where the field coil is placed. In the following, the stator core in Figure 6.3 will be referred to as 'stator 1', and the stator ring as 'stator 2'. There are two radial airgaps, between stator 1 and the rotor, and between the rotor and stator 2. With this topology the slip-rings are also removed, but the mechanical coupling from the rotor to the shaft is more complicated. A mould could be used to fit both sides

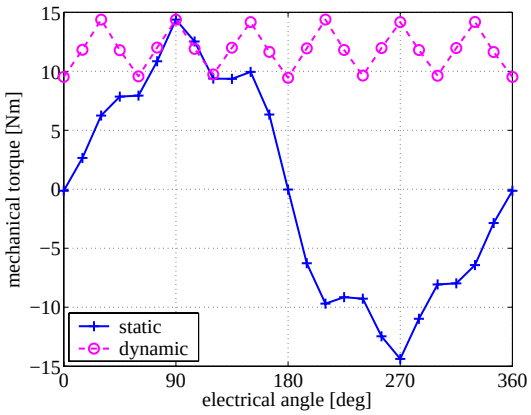

Figure 6.2: Torque response in Design 1.

of the rotor into one piece, which is then joined to the shaft using a set of radial bars on one side of the machine. On the other side the stator ring and the stator core are coupled together mechanically.

From FE simulations it could be observed that the length of the core in stator 1 (zyc) could be reduced to 41% of the original value in Design 1. The thickness of the core (dy) is however increased to almost 3 times. The only reason for this is to provide the mechanical coupling between stator 1 and the shaft (through bearings). The dimensions of the teeth body and tips were basically unchanged. Only the slot opening was decreased to 24% of the tooth pitch, compared to 33% in Design 1. In the rotor, the thickness of the sides attached to the claw-poles (ztr) was increased by 50%, matching the width of the closest iron parts in stator 2. This was done to decrease the reluctance of the magnetization path, and in fact the total length of the machine is directly affected by this measure. The radial height of these sides was kept to a minimum since they penalize the diameter of the machine. However, they can not bee too small since they also provide the mechanical coupling between the claw-poles in the absence of the attachment to the shaft. The angle span at the base of the claw-poles was maintained constant. The angle at the tips was increased by around 50%. This decreased the reluctance in the claw-poles and had little effect on the leakage between them, since their radial length at the base (dr) was halved. Finally, the thickness of the yoke in stator 2 (dy2) was maximized to

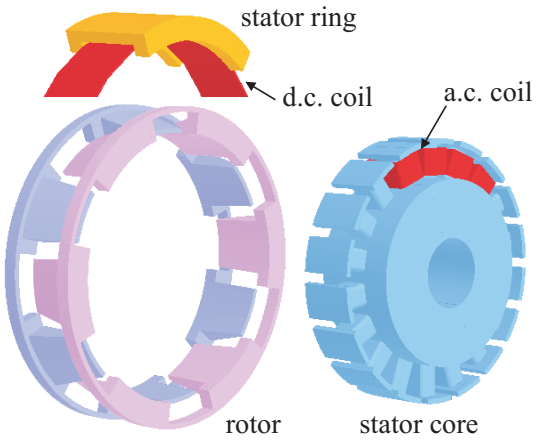

Figure 6.3: Design 2.

reduce the reluctance along the magnetization path. However, it also reduces the space available for the d.c. coil since it was assumed that this coil was constrained within stator 2. But in fact, the coil could be extended further into the rotor, between the sides of the claw-poles, provided a suitable mechanical support system.

Iron losses

The ratio between the alternating and rotating losses for the fundamental in the stator is shown in Figure 6.4(a), and the corresponding flux density in Figure 6.4(b). As in Design 1, the alternating losses are concentrated in the body of the teeth (1.2 T), while the rotational losses are mainly located in the tips. Rotational losses are also expected in the parts of stator 2 close to the rotor (0.3 T), and the core in stator 1 close to the teeth (0.6 T). However, the flux density is very little in most regions of the core, especially those close to the shaft, and there is almost no variation in their value which is the reason for the unity ratio in these elements. The ratio and the flux density for the third harmonic in the rotor are shown in Figure 6.4(c) and Figure 6.4(d). The losses are mainly due to rotation in the claw-poles, although the flux density is low (0.2 T).

A summary of the losses in the stator and in the rotor at load and no load including the harmonics is presented in Figure 6.5(a) and Figure 6.5(b) respec-

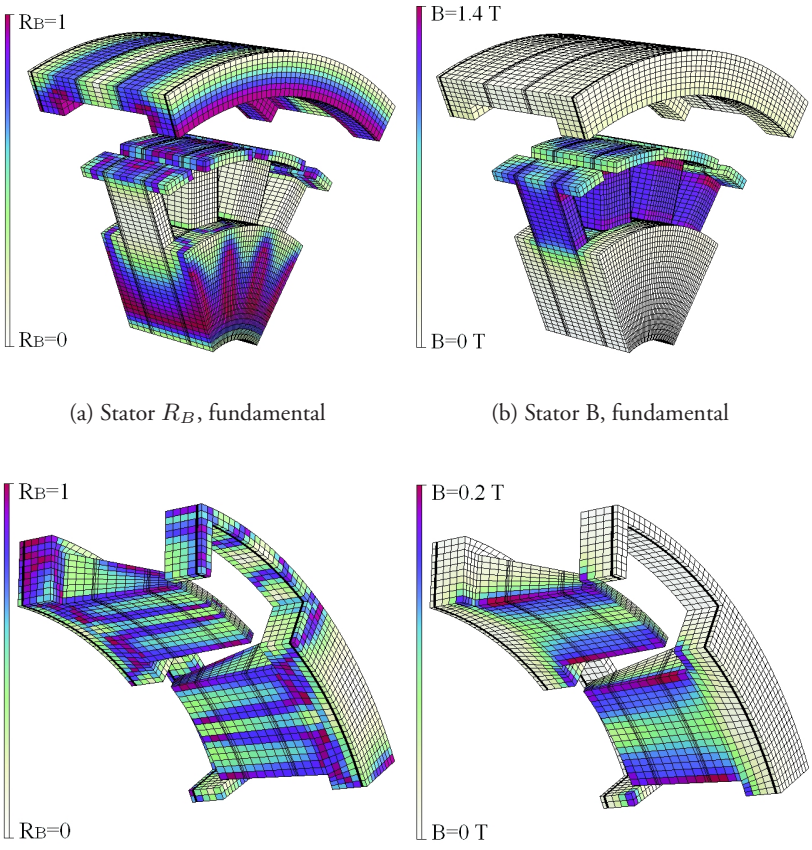

(a) Stator R_B, fundamental

(b) Stator B, fundamental

(c) Rotor R_B, 3rd harmonic

(d) Rotor B, 3rd harmonic

Figure 6.4: Design 2 R_B and flux density distribution for the fundamental in the stator and the third harmonic in the rotor, no load.

tively. In both cases, the highest losses are due to the fundamental component of the stator. The overall losses are increased by 50% when the machine is loaded, and there is also an important increase of the losses due to the rotor third harmonic. This contributes to almost triplicate the losses in the rotor at load, while in the stator alone the losses are increased by 31%. Table 6.4 shows a summary of the alternating and rotating loss components calculated at different parts of the machine. The teeth body stand for around 75% of the total alternating losses at load and no load. The teeth tips are the most important contributor to the rotational losses, around 30% at no load and load. The core of stator 1 and the claw-poles experiment the most significant increase in the rotational losses at load, while these losses in stator 2 are decreased by around 35%. The rotational losses are the most important both at no load and load, corresponding to 83% and 76% of the total losses respectively.

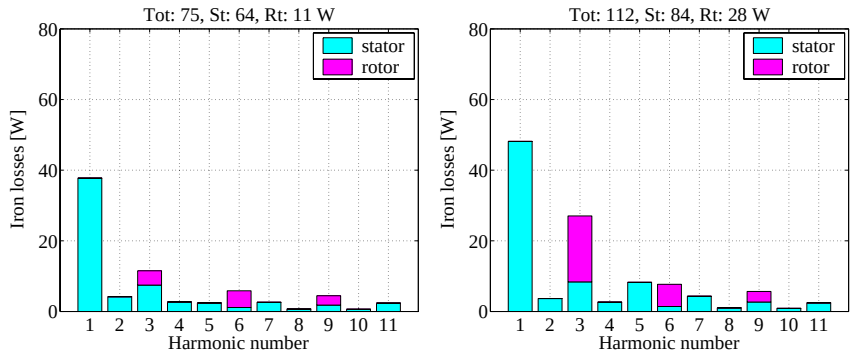

(a) No load (b) Load

Figure 6.5: Distribution of the iron losses in Design 2 as a function of the harmonic number.

Thermal model

The paths considered for the dissipation of the losses in Design 2 are shown in Figure 6.6. Only the sides of the core in stator 1 can be used to cool 'Pac', since the shaft passes through the centre of the core. The rotor is not completely enclosed as in Design 1 and therefore it was assumed that the rotor losses were

Table 6.4: Summary of the predicted iron losses in Design 2. [W]

	No Load		**Load**	
Part	Alternation	Rotation	Alternation	Rotation
St. 1 core	1.2	9.4	2.4	15.3
St. 1 teeth body	10.0	5.8	18.9	5.7
St. 1 teeth tip	1.2	18.7	2.9	27.6
St. 2 core	0.2	7.4	0.1	5.1
St. 2 sides	0.1	9.8	0.0	5.8
rotor sides	0.1	2.2	0.2	5.3
claw-poles	0.2	8.9	2.0	20.4
Total	13.0	62.2	26.5	85.2

dissipated directly through the airflow caused by the rotor rotation. This airflow could be in turn cooled through the external surfaces of the water channels, although the temperature increase in the water due to this effect was not taken into consideration in the calculations. The area available to cool the field winding is considerably reduced compared to Design 1, and this will constrain the field current. The iron losses in stator 1 were grouped in a similar way as in Design 1, whereas the iron losses in stator 2 were separated into those in the core above the d.c. coil and on its sides.

As in Design 1, it was assumed that the coolant would flow through a duct of exactly the same shape as the cooled surface and a thickness of 3 mm. The water flow of 1.2 liter/minute ($\dot{Q}$) at 27^{o}C was split equally for the a.c. and d.c. cooling. The heat transfer coefficient was calculated using a similar formulation as in Design 1, i.e. forced convection over a plate. Symmetry was exploited, and this formulation was applied to only one side of the core in stator 1, and to half of the cylinder defined by stator 2. The coefficient for the cooling surface in stator 1 was calculated considering a flow of $\dot{q}_{ac} = \dot{Q}/8$ through half the surface in one side A_{plt} (6.1), and the length L_{plt} corresponding to this path (6.2). This length is the geometric characteristic used to calculate the Reynolds and Nusselt numbers. The speed of flow is obtained from (6.3). For stator 2, the water flow through one half of the cylinder was $\dot{q}_{dc} = \dot{Q}/4$. The sides

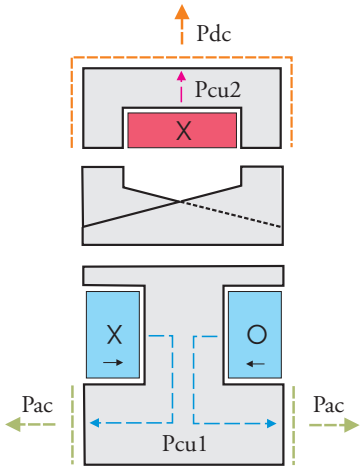

Figure 6.6: Thermal dissipation in Design 2.

of stator 2 will also contribute to the cooling, and their area were added to the cylindrical surface, forming an equivalent duct. For simplicity, the length of this duct was taken as half the circumferential length of the machine at the outer radius. A summary of the coefficients obtained for the heat transfer calculation in stator 1 and 2 is shown in Table 6.5. The heat transfer coefficient from stator 2 is very similar to the cylindrical surface in Design 1, while the coefficient for stator 1 is considerably increased. This is mainly due to the shorter length of the cooling path.

$$A_{plt} = \frac{1}{2}\pi(ros1^2 - ris1^2) \tag{6.1}$$

$$L_{plt} = ros1 - ris1 + 2\pi(ros1 + ris1)\frac{1}{4} \tag{6.2}$$

$$U_{ac} = \frac{\dot{q}_{ac}}{A_{plt}/L_{plt} \cdot w_{dct}} \tag{6.3}$$

The temperatures are calculated starting from the heat exchange between the surface of the motor and the coolant. For 'Pac' a similar thermal circuit as the one proposed in Chapter 4 is used. The temperature in the cooled surface of stator 1 is given by (6.4), where Asf_{ac} is the surface on both sides of the core.

Table 6.5: Parameters for heat transfer calculation in Design 2

Coefficient	**Stator 1**	**Stator 2**
Tm [^{o}C]	49	45
Δ T$_w$ [^{o}C]	5	8
U [m/s]	0.033	0.022
Re	8390	11711
Pr	3.7	3.9
Nu	93	113
A	0.664	0.664
m	0.50	0.50
n	0.33	0.33
hconv [W/mK]	421	229

The losses dissipated through this path are the total losses in the a.c. winding and the iron losses in stator 1. The temperature in the surface of stator 2 was calculated using (6.5), where Asf_{dc} is the total cooling area around the surface. The losses in this case corresponded to the copper losses in the d.c. coil and the iron losses in stator 2. The copper losses in the coils were calculated as in Design 1.

$$Tsf_{ac} = \frac{Pcu_{ac} + p \cdot (Pfe1_{ac} + Pfe2_{ac})}{Asf_{ac} \cdot hconv_{ac}} + T_{\infty 1} \tag{6.4}$$

$$Tsf_{dc} = \frac{Pcu_{dc} + Pfe_{dc}}{Asf_{dc} \cdot hconv_{dc}} + T_{\infty 2} \tag{6.5}$$

The temperature in the core of stator 1 was calculated using (6.6). The length Lsc_{ac} corresponds to half the length from the center of the core surface attached to the teeth to the cooling surface at the level of the shaft, as indicated in Figure 6.7(a). The area Asc_{ac} is calculated as the arithmetic average between the whole core surface at the level of the teeth and the area of the cooling sides Asf_{ac}. The temperature in the teeth wall is calculated using (6.7), in the same way as it was done for Design 1, but now excluding the iron losses in the claw-poles. The rest of the equations for 'Pac' up to the hot spot in the a.c. winding

are identical to Design 1. The temperature in the wall of stator 2 is calculated using (6.8). The length Lsw_{dc} is the arithmetic average between Lp_1, Lp_2 and Lp_3 in Figure 6.7(b), and the area Asw_{dc} is the average between the cooled surface and that in contact with the wall insulation, as indicated in the figure.

$$Tcr_{ac} = \frac{(Pcu_{ac} + p \cdot (Pfe1_{ac} + Pfe2_{ac}))Lsc_{ac}}{Asc_{ac} \cdot \kappa_{fe}} + Tsf_{ac} \quad (6.6)$$

$$Twl_{ac} = \frac{p \cdot (Pcu^1_{ac} + Pfe1_{ac})Lcw_{ac}}{Acw_{ac} \cdot \kappa_{fe}} + Tcr_{ac} \quad (6.7)$$

$$Twl_{dc} = \frac{(Pcu_{dc} + Pfe_{dc})Lsw_{dc}}{Asw_{dc} \cdot \kappa_{fe}} + Tsf_{dc} \quad (6.8)$$

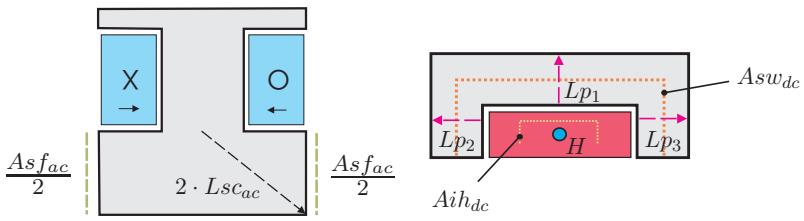

(a) Stator 1 yoke element (b) Stator 2 element

Figure 6.7: Parametrization of the stator 1 and stator 2 thermal elements.

The temperature in the surface of the d.c. winding closest to the iron is calculated using (6.9). The length of the path is the insulation thickness $insl$. The area Awi_{dc} is proportional to Asw_{dc}, but now taken through the middle of the insulation. The hot spot in the coil was located at its geometrical center, as shown in Figure 6.7(b) (H). The temperature at this point was calculated using (6.10). The length Lih_{dc} is the arithmetic average between the distance from the hot spot to the longest and shortest sides of the coil (in the radial and axial directions). The area Aih_{dc} was calculated as half the area corresponding to the longest outer side of the coil, plus two times half the area corresponding to the shortest side, as indicated in the figure. The temperatures in the different

Table 6.6: Temperature distribution in Design 2 [^{o}C]

Part	a.c. path	d.c. path
Tsf	66	60
Tcr	90	
Twl	110	67
Tis	136	122
Thp	140	140

parts of the machine are summarized in Table 6.6.

$$Tis_{dc} = \frac{Pcu_{dc} \cdot insl}{Awi_{dc} \cdot \kappa_{kapton}} + Twl_{dc} \tag{6.9}$$

$$Thp_{dc} = \frac{Pcu_{dc} \cdot Lih_{dc}}{Aih_{dc} \cdot \kappa_{coil}} + Tis_{dc} \tag{6.10}$$

The static and dynamic torque response at the thermal limit are shown in Figure 6.8. The maximum torque is 7.8 Nm and the ripple is 28% of the peak torque. The Ampere turns in the one a.c. coil are 670 A, and in the d.c. coil 1525 A. The total copper losses are 449 W (137 W a.c. and 312 W d.c.). The copper losses account for 80% of all the losses in the active parts of the machine. The efficiency of the machine at 1500 r.p.m. is 69%.

6.4 Conventional EMSM

The third topology studied is shown in Figure 6.9, and it will be referred to as 'Design 3'. This configuration resembles the conventional design of an electrically magnetized synchronous machine, where the field coils in the rotor are accessed through slip-rings. This is a radial machine that could be entirely built from iron laminations. However, iron powder allows both the stator yoke and the teeth tips to be extended above the teeth body, which leaves more space for the winding. For the same reason iron powder was used in the stator core in Design 2, where the flux flow is only radial. It can be argued that the massive yokes in the stator core in Design 2 and the rotor core in Design 3 could be built from laminations. However, it was tested in FEM that the difference in

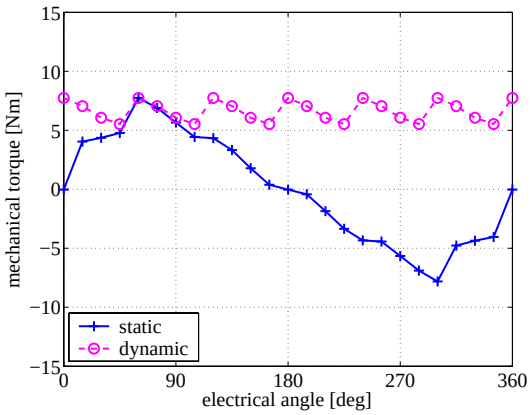

Figure 6.8: Torque response in Design 2.

the torque response is negligible, since the linking flux is still constrained by the lower permeability of the iron powder used in the teeth.

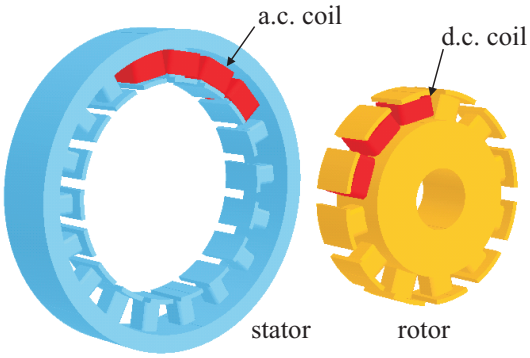

Figure 6.9: Design 3.

The stator of the machine is very similar to that in Design 1. The only differences are the length (zyc), which is reduced by 44% and the slot opening (wos), which is reduced by 28% to compensate for the ripple. The rotor has the shape of an inverted stator and the teeth have the same axial dimensions as those in the stator. The length of the rotor yoke was minimized, and it matched

the axial length of the teeth tips (ztps2). The slot opening in the rotor (wos2), as in the stator, was adapted for an optimal torque response.

Iron losses

The ratio between the alternating and rotating losses for the fundamental in the stator is shown in Figure 6.10(a), and for the third harmonic in the rotor in Figure 6.10(c). As in the previous designs, the alternating losses are concentrated in the body of the teeth, where the flux density is around 1.2 T. The rotational losses dominate at the teeth tips (0.8 T) and parts of the yoke located around the teeth connection. In the rotor, rotational losses are expected mainly in the tips, although the flux density is only around 0.2 T. Little losses are expected at no load in the body of the rotor teeth and the yoke, where the flux density is too small.

The losses per harmonic component in the stator and the rotor at load and no load are shown in Figure 6.11. At load the stator losses are almost doubled and the rotor losses are triplicated. The most important contribution to the stator losses is still due to the first harmonic, and for the rotor the third harmonic dominates clearly at load. A summary of the contribution to the total losses from the alternating and rotating components in different parts of the machine is shown in Table 6.7. At no load, 70% of the alternating losses are located in the stator teeth body. At load, the alternating losses are increased overall, but still the stator teeth body stands for 63% of the total. The rotational losses at no load are dominated by the stator teeth tips and back core, and their values are almost doubled at load. In the rotor, the teeth tips contribute to around 20% of the total rotational losses in the machine. Overall, the rotational losses represent 71% and 66% of the total losses at no load and load respectively.

Thermal model

The paths considered for the dissipation of the losses in Design 3 are shown in Figure 6.12. The path for the dissipation of 'Pac' is identical to that in Design 1, although the cooling surface is reduced together with the length of the machine. The copper losses from the d.c. coils mounted in the rotor ('Pcu2') must be air-cooled. The coolant volumetric flow in the stator is the same as in the stators in the previous designs, and therefore a smaller pump could be purchased, which in turn will also compensate for the additional cost of the air-cooling system.

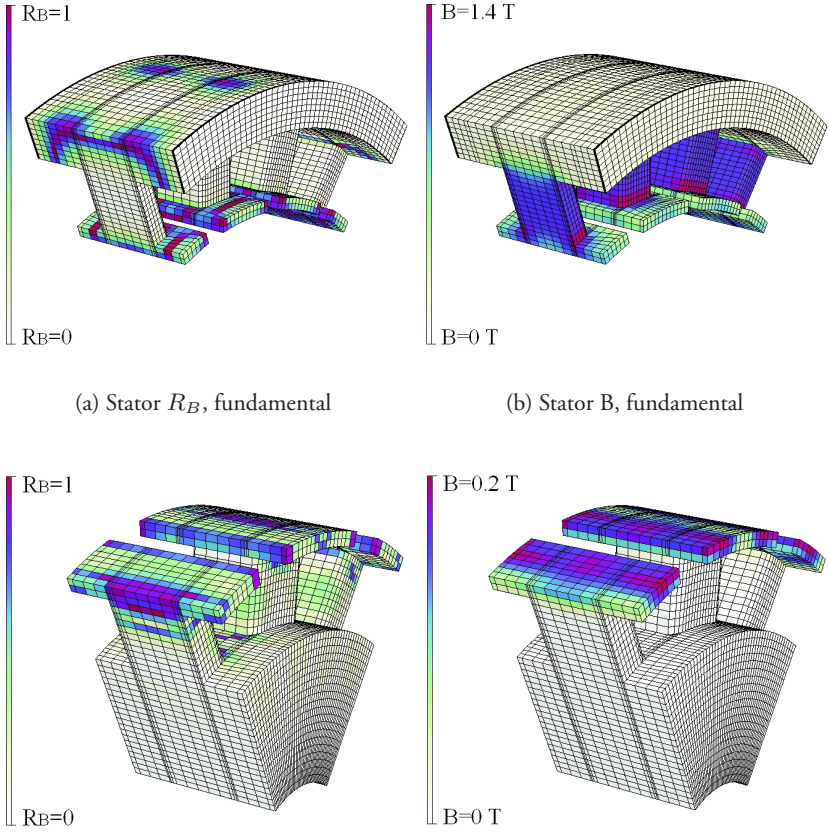

(a) Stator R_B, fundamental

(b) Stator B, fundamental

(c) Rotor R_B, 3rd harmonic

(d) Rotor B, 3rd harmonic

Figure 6.10: Design 3 R_B and flux density distribution for the fundamental in the stator and the third harmonic in the rotor, no load.

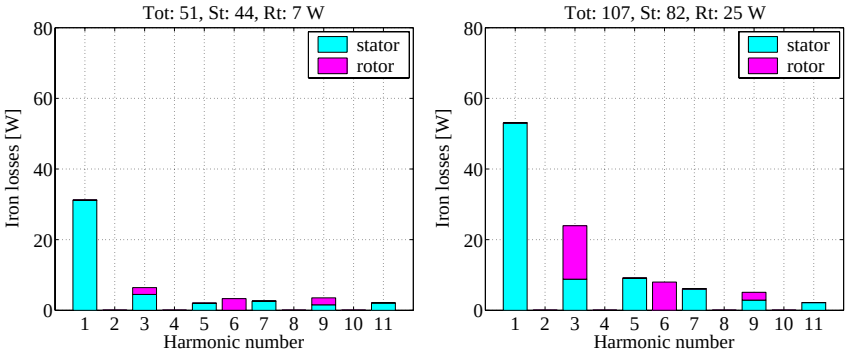

(a) No load (b) Load

Figure 6.11: Distribution of the iron losses in Design 3 as a function of the harmonic number.

Table 6.7: Summary of the predicted iron losses in Design 3. [W]

	No Load		**Load**	
Part	Alternation	Rotation	Alternation	Rotation
St. back-core	3.0	11.8	6.6	23.4
St. teeth body	10.2	4.4	22.9	4.8
St. teeth tip	0.9	13.6	3.4	21.1
Rt. back-core	0.0	0.6	0.2	2.2
Rt. teeth body	0.1	0.4	0.9	5.9
Rt. teeth tip	0.2	5.8	2.3	13.8
Total	14.4	36.6	36.3	71.2

The iron losses in the stator were grouped as in Design 1. The iron losses in the rotor were assumed to be dissipated directly to the air, as in Design 2, thus not contributing to heat the coils.

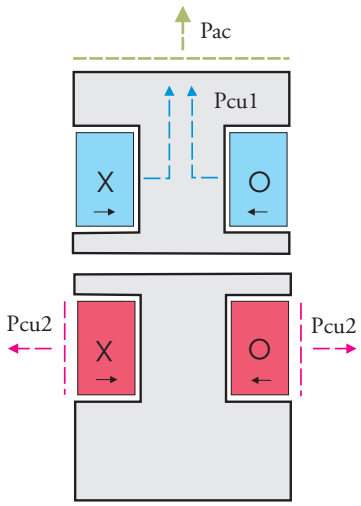

Figure 6.12: Thermal dissipation in Design 3.

In principle, it was assumed that no losses were transferred between the stator and the rotor through the airgap. The open rotor construction allows the heat to be removed directly from the surface of the d.c. coils by an axial airflow if enough space is left between these coils in the slots. It was assumed that a separate fan would be used to provide an airflow of 10 m/s along the lateral surfaces of each coil, as shown in Figure 6.13. The fan could be attached to the rotor if the cooling could be compromised at low speeds, otherwise it should be mounted separately. A typical fan of 80 mm diameter and 15 mm length produces at 1500 r.p.m. a flow of 15 CFM (cubic feet per minute), which is equivalent to 0.42 cubic meter per minute. Assuming that all this flow is driven through an area equivalent to all the ducts between the coils, with an average thickness of 1.75 mm each, a speed of 21.5 m/s is obtained. However, the resistance of the body affects the actual flow, which was therefore assumed to move with around half the ideal speed. In machines where the rotor losses are cooled through the stator, such as small asynchronous machines, the

conduction/convection through the airgap is usually calculated using a Nusselt number of 2 (Bjorklund and Kays, 1959), (Becker and Kaye, 1962), (Aoki et al., 1967). This coefficient was obtained empirically for smooth surfaces and laminar flow. Gazley (1958) carried out a similar study considering a more realistic airgap with the slotted stator, and it was shown that the heat conduction decreases because of the slots. However, according to Gazley, a convective heat transfer component appears, and a value of $Nu = 2.5$ was obtained for laminar flow.

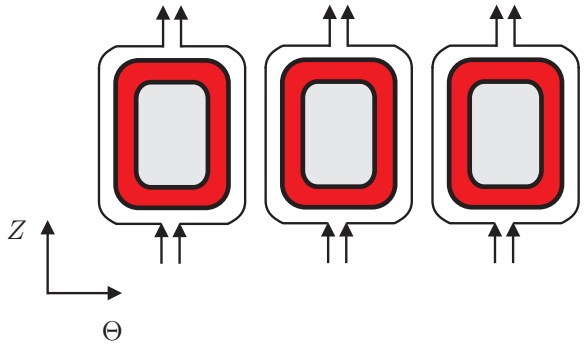

Figure 6.13: Air flow around the rotor coils.

The heat transfer coefficient from the stator cylindrical surface was calculated in the same way as in Design 1. The water flow ($\dot{Q}$) is now 0.6 liter/minute, and the flow through half the cylinder is $\dot{q}_{ac} = \dot{Q}/2$. The parameters for the heat transfer calculation in the stator are summarized in Table 6.8. Compared to Design 1, the speed of the flow is increased since the cooling surface is reduced. This results in an increase in the Reynolds and Nusselt numbers, and the heat transfer coefficient is 33% higher than in Design 1. The coefficient from the surface of the rotor coils is calculated using a similar formulation. The cooling area corresponds to the external surface of the coils (parallel to the teeth body), and the length of the path to half the perimeter of one coil, as described by the arrow lines in Figure 6.13. The calculations of the dimensions of the d.c. coils is similar to those in the stator described in Chapter 4. The cross-sectional coil area A_{dc} (6.11) is however reduced by 15% in order to allocate space between the coils for the axial airflow, as described above.

This affected obviously the thickness and the resistance of the coil.

$$A_{dc} = \min(Aaxi_{dc}, Atan_{dc}) \cdot 0.85 \tag{6.11}$$

The inlet temperature of the cooling air was selected to be equal to that of the water. This ensures that there is no heat exchange between the cooling water and the airflow, maintaining two separate circuits. The film temperature was selected as the average between the inlet and outlet temperatures, as explained in Chapter 4. For the calculation of the temperature increase in the rotor coils only the copper losses were considered, and the air volumetric flow was selected as the equivalent of 15 CFM. The coefficients obtained for the rotor are also summarized in Table 6.8. The high temperature in the surface of the coils increases considerably the film temperature. A 16% higher Reynolds number is obtained compared to the water cooled circuit, although the Prandlt and Nusselt numbers are significantly decreased. This results in a low heat transfer coefficient, around one sixth of the value for water cooling.

It is assumed that the hot spot of the d.c. coils is located at the center of the contact surface between the coils and the teeth insulation. The temperature in the cooled surface of the coils is calculated using (6.12), where Acs_{dc} is the area equivalent to the surface of all coils, and Pcu_{dc} corresponds to all the copper losses in the rotor. The temperature in the hot spot is calculated using (6.13), where Lih_{dc} corresponds to the thickness of a d.c. coil and Aih_{dc} to half Acs_{dc}. The temperatures in the different parts of the machine are summarized in Table 6.9.

$$Tsf_{dc} = \frac{Pcu_{dc}}{Acs_{dc} \cdot hconv_{dc}} + T_{\infty 2} \tag{6.12}$$

$$Thp_{dc} = \frac{Pcu_{dc} \cdot Lih_{dc}}{Aih_{dc} \cdot \kappa_{coil}} + Tsf_{dc} \tag{6.13}$$

The static and dynamic torque response at the thermal limit are shown in Figure 6.14. The maximum torque is 8.0 Nm and the ripple is 25% of the peak torque. The Ampere turns in one a.c. coil are 960 A, and in one d.c. coil 473 A. The total copper losses are 282 W (181 W a.c. and 101 W d.c.). The copper losses account for 72% of all losses in the active parts of the machine at load. The efficiency of the machine at 1500 r.p.m. is 76%.

Table 6.8: Parameters for heat transfer calculation in Design 3

Coefficient	**Stator**	**Rotor**
Tm [^{o}C]	47	84
Δ T$_w$ [^{o}C]	6	12
U [m/s]	0.039	10.0
Re	20897	24235
Pr	3.8	0.7
Nu	149	92
A	0.664	0.664
m	0.50	0.50
n	0.33	0.33
hconv [W/mK]	303	54

Table 6.9: Temperature distribution in Design 3 [^{o}C]

Part	a.c. path	d.c. path
Tsf	63	136
Tcr	72	
Twl	96	
Tis	130	
Thp	140	140

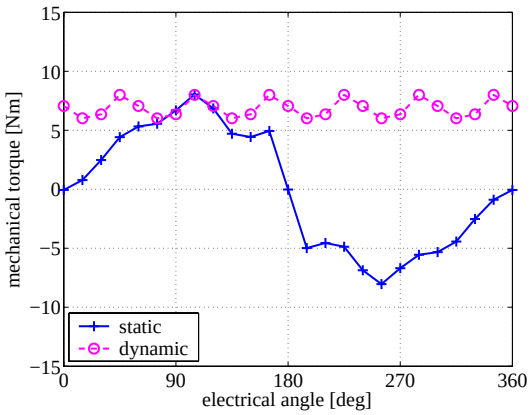

Figure 6.14: Torque response in Design 3.

6.5 Surface mounted PMSM

The fourth topology studied is shown in Figure 6.15, and it will be referred to as 'Design 4'. The rotor in Design 3 has been replaced with a surface mounted permanent magnet rotor, while the stator is practically unchanged. Only the slot opening was reduced to 8% of the tooth pitch to reduce the torque ripple. Iron-powder is used everywhere although in practice the rotor yoke could be laminated. However, that will have little effect in the results, as pointed out above for Design 2 and 3.

Today most permanent magnet machines use neodymium-iron-boron (NdFeB) magnets due to their high energy density, high remanence and good coercitivity at relatively high temperatures (Sadarangani, 2000). However, they are still more sensitive to very high or low temperatures compared to samarium-cobalt magnets (SmCo), and they are also more sensitive to humidity, which leads to corrosion problems. However, NdFeB magnets are approximately 20%-30% cheaper than SmCo magnets, and the latter are mainly used in special applications such as military equipment and robots. The permanent magnet material selected for Design 4 is of the NdFeB type (Vacodym677), and its demagnetization characteristics are shown in Figure 6.16.

Techniques to reduce the torque ripple in permanent magnet machines are well reported in the literature, and a review is presented by Jahns and Soong

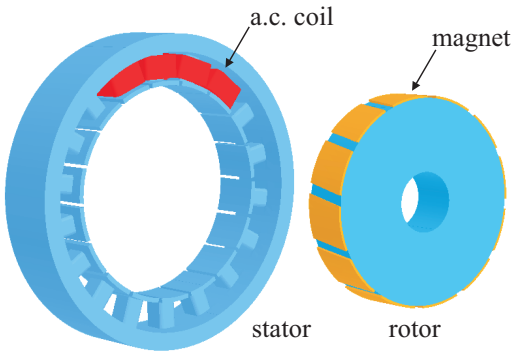

Figure 6.15: Design 4.

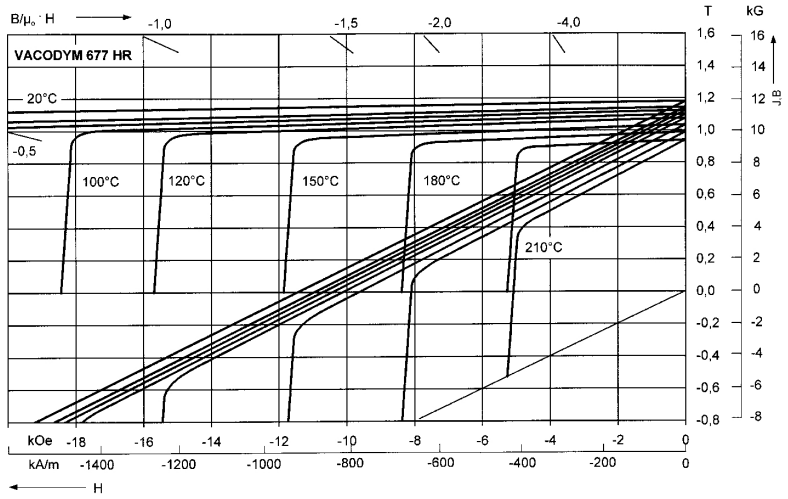

Figure 6.16: Demagnetization curves for the permanent magnet.

(1996). From the design point of view, only skewing of the magnets and minimizing the slot opening were explored. The magnets were skewed by half a slot pitch. It was found in FEM that an optimal response was obtained choosing a magnet arc of $(k + 0.22) \cdot \tau_s$, where k is the optimum integer number of teeth under a pole ('1' in our case), and τ_s is the slot pitch. This value is slightly higher than the one proposed in the literature, where the pole arc is usually selected as $(k+0.14) \cdot \tau_s$ or $(k+0.17) \cdot \tau_s$ (Li and Slemon, 1988), (Ishikawa and Slemon, 1993). However, the optimal PM arc width depends also on other parameters such as the magnetisation type, the airgap thickness, and the slot opening. The airgap thickness was selected as 1 mm above the magnet to account for manufacturing tolerances of the magnets, glue thickness and the bandaging used for protection and centrifugal forces. As pointed out above, the slot opening was significantly reduced compared to the other designs, which has the drawback of increased leakage between the teeth tips. This results in a lower average torque at the cost of reduced torque ripple. The height of the magnet was adjusted in order to obtain the same fundamental airgap flux density as in Design 1 at no load (0.55 T), which corresponded to a height of 1.5 mm. It should be noted that this value is higher than that for Design 2 (0.37 T) and Design 3 (0.39 T).

Protection against demagnetization

Permanent magnets can be partially or totally demagnetized if a strong magnetic field is applied in the opposite direction of magnetization. In electrical machines this phenomena is produced by the armature reaction, i.e. the field produced by the currents in the armature coils. The point when demagnetization starts varies with temperature, and it is given by the 'knee' in the demagnetization curve as shown in Figure 6.16. The thickness of the permanent magnet has to be sufficient to withstand these fields without suffering from demagnetization. This minimum thickness can be easily calculated from a simplified MEC model for the flux flow through a magnet, as shown in Figure 6.17 (Andersson, 2000). The MEC models a flux-tube (Ostović, 1989) closing the path in the machine through two adjacent magnets, although only one is represented in the figure. The flux-tube has an infinitely small cross-sectional area, A, and both the linking flux ϕ and the flux density B_m are constant along the tube. The magnet is modelled as a m.m.f. in series with a reluctance. The m.m.f. is a function of the magnet height h_m and the coercivity H_c. The m.m.f. drop in the airgap is given by R_g, and the m.m.f. from the armature reaction is F_i. In our case, at the

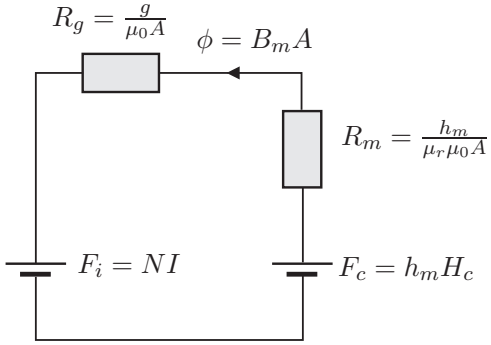

Figure 6.17: MEC model for magnet flux.

position of maximum torque, the contribution from each phase is $F_a = I \cdot N$, $F_b = -I/2 \cdot N$ and $F_c = -I/2 \cdot N$. The total contribution along the path closed by both magnets is therefore $F_t = 2N \cdot I$, and considering only one magnet gives $F_i = N \cdot I$. Solving the magnetic circuit yields (6.14).

$$h_{m-min} = \frac{NI + B_m \frac{g}{\mu_0}}{H_c - \frac{B_m}{\mu_r \mu_0}} \tag{6.14}$$

Assuming that the magnet working temperature is 150^{o}C at most, the demagnetization point corresponds to a negative flux density (-0.2 T), and it was selected that $B_m = 0$ to give certain margin before reaching this point. The minimum magnet height calculated was 1.23 mm. In practice, and given the lower permeability of the iron powder, the m.m.f. drop in the iron also should be included, $R_{fe} = l_{fe}/(2 \cdot \mu_{fe} \mu_0 A)$, where l_{fe} is the total length along the iron of the flux tube defined by the two magnets, and μ_{fe} is the permeability in the iron, selected at double the airgap flux density (1.1 T). The contribution from this reluctance term is added to the one from the airgap and both are multiplied by B_m, which in this case is zero and therefore there is no difference in the minimum calculated magnet height. It can be therefore concluded that the magnet will be protected against demagnetization from the armature reaction. In general, permanent magnet machines are designed for an airgap flux density around 0.8 T, and the thickness of the magnet is considerably increased. The

only reason for keeping the fundamental flux density at 0.55 T in this study is for the sake of comparison mainly with Design 1.

Iron losses

The ratio between the alternating and rotating losses for the fundamental in the stator is shown in Figure 6.18(a), and for the third harmonic in the rotor in Figure 6.18(c). The results for the stator are very similar to those in Design 3, although the flux density is now increased. The alternating losses are concentrated in the body of the teeth, where the flux density is around 1.6 T. The rotational losses are mainly located in the teeth tips (1.2 T) and in the back core, where the decrease in the flux density (0.4 T) is compensated by a greater iron volume. The losses in the permanent magnets were not calculated. However, eddy-current losses are expected in sintered magnets since the insulation between particles is minimized, and they may be problematic in high-speed machines (Polinder and Hoeijmakers, 1997).

The losses per harmonic component in the stator and the rotor core at load and no load are shown in Figure 6.19. The pattern is similar to Design 3, with the highest losses due to the stator fundamental component. The rotor losses are very small, and their main contribution is due to the third harmonic at load. The total losses are increased by 45% when the machine is loaded. A summary of the contribution to the total losses from the alternating and rotating components in different parts of the machine is shown in Table 6.10. At no load most of the alternating losses are due to the teeth body, and the rotational losses are mainly distributed between the back-core and the teeth tips. At load, 69% of the alternating losses are still located in the teeth body. Also, the rotational losses increase considerably in the back-core of the rotor and the stator, while the losses in the tips are slightly decreased. Overall, the rotational losses represent 69% and 62% of all the losses in the machine at no load and load respectively.

Thermal considerations

The thermal model for the stator is identical to that in Design 3. The only difference in the stator structure in Design 4 is the size of the slot opening, which has no effect in the cooling. Therefore, the stator current and the temperature distribution are the same as in Design 3. As pointed out above, the losses in the magnets were not considered, and the losses in the rotor core are very little.

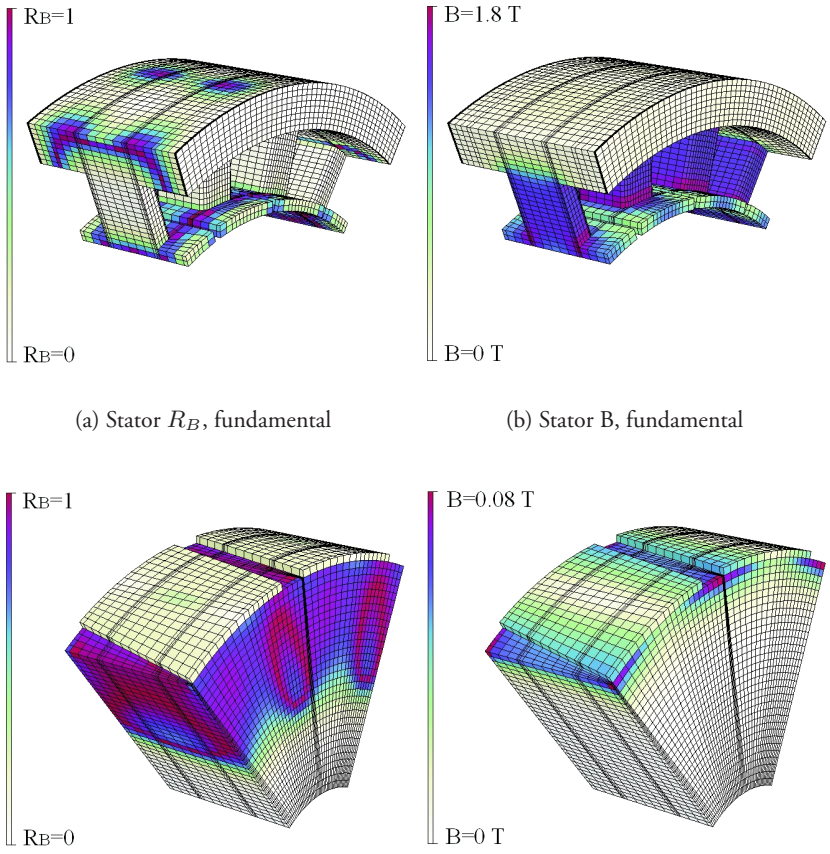

(a) Stator R_B, fundamental

(b) Stator B, fundamental

(c) Rotor R_B, 3rd harmonic

(d) Rotor B, 3rd harmonic

Figure 6.18: Design 4 R_B and flux density distribution for the fundamental in the stator and the third harmonic in the rotor, no load.

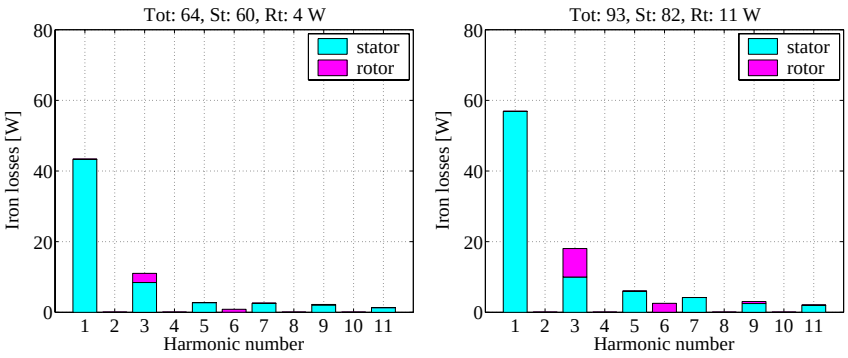

(a) No load (b) Load

Figure 6.19: Distribution of the iron losses in Design 4 as a function of the harmonic number.

Table 6.10: Summary of the predicted iron losses in Design 4. [W]

	No Load		**Load**	
Part	Alternation	Rotation	Alternation	Rotation
St. back-core	4.4	14.4	7.2	22.8
St. teeth body	14.5	6.4	24.4	5.6
St. teeth tip	1.3	19.6	3.8	17.7
Rt. back-core	0.0	3.6	0.0	11.2
Total	20.2	44.0	35.4	57.3

Therefore it was assumed that the rotor losses could either be neglected or assumed to be dissipated through the airflow produced by a fan, as in Design 3. The magnet selected shows a robust behaviour against temperature changes up to 150^{o}C, with the demagnetization point located in the negative flux density region. The demagnetization curve was anyway selected at 150^{o}C to account for the maximum temperature that the magnet is expected to reach.

The static and dynamic torque response at the thermal limit are shown in Figure 6.20. It can be observed that the static shape is smoother than in the previous designs, and that the torque ripple is importantly reduced to about 9% of the peak torque, which is 10.5 Nm. As in Design 3, the Ampere turns in one a.c. coil are 960 A, and the copper losses are 181 W. The copper losses account now for 66% of all the losses in the active parts of the machine at load (excluding the magnets). The efficiency of the machine at 1500 r.p.m. is 86%.

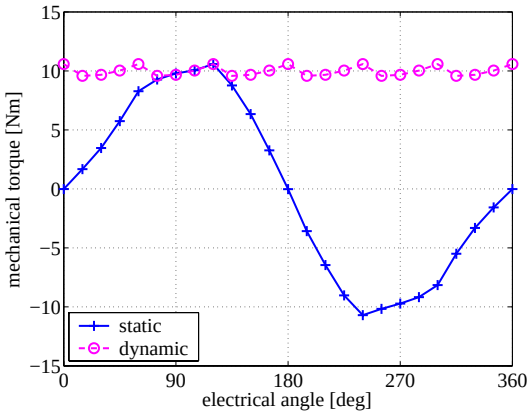

Figure 6.20: Torque response in Design 4.

6.6 Discussion

A summary of the properties of all the topologies studied in this chapter is shown in Table 6.11. The average torque will be used for comparison, and it is calculated from the values of the peak torque and the torque ripple. This ripple is highest in Design 1 and lowest in Design 4. The mass of the active parts of the machine is also listed, together with that of the bakelite mould used

to fix the claw-poles. It can be observed that Design 1 outputs most torque, although its weight and volume are around 80% and 65% higher than in the other designs respectively. This is mainly due to the end-plates used for the magnetization. Design 1 presents also the highest iron and copper losses. The rotor inertia in Design 1 and 2 was calculated including the bakelite mould, with a density of 1.5 kg/m^3. This lower density helps Design 1 to keep the lowest inertia. The inertia in Design 3 was calculated including the rotor coils, and in Design 4 including the magnets. However, it should be noted that in a commercial machine, the rotor in Design 4 would be probably built with holes in the core to decrease its weight and inertia, but this has not been taken into consideration in the comparison. The efficiency is calculated from the averaged torque values, and it is highest in the PM machine. The per unit material cost was calculated as a function of the mass of the active parts of the machine. The price of the iron powder varies between 1 and 1.5 euro/kg. It was assumed that the cost of the iron powder pressed into shape was 2 euro/kg (1 p.u.). The price of copper was approximated as 5 p.u. (10 euro/kg), and the price of the NdFeB magnet was 50 p.u. (100 euro/kg). With these figures it can be observed that Design 4 is the most expensive machine, mainly due to the permanent magnets, closely followed by Design 1. The ratio of average torque per weight is similar in Design 1, 2 and 3, while it is around 40% higher in Design 4. Considering the torque per volume, Design 4 leads by about 50%. The cost per torque output is however also highest in Design 4, closely followed by Design 3, and around 32% higher than in Design 1 and 2.

6.7 Conclusions

Among the three electrically magnetized machines, the conventional design (Design 3) presents the highest average torque per weight and per volume. The difference with Design 1 is however less than 8%. Design 3 is also the most expensive of the three topologies. Design 1 and 2 have a similar cost per torque, which is about 18% lower than in Design 3. The PM machine (Design 4) presents the best performance of all the machines regarding efficiency, and the ratio of torque per weight and torque per volume, leading by around 12%, 40% and 50% respectively. It is however also the most expensive machine considering the cost per output torque. Design 2 is the less expensive of all the machines per output torque, closely followed by Design 1. The cost of Design 4 is about 32% higher. It should be noted that the cost of the slip-rings has not been

Table 6.11: Summary of the properties of all designs

Component	**Design 1**	**Design 2**	**Design 3**	**Design 4**
Temp. rise [^{o}C]	100	100	100	100
Outer diameter [mm]	200	200	200	200
Length [mm]	76.0	50.0	42.7	42.7
Peak torque [Nm]	14.4	7.8	8.0	10.5
Torque ripple [%]	33	28	25	9
Average torque [Nm]	12.0	6.7	7.0	10.0
Mass iron [kg]	9.7	5.5	4.7	5.6
Mass copper [kg]	2.8	1.5	2.4	1.7
Mass magnet [kg]	0	0	0	0.236
Mass mould [kg]	0.5	0.3	0	0
Total mass [kg]	13.0	7.3	7.1	7.5
Iron losses [W]	173	112	107	93
Copper losses [W]	545	449	282	181
Total volume [lit]	2.38	1.57	1.34	1.34
Inertia [kg m^2]	5.1e-3	9.8e-3	6.0e-3	6.9e-3
Efficiency [%]	72	65	74	85
Material cost [p.u.]	23.7	13.0	16.7	25.9
Torque/weight	0.92	0.92	0.99	1.33
Torque/volume	5.04	4.27	5.22	7.46
Cost/torque	1.98	1.94	2.39	2.59

included in Design 3, neither the cost of the machine assembly, which may be more problematic for the PM topology.

It is therefore shown that the PM machine presents superior electromagnetic performance compared to the electrically magnetized machines at normal operation. In fact, the main advantages of using electrical magnetization would be at field weakening operation, not included in the comparison.

Chapter 7

Prototype and measurements

7.1 Introduction

In this chapter, the prototype construction process will be described, as well as the results from the measurements. The parts of the prototype were manufactured at ProEngCo AB, in Sweden. Some adaptations had to be introduced to the original model to facilitate the manufacturing and the assembling process. They will inevitably affect to some extent the performance of the machine.

A new cooling system was designed, which implied that the model for the heat removal from the surface had to be adapted accordingly, and it is described in this chapter. Differences in the material used for the main insulation and the diameter of the conductors also affected the current loading at thermal limit, so the iron losses had to be re-calculated. The control system was implemented in dSPACE, and vector control was used to control the currents feeding the prototype machine. Finally, an idea consisting of feeding the field winding from the rectified three phase armature currents at the neutral point has also been tested.

7.2 Construction of the prototype

The machine structure was divided into a series of components that were produced separately and then assembled together after inserting the coils. These components were machined from blocks of pressed iron powder, which was preferred for prototyping rather than developing the specific pressing tools for each component. The iron powder Somaloy500 with the lubricating binder

0.6% LB1 was selected since it could be more easily machined compared to the same powder using the lubricant 0.5% Kenolube, although at the expense of a lower maximum permeability (300 vs. 500) and higher hysteresis losses. On the other hand, LB1 gives higher transverse rupture strength (100 MPa vs. 50 MPa TRS) and higher resistivity. The powder was warm compacted at 800 MPa and 120^{o}C, which increases the strength after pressing (green strength) and improves the magnetic properties, mainly due to the higher density compared to conventional compaction. The material was then cured at 250^{o}C for 60 minutes to melt the lubricant and further increase the strength. It should be pointed out that if Kenolube was used instead, then the heat treatment would be at a higher temperature (500^{o}C), which removes the stresses and decreases the hysteresis losses. The temperature for the heat treatment should be kept within the specified limits, since otherwise at higher temperatures the coating between the particles is destroyed and the eddy current losses become too high.

Stator core

The stator core was divided through the middle into two rings with slots on their common edge to allocate the teeth and to insert the cables connecting the coils, see Figure 7.1. Each ring consisted of six modules glued together using a high temperature epoxy glue. The layer of glue between the modules was 0.02 mm thick. The teeth were machined into one piece each. The top of the part of the teeth inserted into the core had a salient edge to withstand the attraction forces in the airgap and hold the teeth in position. This edge did not extend over the actual width of the teeth in order to allow the insertion of the pre-pressed coils from the top. However, the idea of pressing the coils was later abandoned and the coils were directly wound around the teeth. The wound teeth were inserted into one of the rings, and thereafter the second ring was placed on top. The length of the gap between the core back and tooth was controlled to be within 0.05 ± 0.02 mm, and would therefore have negligible influence upon the magnetic performance. It should be noted that the teeth and the core were not glued together. This was convenient since they could be easily dismantled during assembly.

End-plates

The end-plates were built from six modules and they were attached to an aluminium plate used for cooling, see Figure 7.2. The end-plates expanded until

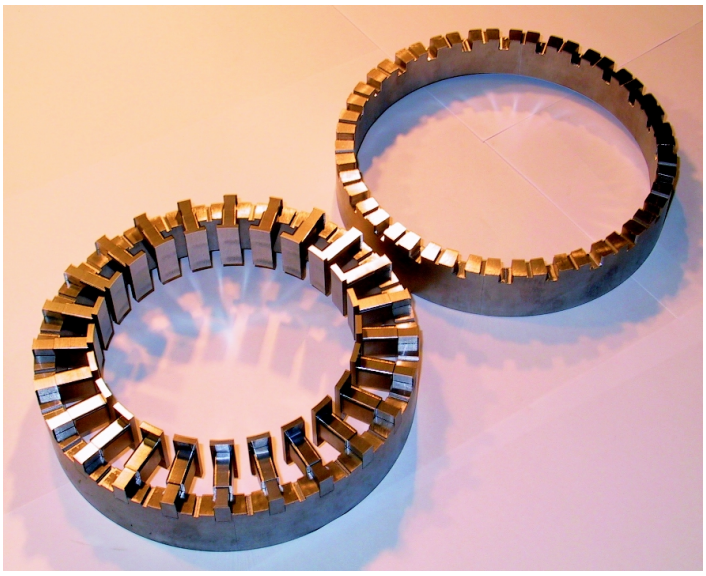

Figure 7.1: Stator core sides and teeth mounted.

the outer diameter of the machine, and they were screwed into the stator housing. At the level of the stator core, the surface was machined with a 45^o slope, matching the corresponding core surface when mounted. The d.c. coils were accessed through two axial slots machined in the stator core.

Rotor

All the claw-poles with the same polarity formed a structure as shown in Figure 7.3 (built from four modules each). The two structures were glued onto a bakelite mould constructed to match their geometry. The finished rotor is shown in Figure 7.4. It should be noted that the bakelite mould extended beyond the inner radius of the claw-pole structures, providing magnetic insulation between the claw-poles and the shaft in order to minimize the homopolar flux. Two nuts screwed on the sides of the shaft were used to adjust and fix the axial position of the rotor when mounted.

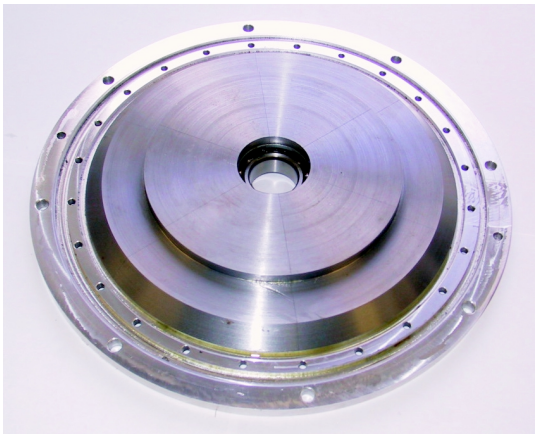

Figure 7.2: End-plate.

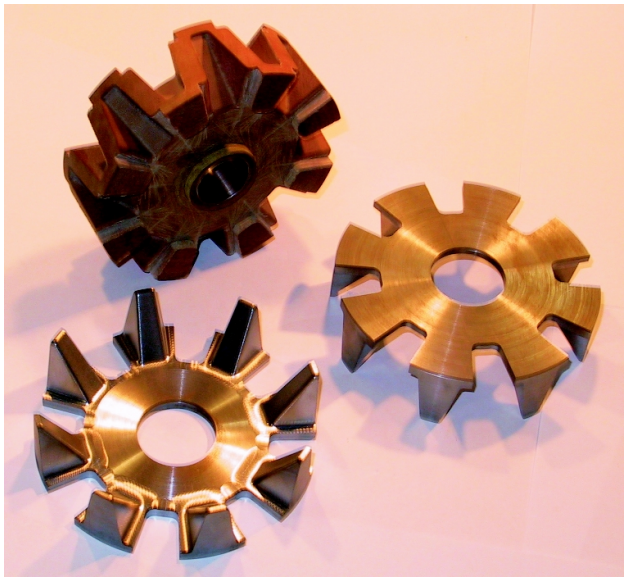

Figure 7.3: Rotor parts.

Figure 7.4: Finished rotor.

Windings

The number of turns in the a.c. winding were adjusted to keep the maximum d.c. link voltage below 300 V, as required for the laboratory equipment. The linking flux from one phase at no load and load calculated in FEM is shown in Figure 7.5. For 54 turns per coil, the corresponding phase and phase to phase voltages at 1500 r.p.m. are shown in Figure 7.6.

Each one of the 54 turns around a tooth consisted of three parallel wires with a bare diameter of 0.63 mm each, and a coating of 0.015 mm. For the insulation in the slots DMD was used, which consists of three polyester layers (fibre - film - fibre). The thickness of the insulation layer in the body of the teeth was 0.16 mm, and in the back core 0.40 mm. The practical slot fill factor was 48%. It should be noted that the slots could not be completely filled since the conductors had to be accessed radially from outside the stator back-core due to the space limitation in the axial direction. The holes were machined at the middle of the core between two teeth for the sake of symmetry, but this complicated a great deal the insertion of the cables. Therefore, only one cable was inserted through each hole, to connect either the beginning or

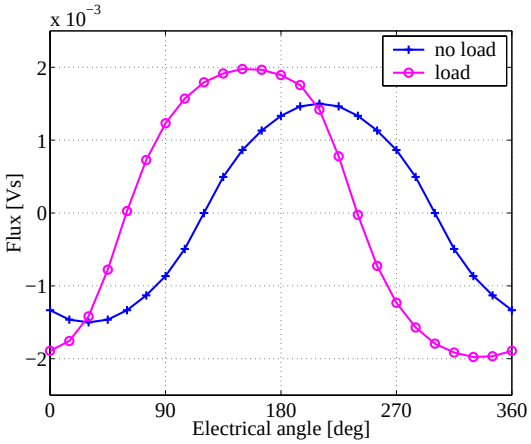

Figure 7.5: Linking flux in one phase from FEM.

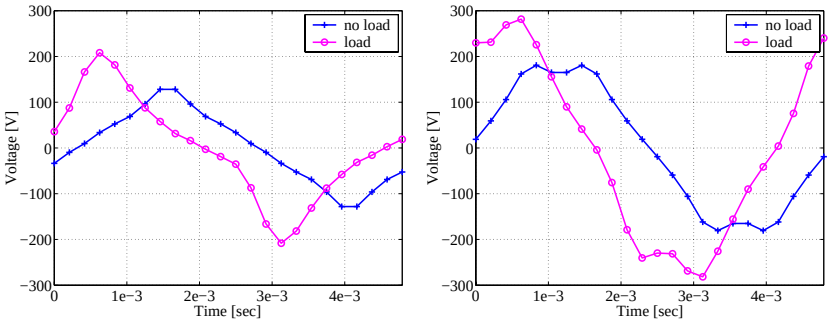

(a) Phase voltage (b) Phase to phase voltage

Figure 7.6: Induced voltage derived from FEM.

the end of the tooth coil, while the connection to the next coil in the phase was done inside the machine. In this way, half of the connections were made outside the machine and the other half inside. It was preferred to avoid long loose connections between the coils inside the machine since there is virtually no air-flow to cool these cables.

The number of turns in the d.c. coils was adjusted so as to make possible to connect the machine with series magnetization (Alaküla, 2004). Each end-plate was wound with 74 turns of a single wire with 1.20 mm bare diameter and a coating of 0.04 mm. The main insulation was 0.24 mm thick. The slot fill factor for the d.c. winding was 58%. The a.c. and d.c. coils were impregnated by soaking with Ultimeg 2000 enamel and cured for 6 hours at 130^{o}C. A picture of a finished d.c. coil attached to the end-plate is shown in Figure 7.7.

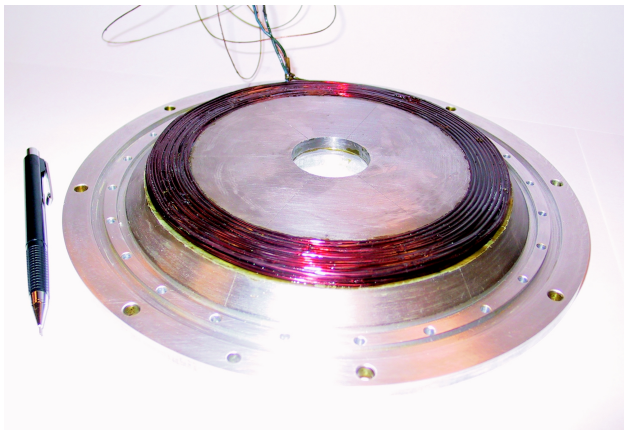

Figure 7.7: Finished end-plate.

A thermocouple sensor was inserted in six a.c. coils (two per phase) and the two d.c. coils to measure the temperature. The a.c. coils equipped with sensors were evenly located every four teeth around the stator. The sensor was a cable consisting of two conductors welded at the measuring point, which was located in the middle of the coils. The sensor cable was of the type K manufactured by Pentronic AB in Sweden.

Cooling system

A pump was used to provide a water coolant flow of approximately 4 liter/minute. The coolant in turn was refrigerated by water in a heat exchanger (Alfa Laval DOC14-20H) before being recirculated into the machine. The water was taken directly from the tap and was disposed after leaving the heat exchanger. An aluminium cover was screwed on the side of the aluminium housing mounted on an end-plate. The coolant circulated in the cavity between the cover and the housing and was then conducted through axial ducts machined in the housing of the stator core, one above each tooth. The flow coming out from the other side of the ducts circulated around the cavity of the second end-plate before leaving the machine through a valve on the top. A CAD plot of the machine and the cooling system is included in Figure 7.8. The finished stator with the housing is shown in Figure 7.9, where the axial ducts for the cooling are visible. It can be seen also the cables introduced radially through the core for the connection of the coils.

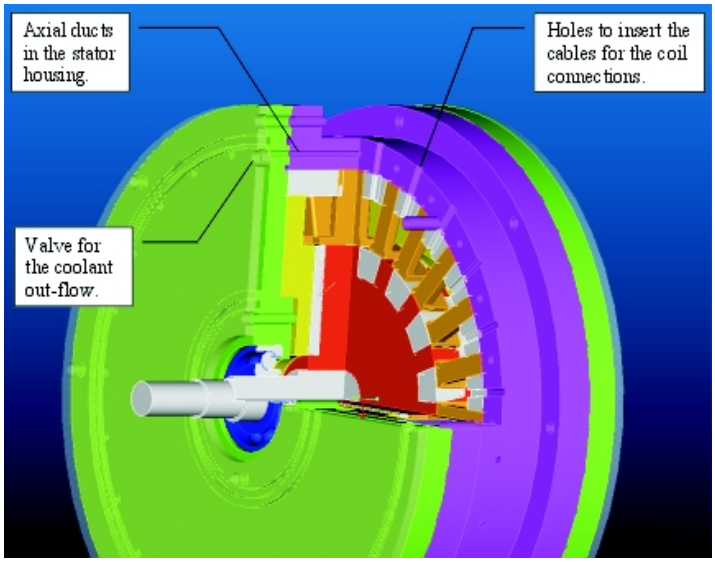

Figure 7.8: Plot of the cooling system in the machine.

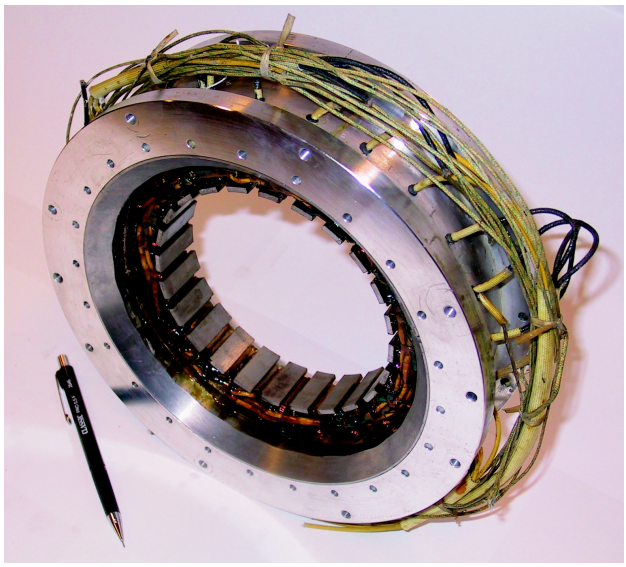

Figure 7.9: Finished stator with housing.

7.3 Adaptation of the thermal model

The thermal model for the heat removal from the surfaces of the stator core and end-plates had to be adapted to the new cooling system used. The model for the heat transfer from the center of the coils to these surfaces is however identical to that described in Chapter 4.

Heat transfer coefficient

The heat transfer coefficient from the surface of the end-plates was calculated using the formulation for forced convection over a plate. Figure 7.10 shows the end-plate and half the number of outlets from the axial ducts, represented by small holes located around the periphery of the plate. Symmetry was exploited, and only half the surface was considered. The idea was to define an equivalent duct with an area corresponding to the cooling area divided by the number of ducts. The equivalent length was approximated as the mean average length from the center of the holes to the machine outlet, located at the level of the upper hole. The dashed lines in the figure indicate the path for the water flow

from some of the holes to the outlet. It can be observed that, for example, for hole number 13 the path is circular when it arrives at the inner radius of the plate, so the length was increased accordingly. The coolant flow through the equivalent duct corresponded simply to the flow from one axial duct. Its cross-sectional area was calculated dividing the equivalent cooling area by the equivalent length of the duct and multiplying by the thickness of the cavity where the coolant flows between the end-plate and the cover.

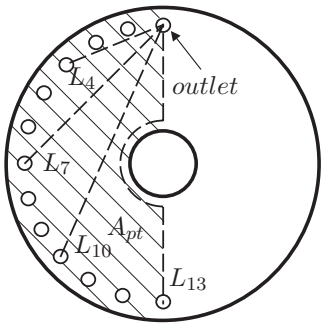

Figure 7.10: Cooling of the end-plate.

The heat transfer coefficient was calculated similarly in both end-plates, the only difference being the mean temperature of the coolant, which affects its properties. The temperature increase was calculated when the coolant leaves the first end-plate, the axial ducts and the second end-plate. The increase in temperature at each stage was calculated using the formulation in (4.29). The inlet temperature was known (11^oC), and applying the formulation to the first plate resulted in the temperature of the coolant entering the axial ducts. In the same way, applying the formulation to these ducts yielded the coolant temperature entering the second end-plate, and finally the outlet temperature. The properties of the coolant using (4.29) were calculated at the inflow temperature at each stage. The properties of the coolant used to calculate the heat transfer coefficient were calculated at the average temperature between the inflow and the outflow at each stage.

The heat transfer coefficient from the axial ducts expanding through the stator back-core was calculated using the formulation for forced convection inside a tube. The geometric characteristic was the diameter of the duct D (4 mm). It

was found that the flow in the ducts was laminar, and the formulation in (7.1) (Sieder and Tate, 1936) was used to calculate the Nusselt number. In this equation L is the length of the tube and μ_s is the viscosity of the fluid evaluated at the temperature of the interior surface of the tube. Obviously this temperature was a priori unknown, so an iteration process had to be implemented.

$$Nu = 1.86 \cdot (Re_D \cdot Pr)^{1/3} \cdot \left(\frac{D}{L}\right)^{1/3} \cdot \left(\frac{\mu}{\mu_s}\right)^{0.14} \tag{7.1}$$

The experiments to check the thermal model were carried out at 500 r.p.m. The Ampere turns in one a.c. coil were 827 A, and in one d.c. coil 984 A. A summary of the values obtained for the heat transfer coefficient calculation is shown in Table 7.1. The predicted iron losses are shown in Figure 7.11.

Heat transfer model

The heat transfer model up to the surface of the stator core and the end-plates was identical to that presented in Chapter 4. Only the diameter of the copper conductors and their insulation was updated, as well as the thickness and the thermal properties of the main insulation (DMD). According to the manufacturer, the thermal conductivity of DMD was 0.041 W/mK, which was about one third than that for Kapton (0.12 W/mK). This negative effect in the thermal performance of the machine was partially compensated by the reduction in the insulation thickness, from 0.5 mm assumed in the models to 0.15 mm in the teeth and 0.24 mm in the end-plates of the prototype.

The temperature at the inner surface of the axial ducts was calculated using (7.2). All the losses from the iron-powder and the copper are cooled through this path. No losses were assumed in the aluminium casing. The area A_{duct} corresponded to the interior area off all the ducts in the casing together, and $T_{\infty d}$ is the average temperature of the coolant in the ducts. Similarly, the temperature in the surface of the aluminium casing attached to the end-plate was calculated using (7.3). The area A_{cas} corresponded to the surface area of the casing, and $T_{\infty c}$ was the average temperature of the coolant in the corresponding plate. The value of $hconv_{dc}$ was selected depending on the plate analyzed.

$$Tal_{ac} = \frac{Pcu_{ac} + p \cdot (Pfe1_{ac} + Pfe2_{ac}) + Pfe_{rC}}{A_{duct} \cdot hconv_{ac}} + T_{\infty d} \tag{7.2}$$

Table 7.1: Parameters for the heat transfer calculation, 500 r.p.m.

Coefficient	End-plate 1	Back-core	End-plate 2
Tm [^{o}C]	11.3	12.3	13.3
Δ T$_w$ [^{o}C]	0.54	1.48	0.54
U [m/s]	0.15	0.22	0.15
Re	25170	726	26457
Pr	7.89	8.63	7.46
Nu	208	13	209
hconv [W/mK]	667	1947	674

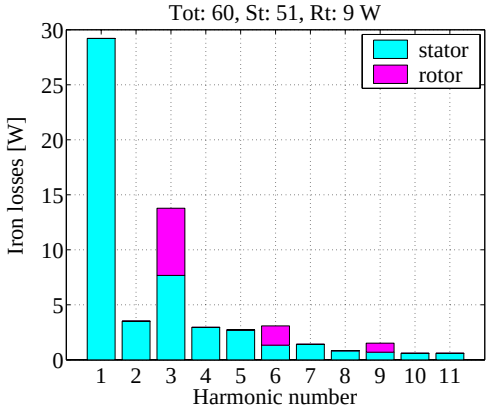

Figure 7.11: Predicted iron losses at load, 500 r.p.m.

$$Tal_{dc} = \frac{Pcu_{dc}/2 + Pfe_{dc} + Pfe_{rT}}{A_{cas} \cdot hconv_{dc}} + T_{\infty c} \quad (7.3)$$

The temperature in the surface of the back-core was calculated using (7.4), where Lld_{ac} is the average length between the top and the bottom distance of the duct to the core surface, following the edge of the duct. The value of Ald_{ac} corresponds to the average between the surface of the back-core (Asf_{ac}) and the inner surface of all the ducts together (A_{duct}). The value of κ_{al} is the thermal conductivity of the aluminium (165 W/mK). For the end-plates (7.5) was used, were Llc_{dc} is simply the thickness of the casing attached to the end-plates (5 mm), and Alc_{dc} is the area of the cooling surface in the aluminium casing. The results at the different parts of the machine are summarized in Table 7.2, for the current used in the experiments.

$$Tsf_{ac} = \frac{(Pcu_{ac} + p \cdot (Pfe1_{ac} + Pfe2_{ac}) + Pfe_{rC})Lld_{ac}}{Ald_{ac} \cdot \kappa_{al}} + Tal_{ac} \quad (7.4)$$

$$Tsf_{dc} = \frac{(Pcu_{dc}/2 + Pfe_{dc} + Pfe_{rT})Llc_{dc}}{Alc_{dc} \cdot \kappa_{al}} + Tal_{dc} \quad (7.5)$$

The end-plate that is cooled first in the thermal circuit will be referred to as the *first* end-plate, and that where the outlet is located will be referred to as the *second* end-plate. From the experiments, the measured temperature in the coil attached to the first end-plate was 149^{o}C, while the temperature in the coil in the second end-plate was 126^{o}C. The d.c. coils were wound radially onto the end-plates, and they were fixed axially using enamel. One of the two ends in each coil was inserted in a narrow slot machined in the end-plate to facilitate the winding process. During assembly, the insulation of this wire in the first end-plate was damaged, originating a short-circuit. Therefore, the coil had to be separated from the plate for reparation and then glued back. This process probably affected the fitting of the coil into the plate, and in turn the thermal path. Actually, this coil should present a lower temperature than the second d.c. coil, since it is cooled by the water coming directly from the pump at a lower temperature. Compared to the prediction, the measured temperature in the second coil is 19% higher. It should be noted that the copper is not pressed naturally into the side of the plate during the winding process. The fact that a thermal sensor was included in the coil did not allow to keep an ordered layer of wires on top of each other and the proper fit into the side of the plate. The

Table 7.2: Simulated temperature distribution [^{o}C]

Part	End-plate 1	Back-core	End-plate 2
Tal	19.6	19.8	21.5
Tsf	19.8	20.2	21.7
Tcr	28.6		
Twl	38.7	63.8	40.7
Tis	89.0	103.7	91.0
Thp	104.4	113.0	106.3

layer of enamel used for this purpose provides further insulation, which in turn decreases the efficiency of the heat transfer from the coils to the iron.

The temperature from the six armature coils equipped with sensors differed between each other by up to 10^{o}C at steady state when the machine was loaded. The average temperature was 138^{o}C, which is 22% higher than predicted. However, the models assume that 20% of the copper losses from the armature coils are transferred directly to the back-core through the top of the coil. When the machine was assembled, an empty space around 1 mm was left between the top of the coils and the back-core in order to avoid squeezing loose wires when the second core ring was mounted. This, added to the thicker insulation on the back-core (0.4 mm) effectively isolates the top of the coil. If 100% of the copper losses are transmitted through the teeth, then the predicted temperature is 133^{o}C instead of 113^{o}C, which is less than 4% difference compared to the average measured value. The accuracy in the iron loss calculation also affects the difference between the predicted and measured temperature distribution. However, for example the iron losses in the a.c. path need to be increased by 20% in order to increase 1.3^{o}C the temperature in the armature coils, so their influence in this case is minor.

7.4 Experimental set-up and instrumentation

The prototype was loaded with a d.c. machine through a torque transducer of the type Fast Technology TM-HR-Rd-20, see Figure 7.12. The nominal power of the d.c. machine was 2.2 kW at 1500 r.p.m. Also shown in the picture

are four of the eight multimeters used to measure the temperature from the sensors. The field winding in the machine was fed from a d.c. supply of the type SM 70-22 manufactured by Delta Elektronika. A Tektronix TDS 640 A oscilloscope was used for the voltage measurements. An inductance meter of the type ELBRO LC-6043 was used to measure the inductance in the tooth coils. Each machine was connected to a converter, where the switches were controlled from a digital card connected to a PC using dSPACE. Analog modules were used to estimate the speed and the flux in the machines and to measure their current. Figure 7.13 shows the hardware used to control the machines.

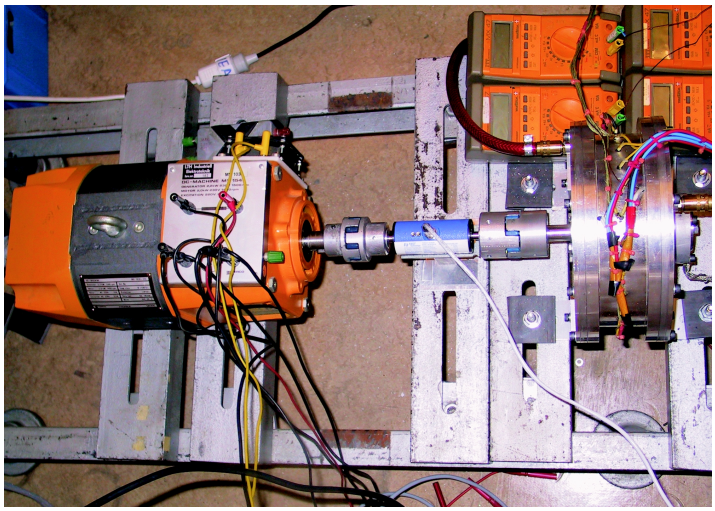

Figure 7.12: Test-bench used for the measurements.

7.5 Control

The control system was implemented in SIMULINK, see Figure 7.14, and then compiled into dSPACE for the real-time control. The measured values are introduced in the model through the 'Feedback' block. The output from the PWM modulators are connected to the converters through the dSPACE interface. It was possible to connect any of the signals from the SIMULINK model into the dSPACE user interface for visualization and real-time adjustments of, for example, the references and controller parameters. The d.c. machine was

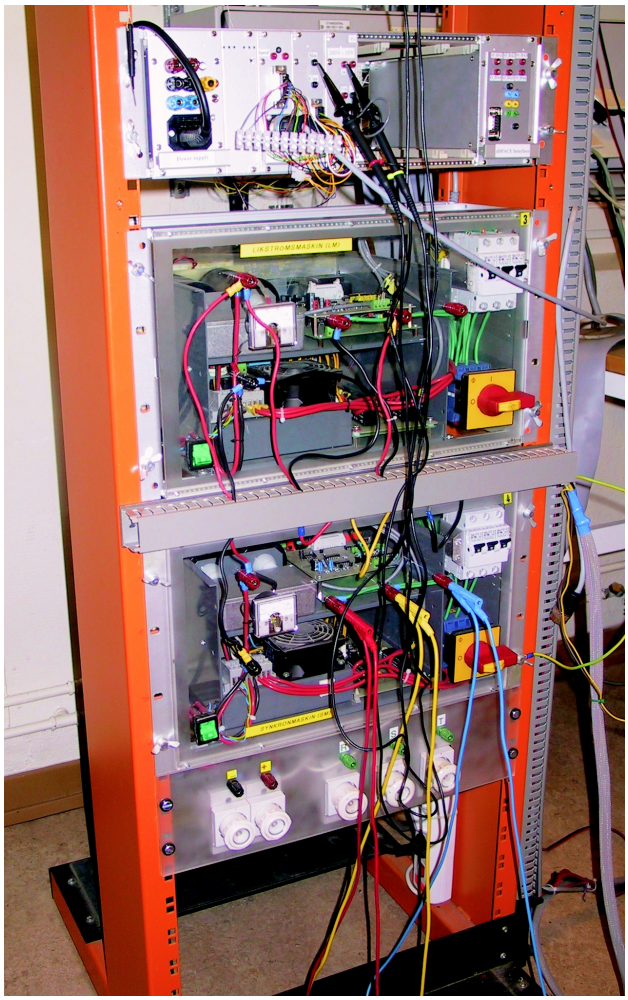

Figure 7.13: Set-up for the control equipment.

speed controlled, while the prototype was torque controlled. A PI controller was used to set the reference for the torque in the d.c. machine depending on the difference between the measured and reference speeds. The speed controller parameters were calculated using symmetric optimum (Alaküla, 2002). The proportional gain was $K_{pw} = J/(a \cdot T_{fw})$, where J is the inertia, T_{fw} is the speed filter time constant, and a is a constant controlling the relative damping of the poles. With $a = 3$, the speed control system will be on the limit of complex poles. The integral time constant was $T_{iw} = a^2 \cdot T_{fw}$, and the integral gain was $K_{iw} = 1/T_{iw}$. The torque reference output from the speed controller was transformed into current (i_a) dividing by the nominal flux in the machine, and another PI controller was used to control this current. The current controllers for the d.c. machine and the prototype were deduced using *predictive dead beat control* (Alaküla, 2002). For the d.c. machine, the controller equation is given by (7.6), where the proportional and integral components can be distinguished clearly, and the e.m.f. ($e_a(k)$) represents the so-called feed forward term. The values of L_a and R_a correspond to the inductance and resistance of the winding in the d.c. machine, and T_s is the sampling time (corresponding to 5 kHz). The reference voltage u_a^* is modulated with a triangular carrier wave, which sets the switching pattern in the converter connected to the machine.

$$\begin{aligned} u_a^* &= \left(\frac{L_a}{R_a} + \frac{R_a}{2}\right) \cdot \left[(i_a^*(k) - i_a(k)) + \frac{T_s}{L_a/R_a + T_s/2} \cdot \right. \\ &\quad \left. \cdot \sum_{n=0}^{n=k-1} (i_a^*(n) - i_a(n))\right] + e_a(k) \end{aligned} \tag{7.6}$$

Vector control was used to control the currents in the prototype. The theory of vector control is well reported in the literature (Vas, 1990) (Novotny and Lipo, 1996), and the basics are explained in the second part of this thesis. It is based on the concept that alternating currents in the machine can be expressed as a rotating vector. From a synchronous coordinate system attached to the stator or the rotor flux, the rotating vector is expressed as the combination of two d.c. current components along the x (i_{sx}) and y (i_{sy}) axis of the rotating frame, which can be controlled independently. In the prototype, the equations for the PI controllers governing the current are given in (7.7) and (7.8). It can be observed how the reference voltage for one axis is dependent on the current in the other axis through the feed forward term, where ω_r is the rotor speed, and Ψ_m is the linking flux in the machine. The location of the rotating frame is

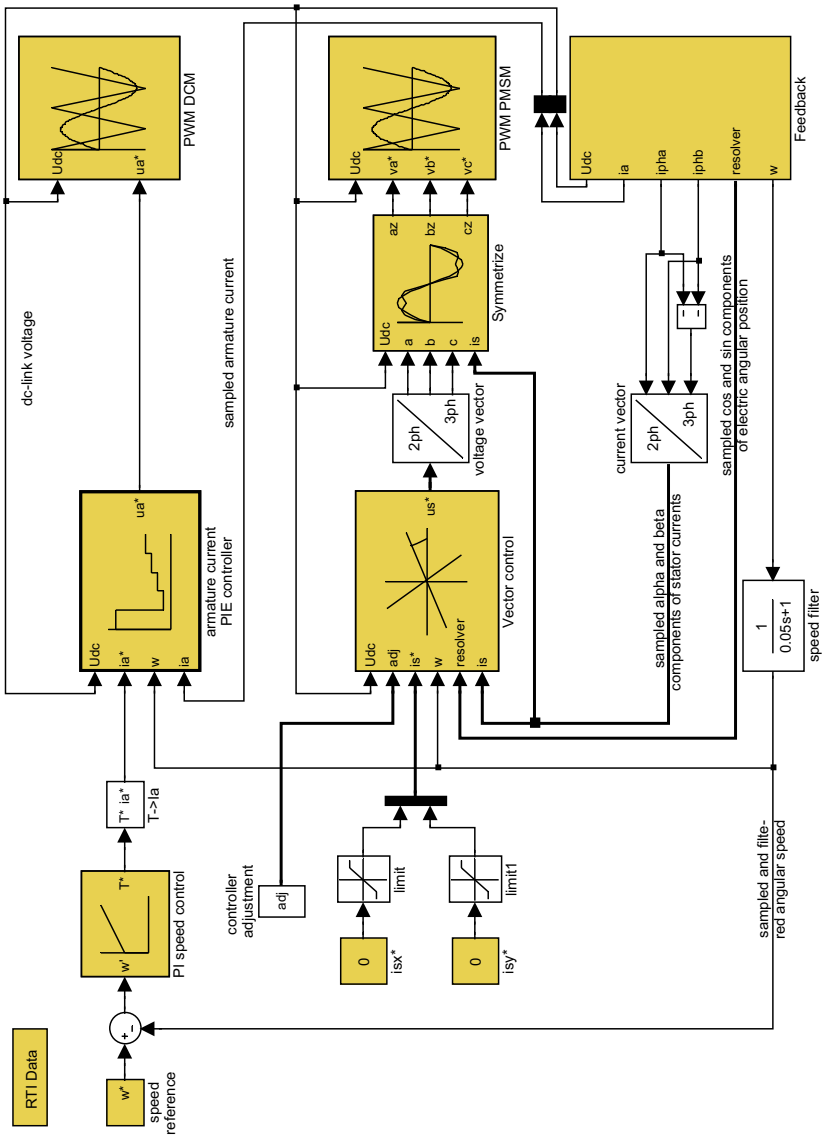

Figure 7.14: Structure of the control system.

measured using a resolver mounted in the machine. The actual values of i_{sx} and i_{sy} are obtained from the measured three phase currents. These currents are first transformed to the two phase stationary α/β system and then to the rotating x/y frame using the angle from the resolver. The conversion from three to two phases was done using the power invariant transformation (Alaküla, 2002). The output reference voltage from the controller is transformed back to three phases, which are symmetrized using third harmonic injection. This increases the modulation depth by 15%. Finally, the resultant voltages are modulated using a triangle carrier wave, which sets the switching pattern in the converter connected to the prototype.

$$u^*_{sx} = \left(\frac{L_{sx}}{T_s} + \frac{R_s}{2}\right) \cdot \left[(i^*_{sx}(k) - i_{sx}(k)) + \frac{T_s}{L_{sx}/R_s + T_s/2} \cdot \cdot \sum_{n=0}^{n=k-1} (i^*_{sx}(n) - i_{sx}(n))\right] - \omega_r \cdot L_{sy} \cdot i_{sy}(k) \quad (7.7)$$

$$u^*_{sy} = \left(\frac{L_{sy}}{T_s} + \frac{R_s}{2}\right) \cdot \left[(i^*_{sy}(k) - i_{sy}(k)) + \frac{T_s}{L_{sy}/R_s + T_s/2} \cdot \cdot \sum_{n=0}^{n=k-1} (i^*_{sy}(n) - i_{sy}(n))\right] + \omega_r \cdot (\Psi_m + L_{sx} \cdot i_{sx}(k)) \quad (7.8)$$

The values of the inductances L_{sx} and L_{sy} where derived from the linking flux at load and no load calculated in FEM (Figure 7.5). The general equation for the stator flux is given in (7.9), where i_f is the field current. At load, Ψ_s corresponds to the maximum value of the curve for the load flux. From (7.9), the particular case when there is no armature current can be expressed as in (7.10), from where L_{sx} is calculated. The value of Ψ_{nl} corresponds to the maximum value of the curve for the no load flux. The equation when the no load flux is zero is given in (7.11). The value of Ψ_{s0} corresponds to the load flux at the point when the no load flux is zero. Finally (7.12) expresses the x/y currents as a function of the phase current vector. Combining (7.9), (7.11) and (7.12), and knowing the value of L_{sx} from (7.10) yields the value of L_{sy}, i_{sx} and i_{sy}. The values obtained are $L_{sx} = 5.54 \cdot 10^{-3}$ H, $L_{sy} = 6.41 \cdot 10^{-3}$ H, i_{sx}=-6.2 A, and i_{sy}=17.70 A. The currents correspond to a total Ampere turns of 827 A in one a.c. coil (1082 A in one d.c. coil), as used for the FEM results in Figure 7.5. Finally, is should be noted that the value of the resistance of one

phase was $R_s = 0.8\,\Omega$.

$$
\begin{aligned}
{\Psi_s}^2 &= (L_{sx}(i_f + i_{sx}))^2 + (L_{sy} \cdot i_{sy})^2 && (7.9)\\
\Psi_{snl} &= L_{sx} \cdot i_f && (7.10)\\
{\Psi_{s0}}^2 &= (L_{sx} \cdot i_{sx})^2 + (L_{sy} \cdot i_{sy})^2 && (7.11)\\
{i_s}^2 &= {i_{sx}}^2 + {i_{sy}}^2 && (7.12)
\end{aligned}
$$

7.6 Measurements

Coil inductance

The inductance in the coil in every tooth was measured with the teeth standing alone and when they were mounted in one core ring (half core). The results are shown in Figure 7.15. The reference for the level of the half core values is zero. The difference in the standard deviation between the maximum and minimum inductance of the teeth alone was 8%. When they were mounted in half the core this difference was 14%. Around half the coils were unwound and the number of turns was controlled to be 54 in all of them. When they were re-wound, they had the same old inductance. Therefore, the differences should be due to the teeth rather than the winding. It is possible that the bulk material from where the teeth were machined (six teeth per bulk) was not completely homogeneous, which in turn would affect the magnetic properties of the teeth.

If the teeth were mounted in the order shown in Figure 7.15, the standard deviation of the total inductance of phase A, B and C would be 0.3%, -3.9% and 3.6% respectively. Simply by swapping teeth number 2 and 21, this deviation was reduced to 0.3%, 0.0% and -0.3%. In order to get a smoother change in the inductance of every phase and between the phases around the machine the tooth pair 7-10 was swapped in phase A, 14-17 in phase B, and 6-15 and 15-21 in phase C. The goal was to distribute the coils so that the average between two adjacent positions in one phase was as close as possible to the mean average of the eight positions in that phase. Also, that the addition of the inductance of the eight groups of three adjacent coils (corresponding to different phases) is as constant as possible. Only six of the eight teeth in every phase could be freely swapped, since the other two were provided with a thermal sensor to measure the temperature at a particular position around the machine, and they only could be swapped with each other. Figure 7.16 shows the distribution

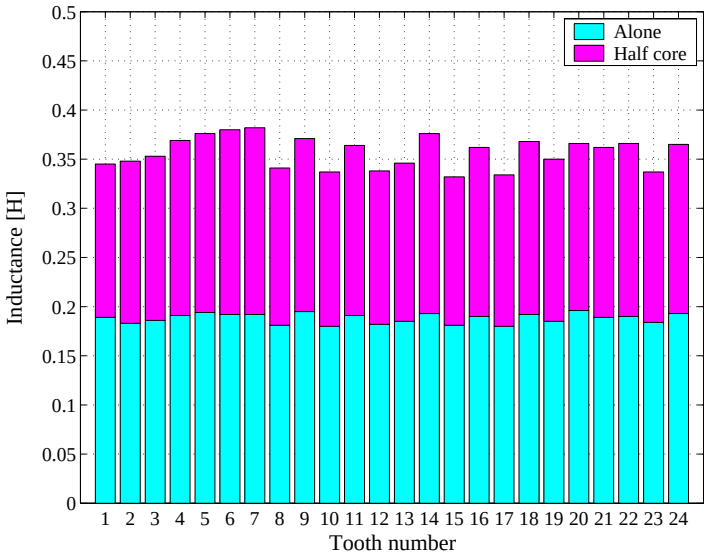

Figure 7.15: Inductance measurements in the teeth coils.

of the inductance in the eight consecutive teeth in each phase before and after the teeth swapping. The total inductance of each group of three adjacent teeth around the machine is shown in Figure 7.17.

Induced voltage

The induced voltage at no load was measured with the machine rotating at nominal speed (1500 r.p.m.) driven by the d.c. machine. The voltage was measured in an oscilloscope and saved for further post-processing. The three phases produced the same induced voltage, although it was observed that the peak voltage was 20% lower than predicted. However, the shape resembled reasonably the simulated results, as shown in Figure 7.18. In this figure the measured voltage has been amplified by 20% in order to match the amplitude from the simulated curve. The reasons for the lower induced voltage could be a lower permeability in the iron-powder material, and/or a distortion of the magnetic circuit. It was observed that the shaft was magnetic, which indicates the existence of homopolar flux. The rotor claw-pole structures were isolated

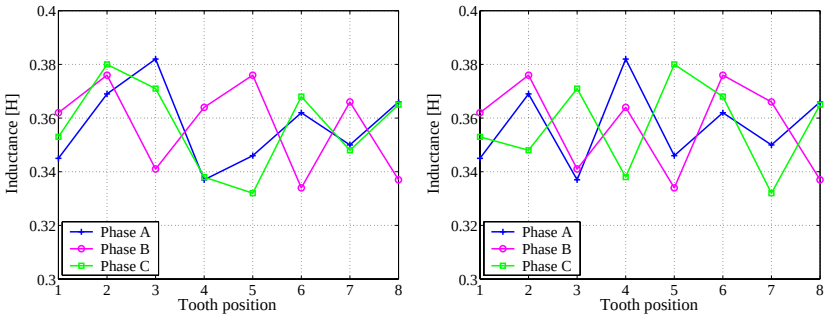

(a) Original inductance.

(b) Inductance after swapping.

Figure 7.16: Distribution of the inductance along the eight coils in each phase.

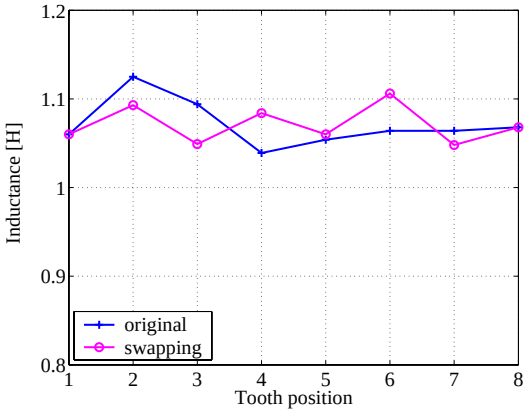

Figure 7.17: Sum of the inductances in the eight groups of three coils.

from the shaft through a 5 mm layer of bakelite. The space between the inner radius of the end-plates and the surface of the shaft was 6.5 mm. It is possible that there is a leakage flux to the shaft directly from the end-plates, but it is more likely to travel through the bearings. This leakage path was not considered in the simulations, and it is likely the cause of the disagreement between the predicted and measured induced voltage.

There are other constructional details that can affect the magnetic circuit. First of all, the holes between the teeth used to introduce the conductors have a dimension of 5x5 mm and they were not included in the model. These holes affect the linking flux flowing between the teeth through the core in the circumferential direction. However, their influence in the axial magnetization path is probably not too significant since they are located exactly in the middle of the core. Another source of disagreement could be the possible air gaps that appear between the core rings and between the core and the end-plates if they are not adjusted properly. However, with a proper mechanical design these gaps will be considerably too small to have a significant effect. In general, a lower induced voltage indicates a decrease in the linking flux, which in turn will also reduce the torque delivered by the machine.

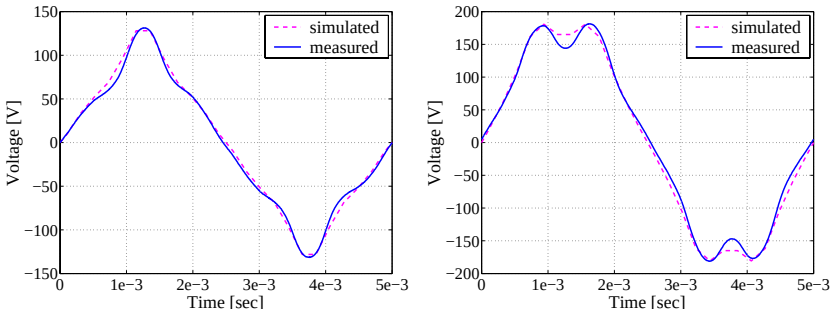

(a) Phase voltage

(b) Phase to phase voltage

Figure 7.18: Comparison between the simulated and measured induced voltage, 1500 r.p.m. Measured voltage amplified by 20%.

Average torque

The average torque from the prototype was measured with a torque sensor. It could also be calculated by multiplying the current in the d.c. machine by its magnetizing flux (1.35 Vs). The accuracy of this procedure was within 1 Nm compared to the value from the transducer. The torque was measured at four levels of magnetization up to the nominal value, and different combinations of the i_{sx} and i_{sy} armature currents. The maximum value of these currents was selected so that the resultant current in all the combinations did not exceed the value at thermal limit by more than 10%. The results are shown in Figure 7.19. It can be observed that the shape is very similar in all the cases, although the torque increases for higher field currents. The output torque from the prototype is governed by (7.13) (Alaküla, 2002). In the prototype, L_{sy} is higher than L_{sx}. For a given i_{sy}, the absolute value of the torque increases for a negative i_{sx} and decreases for a positive i_{sx}, as can be observed from the experimental results.

$$T = \Psi_m \cdot i_{sy} + (L_{sx} - L_{sy}) \cdot i_{sx} \cdot i_{sy} \tag{7.13}$$

The average torque measured for i_{sx}=-6.2 A, i_{sy}=17.7 A, and i_f=14.6 A was 10.4 Nm. The simulated torque response for these currents is shown in Figure 7.20. The average value of the torque considering the ripple is 11.88 Nm, which means that the measured torque is 14% lower than the estimated from FEM. This is not unexpected, since the linking flux is also reduced compared to the measurements as indicated above.

Iron losses

The core losses were measured using the calibrated d.c. machine as a prime mover. The mechanical losses in the system were measured with the two machines coupled together and with no excitation in the synchronous machine. The input power to the d.c. machine was measured for speeds up to 1500 r.p.m. in steps of 37.5 r.p.m. The speed was determined from the electrical frequency measured from the resolver output signals. This procedure was then repeated with field excitation in the synchronous machine (i_f=14.6 A). The difference between the input power from both experiments minus the resistive copper losses in the d.c. machine yielded the core losses at no load. The measured mechanical and core loss energy are shown in Figure 7.21. For comparison, the predicted losses in FEM are also included in the plot. The loss energy is simply obtained dividing the losses (W) by the electrical frequency (Hz).

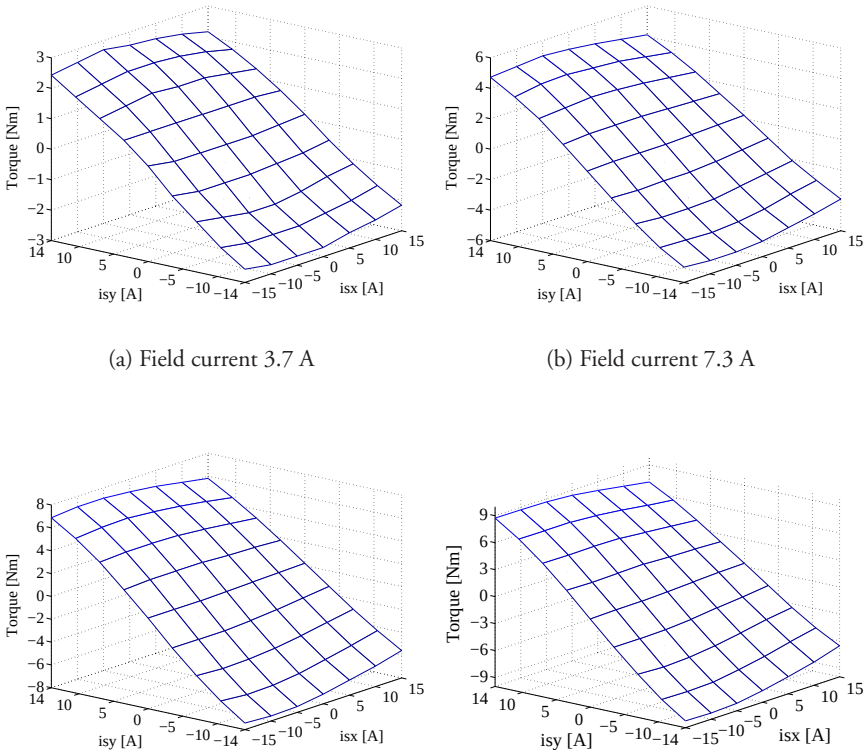

(a) Field current 3.7 A

(b) Field current 7.3 A

(c) Field current 11.0 A

(d) Field current 14.6 A

Figure 7.19: Measured average torque for different field currents.

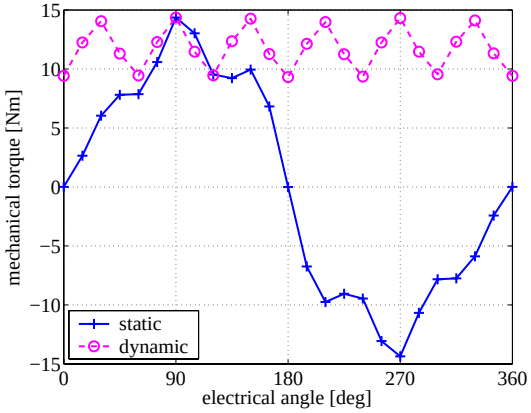

Figure 7.20: Simulated torque response for i_{sx}=-6.2 A, i_{sy}=17.7 A, i_f=14.6 A.

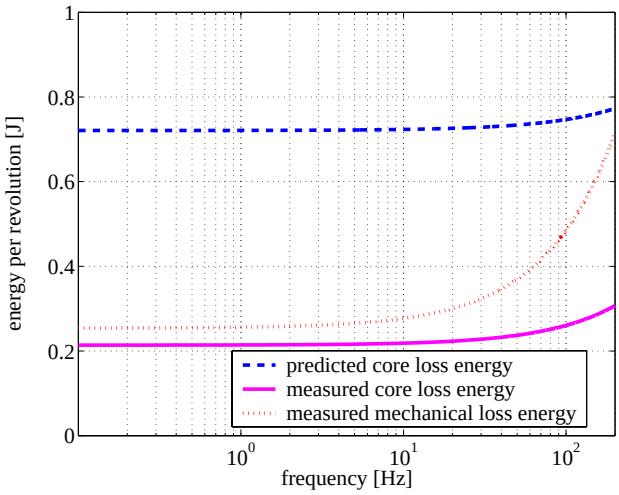

Figure 7.21: Measured and predicted losses at no load.

It can be observed how the mechanical loss energy increases more rapidly with the frequency, while the predicted and measured core loss energy follow a more similar pattern. However, the overall measured core loss is considerably reduced compared to the predictions. The hysteresis energy loss is independent on the frequency, and the measured value is 70% lower than the estimated (at 0 Hz). The dynamic loss energy (eddy current and anomalous) is a function of the frequency, and the estimated value is 45% lower than the measured at 200 Hz. It should be pointed out that the predicted response in Figure 7.21 has been obtained adapting the coefficients in the loss formulation to the lubricating binder LB1. Indeed, the coefficients presented by Guo et al. (2003) (Chapter 3) are for the lubricant Kenolube. Skarrie (2001) measured the coefficients for the alternation losses in a powder core inductor, and they were used to estimate the losses due to alternation in the machine, see Table 7.3 (C_{ha}, C_{ea}, C_{aa}, h). The hysteresis losses due to rotation where calculated using Guo's formulation and then multiplied by the coefficient C_{ff} which is the ratio between the alternating hysteresis component from Skarrie and Guo. The eddy current rotational component (C_{er}) was already zero in Guo's formulation, and the anomalous component (C_{ar}) was also set to zero since it could not be deduced from the available data.

One of the reasons contributing to the mismatch in the losses is the fact that the real machine is actually less magnetized compared to the model in the simulations, as it was observed from the induced voltage measurements. The hysteresis losses are proportional to B^h, where B is the flux density. If the linking flux in the prototype was increased by 20% to match that in the FEM model, and assuming that this increase is evenly distributed in all parts of the machine, then the measured hysteresis losses would be increased by 34%. Nevertheless, the hysteresis losses would still be 60% lower than the estimated. On the other hand, the dynamic losses would also be considerably increased since the eddy current losses are proportional to B^2 and the anomalous losses to $B^{1.5}$. This would increase the curvature of the measured response at higher frequencies, indicating that the dynamic losses would be even more underestimated. However, in the formulation for the estimation of the dynamic losses only the anomalous losses due to alternation are included. The eddy current losses due to alternation and rotation as well as the rotational anomalous losses are neglected for LB1, which is probably the reason for the lower predicted dynamic losses. Bulk eddy current losses are also a function of the geometry, as indicated by Lange et al. (2000) and Hofer (2004). The weight of the SMC parts in the

Table 7.3: Coefficients for the iron loss calculation

Coefficient	Adapted value
C_{ha}	0.16
C_{ea}	0
C_{aa}	$4.38 \cdot 10^{-3}$
h	1.6
C_{ff}	0.16/0.14
C_{er}	0
C_{ar}	0

machine presented by Guo et al. (2003) is around half compared to the prototype in this thesis, and therefore higher dynamic losses would be expected in the measurements compared to the estimations.

Finally, it should be noted that the harmonic loss formulation proposed in this thesis does not consider the bias field of the d.c. excited core. Therefore, all the harmonics are assumed to follow a symmetrical major hysteresis loop (with different amplitudes) around the center B=0, H=0. However, if the harmonic has a bias d.c. component, there will be an asymmetric behaviour, and even minor loops as shown in Figure 7.22. This could be the case in the regions around the surface of the end-plates close to the rotor, where there is a strong bias d.c. component (the field is not reversed), which is added to the partial rotation of the flux vector with the rotor rotation. In general, it is evident that the core loss prediction is a complicated process where many variables have to be taken into consideration.

7.7 Series Magnetization

The concept of series magnetization in a three phase electrically magnetized synchronous machine was developed by Alaküla (2004). It is based on that the stator winding is connected through a three-phase diode rectifier to the field winding, as shown in Figure 7.23. In this way the additional power supply for the field current can be suppressed. Studies on commercial machines re-adapted for series magnetization have been reported earlier by Tonin (2003)

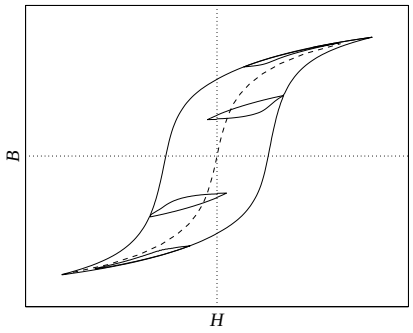

Figure 7.22: Major hysteresis loop and minor loops. Source (Skarrie, 2001).

and Hagstedt (2004).

Figure 7.24 shows a sample of three sinusoidal currents shifted 120 degrees in time, and the rectified curve corresponding to the field current. It can be observed that this current has a ripple with a frequency of six times the fundamental electrical frequency. The average field current can be calculated using (7.14), where $|\vec{i}_s|$ is the modulus of the phase current. The number of conductors in the d.c. coils for series magnetization is calculated using (7.15), where It_{dc} and It_{ac} are the Ampere turns in the field and armature coils, and Nc_{ac} is the number of conductors in an armature coil. The number of turns in the field winding of the prototype were calculated using this method.

$$\bar{i}_f = \frac{6}{2\pi}|\vec{i}_s| \int_{\pi/2-\pi/6}^{\pi/2+\pi/6} \sin\theta d\theta = \frac{3}{\pi}|\vec{i}_s| \tag{7.14}$$

$$Nc_{dc-series} = \frac{It_{dc}}{3/\pi \cdot It_{ac}/Nc_{ac}} \tag{7.15}$$

The measured average torque for a given combination of i_{sx} and i_{sy} is shown in Figure 7.25(a). The corresponding measured field current is shown in Figure 7.25(b). It can be observed that when i_{sy} is positive, the torque increases with negative i_{sx}, which indicates that $L_{sy} > L_{sx}$ according to (7.13). However, when i_{sy} is negative, the torque slightly increases negatively for positive values of i_{sx}. This is very likely due to a slight misalignment of the resolver,

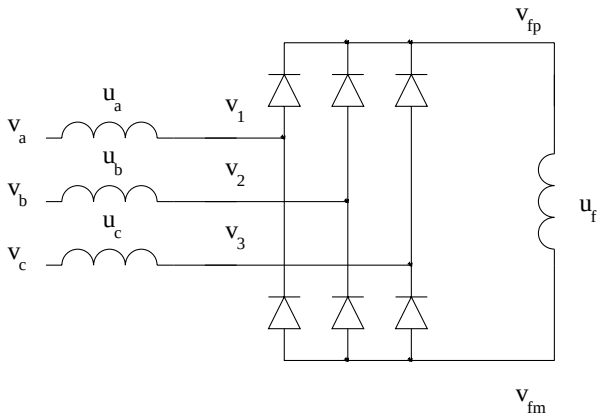

Figure 7.23: Connections for the series magnetized synchronous machine.

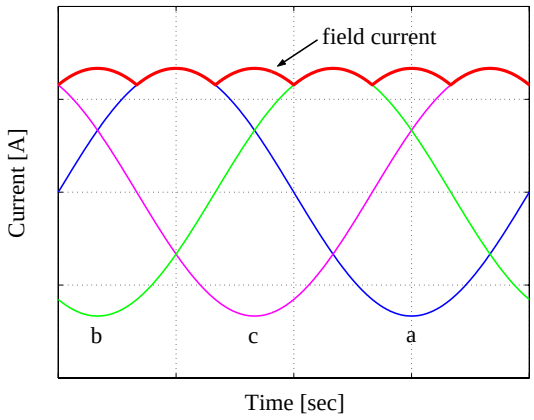

Figure 7.24: Rectified field current.

as can be observed from the torque values corresponding to i_{sy}=0, which are not exactly zero all the time. In fact, before these measurements were carried out, the machine had to be dismantled since the rotor needed to be repaired as the connection to the shaft became loosen. When the machine was mounted back it is possible that the resolver was not aligned with the same accuracy as before. Indeed, from Figure 7.19 it can be observed that the line at $i_{sy} = 0$ is much more straight, and these measurements were performed before the reparation. According to the results for series magnetization at $i_{sy} = 0$, the torque curve should be shifted so that the values corresponding to $i_{sx} > 0$ are slightly lifted up, and those for $i_{sx} < 0$ are slightly pushed down. Then the relation $L_{sy} > L_{sx}$ would be valid for all the current combinations.

The average torque measured for i_{sx}=-6.2 A and i_{sy}=17.7 using series magnetization was 10.6 Nm, which is very similar (only 2% higher) to the value obtained from separate magnetization. Of course, the slight misalignment of the resolver influences the results, but its effect decreases at lower absolute values of i_{sx}, as observed from Figure 7.25(a). In fact it was measured that the field current for the given combination of i_{sx} and i_{sy} above was around 5% higher than the nominal value for separate magnetization. If the output torque is reduced proportionally, then the difference between the torque values obtained for separate and series magnetization would be within only a few percent.

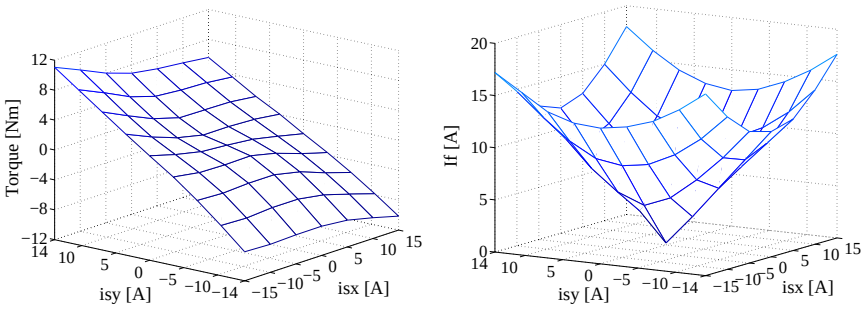

(a) Average torque.

(b) Field current.

Figure 7.25: Measured average torque and field currents for series magnetization.

7.8 Conclusions

The practical details on the construction of the prototype have been presented. The thermal model had to be re-adapted to the new cooling system. The predicted temperature in the d.c. coils was underestimated by 19%. This could be due to the improper fit of the coil into the side of the plate, and the added insulation from the layer of enamel used to fix it. In the a.c. coils the accuracy was within 4% assuming that the heat transfer from the top of the coils to the back-core is negligible. Therefore it can be concluded that the thermal models are reasonable.

It was observed that the inductance from different tooth coils varied by up to 14%. This is probably due to inhomogeneities in the bulk material from where the teeth were machined. The teeth were distributed so that the inductance from the three phases was the same, and this was confirmed from the induced voltage measurements. However, compared to the predictions, the measured induced voltage was 20% lower, although the shape resembled well that from FEM. The reason for the lower voltage is probably the leakage path between the end-plates through the shaft. The holes between the teeth for the winding connections also affected the magnetic circuit.

The coefficients for the iron loss calculation were not available for the lubricant LB1. Instead they were roughly adapted from studies performed in inductors using the same material. The measured hysteresis losses were around 60% lower than the estimations, assuming that the flux density is uniformly increased by 20% to match that in the model. The estimated dynamic losses are at least 45% lower than the measured. A source of error is the fact that the harmonic loss formulation does not consider the bias field of the d.c. excited core, neglecting therefore minor hysteresis loops. In general, the iron loss estimation is a complicated issue, since the material parameters are difficult to obtain and some of them depend on the machine size. The flux variation in different parts of the machine can be estimated from FEM, but the proper adaptation of the iron loss formulation is more complicated. It should be noted that in the FEM model the effects of the eddy currents on the field distribution is not taken into consideration. This can therefore introduce inaccuracies in the model that affect the prediction of the iron losses and the output voltage.

The measured average torque at thermal limit was 14% lower than predicted, which is related to the reduction of the linking flux. The idea of series magnetization has been tested. It is shown that the output torque for the given

design current is very similar to that with separate magnetization. It is therefore demonstrated how traditional disadvantages of electrically magnetized synchronous machines, such as slip-rings and the power source for the field, can be overcome with the prototype machine.

Chapter 8

Conclusions

In this first part of the thesis a novel topology of electrically magnetized synchronous machine has been designed to solve the main drawbacks in the more conventional design: the slip-rings, and the power source for the d.c. winding. The slip-rings are suppressed, since the field winding is removed from the rotor and placed in magnetically conducting end-plates. This requires three-dimensional flux flow, which is achieved using SMC. The windings in the machine have been designed to exploit the concept of series magnetization. This consists of feeding the field winding directly from the rectified three phase armature currents at the neutral point, therefore eliminating the need for the d.c. power source.

In this chapter a summary of the results obtained is presented, followed by some topics suggested for future research in this field.

8.1 Summary

MEC

A Magnetic-Equivalent-Circuit model has been developed including a method to account for non-linearities, which is based on the linearization of the BH curve. The method provides very fast and accurate results for the flux distribution in the machine at load and no load compared to FEM. Modifications to accomplish forward and backward rotation were included in the model. A simplified method was used to assess the shape of the torque response. It was observed that a change in the area of the airgap reluctances affected significantly

the amplitude of the torque response, while the shape was properly predicted.

Leakage reduction

From the FE simulations it was estimated that the leakage in the machine was around 70%. The main leakage path is from the tips of the claw-poles to the opposite end-plate. A study was carried out to assess the effectiveness of including permanent magnets around the claw-poles to reduce the leakage. Using ferrite magnets the leakage is marginally decreased by up to 10%. However, combining NdFeB and ferrite magnets, the leakage is reduced by up to 50%. Including NdFeB magnets all around the claw-poles modifies the pattern of magnetization and increases the output torque between 53% and 113%, for designs with 12 and 24 poles respectively.

Comparison with other topologies

The prototype design has been compared by simulation with three alternative topologies: an outer-rotor claw-pole machine, a conventional electrically magnetized machine, and a surface permanent magnet machine. Among the electrically magnetized machines, the conventional design has a slightly higher average torque per weight and per volume (8%) compared to the prototype design. The latter has however around 18% lower material cost per output torque. The PM machine presents superior electromagnetic performance compared to the electrically magnetized machines. The torque density is around 40% higher. It is however also the most expensive machine considering the cost per output torque, which is around 32% higher than in the prototype design.

Measurements

The shape of the measured induced voltage was almost identical to that predicted in FEM. However, the amplitude of the flux was around 20% lower than predicted, and the average torque was reduced by 14%. This could be due to the leakage path between the end-plates through the shaft, not included in the models. Constructional details such as the holes between the teeth to connect the coils can also contribute to reduce the linking flux.

The thermal network model predicted reasonably the temperature rise in the windings. In the armature coils the temperature was predicted with an accuracy of 4% assuming that there is no heat transfer from the top of the coils

to the core. This is reasonable since a gap was left in this region to facilitate the mounting process. The temperature in the field coils was underestimated by 19%. This could be due to the improper fit of the coil into the side of the plate, and the added insulation from the layer of enamel used to fix it. These details introduce uncertainties in the model that are very difficult to assess, but which would contribute to increase the estimated temperature.

Despite the efforts to model precisely the field variation in the machine, the iron loss prediction was rather inaccurate. This is partially due to the lack of proper coefficients for the lubricant LB1 to be used in the loss formulation. Nevertheless, the results indicated that the measured hysteresis losses were 60% lower than predicted, while the estimated dynamic losses were at least 45% lower than the measured.

8.2 Future work

Regarding the MEC model, the formulation for mesh rotation could be further improved, including more sophisticated methods to calculate the torque response.

The constructional details of the prototype affect to some extent the performance of the machine compared to the predictions in the models. The coupling between the end-plates, the bearings and the shaft could be included in the electromagnetic finite element model to assess the amount of flux leaking through the shaft. The holes in the back-core for the connections of the windings should also be included.

The thermal characteristics of the machine could be more accurately modelled in thermal FEM. However, although the geometry is better discretized in FEM, there are still uncertain parameters that have to be input, such as the degree of contact between different materials at the boundaries, the heat transfer coefficient, etc. These parameters can affect significantly the output results.

The proper parameters for the iron loss formulation using the lubricant LB1 should be measured. The loss calculation should be also improved. Although it is instructive to calculate the iron losses as a function of the harmonic number, simply adding them to calculate the total losses is not adequate in non-linear systems. However, this procedure is frequently used in the literature, mainly due to the lack of more advanced models. A proper model to calculate the iron losses should take into consideration minor hysteresis loops, including the bias field of the d.c. excited core.

An algorithm should be implemented in the control system to compensate for the high torque ripple in the machine. This can be achieved by adding a harmonic component to the currents with the proper frequency and phase.

A sensitivity study should be carried out to assess the change in the magnetic properties of the teeth when they are machined from iron-powder bulks of different size.

The comparison of the four machines indicated that the PM machine clearly presents superior electromagnetic performance at normal operation. However, a similar comparison should be carried out at field weakening operation, where the electrically magnetized machines operate more advantageously.

Bibliography

Alaküla, M. (2002). *Power electronic control*. Dept of Industrial Electrical Engineering and Automation, Lund University, Sweden.

Alaküla, M. (2004). International Patent Application PCT/SE2004/000396. *Synchronous machines*.

Andersson, S. (2000). *Optimization of a servo motor for an industrial robot application.* Licentiate Thesis, Dept of Industrial Electrical Engineering and Automation, Lund University, Sweden.

Aoki, H., Nohira, H., Arai, H. (1967). Convective heat transfer in an annulus with an inner rotating cylinder. *Bulletin of JSME*, vol. 10, no. 39, pp. 523-532.

Arkkio, A. (2002). *Thermal analysis of high-speed electrical machines.* Postgraduate Seminar on Electromechanics, Laboratory of Electromechanics, Helsinki University of Technology, Finland.

Becker, K.M., Kaye, J. (1962). Measurements of diabatic flow in an annulus with an inner rotating cylinder. *Journal of Heat Transfer*, 84, pp. 97-105.

Bjorklund, I.S., Kays, W.M. (1959). Heat transfer between concentric rotating cylinders. *Journal of Heat Transfer*, 81, pp. 175-186.

Blarigan, P.V., Paradiso, N., Goldsborough, S. (1998). Homogeneous charge compression ignition with a free piston: a new approach to ideal Otto cycle performance. *Society of Automotive Engineers*, SAE paper nr 982484.

Boglietti, A., Cavagnino, A., Staton, D.A. (2004). Thermal sensitivity analysis for TEFC induction motors. *Proceedings of IEE International Conference on Power Electronics, Machines and Drives*, Edinburgh, UK, pp. 160-165.

Bottauscio, O., Canova, A., Chiampi, M., Repetto, M. (2002). Iron losses in electrical machines: influence of different material models. *IEEE Transactions on Magnetics*, vol. 38, no. 2, pp. 805-808.

Cros, J., Viarouge, P. (2002). Synthesis of high performance PM motors with concentrated windings. *IEEE Transactions on Energy Conversion*, vol. 17, no. 2, pp. 248-253.

Driesen, J., Belmans, R.J.M., Hameyer, K., Stephenson, D. (2001). Finite-element modeling of thermal contact resistances and insulation layers in electrical machines. *IEEE Transactions on Industry Applications*, vol. 37, no. 1, pp. 15-20.

Erlandsson, O. (1998). *Alvar engine, an engine with variable compression ratio, experiments and tests.* MSc Thesis, Dept of Heat and Power Engineering, Division of Combustion Engines, Lund University, Sweden.

Erlandsson, O., Lundholm, G., Söderberg, F., Johansson, B., Wong, V.W. (1998). Demonstrating the performance and emission characteristics of a variable compression ratio, Alvar-cycle engine. *Society of Automotive Engineers*, SAE paper nr 982682.

Gazley, C. (1958). Heat transfer characteristics of rotational and axial flow between concentric cylinders. *Transactions of the ASME*, vol. 80, no. 1, pp. 79-90.

Guo, Y., Zhu, J.G., Zhong, J.J., Wu, W. (2003). Core losses in claw pole permanent magnet machines with soft magnetic composite stators. *IEEE Transactions on Magnetics*, vol. 39, no. 5, pp. 3199-3201.

Hagstedt, D. (2004). *Analysis of a series magnetized Lundell alternator.* MSc Thesis, Dept of Industrial Electrical Engineering and Automation, Lund University, Sweden.

Hamdi, E.S. (1994). *Design of small electrical machines*. John Wiley & Sons Ltd., UK.

Henneberger, G., Küppers, S., Ramesohl, I. (1996). Numerical calculation, simulation and design optimisation of claw pole alternators for automotive application. *IEE Colloquium on Machines for Automotive Applications*, Digest No 1996/166.

Hofer, U. (2004). High speed motor design issues using soft magnetic composites. Invited paper, The UK Magnetics Society, *Seminar on SMC and their use in electrical machines*, Newcastle, UK, Nov. 2004, 4 pp.

Holman, J.P. (1992). *Heat transfer*. 7th edition, McGraw-Hill.

Höganäs AB S-26383, Höganäs, Sweden, SOMALOY^{TM}500, SMC 97-1, AB Ruter Press.

Höganäs AB S-26383, Höganäs, Sweden, *SMC School*, 27-28 November, 2001.

Ishikawa, T., Slemon, G.R. (1993). A method of reducing ripple torque in permanent magnet motors without skewing. *IEEE Transactions on Magnetics*, vol. 29, no. 2, pp. 2028-2031.

Jack, A.G. (2003). Exploring design opportunities offered by SMC for electrical machines. *IEEE International Electric Machines and Drives Conference*, SMC seminar tutorial, 1 June, 2003.

Jack, A.G., Mecrow, B.C., Dickinson, P.G., Stephenson, D., Burdess, J.S., Fawcett, N., Evans J.T. (2000). Permanent-magnet machines with powdered iron cores and prepressed windings. *IEEE Transactions on Industry Applications*, vol. 36, no. 4, pp. 1077-1084.

Jahns, T.M., Soong W.L. (1996). Pulsating torque minimization techniques for permanent magnet AC motor drives - A review. *IEEE Transactions on Industrial Electronics*, vol. 43, no. 2, pp. 321-330.

Jokinen, T., Saari, J. (1997). Modelling of the coolant flow with heat flow controlled temperature sources in thermal networks. *IEE Proceedings on Electric Power Applications*, vol. 144, no. 5, pp. 338-342.

Kazuaki, S., Kaoru, K., Toshiaki, K., Yuji, H. (2000). Development of electric motors for the Toyota hybrid vehicle PRIUS. *17th International Electric Vehicle Symposium & Exposition*, Montréal, Canada, Record from the CD-ROM.

Kylander, G. (1995). *Thermal modelling of small cage induction motors.* PhD Thesis, School of Electrical and Computer Engineering, Chalmers University of Technology, Sweden.

Lange, A., Canders, W.R., Mosebach, H. (2000). Investigation of iron losses of soft magnetic powder components for electrical machines. *Proceedings of International Conference on Electrical Machines*, Helsinki, Finland, pp. 1521-1525.

Li, T., Slemon, G.R. (1988). Reduction of cogging torque in permanent magnet motors. *IEEE Transactions on Magnetics*, vol. 24, no. 6, pp. 2901-2903.

Luomi, J. (1993). *Electromagnetic field analysis.* Summer seminar for postgraduates, Tammsviks Kursgård, Bro, Sweden, 15-21 August 1993.

Ma, L., Sanada, M., Morimoto S., Takeda Y. (2003). Prediction of iron loss in rotating machines with rotational loss included. *IEEE Transactions on Magnetics*, vol. 39, no. 4, pp. 2036-2041.

Mellor, P.H., Roberts, D., Turner, D.R. (1991). Lumped parameter thermal model for electrical machines of TEFC design. *IEE Proceedings -B on Electric Power Applications*, vol. 138, no. 5, pp. 205-218.

Miller, T.J.E. (1993). *Switched reluctance motors and their control*. Oxford University Press, UK.

Moallem, M., Dawson, G.E. (1998). An improved magnetic equivalent circuit method for predicting the characteristics of highly saturated electromagnetic devices. *IEEE Transactions on Magnetics*, vol. 34, no 5, pp. 3632-3635.

Novotny, D.W., Lipo, T.A. (1996). *Vector control and dynamics of AC drives*. Oxford Science Publications, Wisconsin, USA.

Ostović, V. (1989). *Dynamics of saturated electric machines*. Springer-Verlag, USA.

Ostović, V., Miller, J.M., Garg, V.K., Schultz, R.D., and Swales, S.H. (1999). A magnetic-equivalent-circuit-based performance computation of a Lundell alternator. *IEEE Transactions on Industry Applications*, vol. 35, no 4, pp. 825-830.

Ottosen, N., Petersson, H. (1992). *Introduction to the Finite Element Method*. Prentice Hall Europe, UK.

Polinder, H., Hoeijmakers, M.J. (1997). Eddy-current losses in the permanent magnets of a PM machine. *Proceedings of IEE International Conference on Electrical Machines and Drives*, Cambridge, UK, pp. 138-142.

Sadarangani, C. (2000). *Electrical machines - Design and analysis of induction and permanent magnet motors*. Dept of electric power engineering, electrical machines and power electronics, Royal Institute of Technology, Sweden.

Sieder, E.N., Tate, C.E. (1936). Heat transfer and pressure drop of liquids in tubes. *Ind. Eng. Chem.*, vol. 28, no. 4, p. 1429.

Skarrie, H. (2001). *Design of powder core inductors.* Licentiate Thesis, Dept of Industrial Electrical Engineering and Automation, Lund University, Sweden.

Stenlåås, O. (2004). *On the impact of piston motion and in-cylinder charge composition on energy release, auto ignition and emission formation in premixed charge internal combustion engines.* PhD Thesis, Dept of Heat and Power Engineering, Division of Combustion Engines, Lund University, Sweden.

Stewart, M. (1997). *Design and analysis of a variable-compression-ratio internal-combustion engine - The Alvar engine concept.* MSc Thesis, Dept of Mechanical Engineering, Massachusetts Institute of Technology, USA.

Taniguchi, C. (2000). *Rotor of rotary machine having claw poles and auxiliary permanent magnets*. United States Patent number 6011343.

The Royal Commission on Environmental Pollution (2000). *22nd Report, Energy - The changing climate, Chapter 2: On causes and effects of climate change*. http://www.rcep.org.uk/newenergy.htm, UK.

The Swedish Energy Agency (2003). *Energy in Sweden 2003, Chapter 4: Energy use*. http://www.stem.se, Sweden.

Tonin, D. (2003). *A novel synchronous drive using series magnetized synchronous machine with a special position sensing.* MSc Thesis, Dept of Industrial Electrical Engineering and Automation, Lund University, Sweden.

Vas, P. (1990). *Vector control of AC machines*. Oxford University Press, UK.

Vong, P.K., Rodger, D. (2003). Coupled electromagnetic-thermal modeling of electrical machines. *IEEE Transactions on Magnetics*, vol. 39, no. 3, pp. 1614-1617.

Wong, H.Y. (1977). *Handbook of essential formulae and data on heat transfer for engineers*. Longman Inc., New York, USA.

Wong, V.W., Stewart, G., Lundholm, G., Höglund, A. (1998). Increased power density via variable compression/displacement and turbocharging using the Alvar-cycle engine. *Society of Automotive Engineers*, SAE paper nr 981027.

Zhou, P. (1993). *Numerical analysis of electromagnetic fields*. Springer-Verlag, New York, USA.

Zhu, J.G., Ramsden, V.S. (1998). Improved formulations for rotational core losses in rotating electrical machines. *IEEE Transactions on Magnetics*, vol. 34, no 4, pp. 2234-2242.

Appendix A

Equations for the MEC network

The permeances (P) of the elements used in the MEC model are listed below. They are easily converted into reluctances ($R = 1/P$). The equations are parametrized according to the geometry, and these parameters are described in Appendix B. The permeability of each iron element is a function of the interval in the BH curve where its flux density is located during the iteration process. The equations have not been completely simplified in order to allow the reader to understand the geometrical considerations used in the calculations.

$$\alpha = \frac{2\pi}{N_s} \tag{A.1}$$

$$Pyx1 = \mu_0\,\mu_{pyx1}\frac{\alpha/2\cdot\left(ros^2-(ros-dy)^2\right)}{zyt-zdx+zdx/2+zts/8} \tag{A.2}$$

$$Pss1 = \mu_0\,\mu_{pss1}\frac{\left(2\pi(ror+ros-dy)/2\right)/N_s\cdot zdx}{ros-dy-ror+dy/2} \tag{A.3}$$

$$Psr1a = \mu_0\,\mu_{psr1a}\frac{2\pi(ror-dr+ror)/2}{N_s}zdx/\frac{dr}{2} \tag{A.4}$$

$$Psr1b = \mu_0\,\mu_{psr1b}\frac{\alpha/2}{2}\left(ror^2-rir^2\right)\frac{1}{2}/zdy \tag{A.5}$$

$$Psc1 = \mu_0\,\mu_{psc1}\frac{wot\cdot ris\cdot ztps/4}{\sqrt{\left(wot/2\cdot(ris+dos)-wt/2\right)^2+dos^2}} \tag{A.6}$$

$$Pps1 = \mu_0\,\mu_{pps1}\cdot wt\cdot zts/ds \tag{A.7}$$

$$Pcr1a1 = \mu_0\,\mu_{pcr1a1}\frac{\alpha/2}{2}\left(ror^2 - rir^2\right)/ztr \tag{A.8}$$

$$Pcr1a2 = \mu_0\,\mu_{prtt}\frac{(\alpha-(2\pi/N_p - wtr1))/2}{2}\cdot \cdot\frac{ror^2-(ror-dr)^2}{\sqrt{(ztpr/2)^2+(dr/2)^2}} \tag{A.9}$$

$$Pyp12 = \mu_0\,\mu_{pyp12}\frac{zts\cdot dy}{(2\pi(ros-dy+ros)/2)/N_s} \tag{A.10}$$

$$Pgr1 = \mu_0\frac{wot}{2}\,ror\cdot ztps/g1 \tag{A.11}$$

$$Pge1 = \mu_0\frac{\alpha/2}{2}\left(ror^2 - rir^2\right)/g2 \tag{A.12}$$

$$Psr1_\sigma = \mu_0\frac{(\alpha-(2\pi/N_p - wtr3))/2}{2}\cdot \cdot\frac{ror^2-(ror-dr)^2}{zrt-ztpr-ztr+g2} \tag{A.13}$$

$$Psf1_\sigma = \mu_0\cdot wot\cdot ris\cdot dos/(ztr+g2) \tag{A.14}$$

$$Pcs12_\sigma = \mu_0\cdot ztps\cdot dos/\left(\frac{2\pi(ris+dos+ris)/2}{N_s} - \right. \left. - wot\,\frac{ris+dos+ris}{2}\right) \tag{A.15}$$

$$Pcr14_\sigma = \mu_0\left(\sqrt{ztpr^2+(dr-htr3)^2}+ztpr\right)\frac{dr}{2}/ \tag{A.16}$$
$$/\left[\frac{ror-dr+ror}{2}\left(\frac{2\pi}{N_p}-wtr1+\frac{2\pi/N_p-wtr3}{2}\right)\right]$$

$$Pcr2a2 = \mu_0\,\mu_{prtt}\frac{\alpha-(2\pi/N_p-wtr1)/2}{2}\cdot \cdot\frac{ror^2-(ror-dr)^2}{\sqrt{(ztpr/2)^2+(dr/2)^2}} \tag{A.17}$$

$$Psr2_\sigma = \mu_0\frac{wtr3-(\alpha-(2\pi/N_p-wtr3))/2}{2}\cdot \cdot\frac{ror^2-(ror-htr3)^2}{zrt-ztpr-ztr+g2} \tag{A.18}$$

$Psc2 = Psc1\frac{\mu_{psc2}}{\mu_{psc1}}$
$Pps2 = Pps1\frac{\mu_{pps2}}{\mu_{pps1}}$
$Pyp23 = Pyp12\frac{\mu_{pyp23}}{\mu_{pyp12}}$
$Pcr3a2 = Pcr2a2\frac{\mu_{prtb}}{\mu_{prtt}}$
$Psc3 = Psc2\frac{\mu_{psc3}}{\mu_{psc2}}$
$Pps3 = Pps2\frac{\mu_{pps3}}{\mu_{pps2}}$
$Pyp31 = Pyp23\frac{\mu_{pyp31}}{\mu_{pyp23}}$
$Pcr4a2 = Pcr1a2\frac{\mu_{prtb}}{\mu_{prtt}}$
$Plea12 = 2\mu_{rtt}Pcs1_{\sigma}$
$Plea13 = 2\mu_{rtb}Pcs1_{\sigma}$
$Psr3_{\sigma} = Psr2_{\sigma}$
$Pcr4a1 = Pcr1a1$
$Psr4b = Psr1b$
$Pgr4 = Pgr1$
$Pge4 = Pge1$
$Pcr4_{\sigma} = Pcr1_{\sigma}$
$Psr4_{\sigma} = Psr1_{\sigma}$
$Pyx2 = Pyx3 = Pyx1$
$Pss2 = Pss3 = Pss1$
$Psr2a = Psr3a = Psr1a$
$Psr2b = Psr3b = 2Psr1b$
$Pcr2a1 = Pcr3a1 = 2Pcr1a1$
$Pgr2 = Pgr3 = 2Pgr1$
$Pge2 = Pge3 = 2Pge1$
$Psf2_{\sigma} = Psf3_{\sigma} = Psf1_{\sigma}$
$Pcs2_{\sigma} = Pcs3_{\sigma} = Pcs1_{\sigma}$
$Pcr2_{\sigma} = Pcr3_{\sigma} = Pcr1_{\sigma}$

Appendix B

Parametrization of the machine

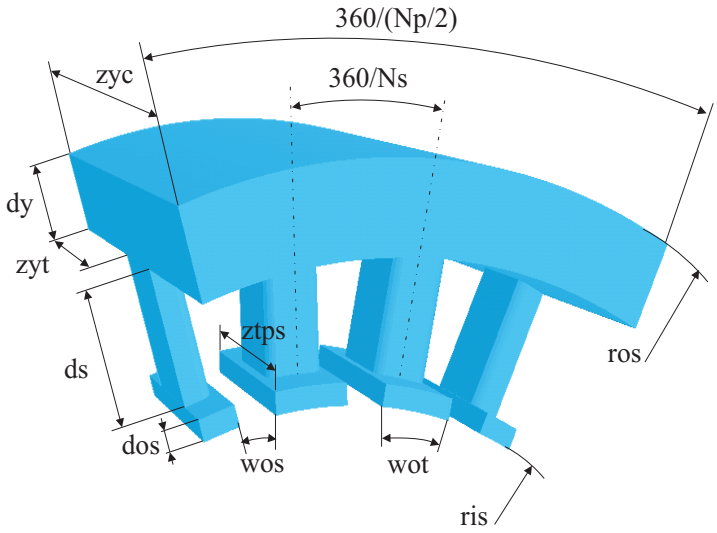

Figure B.1: Stator teeth and yoke.

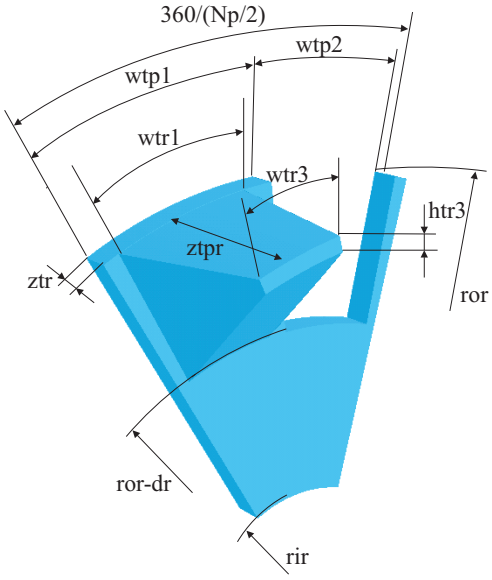

Figure B.2: One rotor claw-pole structure.

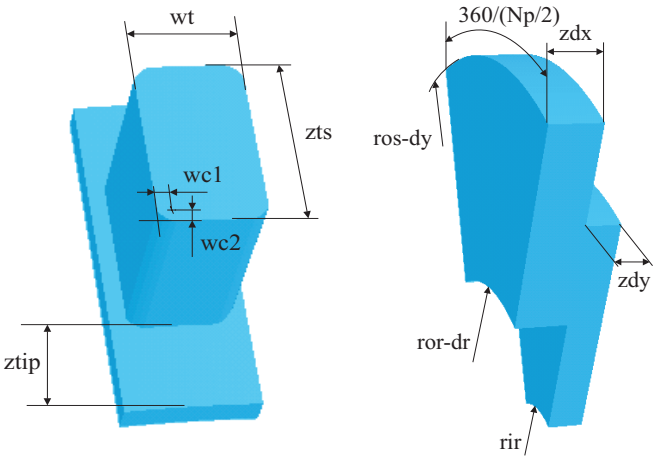

(a) Stator tooth (b) Stator end-plate

Figure B.3: Details of the stator tooth and end-plate.

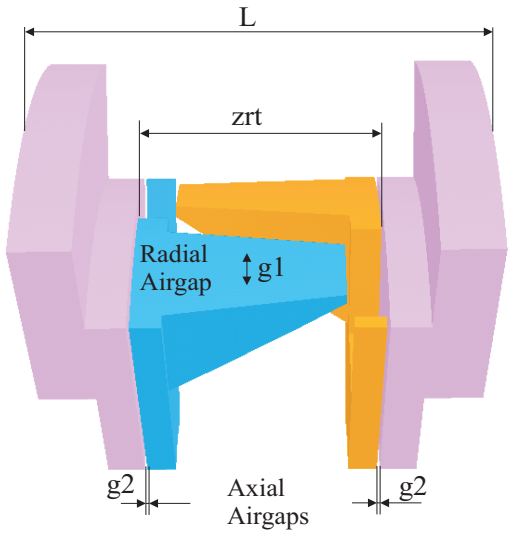

Figure B.4: Claw-pole rotor and end-plates.

Table B.1: Dimensions of the prototype [mm]

Dimension	**Value**	**Dimension**	**Value**
Np	16	ztpr	30.16
Ns	24	ztip	7.97
L	76.04	zdx	10.00
ros	100.00	zdy	6.67
ris	67.50	zrt	41.70
ror	66.90	wt	9.05
rir	19.00	wc1	1.13
dy	11.30	wc2	1.13
ds	18.27	wos	5.00^o
dos	2.93	wot	10.00^o
dr	22.49	wtp1	24.75^o
htr3	2.18	wtp2	18.00^o
zyc	76.04	wtr1	18.00^o
zyt	30.36	wtr3	10.81^o
zts	15.32	g1	0.60
ztps	31.26	g2	0.50
ztr	5.22		

Appendix C

Equations for the thermal network

The equations used for the thermal model are listed below. The parameters in the equations represent parts of the geometry, and they are defined in Appendix B.

$$Asf_{dc} = \pi(ros^2 - rir^2) + 2\pi(ror - dr) \cdot zdx \quad \text{(C.1)}$$

$$Asf_{ac} = 2\pi \cdot ros \cdot zyc \quad \text{(C.2)}$$

$$Asc_{ac} = 2\pi(ros + dy + ros)\frac{1}{2}zyc \quad \text{(C.3)}$$

$$Lcw_{ac} = \left(\frac{1}{2}\sqrt{(ds + dos)^2 + (wt/2)^2} + \right. \\ \left. + \frac{1}{2}\sqrt{(ds + dos)^2 + (zts/2)^2}\right)\frac{1}{2} \quad \text{(C.4)}$$

$$Acw_{ac} = (2 \cdot ds(wt + zts) + zts \cdot wt)\frac{1}{2}N_s \quad \text{(C.5)}$$

$$Lsw_{dc} = \frac{1}{4}\left(\sqrt{(zdx + zdy/2)^2 + dy^2} + zdx + \sqrt{zdx^2 + dr^2} + \right. \\ \left. + (dr + \frac{1}{2}(ror - dr + rir))\right) \quad \text{(C.6)}$$

$$Asw_{dc} = 2\pi\frac{1}{2}(ror - dr + ror) \cdot \frac{1}{2}(zdx + zdy) + \\ + \pi\left(\left(\frac{ros - dy + ros}{2}\right)^2 - \left(\frac{ror - dr + ror}{2}\right)^2\right) \quad \text{(C.7)}$$

$$h_{th} = ds - 2 \cdot insl \tag{C.8}$$

$$Awi_{ac} = 2 \cdot h_{th}((wt + insl) + (zts + insl)) \cdot N_s \tag{C.9}$$

$$\begin{aligned} Awi_{dc} = {} & 2\pi(ros - dy - \frac{1}{2}insl)zdy + \\ & +2\pi(ror + \frac{1}{2}insl)(zdy - \frac{1}{2}insl) + \\ & +\pi((ros - dy - \frac{1}{2}insl)^2 - (ror + \frac{1}{2}insl)^2) \end{aligned} \tag{C.10}$$

$$Lih_{ac} = \frac{1}{2}(2\pi(ris + dos + \frac{1}{2}ds)/N_s - wt) \tag{C.11}$$

$$Aih_{ac} = 2 \cdot h_{th}((wt + 2 \cdot insl) + (zts + 2 \cdot insl))\frac{1}{2}N_s \tag{C.12}$$

$$Lv_{dc} = (ros - dy - insl) - (ror + insl) \tag{C.13}$$

$$Lih_{dc} = \frac{1}{2}((zdy - insl) + \frac{1}{2}Lv_{dc}) \tag{C.14}$$

$$\begin{aligned} Aih_{dc} = {} & 2\pi(ros - dy - insl - \frac{1}{4}Lv_{dc}) \cdot \frac{1}{2}(zdy - insl) + \\ & +2\pi(ror + insl + \frac{1}{4}Lv_{dc}) \cdot \frac{1}{2}(zdy - insl) + \\ & +\pi((ros - dy - insl - \frac{1}{4}Lv_{dc})^2 - \\ & -(ror + insl + \frac{1}{4}Lv_{dc})^2) \end{aligned} \tag{C.15}$$

Appendix D

Dimensions of the alternative machines

In this appendix the dimensions of the topologies analyzed in Chapter 6 are summarized. For Design 1, which is a 12-pole version of the prototype, only the circumferential measures are included, since the rest are exactly the same as in the prototype, and can be found in Appendix B.

The measures for Design 2, the outer rotor claw-pole machine, can be expressed as a function of those of the prototype, only changing the definition of some components (marked with '*'). The value of 'ris2' and 'ros2' correspond to the inner and outer radius of the stator part above the claw-poles. The thickness of its yoke is given by 'dy2'. Similarly, 'ris1' and 'ros1' correspond to the

Table D.1: Dimensions of Design 1 [mm]

Dimension	Value	Dimension	Value
Np	12	wot	13.33^o
Ns	18	wtp1	33.00^o
wt	12.06	wtp2	24.00^o
wc1	1.50	wtr1	24.00^o
wc2	1.50	wtr3	14.40^o
wos	6.66^o		

Table D.2: Dimensions of Design 2 [mm]

Dimension	**Value**	**Dimension**	**Value**
Np	12	ztpr	30.16
Ns	18	ztip	7.97
L	50.00	ros1*	72.25
ros2*	100.00	ris1*	19.00
ris2*	88.00	zrt	50.00
ror	87.40	wt	12.10
rir	72.85	wc1	1.51
dy2*	6.90	wc2	1.51
ds	18.27	wos	4.80^o
dos	2.93	wot	15.20^o
dr	11.63	wtp1	33.00^o
htr3	2.61	wtp2	24.00^o
zyc	31.26	wtr1	24.00^o
zyt	7.97	wtr3	21.84^o
zts	15.32	g1	0.60
ztps	31.26	dy1*	32.06
ztr	7.83		

inner and outer radius of the stator below the claw-poles. The thickness of its yoke is given by 'dy1'. The airgap 'g1' is the same between the rotor and the upper and the lower stator parts.

The measures of the more conventional synchronous machine without claw-poles, Design 3, are given in Table D.3. The parametrization of the stator is similar to that of the prototype and Design 1. Actually, the rotor has a similar shape but inverted, and the parameters expressing the same measure as in the stator are marked with '*'.

Table D.3: Dimensions of Design 3 [mm]

Dimension	Value	Dimension	Value
Np	12	zyt2*	7.97
Ns	18	ztip	7.97
L	42.70	ztip2*	7.97
ros	100.00	zts2*	15.32
ris	67.50	ztps2*	31.26
ror	66.90	wt	12.06
rir	19.00	wc1	1.50
dy	11.30	wc2	1.50
ds	18.27	wos	4.80^o
dos	2.93	wot	15.20^o
ds2*	15.75	wt2*	16.75
dos2*	2.93	wc12*	1.50
zyc	42.70	wc22*	1.50
zyt	13.70	wos2*	8.0^o
zts	15.32	wot2*	22.0^o
ztps	31.26	g2	0.60
zyc2*	31.26		

Part II

Acoustic Noise in Electrical Machines

Chapter 9

Introduction

9.1 Background

Major contributions on acoustic noise in adjustable-speed a.c. electric motor drives have been made during the last 20 years in connection with the advent of more and more cost effective and powerful frequency converters. The new installations of adjustable-speed drives in industry and commercial buildings are today mainly embodied as a.c. induction motor drives, i.e. as low-maintenance, brush-less drives, pushing traditional d.c. brush-commutator motor drives aside. The level of motor noise radiated increased considerably, as a consequence, due to the current harmonics introduced by the switching technology in the converter. This thesis focuses on the embodiment of the frequency converter what regards modern voltage and airgap flux modulation techniques. The literature referenced here is therefore limited to recent publications on adjustable-speed a.c. electric motor drives although the author is well aware that the history of a.c. drives extends long before the solid-state era, with key engineering developments in the late nineteenth century and the first half of the twentieth century (Jahns and Owen, 2001).

Noise sources

In general, three different sources of noise can be distinguished in electric machines: mechanical, aerodynamic and electromagnetic. The mechanical component is mainly influenced by the way the stator sheets are mounted into the core of the motor, the coupling to the load, rotor unbalance, as well as the vibration of the bearings and the amount of damping material present in the structure.

The aerodynamic component is only dependent on the fan used in air cooled machines. The electromagnetic component is due to the action of magnetic forces in the airgap. These forces are influenced by the harmonics present in the voltage feeding the machine, slot combinations, saturation, magnetostriction and eccentricity among others.

After all, noise is produced due to the mechanical vibrations that take place in the machine. Hence, it is important to evaluate how the different components of the structure influence the noise emissions. One factor to take into consideration is that the machine usually presents some changes compared to the original design, due to the tolerances introduced during the manufacturing process, which become more important in mass production. Starting from the same prototype design, it is not unusual to find machines with a rather different acoustical behaviour, as analyzed by Zhu et al. (1997), and Lo et al. (2000). The main variations are found in the eccentricity of the rotor relative to the stator, which is one important source of noise. By using acoustical simulation, Ramesohl et al. (1999) studied the effects of different manufacturing tolerances in mass produced electric machines. Electromagnetic and structural models using the finite element method (FEM) were used to calculate the force densities which were applied to an acoustic model using the boundary element method (BEM).

Eccentricity is one important factor that has to be taken into consideration when studying the acoustic response of an electric machine. There are namely two types of eccentricity: static and dynamic. Static eccentricity appears when there is an incorrect positioning of the rotor with respect to the stator bore. In this case, when the rotor rotates the position of minimal radial airgap length is fixed in space. Dynamic eccentricity occurs when the center of the rotor is not at the center of the rotation, and the position of minimum airgap rotates with the rotor. Dynamic eccentricity is usually checked in the manufacturing stage and compensated by means of dynamic balancing. However, static eccentricity is hardly checked during the production process and its contribution to the generation of audible noise has been studied by Delaere et al. (1998).

One of the optimization parameters in electric machine design is the size of the motor, and thus the amount of iron needed to achieve a certain performance. Reducing the size of the core decreases the stiffness of the stator structure, which in turn becomes more sensitive to forces acting on it. Therefore, there is a compromise between cost and noise. Dealing with this issue, an optimization process was developed by Hadj Amor et al. (1995) where, for

randomly selected dimensions of the structure, the noise is estimated and in this way the dimensions of the motor producing the least noise can be found. The results obtained suggested the existence of only one minimum, which not surprisingly corresponded to a very heavy and expensive motor.

The stiffness of the stator is also directly influenced by the amount of damping material present on it, as explained by Verma and Balan (1998). Damping materials in the stator are the windings, laminations and insulation. Experiments carried out with a stator shell, both with no laminations and a laminated stator, confirmed that the noise level was around 20 dB lower in the case of the laminated stator, due to its higher amount of damping. Besides, the peaks along the frequency scale in the noise spectrum were more flattened. However, the stiffness of the laminated stator is lower than the stator shell with no laminations, which means that there will be several more resonances falling in the audible frequency range. This behaviour is further affected by the fact that the damping at these frequencies is reduced, as it is proportional to the resonant frequency and the damping ratio, i.e. the benefits of damping are less accentuated at lower frequencies, but still the overall acoustic emissions are lower when damping is present.

The stiffness of the machine is also increased when coupling the motor to the ground (foot mounting) and the load (shaft mounting). The effect on the acoustical emissions of this coupling was analyzed by Zhu et al. (1999) who showed that, although additional natural frequencies are added to the system, the coupling restricts the stator vibration, as its stiffness is increased. The result is that the acoustic noise produced by the machine is reduced. Further, it was shown that even if two similar motors present quite a different acoustic behaviour at no load, when loaded not only the acoustic noise is reduced, but also the acoustic behaviour of both machines becomes much more similar.

In fact, the noise produced by one induction machine can change considerably depending on the ratio between the stator and rotor slots. In general, odd rotor slot numbers should be avoided. A more complete study was presented by Kobayashi et al. (1997), where transient magnetic field FEM and harmonic analyses using Fourier series expansion were used together to compute the forces for a given number of stator and rotor slots. It was found that the level of acoustic noise is dependent on the first space harmonic order, which was not always predicted by analytical calculations based on the slot ratio of the machine.

While the sources responsible for the acoustic noise in electric machines are widely accepted, there is a lack of consensus about the physical mechanisms of

noise production in the machine. The most accepted theory is that the stator vibrations are produced by the radial components of the electromagnetic airgap forces, whereas tangential forces are usually neglected. However, tangential forces can play an important role in large machines, as discussed by Garvey and Le Flem (1999). The influence of magnetostriction is not yet clear. It is a phenomenon that results from the change in the dimensions of the iron when a magnetic flux passes through it. The iron tends to contract along the direction of the flux and tends to expand in the other two directions, and this process increases the level of vibration in the machine. Belmans and Hameyer (1998) considered that although the effect of magnetostriction in theory can contribute to the audible noise, in practice its contribution is negligible. However, a method was presented by Garvey and Glew (1999) to compute the effects of magnetostriction in the stator core and to show its importance. By conducting a series of experiments, Låftman (1997) found that the magnetostrictive forces are about the same magnitude as the Maxwell forces in medium sized induction machines (a few tens of kilowatts) and therefore they would have a major importance in the production of noise in electrical machines.

Finally, the effects of the geometrical and constructional irregularities were presented by Chang and Yacamini (1996). It was found that these irregularities introduce asymmetrical behaviour, which results in an enriched frequency response spectrum. The asymmetry frequencies are caused mainly by the stator winding and frame irregularities which means that the design details of the winding and the frame will play a very important role in the mechanical behaviour of electrical machines and should not be treated simply as an additional mass. Hence, electrical machines should be designed and constructed as symmetrical as possible, in particular the winding overhang.

Electromagnetic force computation

In order to predict the noise behaviour of the machine, it is important to evaluate the airgap flux distribution, which is directly linked to the harmonic pattern of the electromagnetic forces acting on the stator. Many theories have been developed for their analytical computation and approximations need to be introduced in order to model the numerous details in the machine affecting the airgap forces such as saturation, slot shape, etc. Some of the theories proposed provide a quick and relatively accurate prediction of the expected airgap force frequencies, although it is not simple to calculate their magnitude. A modi-

fied one-dimension theory was used by Gerling (1994) taking into account the changes in the reluctance along the airgap due to the stator slots, while no rotor slots were considered. The main idea is to use the geometrical airgap in the region of a stator tooth, and enlarge it only in the region along a slot opening by a factor dependent on the average length of the field lines penetrating through the slot. This procedure shows more accurate results than considering a general enlargement of the geometrical airgap through the whole surface to account for the effects of the stator slot openings. A new correction factor associated with the depth of the slot openings improved considerably the accuracy when predicting the amplitudes of the harmonics.

Another approach accounting for the effects of stator and rotor slotting, eccentricity, iron saturation and the interactions between the various stator and rotor current components was presented by Vandevelde and Melkebeek (1994), using the rotating field theory and the permeance wave technique. The airgap flux density components were then obtained by multiplying the permeance waves, in which the effects of slotting, eccentricity and saturation were modelled, by the magnetomotive force. A more accurate model based on a magnetic equivalent circuit method (MEC) was also elaborated for the calculation of the flux components and the resulting radial magnetic forces (Vandevelde and Melkebeek, 1997).

The effects of both stator and rotor slot openings under load and no load conditions were studied analytically by Cho and Kim (1998), taking into consideration the effects of skewing and the rotation of the rotor, as well as eccentricity. At no load the model was accurate in predicting the frequencies of the harmonics but not the amplitudes. Besides, at load there were slight discrepancies in the magnitude of the main flux. Hubert and Friedrich (2002) presented a semi-analytical method to identify the harmonic components of the airgap electromagnetic force and the resonance frequencies of the stator in a small induction machine. Noise was reduced simply by missmatching these components with a suitable change in the fixed switching frequency in the modulator.

Although the analytical approaches present certain limitations, their short computation time proves to be helpful for a quick assessment of the force spectrum in the machine. However, for more accurate calculations, the use of finite element methods is more appropriate, although the computation time is considerably increased. The developments in computing technology through the years has contributed to spread the use of FEM packages for electromagnetic an mechanical analyses, among others. Since the noise problem in electrical

machines is a consequence of the interaction between electromagnetic and mechanical forces, both packages need to be used together. In this way, Ishibashi et al. (1998) presented an algorithm to predict the shape of the vibration modes of a machine at no load, combining electromagnetic and mechanical FEM analyses. It was found that the vibration response of one mode depends on the mode of the nearby natural frequency, and not on the mode of the electromagnetic force wave.

The use of FEM is mainly limited to low frequencies, since the number of elements increases in a quadratic way. For higher frequencies, a new method suitable for calculations of noise and vibration in electrical machines was developed by Wang et al. (2002). The method was called statistical energy analysis (SEA), commonly used for ship and aircraft structures but not earlier applied to electrical machines. The main idea is to divide the whole structure into groups of components presenting similar modal energy storage and then estimate the vibration energy of each subsystem by solving the energy balance equations which relate the power flow from one subsystem to another. In the case of induction machines these structures correspond to those presenting similar modes of vibration.

Influence of the modulation strategies

The electromagnetic noise component acquired a great importance with the arrival of converters. Many research efforts were directed towards the manipulation of the switching pattern so as to mismatch between the new harmonics introduced in the currents and the resonant frequencies of the machine structure, which proved to be the cause of increasing noise in the new drives (Belmans et al., 1991). One of the most widespread modulation techniques is *pulse width modulation* (PWM), where the states of the switches are selected by comparing the actual value of the command signal, which is output from a regulator, with a constant frequency carrier wave. Increasing the switching frequency above the audible spectrum range (20 Hz - 20 kHz) would indeed reduce the noise perceived from the motor, but drawbacks appear in the converter instead. Switching faster involves an increase of the power lost in the switches as well as the amount of electromagnetic noise produced by the converter. In order to avoid these side effects, the switching frequency should be maintained between the range from 3 kHz up to 12 kHz, which is within the sensitive human hearing range. Increasing the switching frequency may also contribute

to the appearance of strong subharmonics, causing more single tones, which are perceived as highly disturbing by the human ear (Belmans and Hameyer, 1998). An alternative to PWM is *pulse frequency modulation* (PFM), where the frequency of the carrier wave is changed continuously in order to spread the harmonic components over the whole spectrum. The results obtained using this technique showed a better acoustical response compared to PWM, as described by Stemmler and Eilinger (1994). The frequency can be changed in a random fashion (Habetler and Deepakraj, 1991), (Covic and Boys, 1998), or among some predetermined values, selected in a way that they do not interact with any of the resonant frequencies of the motor (Garcia-Otero and Devaney, 1994), (Bologniani et al., 1999).

In the last decade new control strategies have been developed in order to achieve better performance in the drives. As a consequence, the switching pattern in the converter is modified, which in turn results in a different acoustical response. The noise emissions from a direct torque controlled (DTC) drive are analyzed by Xu et al. (2000). It was shown that DTC controlled drives have similar spread spectrum features as in the case of random PWM modulation, which is generally regarded as less irritating. However, the wideband of their harmonic spectra is more likely to induce mechanical resonances, which sometimes may lead to higher noise emissions. The noise level was found to increase with the load, although an optimal flux level for minimal noise was also found.

Noise reduction techniques

A means to reduce the noise by arranging the winding in the machine was presented by Hupe and Kennel (1989). Two inverters were used to drive a large induction machine equipped with two separate windings. The noise and the current ripple were reduced by triggering two PWM inverters with inverse pulses so that the switching frequency harmonic voltages are in antiphase. This method is only practical for very high power rating induction machine drives. For smaller motors a similar configuration was described by Chau et al. (2000) where an increase in the power and a reduction of the noise was achieved by purposely selecting the phase of the two carriers of the dual inverters, depending on the number of poles used for different machine operations.

The advantages of using magnetic bearings over conventional ones in order to reduce the noise emissions has been reported by Maliti (2000). Active noise control can also be applied for noise reduction in electrical machines (Belkhayat

et al., 1997). In order to suppress some magnetic noise components, it is possible to inject into the stator a number of current harmonics, and control their magnitudes and phases with their frequencies linked to the rotation speed. If one of the force waves has the same magnitude, frequency and mode number as the natural one but is in opposite phase, the two force waves will nullify and the corresponding magnetic noise will disappear. However, the process of active noise reduction is considerably expensive since it requires sensors and advanced control tools for real time processing.

Classical books treating different aspects of acoustic noise and vibration in electrical machines are published by Yang (1981) and Timar (1989).

9.2 Objectives and contributions

Although the acoustic influence of different modulation strategies such as DTC, PWM and PFM is available in the literature, there is a lack of studies treating the acoustic problem in vector controlled drives. Since the use of this control strategy is widely spread in electrical drives, therefore the importance of examining its noise emissions. Hence, the major objective of this part of the thesis is to investigate the mechanisms responsible for the noise emissions when the vector control strategy is used in induction motor drives. With this purpose, a digital drive system has been developed for a 2.2 kW induction motor, and this tool has been used for the experimental evaluation of the noise emissions when the flux and/or the torque are modulated with high frequency noise signals. The study does not take into consideration the harmonics introduced by the switching in the converter. These harmonics are moved outside the frequency range for the measurements, by using a 20 kHz switching frequency.

Another objective of this work is to develop a process for the prediction of the noise emissions of electromagnetic origin, by means of numerical simulations. In this way, the acoustic behaviour of a machine using a certain control strategy could be studied and optimized already at the design stage. The deterministic method is used for the noise prediction, where the electromagnetic forces are calculated using a model based on FEM. The vibration characteristics are determined using a structural model, also normally based on FEM. The results from these two models are combined into an acoustic model, based on BEM, where the radiated noise is calculated.

The nature of vector control links the modulation of the currents to a characteristic force distribution in the machine, where the influence of radial and

tangential forces may be weighted in order to develop suitable structural changes to reduce the noise emissions. A study of some structural changes in the conventional stator of an electrical machine has been conducted with this objective. In particular, the effect of introducing air gap layers around the outer part of the stator core in order to interfere with the natural transmission path of the vibrations has been analyzed.

9.3 Outline

The material in this part of the thesis is divided into seven chapters. In this Chapter, a general literature review dealing with relevant aspects of acoustic noise in electrical machines has been presented.

Chapter 10 deals with the practical implementation of the control system used for the experiments. Its dynamic capabilities are demonstrated inducing the machine to vibrate with high frequency music signals.

In Chapter 11 the results from the measurements are presented. Sound pressure and sound power measurements were conducted inside an anechoic chamber at no load and load. The sound power measurements were performed using the sound intensity measurement technique.

Chapter 12 presents an analytical computation of the airgap force in the machine. The method assumes ideal iron, and the slotting effects are included. The purpose of this study is to validate the electromagnetic FEM model used for the noise prediction.

Chapter 13 deals with the noise prediction process, based on numerical simulations using FEM and BEM. The available structural models are described first, followed by the electromagnetic and acoustic calculations. The results are compared to the measurements in Chapter 11.

Chapter 14 presents a study of the effect that peripheral air gaps in the stator core have in the overall acoustic emissions. The study was performed using FEM and BEM models and serves as a complement to previous experimental work using a similar concept.

Finally, in Chapter 15 a summary of the most important results and conclusions of this part of the thesis is presented. It also contains some suggestions for possible future work in this area.

Chapter 10

Control system

10.1 Introduction to Vector Control

Electrically driven industrial and household applications most often require the flexibility of adjusting the speed of the process depending on the demands. This is achieved by means of rapid changes in the shaft torque of the electrical machine incorporated in the drive. In the past, d.c. motors were used extensively in variable-speed drives since their flux and torque could be easily controlled by the field and armature currents respectively. However, the commutator and the brushes in a d.c. motor lead to additional maintenance costs. This is a major drawback compared with alternating current machines, which present the advantage of having smaller dimensions and therefore higher output ratings for low weight and low rotating mass. The developments in the fields of power electronics and computing capability in the past 20 years brought cheaper and more sophisticated converters and digital signal processors (DSP), which made possible the incorporation of a.c. motors into variable speed drives, where new control strategies could be implemented.

The conventional way of controlling the voltages fed into the motor from a frequency converter is to maintain constant the ratio between the amplitude of the voltage and its frequency, i.e. the flux in the machine. With these drives, more commonly known as 'v/f drives', the ratio of the supply frequency to the motor voltage can be increased in the converter, which also increases the slip. This in turn leads to a higher induced voltage in the rotor and subsequently to a larger rotor current. This process is to a large extent dictated by the large rotor time constant, which implies that rapid torque changes are difficult to

implement using a conventional controller.

In order to achieve better transient response, another control strategy known as 'vector control' was introduced. This theory is well reported in the literature (Vas, 1990), (Novotny and Lipo, 1996). The basic principle is that the alternating currents in the machine can be expressed as a rotating vector, and by controlling the amplitude and the phase of this vector, both the amplitude of the flux and the torque can be changed independently. Hence, the dynamics of the machine are set directly by controlling the currents, as in the case of the d.c. motor. However, in an a.c. machine the process is more complicated since not only the modulus of the current vector but also its phase has to be controlled. The control problem of an a.c. motor would then be reduced to the same case as for the d.c. motor if the current vector could be seen as stationary from a proper coordinate system.

The current vector rotates with the synchronous speed ω_s, and the flux in the machine rotates with the same frequency although 'delayed' in phase with respect to the current under a certain load. An observer that is oriented towards the flux vector will see a constant current vector, which can be expressed as a combination of two d.c. components, one pointing in the same direction as the flux vector and the other perpendicular to this direction, as shown in Figure 10.1.

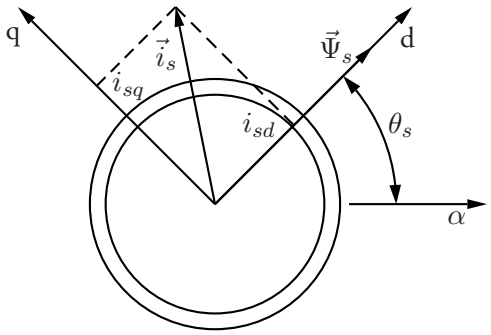

Figure 10.1: Stator flux oriented model.

Two different coordinate systems can be distinguished. On one hand the $\alpha\beta$ system which is stationary and is fixed to the stator structure of the motor. On the other hand the dq system, rotating with the speed ω_s, where the direct

axis d coincides with the stator flux vector (or the rotor flux vector, depending on the control strategy) and the quadrature axis q lies perpendicular to this vector. The stator current $\vec{i}_s$ has two components: i_{sd} along the d-axis, which is the magnetizing component of the current that controls the magnitude of the flux in the machine; and i_{sq} along the q-axis which controls the phase change and thus the speed of the flux vector. In most cases the direct current will be constant, except in the field weakening region. In general, the torque produced in any a.c. machine is expressed as in (10.1) (Krause, 1986).

$$T_e(t) = \frac{3p}{2K^2}\left[\psi_{sd}(t)i_{sq}(t) - \psi_{sq}(t)i_{sd}(t)\right] \tag{10.1}$$

In this equation, p represents the number of pole pairs and K is a scaling constant of the space vector. In an asynchronous machine ψ_{sq} is zero, while ψ_{sd} is maintained constant, so the torque can directly be controlled by changing i_{sq}. While in v/f drives the torque and flux response are coupled with each other, using vector control allows independent control of the currents governing the torque and the flux in an induction motor, and the transient response characteristics become similar to those of separately excited d.c. machines. In terms of control, the 'd.c.' nature of the direct and quadrature currents in an a.c. motor suggests some sort of similarity with the control of d.c. machines. In fact, i_{sd} and i_{sq} correspond to the field and the armature currents respectively in a d.c. motor, and the stationary field imposes a fixed current distribution in the rotor, as shown in Figure 10.2(a). A similar current distribution appears in the rotor of an induction motor under load, with the difference that this distribution is shifted continuously, driven by the time varying stator flux, see Figure 10.2(b). However, an observer placed in the rotating dq system will see a stationary distribution, as in the case of the d.c. motor. Under zero slip conditions, the rotor current is negligible in an induction motor, and only a direct axis current distribution will appear, as shown in Figure 10.3(a). When a load is applied, the slip increases and a quadrature current is induced in the rotor, which must be compensated by an additional stator current, as indicated in Figure 10.3(b), and the sum of the current from the rotor and the stator for the quadrature axis is ideally zero. The resultant current distribution in the stator winding is found by the superposition of the direct and quadrature current distributions. In order to change the torque, the instantaneous three phase currents are changed so that a certain quadrature current is produced, while the direct current remains unchanged. In case that a transient error appears in i_{sd}, that will not result in

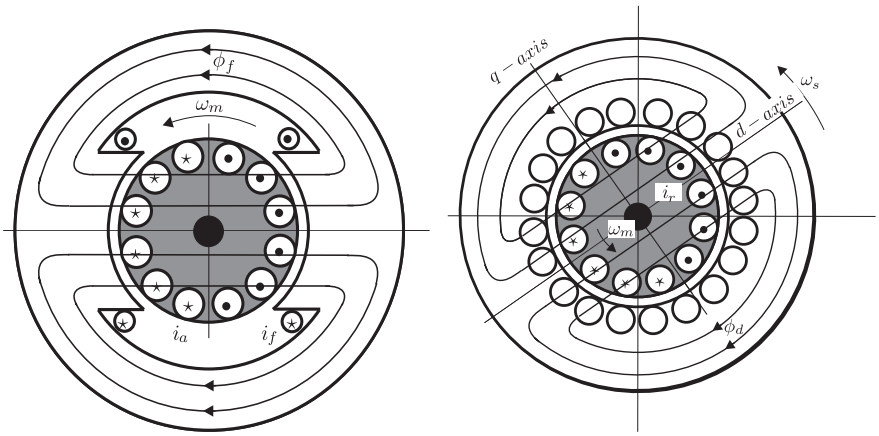

(a) D.C. motor (b) Induction motor

Figure 10.2: D.C. and Induction motor structures.

any significant flux transient, since the flux dynamics are slow. This decoupled response between flux and torque control constitutes the main advantage of vector controlled drives compared to v/f drives, improving the response under transient conditions. However, the behaviour of both drives should be similar under steady state operation. Vector drives are most frequently used with a speed control loop where the torque reference is continually adjusted, in what could be defined as a quasi-continuous transient operation. The advantages of vector control both in ease of control and faster transient response have increased the range of applications where vector drives are being used. As a result of this market trend, the implications of using this type of drive in terms of acoustic noise emissions must be therefore examined.

10.2 Noise emissions in vector controlled drives

The electromagnetic noise emissions in an electrical machine are directly determined by the harmonic content of the relevant forces in the airgap of the machine, where the electro-mechanic energy conversion takes place. Every structure tends to vibrate at certain frequencies, called *resonance frequencies*, with a

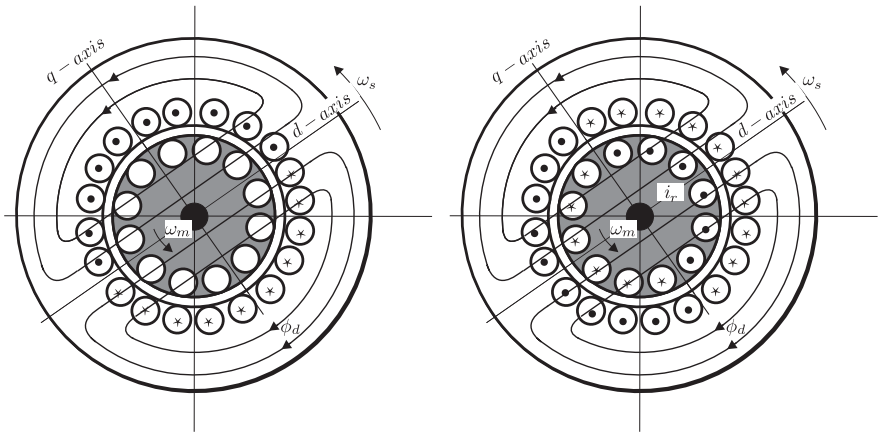

(a) Direct axis current distribution.

(b) Quadrature axis current distribution.

Figure 10.3: Field oriented current distributions in the induction motor.

characteristic deformation, called *mode of vibration*. When the frequency of one harmonic in the airgap force coincides with one of the resonance frequencies of the machine, it vibrates with that frequency in a certain fashion producing noise. The noise emissions at other frequencies depend on their proximity to a resonance frequency and their damping.

The harmonic content of the airgap forces is directly determined by the harmonics present in the motor currents as well as other construction factors such as the effects of the slots, eccentricity, etc. It is not the aim of this work to analyze the influence of the harmonics introduced by the converter or the different construction parameters. Instead, the objective is to experimentally determine how the motor responds acoustically to different current excitations of the direct and/or quadrature currents using vector control, and verify these measurements with the aid of computational tools. The direct current (d-current) controls the flux, and is responsible for the radial forces, while the quadrature current (q-current) controls the torque, and is responsible for the tangential forces. Therefore, apart from measuring the difference in the motor acoustic behaviour when the flux and/or the torque are modulated, the study would

provide information about the role that radial and tangential forces play in the overall acoustic emissions of small electrical machines.

The desired excitation can be achieved by adding to the reference direct and/or quadrature currents an external a.c. signal, that could be a sine wave with a certain amplitude and with a frequency corresponding to one of the resonance frequencies of the stator. The flux is modulated by adding a noise harmonic d_{mod} to the reference for the direct current, as shown in Figure 10.4(a). The amplitude of the current vector will vary in a sinusoidal fashion along the direction of the flux, providing that the quadrature current is set to zero, and therefore exciting the stator with radial forces. The torque is modulated by adding the noise harmonic q_{mod} to the reference for the quadrature current, as shown in Figure 10.4(b). This reference is either zero, at no load, or the corresponding load current. The harmonic q_{mod} will produce a phase shift of the flux vector, which will excite the stator with tangential forces.

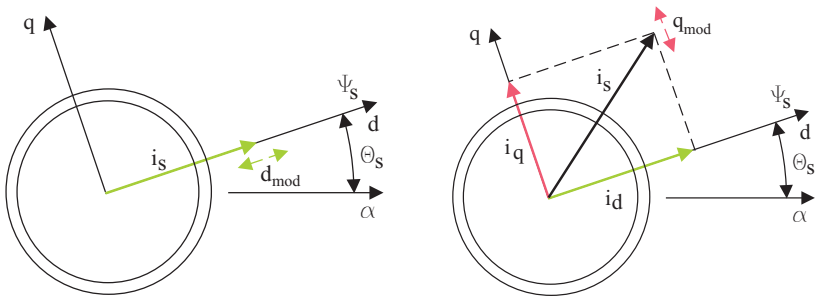

(a) Direct current modulation (b) Quadrature current modulation

Figure 10.4: Modulation of the direct and quadrature currents.

Figure 10.5 illustrates how the stator is excited and the force pattern in the air gap when modulating the torque and the flux. The oval shape corresponds to the force distribution around the airgap for a given current. When only the flux is modulated, the oval shape will shrink and expand in the radial direction. When only the torque is modulated the oval shape will be rotated around the center of the machine, while keeping its amplitude.

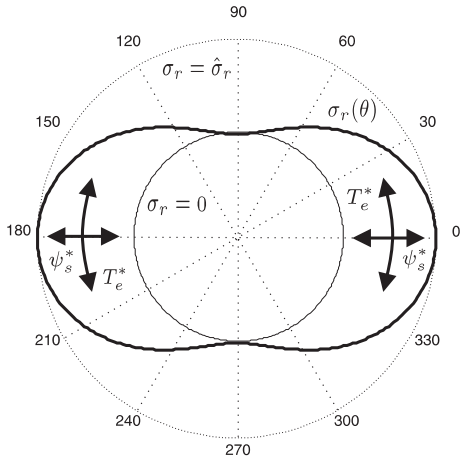

Figure 10.5: Airgap stress distribution and stator excitation for flux and torque modulation.

10.3 Stator flux control

The electrical behaviour of an asynchronous motor can be simplified in terms of an electrical circuit and there are namely two ways of representing the equivalent diagram of an induction motor, depending on the number of parameters taken into account. The five parameter model is presented in Figure 10.6, where the steady state value R_r/s has been replaced by the rotor resistance in series with a voltage source which corresponds to the back EMF. In the equivalent four parameter model the rotor and stator leakage inductances are grouped together in the stator side, as shown in Figure 10.7.

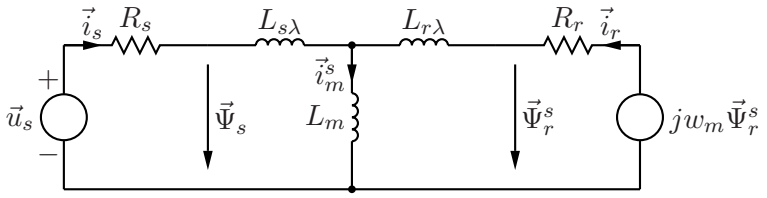

Figure 10.6: Five parameter model.

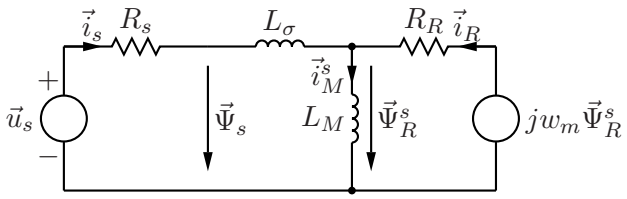

Figure 10.7: Four parameter model.

The parameters in both models are related in the following way:

$$R_R = \left(\frac{L_m}{L_r}\right)^2 \cdot R_r \tag{10.2}$$

$$L_M = \frac{L_m^2}{L_r} \tag{10.3}$$

$$L_\sigma = \sigma L_s \tag{10.4}$$

$$\sigma = 1 - \frac{L_m^2}{L_s L_r} \tag{10.5}$$

The four parameter model will be used to implement the control system and to model the machine. For the control system, it can be assumed that either the rotor or the stator flux vector coincides with the direction of the direct axis. Since measuring the stator currents and estimating the stator flux is more convenient than the rotor flux and currents, the stator flux model represented in Figure 10.1 will be followed. In the stationary $\alpha\beta$ coordinate system the stator voltage can be written in vector form as in (10.6).

$$\vec{u}_s^{\alpha\beta}(t) = R_s\vec{i}_s^{\alpha\beta}(t) + \frac{d\vec{\psi}_s^{\alpha\beta}(t)}{dt} \tag{10.6}$$

This equation can be transformed into the synchronous dq reference frame where the direct axis is aligned with the stator flux vector, which sets the speed of rotation ω_s. The rotor will rotate with the electrical speed ω_m and the slip frequency becomes $\omega_{sl} = \omega_s - \omega_m$. The stator voltage in synchronous coordinates is expressed as in (10.7).

$$\vec{u}_s^{dq}(t) = R_s\vec{i}_s^{dq}(t) + \frac{d\vec{\psi}_s^{dq}(t)}{dt} + j\omega_s\vec{\psi}_s^{dq}(t) \tag{10.7}$$

The voltage can be separated into its direct and quadrature components, introducing that $\psi_{sq} = 0$ and $\psi_{sd} = \psi_s$ for the coordinate system selected, as in (10.8) and (10.9) respectively.

$$u_{sd}(t) = R_s i_{sd}(t) + \frac{d\psi_s(t)}{dt} \tag{10.8}$$

$$u_{sq}(t) = R_s i_{sq}(t) + \omega_s \psi_s(t) \tag{10.9}$$

Based on these equations, the direct and quadrature current controllers can be deduced separately, following the strategy of 'predictive dead beat control' (Alaküla, 2002). The detailed deduction of these controllers is included in Appendix E. It is shown that the controller for the direct current is given by (10.10). This corresponds to a PI controller with a proportional gain equal to $L_M + \frac{R_s T_s}{2}$ and an integral gain equal to $R_s T_s$, where T_s is the sampling time. The reference signals are denoted by the superscript '*'. The actual value of the direct current is obtained from the flux level in the machine, which is difficult to measure. As an alternative, this flux can be estimated as will be described later in this chapter.

$$\begin{aligned} T_s u^*_{sd}(t_k) = R_s T_s \sum_{j=0}^{j=k-1} [i^*_{sd}(t_j) - i_{sd}(t_j)] + \\ + \left(L_M + \frac{R_s T_s}{2} \right) [i^*_{sd}(t_k) - i_{sd}(t_k)] \end{aligned} \tag{10.10}$$

The controller for the quadrature current can also be implemented as a PI controller (10.11). Now the proportional and integral gains are equal to $L_\sigma + \left(R_s + \frac{R_R L_s}{L_M} \right) \frac{T_s}{2}$ and $\left(R_s + \frac{R_R L_s}{L_M} \right) T_s$, respectively. There is also a feed forward term $\omega_m(t_k)\psi_s(t_k)T_s$ which depends on the speed of the machine. This controller assumes as an input the reference value of the quadrature current, which can be easily obtained from the torque equation in (10.12), where only the flux has to be estimated as in the case of the direct controller.

$$\begin{aligned} T_s u^*_{sq}(t_k) = \left(R_s + \frac{R_R L_s}{L_M} \right) T_s \sum_{j=0}^{j=k-1} \left[i^*_{sq}(t_j) - i_{sq}(t_j) \right] + \\ + \left[L_\sigma + \left(R_s + \frac{R_R L_s}{L_M} \right) \frac{T_s}{2} \right] \left[i^*_{sq}(t_k) - i_{sq}(t_k) \right] + \\ + \omega_m(t_k)\psi_s(t_k)T_s \end{aligned} \tag{10.11}$$

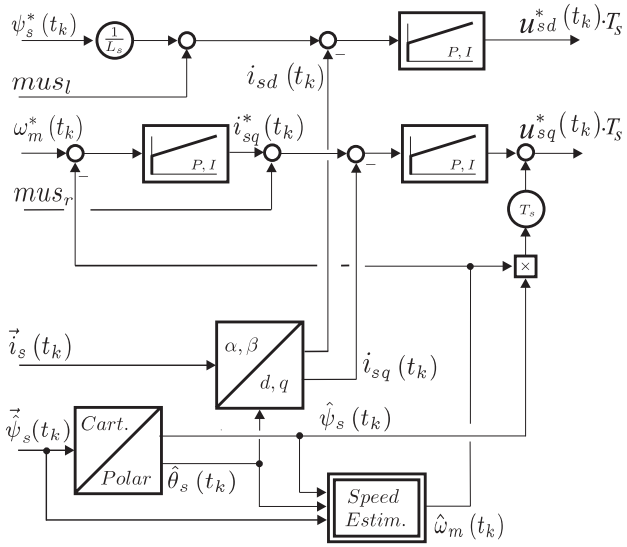

Figure 10.8: Controller structure.

$$i_{sq}^*(t_k) = \frac{T_e^*(t_k)}{\psi_s(t_k)} \tag{10.12}$$

10.4 Implementation

The complete controller structure is presented in Figure 10.8. The set point value for the direct current results from the addition of two signals: the magnetizing current, obtained as the reference flux divided by the stator inductance, and an external noise signal defined as mus_l. The reference value for the quadrature current is set by a speed controller, and another noise signal mus_r is added. The signals mus_l and mus_r correspond in fact to d_{mod} and q_{mod}. In this chapter the experiments will be performed with music signals, therefore the denomination. The measured three phase currents in the motor are input into the controller in stationary coordinates and then transformed to the synchronous frame. This transformation is achieved by estimating the angle of rotation $\hat{\theta}_s$ from the flux vector using the relation in (10.13).

$$|\psi_s| = \sqrt{\psi_{s\alpha}^2 + \psi_{s\beta}^2} \qquad \cos\hat{\theta}_s = \frac{\psi_{s\alpha}}{|\psi_s|} \qquad \sin\hat{\theta}_s = \frac{\psi_{s\beta}}{|\psi_s|} \tag{10.13}$$

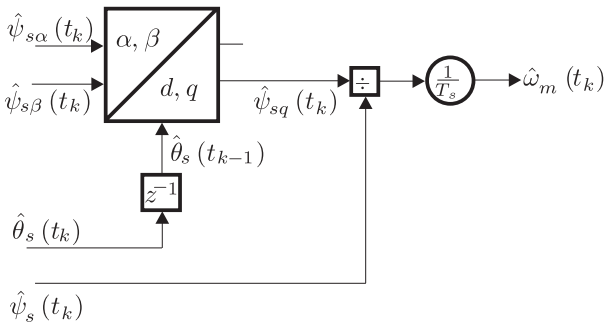

Figure 10.9: Speed observer.

The noise signals can contain passages with a d.c. offset, which added to the quadrature current component will cause the rotor to accelerate since a non zero average torque will be produced. This phenomenon is avoided with the speed control loop, where the actual speed is estimated from the flux vector, as shown in Figure 10.9. The speed of rotation of the flux vector is approximated as the rate of change of the quadrature component of the flux during one sampling interval with respect to its modulus. Figure 10.10 shows the path followed by the flux vector between two consecutive samples. At time t_{k-1} the synchronous frame is rotated so that the direct axis d_{k-1} is aligned with the position of the flux sampled at that time, $\vec{\psi}_{k-1}$. The flux vector will continue rotating but its actual position will not be read until the next sample at time t_k, when the synchronous frame is again rotated so that the new direct axis d_k coincides with the new sampled flux $\vec{\psi}_k$. An observer placed in the old synchronous frame $(d/q)_{k-1}$ will see that the flux vector was rotated by an additional quadrature component ψ_{qk}. The flux at time t_k can be expressed in the old coordinate system as the sum of a direct component $|\vec{\psi}_{k-1}| \equiv |\vec{\psi}_k|$, and a quadrature component ψ_{qk}. The angle of rotation between the two samples is approximated as in (10.14).

$$\delta = \theta_k - \theta_{k-1} = \frac{\psi_{qk}}{|\vec{\psi}_k|} \tag{10.14}$$

The speed of rotation of the flux vector is calculated as the derivative of δ, which in a sampled system can be approximated as $\frac{\delta}{T_s}$, where T_s is the sampling

time. This is actually the process described in Figure 10.9, where the quadrature component of the flux is obtained using in the transformation the angle corresponding to the old synchronous frame, which is easily stored working in a digital system.

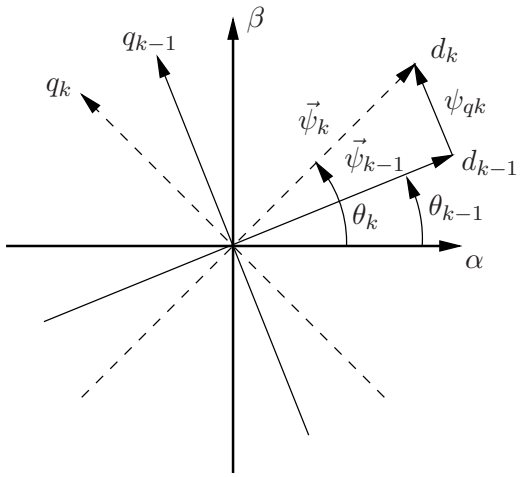

Figure 10.10: Flux vector path.

The flux is estimated by substituting the stator current $\vec{i}_s^{\alpha\beta} \simeq \frac{\vec{\psi}_s^{\alpha\beta}}{Ls}$ into the stator equation (10.6), leading to the expression of a low pass filter in (10.15). The three phase voltages are transformed into the stationary frame and (10.15) is implemented in an analog circuit as shown in Figure 10.11.

$$\vec{u}_s^{\alpha\beta} = \frac{R_s}{L_s}\vec{\psi}_s^{\alpha\beta} + \frac{d\vec{\psi}_s^{\alpha\beta}}{dt} \tag{10.15}$$

The control system and the process were implemented in SIMULINK, and the overall structure is presented in Figure 10.12. The voltage time area output from the controller in stationary coordinates is transformed into three phases which are symmetrized in order to increase the modulation depth of the drive, by centring the reference voltages with respect to the bus voltage window (Holmes, 1997). The switches in the converter are controlled by the modulator, where regularly sampled sine-triangle modulation is used. Since the model

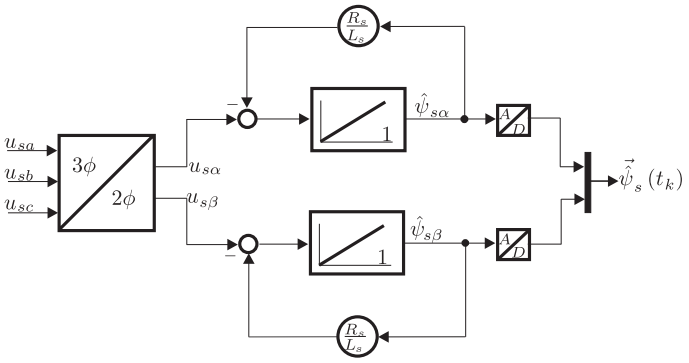

Figure 10.11: Flux observer.

of the induction motor is based on the stator and rotor equations in stationary coordinates, the three phase voltages output from the converter have to be transformed back to stationary coordinates in the simulation. From the motor model, the measured current is fed back to the controller, and from the applied voltage the flux and the speed are estimated in the observer. The external noise signals for the direct and the quadrature current are the controller inputs mus_l and mus_r respectively.

10.5 Musical drive test

An indication of the torque response to a given music sequence was obtained from the simulated results using the structure showed in Figure 10.12. In this case the audio signal is fed into the torque modulation input mus_r, while mus_l is set to zero. The input signal and simulated torque response are given in figures 10.13(a) and 10.13(b). The results provide an overall indication in terms of the ability of the motor torque to track the sound signal, which is quite acceptable.

The performance of the drive has also been experimentally tested. The drive developed consists of a commercial inverter which was re-fitted with a new controller and pulse width modulation boards. The control, vector transformation and symmetrization modules from Figure 10.12 are implemented in software and reside on a dedicated DSP board. The modulator unit, which has a carrier frequency of 19.582 kHz, produces regularly symmetrically sampled PWM sig-

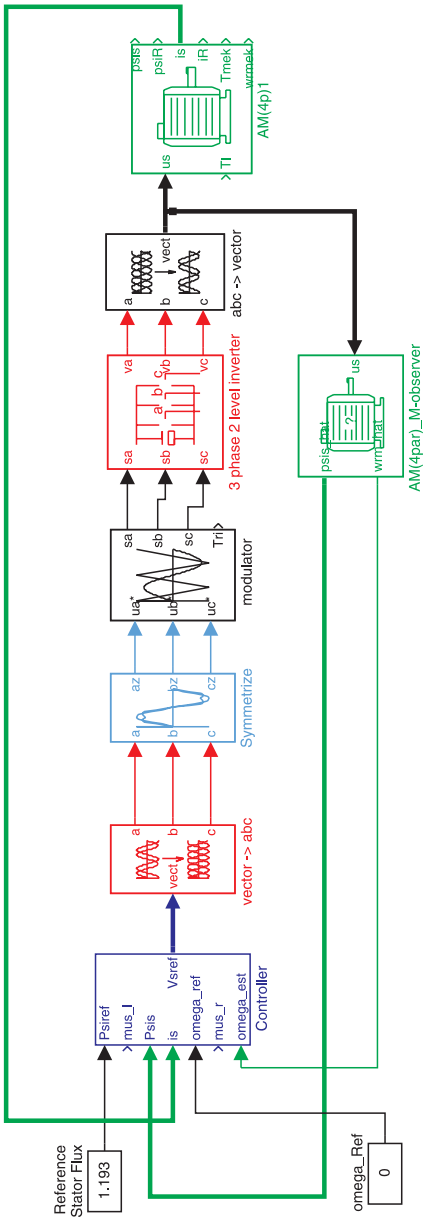

Figure 10.12: Structure of the drive system.

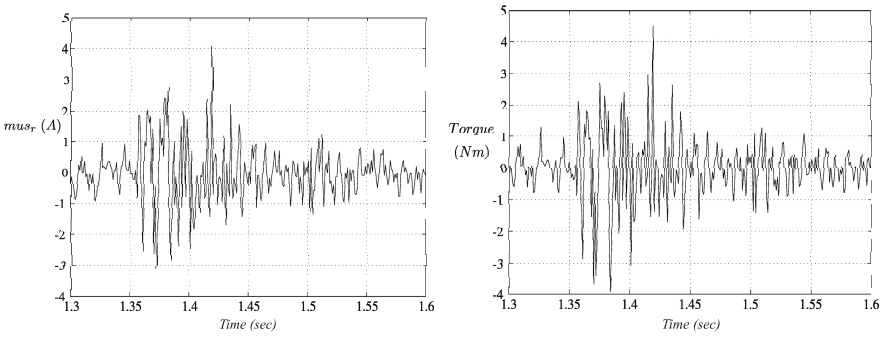

(a) Music input sequence

(b) Torque response

Figure 10.13: Music input and torque response for $mus_r(t)$, $mus_l = 0$.

nals which are connected to the IGBT modules in the converter. A 2.2 kW two pole asynchronous motor was used, which was not connected to any external load. The line currents and the motor voltage are measured and used by the controller and the combined speed/stator flux estimator respectively. The drive was tested by providing either one or both channels of a stereo input amplifier to the drive. As predicted by the simulation, the torque and/or flux ripple followed the musical torque and/or flux reference up to high input frequencies, which is possible using a switching frequency in the modulator of almost 20 kHz. This ripple induces vibrations in the motor structure with the frequency of the music and the machine behaves as a loudspeaker. If the motor is placed on a surface the vibration from the motor structure will be transferred to that surface and further sound amplification will be obtained. Interesting is also to compare the different music quality that was obtained from different surfaces, being the most suitable a wooden box, which best resembles the commercial loudspeakers. When only the torque was modulated, a listener could perceive more low frequency components in the music emitted, whereas the high frequency passages were more accentuated when pure flux modulation was used. As a consequence, the music quality as perceived by the listener was found to be at its 'best' when both flux and torque inputs were used simultaneously. An indication of the audio sound capabilities from this setup was achieved by mea-

suring the 'A' weighted sound power over the audio frequency range. In this case only the audio input mus_r (which modulates the torque reference) was connected to a sinusoidal voltage source whereby the frequency was varied from 200 Hz to 10 kHz. The obtained results, measured in a reverberating room, are shown in Figure 10.14. Included in this figure, by way of reference, is a loudspeaker transfer function. These results indicate that the drive sound levels at opposing ends of the frequency band are lower than those obtained from the loudspeaker. The low frequency sound level fall off is caused by the radiation efficiency of the motor, i.e. the sound radiation efficiency is reduced at lower frequencies (Wang et al., 2002). The high frequency fall off is due to the bandwidth of the current control loop. For a fixed PWM frequency, the number of carrier wave pulses in each period decreases for an increasing frequency of the reference signal and the resolution is then affected by this factor. Also, readily apparent from Figure 10.14 are two motor resonance peaks found near the frequencies 1.3 kHz and 2.7 kHz. It should be pointed out that the machine used for the musical drive presented in this chapter is not the same as the machine used for the experiments in Chapter 11.

10.6 Conclusions

Vector control provides faster transient response compared to conventional v/f drives, and this is achieved by an efficient decoupling of the currents controlling the flux and the torque in the machine. These currents are easily controlled since they are regarded as d.c. components from a rotating coordinate system linked to the stator flux vector. A simulation program including the control system and simplified models for the power electronics, motor and observers has been presented. The control system has been implemented in a DSP card, which in turn is connected to a PWM card where the switching frequency was set to 20 kHz. The performance of the drive was tested by modulating music signals as noise references added to the direct and the quadrature currents. The motor structure resembled the behaviour of the core of a loudspeaker, reproducing efficiently the noise signals. The musical motor application served to demonstrate the capabilities of vector controlled drives implemented in advanced digital systems, leading to a suitable tool for acoustic research in electrical machines. This tool will be used in this thesis to analyze more in detail the acoustic radiation from a similar size induction motor using different combinations of direct and quadrature current excitation at key frequencies, so as to ascertain the mechanisms of

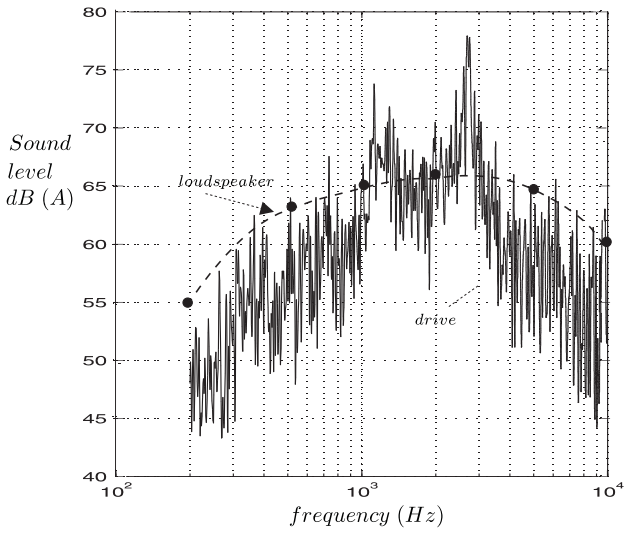

Figure 10.14: Measured sound power of the 'musical' drive for $mus_r(t)$, $mus_l = 0$.

noise production in small electrical machines.

Chapter 11

Acoustic measurements

11.1 Introduction

In this chapter the results of the sound pressure and sound power measurements are presented for different excitations of the direct current (radial force) and the quadrature current (tangential force). The measurements were carried out both at no load and load conditions in an anechoic chamber. Sound measurement techniques have been well reported in the literature (Norton, 1989), (Harris, 1991), and a summary of the most commonly used techniques is presented in Appendix F, together with some basic acoustic terminology. Since the sound intensity measurement technique was used for the experiments, it is described before dealing with the experimental set-up and results.

11.2 Sound intensity measurement technique

Traditionally, the only way of measuring how much sound power a machine radiates was to place the machine in an anechoic or reverberation room and measure the sound pressure, which is related to sound power depending on the nature of the room. However the sound power can also be determined by means of sound intensity measurements (Fahy, 1995), where the power level is measured directly in situ. Sound intensity measurement systems became available in the middle of the 1980's, and practical applications of the technique have since increased at a very fast pace.

The intensity at one point is expressed as the product of the pressure and the particle velocity at that point and is related to the sound power as shown in

(11.1) (Brüel & Kjær, 1986).

$$I = p\vec{u} = \frac{Force}{Area} \cdot \frac{Distance}{Time} = \frac{Energy}{Area \cdot Time} = \frac{Power}{Area} \tag{11.1}$$

Sound intensity measurements are conducted by placing the noise source of interest inside an imaginary surface enclosing the sound source. For simplicity, the enclosure is usually selected to be a rectangular frame. The average intensity flowing through each surface is measured with a sound intensity probe, and the information is stored in a spectrum analyzer. Multiplying this intensity by the area of the surface gives directly the power. The total sound power radiated by the source is calculated by adding the contributions from all the surfaces.

The advantage of this technique is that the measurements can be performed in situ, even with steady background noise and in the near field of machines. The requirement is that no other noise source apart from the one subject to study must be located inside the enclosure. An external noise source will not produce any net contribution to the calculated intensity, since the energy will flow in and out of the enclosure and its overall effect will cancel when the power contributions of the different sides are added. It is important to note that this only holds if the external source is stationary, i.e. its noise does not vary in time, and if there is no absorption material within the box as otherwise some background noise will not flow out of the box again.

Sound pressure can be measured with a single microphone, but particle velocity is more complicated. The equation governing the motion of the fluid particles is the Navier-Stokes equation. Neglecting viscous effects and in the absence of mean flow and turbulence it can be expressed as in (11.2), where r represents the direction of the flow.

$$\rho \frac{\delta u_r}{\delta t} = -\frac{\delta p}{\delta r} \tag{11.2}$$

This equation can be re-written using finite-difference as in (11.3).

$$u_r = -\frac{1}{\rho \Delta r} \int (p_B - p_A) dt \tag{11.3}$$

Hence, the particle velocity can be determined by measuring the pressures p_A and p_B detected by two microphones closely spaced at a distance Δr, as shown in Figure 11.1.

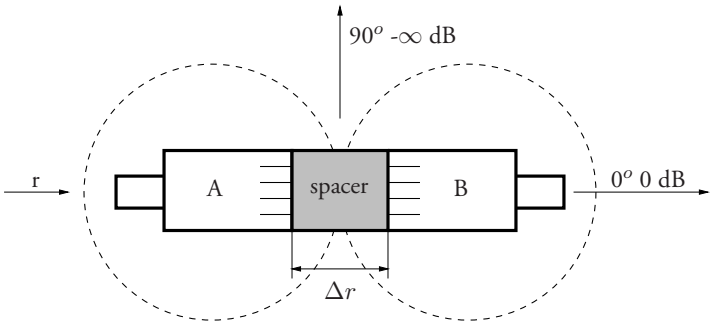

Figure 11.1: Sound intensity microphone and dipole characteristic.

Sound pressure is a scalar quantity, i.e. it is the same whatever the angle of incidence. However, sound intensity is a vector quantity. When a two-microphone probe is used, only the component of the vector along one direction, the probe axis, is measured. The dashed circumferences in Figure 11.1 show an approximation to the dipole behaviour of the sound intensity probe. For sound incident at 90^o from the axis there is no component along the probe's axis, as there will be no difference in the pressure signals from the two microphones. Hence, the reduction in the measured intensity level (in dB) will be infinite because the particle velocity, and hence the intensity is zero. For sound incident at 0^o, there will be zero reduction and the probe will measure the correct value. For sound incident at any other arbitrary angle θ from the axis, the intensity component along the axis will be reduced by a factor of $\cos\theta$.

The choice of spacer depends on the frequency range to be covered, the higher the frequency the shorter the spacer should be for the finite-difference approximation in (11.3) to hold. However, accuracy at low frequencies also depends on the spacer used. In all analyzing systems there will be a small time delay between the two channels which introduces a small phase change, influencing the results. This is a bias error called *phase mismatch error*. For a given probe and analyzer combination, this error can be estimated to be around $\pm$ 0.3^o (Brüel & Kjær, 1986). For an accuracy to within 1 dB the phase change over the spacer distance should be more than five times the phase mismatch. In order to obtain a negligible high frequency error, the wavelength must be at least six times the spacer distance. Thus, for a given spacer the inherent phase mismatch of the equipment will cause a significant error in the measured inten-

sity at low frequencies. Since no single spacer can cover a wide frequency range, the spacer should be selected depending on the frequencies of interest.

When the sound is incident at an angle θ from the probe's axis, the phase change that is detected is reduced by $\cos(\theta)$, and this will imply that the phase mismatch error will become more significant and the measurement range will be further reduced. One indicator of the accuracy of sound intensity measurements is the *pressure-intensity index*, L_K, which is measured simply as the difference between the measured sound pressure level and the measured sound intensity level (Fahy, 1995). By measuring the pressure-intensity index the phase change across the spacer can be determined, and the influence of the phase mismatch in the accuracy of the results can be calculated. In a general sound field, the phase change varies from point to point, but an average global value is often sufficient to give an idea of the accuracy. In an ideal free field, the difference between the sound pressure and sound intensity levels is zero. However, the phase mismatch causes a small difference between the two signals, as if there were some intensity along the spacer. Hence, apart from the errors introduced by the operator during the measurements, which are reported through the pressure-intensity index, there is another source of error inherent to the equipment that cannot be further reduced, and it is called the *residual pressure-intensity index*, L_{KO}. This index can be determined by using calibrating equipment to feed the same signal to the two microphones and measuring the difference between the sound pressure level and the sound intensity level. The dynamic capability L_D of the sound intensity measuring system is defined in (11.4).

$$L_D = L_{K0} - K \tag{11.4}$$

The measured pressure-intensity index L_K should be less than the dynamic capability for an acceptable accuracy in the measurements. For an accuracy to within 1 dB, the constant K is equal to 7 dB, which corresponds to a phase change in degrees along the spacer distance of five times the phase mismatch.

11.3 Experimental set-up and instrumentation

The machine used in the experiments is a three-phase four-pole 415 V 50 Hz 2.2 kW, three phase, induction motor, with 36 and 44 stator and rotor slots respectively, see Figure 11.2. The casing diameter is 163 mm, the total length 278 mm, and the lamination stack 92 mm. This machine was used in purpose

since there was detailed information available about its vibrational behaviour (Wang and Lai, 1999).

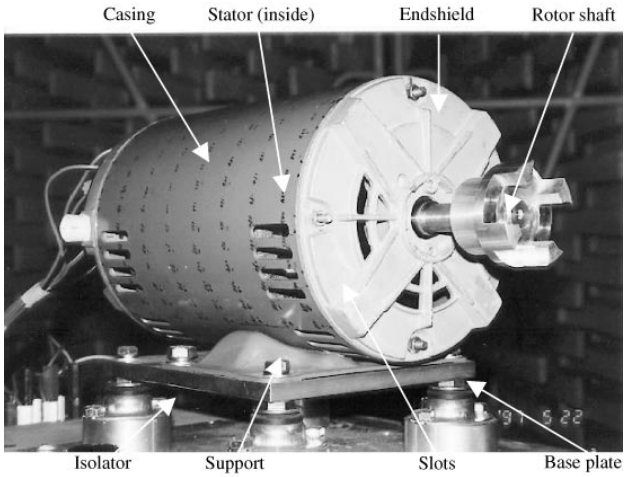

Figure 11.2: The test motor. Source (Wang and Lai, 1999).

The internal dimensions of the anechoic room used for the measurements are 3.5 m x 3.5 m x 3.5 m, and the cut-off frequency is 150 Hz. The motor was mounted on a bench in the center of the room, and the seat was attached to an aluminium plate through the four isolators. This plate was softly connected to another 10 mm thick aluminium plate inserted between the test motor and the load, as shown in Figure 11.3, in order to minimize the noise contribution from the load motor during the measurements.

The equipment for running the machines was placed outside the anechoic room, see Figure 11.4. The load motor was fed by a commercial inverter with a fixed switching frequency of 8 kHz. The test motor was driven from another converter connected to a control system module. This module contained hardware for the estimation of the flux from the three phase measured voltage, the measurement of the currents and the scaling of the d.c. link voltage in the converter. These signals were fed into a DSP card, which had 16 analog inputs, and a 50 pin connector cable was used for the connection between the DSP and PWM cards. The switching frequency set by the modulator was 20 kHz. The

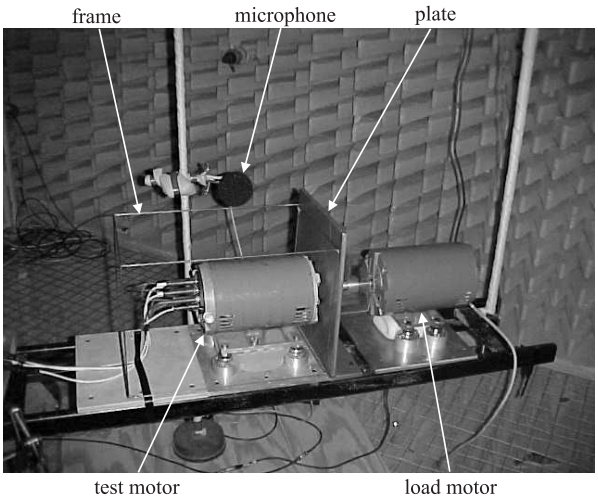

Figure 11.3: Experimental set-up inside the anechoic room.

reference values for the direct and the quadrature main currents in the DSP were adjusted with two potentiometers, and the added noise currents were provided by two separate signal generators.

For the sound pressure level measurements a B&K type 4134 microphone was used, fed from a B&K type 2804 power supply. The signal from the microphone was amplified using a B&K type 2639 amplifier and thereafter sent to the analyzer. The microphone was calibrated using a B&K type 4220 pistonphone, taking into consideration the corrections that should be applied depending on the temperature and pressure measured inside the anechoic chamber. The acoustical response of the motor to random noise excitation in the range from 0 Hz to 10 kHz was tested using the white noise signal from a separate B&K type 4205 sound power source. The microphone used for the measurements was connected to a Hewlett Packard (HP) 3569-A real time frequency analyzer, where the spectrum of the measured noise was stored for further post-processing.

The noise components added from the signal generators have the same frequency, and different amplitude combinations are selected for the direct and quadrature currents. The maximum amplitude of the added noise current is

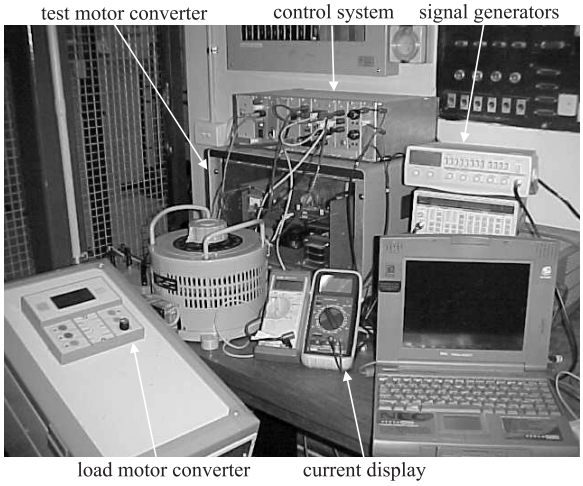

Figure 11.4: Experimental set-up for the control equipment.

referred to as '2m', and its value was determined taking into consideration the saturation limits in the machine. The mean value of the direct current was reduced so that, when the noise current was added, the maximum value of the resultant waveform did not exceed the nominal value of the direct current, see Figure 11.5. The effective magnetizing current in the motor was 2.21 A, which when using the power invariant transformation gives a peak direct current of 3.82 A. The maximum amplitude of the noise excitation ('2m') was selected to be 0.5 A, and subtracting this value from the peak current gives a mean value of the direct current corresponding to 87% of the nominal. Two other values were used for the noise current, corresponding to half and one quarter of the maximum, i.e. 0.25 A and 0.125 A, and they are referred to as 'm' and 'm/2' respectively. When the machine was loaded, the effective quadrature component of the main current was 3.6 A, which corresponded to a peak value of 6.23 A. This current was reduced to 5.7 A in order to avoid exceeding the nominal value when the noise current was added, in the same way as it was done with the direct excitation. Thus all the load tests were conducted at 92% of the rated load.

The values of the total direct and quadrature currents calculated in the DSP were available at its analog outputs. Two multimeters were used to measure their

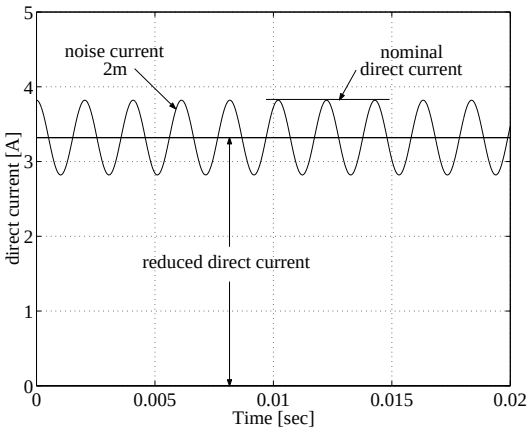

Figure 11.5: Modulation of the direct current.

d.c. components, and an ONO SOKKI CF-350 real time spectrum analyzer was used to check their frequency content. A 'Hanning' window was used and the spectrum was averaged from 256 samples with 50% overlap each time the currents had to be adjusted for the measurements. As expected, it was observed that the current spectrum was completely flat except at the frequency set with the signal generators.

For the sound intensity measurements, a HP 35230-A two microphone sound intensity probe was used, equipped with two 0.5 inch condenser microphones of the type HP 35237-A. The spacer used was 12 mm long, covering 1/3 octave center frequencies from 125 Hz up to 5 kHz. The measurements were performed according to ISO 9614-2 (ISO 9614-2, 1996), which is a draft international standard for measurement of sound power via surface scanning of sound intensity. One requirement is to measure the residual pressure-intensity index for the entire measurement system. This value is directly related to the dynamic capability L_D, by subtracting 7 dB, and should be compared to the pressure-intensity index obtained from the measurements. If the pressure-intensity index is greater than L_D in any 1/1 or 1/3-octave band, the sound power measurement is inadequate in that band. The residual pressure-intensity index of the measurement system was determined using a B&K ZI0055 pistonphone mounted on a B&K UA0914 sound intensity calibrator, and it is shown

in Figure 11.6.

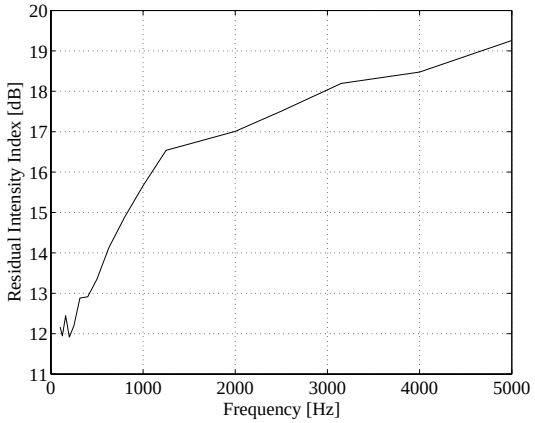

Figure 11.6: Measured residual pressure-intensity index.

Sound pressure as well as sound intensity measurements were conducted in order to assess the sound pressure level (SPL, L_p) and the sound power level (PWL, L_W) from the machine. All the measurements were conducted with the motor placed inside the anechoic chamber. The sound pressure measurements were carried out first with the machine at stand still, at four different positions. The response was measured for two different excitation frequencies, 490 Hz and 1105 Hz. These frequencies correspond to two of the resonance frequencies of the stator-casing coupling measured experimentally in (Wang and Lai, 1999). Various combinations in the amplitude of the direct (D) and quadrature (Q) noise current components were selected as shown in Figure 11.7. The case when white noise is used is referred to as 'wn'. The same experiments were conducted with the machine rotating at 70 r.p.m. This low speed was selected in order to minimize the effects of the aerodynamic and the mechanical noise. The sound intensity measurements require considerably more effort, and a smaller number of combinations were tested, as shown in Figure 11.8. At load, the same experiments as at no load were conducted, with the exception of the stand still tests.

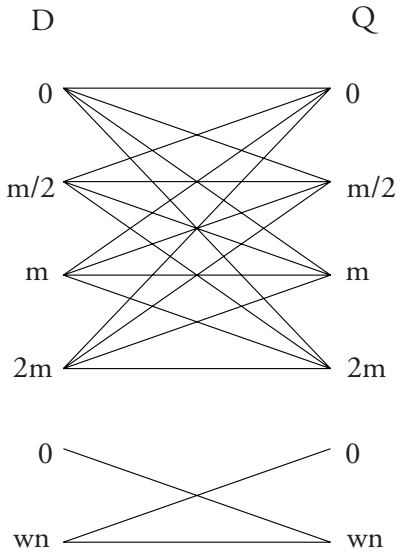

Figure 11.7: Diagram of combinations tested with SPL measurements.

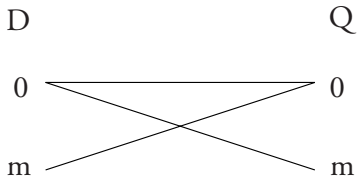

Figure 11.8: Diagram of combinations tested with PWL measurements.

11.4 No load tests results and analysis

Sound pressure tests at stand still and no load.

The measurements were conducted with the rotor fixed at four different positions, spaced 90 degrees between each other. In order to accurately determine the position of the rotor, a mechanical system was attached to the shaft and fixed to the test frame, as shown in Figure 11.9. Four holes were drilled around the wheel attached to the shaft, and by coupling them with the bar resting on the test frame the rotor was rotated to the desired position.

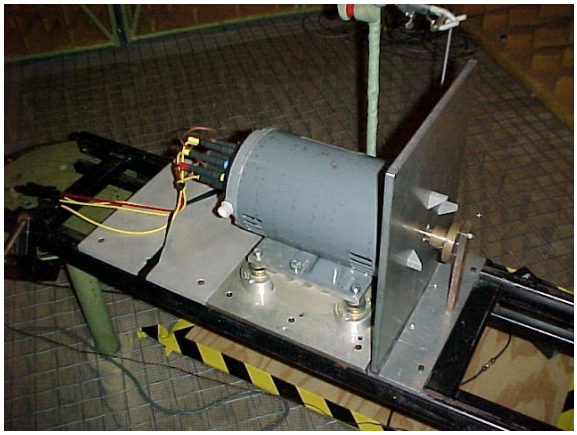

Figure 11.9: Set-up for the stand still tests.

The SPL was measured with a single microphone placed inside the anechoic chamber. The microphone was positioned at half the length of the machine, and the distance to the closest point at the top of the machine was 337 mm in the horizontal direction and 54 mm in the vertical direction. The resolution for the narrow band analysis in the spectrum analyser was 1600 lines in a range from 0 Hz to 6.4 kHz. These results were post-processed in order to obtain a single representative value for each measurement, which would serve as a basis for their comparison. This was achieved by adding the values at the 1600 point frequencies from the spectrum, using (F.2), where L_p is the total SPL and L_{pi} is the SPL at each frequency i.

Figure 11.10 shows the results obtained at the four positions when a noise harmonic of 490 Hz and amplitude 'm' is added to both the direct and quadrature currents. In this figure and similar in this chapter, the modulation of the excitation will be defined in brackets. The value associated with 'd' and 'q' corresponds to the amplitude of the noise current added to the direct and quadrature main currents respectively. Above each plot, the overall value of SPL is included both in dB and dB(A). A comparison between all the cases at the four different positions is shown in Figure 11.11. This comparison is based on the total SPL in dB for each measurement, which was preferred to dB(A) since it gives more appropriate information about the real sound emitted from the motor, without being modified by the frequency response of the human ear.

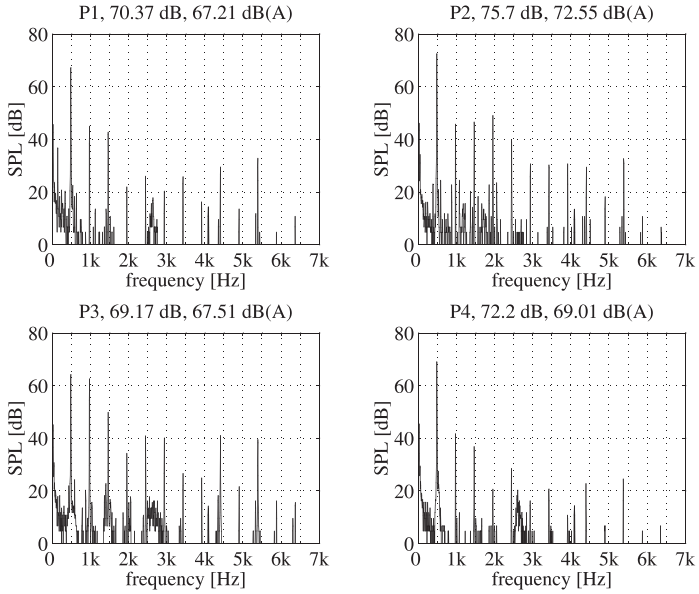

Figure 11.10: SPL at no load, stand still, four positions. Case [d=m, q=m], f=490 Hz. Rotor rotated 0 degrees (P1), 90 degrees (P2), 180 degrees (P3) and 270 degrees (P4).

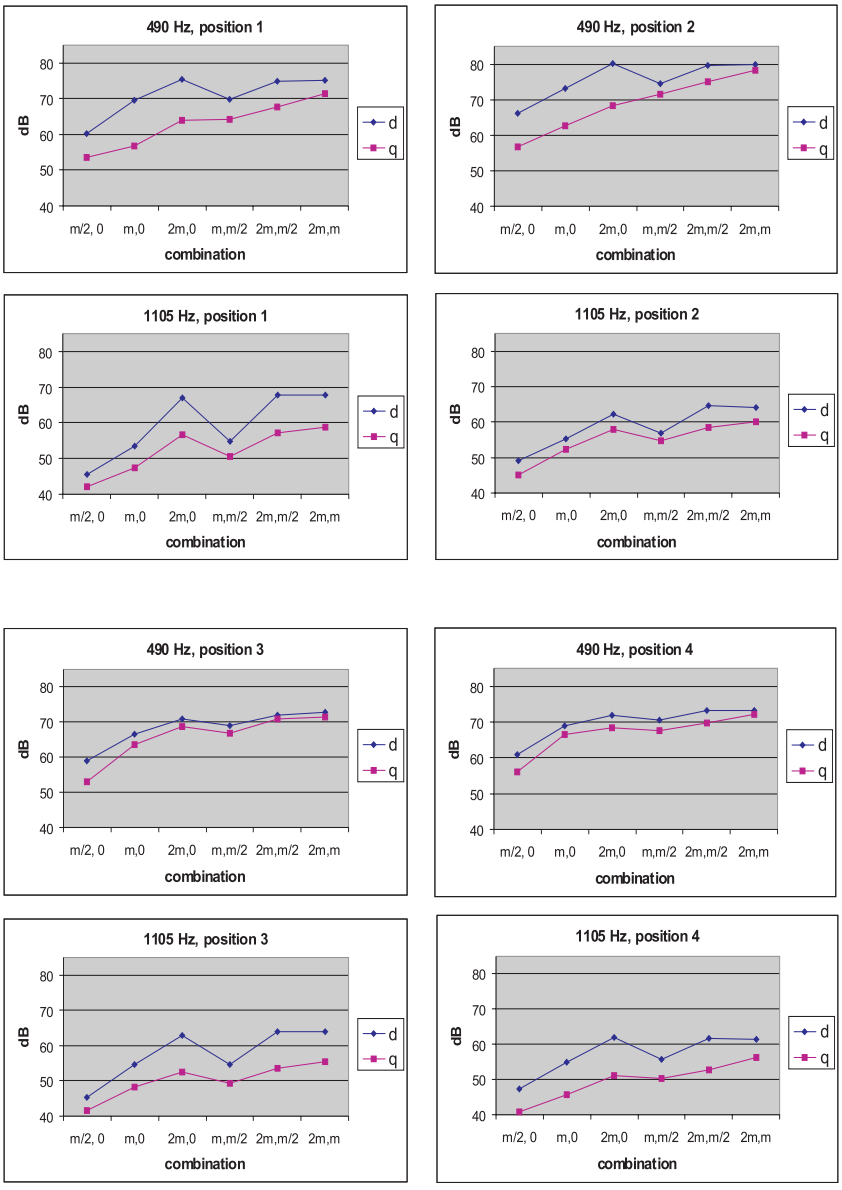

Figure 11.11: Summary of SPL at no load, stand still, four positions.

In Figure 11.11 and similar figures in this Chapter, the different cases are represented as a combination of two terms separated by a coma along the horizontal axis. The values of the curve corresponding to the 'd' current in the legend should be read as the case where the direct current corresponds to the first term and the quadrature current to the second term of the combination. Similarly, for the values of the curve corresponding to the 'q' current in the legend, the quadrature current corresponds to the first term, and the direct current to the second term of the combination. For example, in the combination 'm/2,0' the value of the curve associated with the 'd' in the legend corresponds to the combination [d=m/2, q=0], whereas the value of the curve associated with the 'q' corresponds to the combination [d=0, q=m/2]. Also note that the combinations have been selected so that the value of the modulation of the first term is higher than the second value. This means that the 'd' curve represents the cases where the modulation of the direct current is greater than the quadrature current and this will be referred to as *direct modulation*. The 'q' curve corresponds to the cases where the modulation of the quadrature current is greater than that of the direct current, and this will be referred to as *quadrature modulation*.

From Figure 11.11, it can be observed that for every case the total L_p for the direct modulation is greater than the corresponding quadrature modulation. However, the values for the same case at different rotor positions may vary considerably. For example, in Figure 11.10 the acoustic response at different rotor positions varies from 69.2 dB to 75.7 dB. This indicates that the airgap force exciting the structure is modified. Since the applied current is constant in all positions, the phenomenon should be due to a change in the airgap geometry. This is possible if the airgap is irregular and the position of the minimum airgap length around the machine is changed when the rotor is rotated, i.e. if there is dynamic eccentricity. The airgap forces are then re-distributed, affecting the excitation of the structure and the noise radiation pattern at different rotor positions. This leads to a change in the measured value at a fixed point.

The results obtained by averaging the values between the four different positions are presented in Figure 11.12. As expected, the overall L_p increases with the level of modulation, from 'm/2' to '2m'. The graphs also show that, in all the cases, the level is higher when modulating the direct current than in the case of the quadrature current. At 490 Hz, the differences are around 7 dB when one of the noise currents is set to zero and the other one is modulated with different amplitudes. At 1105 Hz, the difference at these points changes from 4 dB to 9 dB. These increments are maintained at 1105 Hz when both currents

are modulated, while at 490 Hz the direct and quadrature response are closer to each other. Comparing the results at both frequencies, the L_p at 490 Hz is around 10 dB higher than at 1105 Hz.

The main indications from the stand still tests are the higher noise emissions obtained in the case of direct current modulation, as well as the influence of the dynamic eccentricity in the measurements. It was concluded that it was preferable to perform the measurements with the rotor rotating, in order to obtain an average value from all the positions.

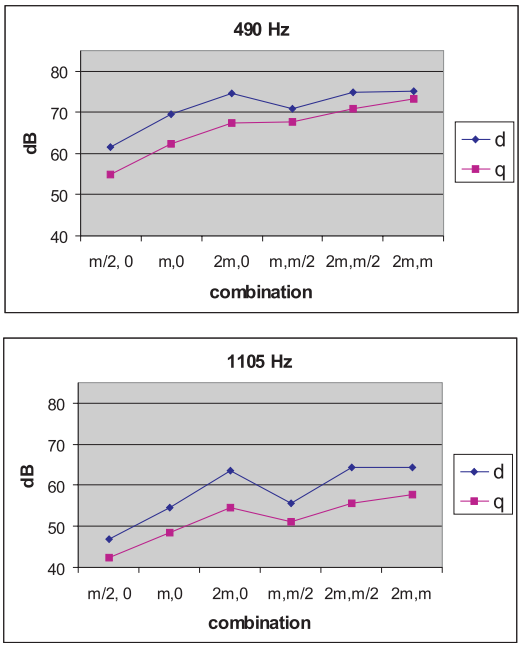

Figure 11.12: Averaged no load SPL results at stand still.

Sound pressure tests at low speed and no load.

A low rotational speed of 70 r.p.m. was selected so as to minimize the mechanical noise caused by the vibration of the machine, and the aerodynamic noise since the machine is cooled by means of a fan attached to the rotor. Nevertheless, the case when no noise current is added to the fundamental was also

measured, see Figure 11.13. The narrow band plot was post-processed and converted into a 1/3 octave band plot, in order to improve its visual inspection. The center frequency was calculated using (F.6) and the single L_p values for the frequencies included in each band were added using (F.2). The total L_p is referred to as *Lpav* and it is included above the narrow band plot. Due to the high switching frequency of 20 kHz used, the contribution from the electromagnetic noise caused by the harmonics in the converter might be neglected and the SPL spectrum in Figure 11.13 could be considered as that from the mechanical and aerodynamic noise together.

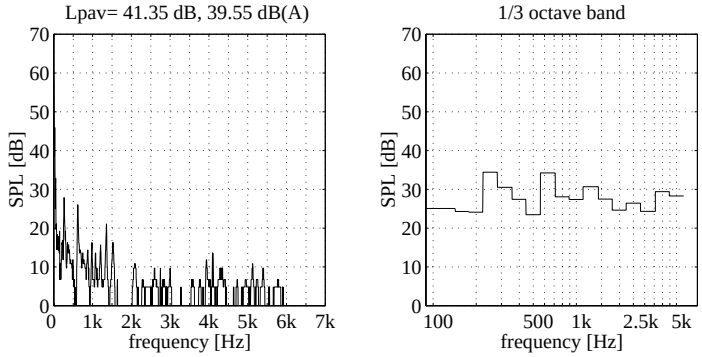

Figure 11.13: SPL at no load, 70 r.p.m. Case [d=0, q=0].

The results when the direct and the quadrature noise currents were fed alternatively from a white noise source are presented in Figure 11.14 and Figure 11.15. It can be observed that the SPL is increased in the order of 20 dB, which implies that the contribution of the mechanical and aerodynamic noise components is negligible compared to the electromagnetic noise caused by the induced harmonics.

A summary of the results for the different current excitations both at 490 Hz and 1105 Hz is presented in Figure 11.16. It can be appreciated that the direct modulation still produces more noise than the quadrature modulation. The difference is more accentuated at 490 Hz, where the average difference in sound pressure level is 5 dB, whereas at 1105 Hz this difference decreases to 2 dB. Generally speaking, the overall SPL increases with the increase in the amplitude of the modulation. The overall sound pressure level is slightly higher at 1105 Hz compared to that at 490 Hz. The increment is more clearly visible

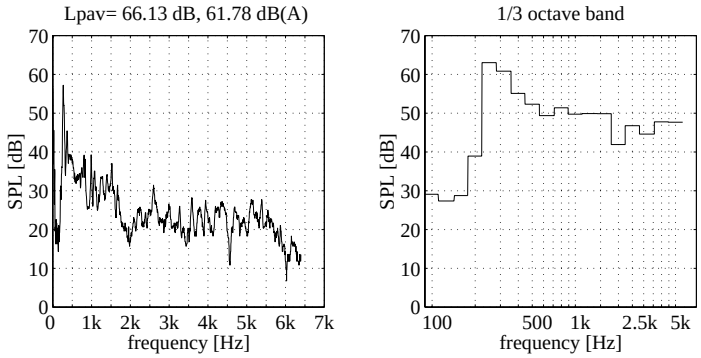

Figure 11.14: SPL at no load, 70 r.p.m. Case [d=wn, q=0].

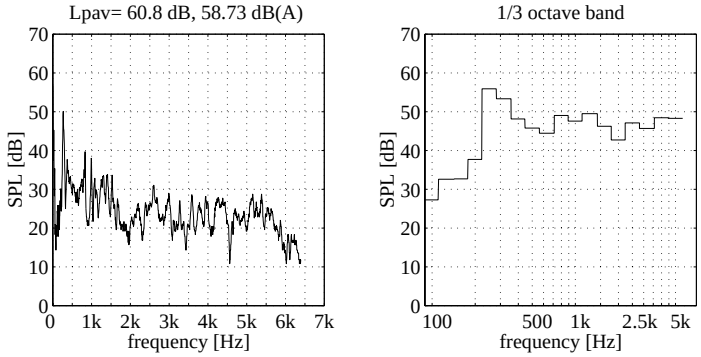

Figure 11.15: SPL at no load, 70 r.p.m. Case [d=0, q=wn].

in the quadrature modulation, with an average difference of 6 dB, than in the direct modulation, where the average difference is 3 dB. In general, the response at 490 Hz and 1105 Hz is different since these two frequencies excite different modes of vibration with different sound radiation patterns.

Compared to the averaged results from the stand still tests, it can be appreciated that the SPL is lower when the machine rotates. Also, the noise level from the 490 Hz harmonic is higher than that from the 1105 Hz harmonic when the machine rotates, while at stand still the opposite is true. Actually, the values from the stand still tests are not a good representation of the average around the whole machine. It might be the case that the values at the four positions give an average higher result compared to other positions around the circumference.

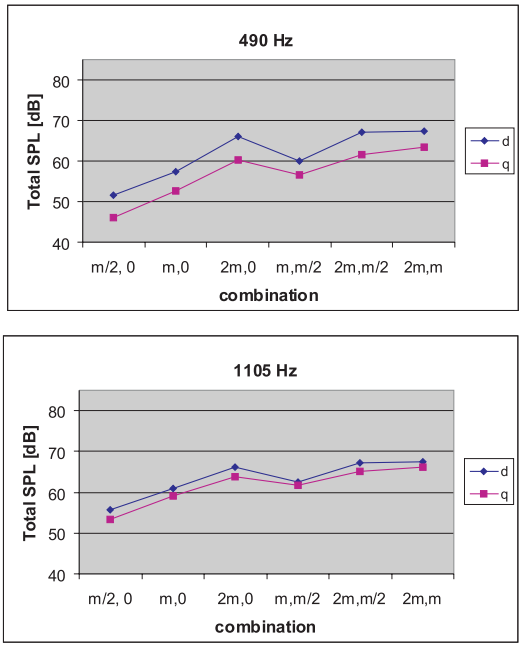

Figure 11.16: Summary of SPL at no load, 70 r.p.m.

11.5 Load tests results and analysis

Sound pressure tests at low speed and load.

The machine was loaded with another identical asynchronous motor. The influence of the noise from the load was minimized by covering it with eight layers of barium loaded vinyl, with a thickness of 1 mm each approximately. The noise recorded when the machines were rotating at 70 r.p.m. without adding noise harmonics is shown in Figure 11.17. The results when white noise was added to the direct and the quadrature currents in the test motor are presented in Figures 11.18 and 11.19. Adding this noise resulted in an increase in the SPL of around 25 dB, so the contribution of the aerodynamic and mechanical noise components can be neglected. Compared to the results obtained at no load, the noise is reduced by between 4 dB and 5 dB. A summary of the results obtained for various combinations of noise currents at the frequencies of

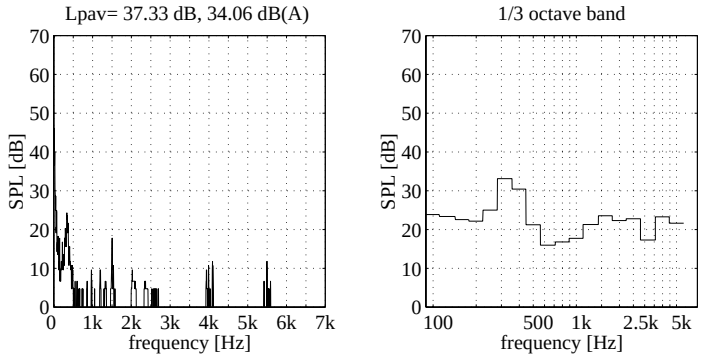

Figure 11.17: SPL at load, 70 r.p.m. Case [d=0, q=0].

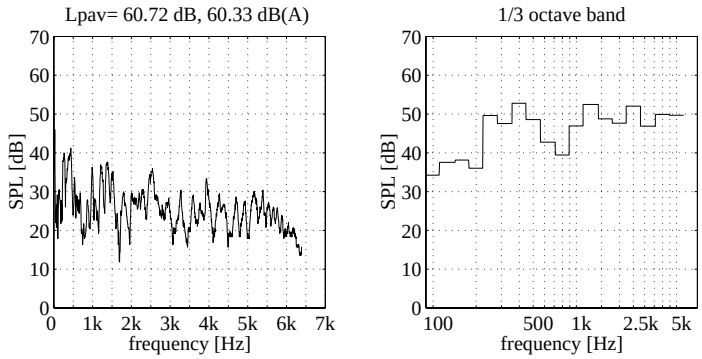

Figure 11.18: SPL at load, 70 r.p.m. Case [d=wn, q=0].

490 Hz and 1105 Hz is presented in Figure 11.20. As in the no load case, the noise emissions are increased with direct modulation compared to the quadrature modulation, now by an average of 5 dB and 2 dB at 490 Hz and 1105 Hz respectively. The SPL at 1105 Hz is slightly higher than at 490 Hz, with an increment of 1 dB and 3 dB for the direct and quadrature currents respectively. A comparison between the no load and load results for all the combinations of the excitation is included in Figure 11.21. Above each plot '(d)' and '(q)' indicate that the combinations in the graph are for direct and quadrature modulation respectively. The noise is decreased for direct and quadrature modulation at 490 Hz by an average 6 dB and 4 dB respectively, whereas at 1105 Hz the decrease is in average 8 dB and 7 dB for direct and quadrature current excitation.

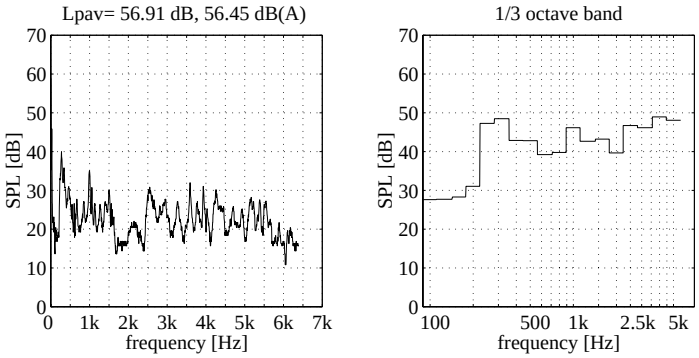

Figure 11.19: SPL at load, 70 r.p.m. Case [d=0, q=wn].

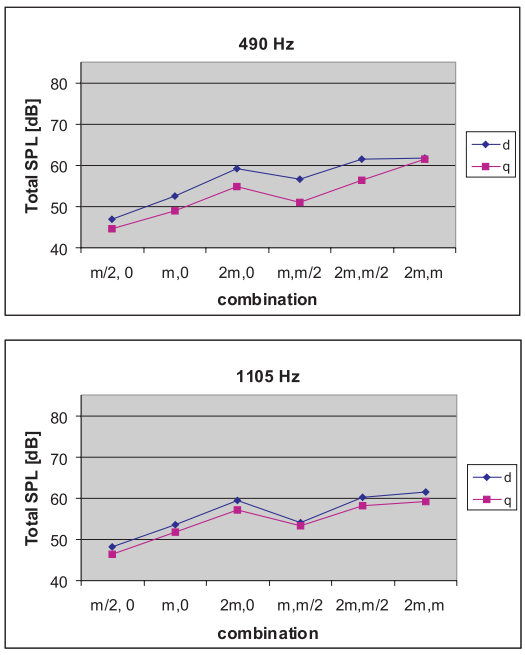

Figure 11.20: Summary of SPL at load, 70 r.p.m.

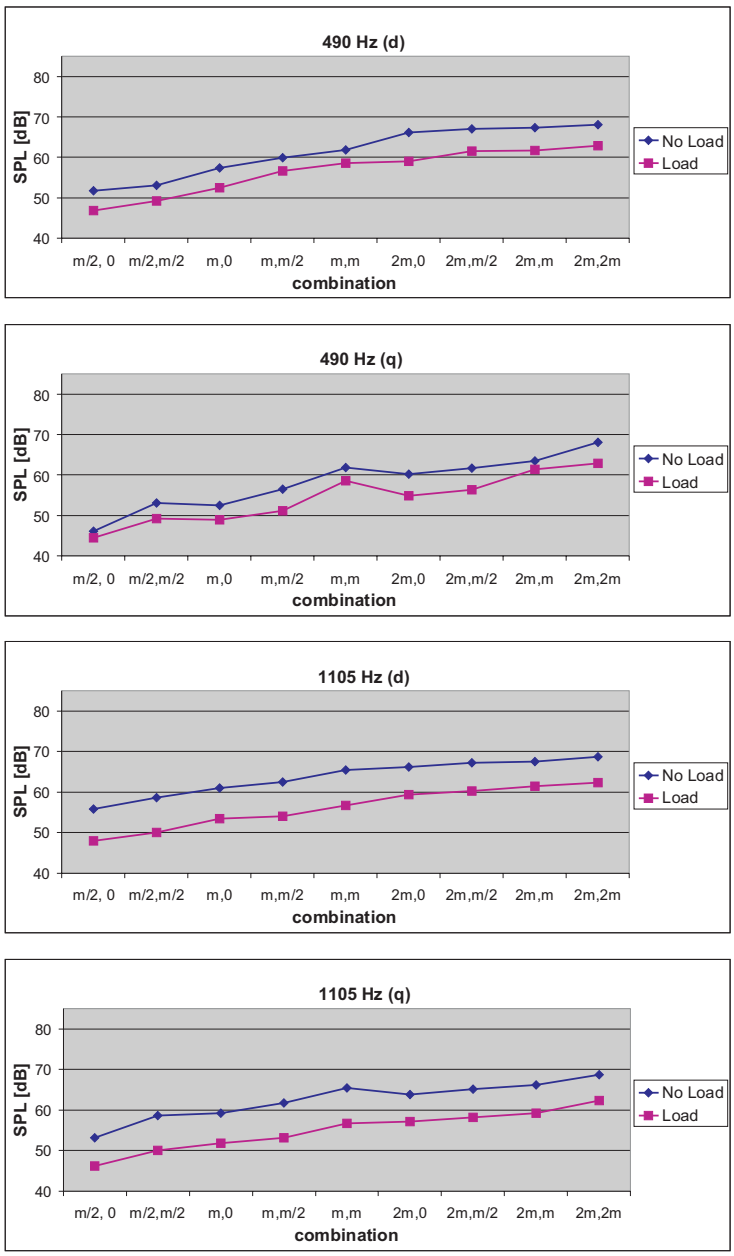

Figure 11.21: Comparison of SPL at no load and load, 70 r.p.m.

11.6 Sound intensity measurements

Sound pressure measurements provide quick information about the level of noise at one particular point inside the anechoic room. However, due to the directionality of the sound radiation in an electrical machine, it would be more appropriate to quantify the acoustic noise radiation by means of the sound power. The radiated sound power from the machine was determined by sound intensity measurements both at no load and load for the cases presented in Figure 11.8. A wired cubic reference frame was placed around the test motor. This frame was attached to the base plate, where the motor rested, and to the vertical plate placed between this machine and the load (Figure 11.3). Therefore only the sound intensity flowing through four sides of the cube had to be measured, since the noise was reflected from the other two sides covered by the plates, and the full results for the no load case are presented in Appendix G, and for the load case in Appendix H. These appendices present the values of the intensity measured through each side of the frame, as well as the measured pressure-intensity index. In the plot of the pressure-intensity index there are two dashed lines (the top line being L_{KO} and the bottom line being L_{KO}-7), which define the dynamic capability L_D of the system. With the exception of some low frequencies in the load measurements, it can be observed that the pressure-intensity index is contained between the limits of the dynamic capability, which supports the validity of the sound intensity measurements.

From the measured sound intensity level in each side, the intensity can be obtained from (F.5), which multiplied by the area of that side leads to the sound power. Adding the contributions of all the free sides provides the total power radiated, and the sound power level is obtained using (F.3). The no load results are shown in Figure 11.22, and the load results in Figure 11.23. The overall PWL is referred to as *LW total* above each plot. A comparison between the total PWL at 490 Hz and 1105 Hz both at load and no load is shown in Figure 11.24. These results confirm that the direct modulation produces more noise than the quadrature modulation. At no load the difference is 4 dB at 490 Hz and 7 dB at 1105 Hz. At load this difference is reduced to 1 dB and 3 dB at 490 Hz and 1105 Hz respectively. It should be noted that the results from single point pressure measurements also indicated that direct modulation produces more noise than quadrature modulation. However, the differences are greater for 490 Hz (5 dB at no load, 4 dB at load) than for 1105 Hz (2 dB at load and no load).

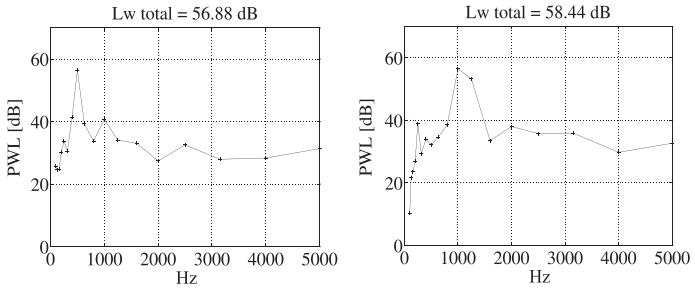

(a) d=0, q=m, 490 Hz (b) d=0, q=m, 1105 Hz

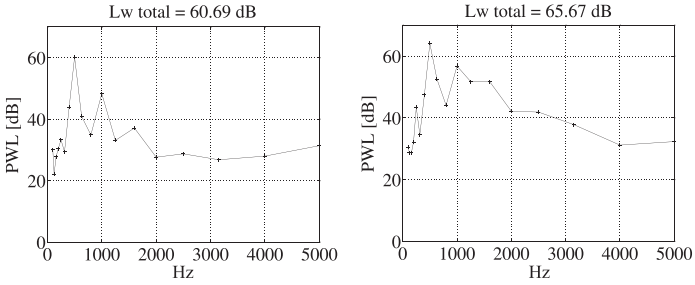

(c) d=m, q=0, 490 Hz (d) d=m, q=0, 1105 Hz

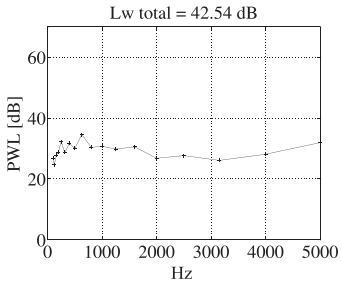

(e) d=0, q=0

Figure 11.22: Summary of PWL results at no load, 70 r.p.m.

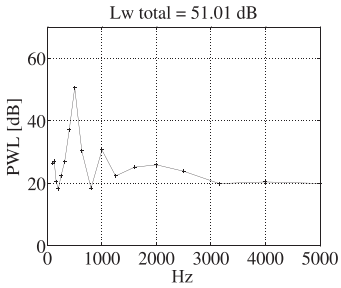

(a) d=0, q=m, 490 Hz

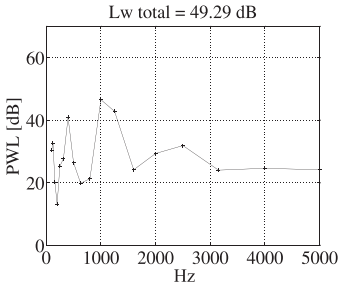

(b) d=0, q=m, 1105 Hz

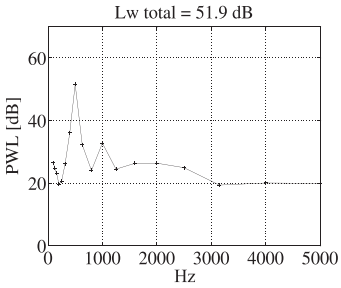

(c) d=m, q=0, 490 Hz

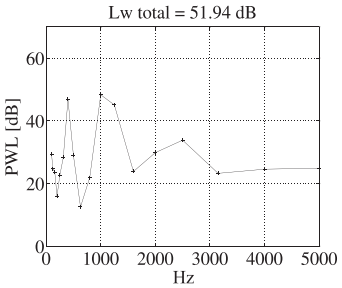

(d) d=m, q=0, 1105 Hz

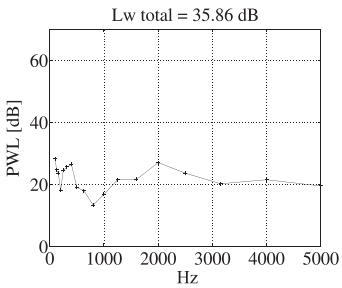

(e) d=0, q=0

Figure 11.23: Summary of PWL results at load, 70 r.p.m.

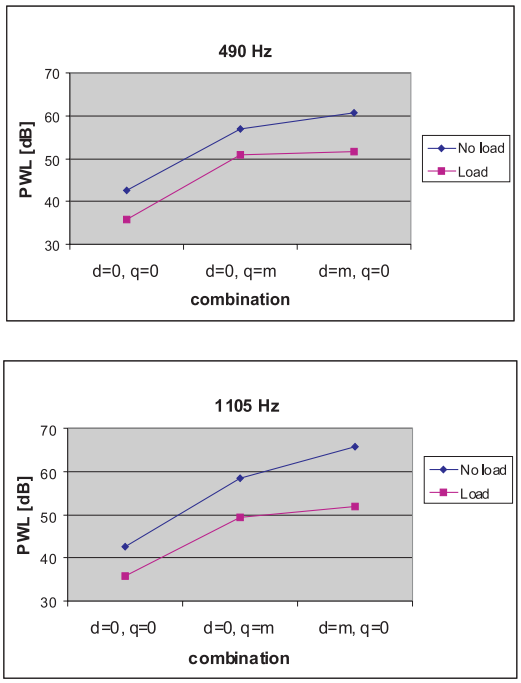

Figure 11.24: Comparison of sound intensity measurement results.

These results highlight the importance of quantifying noise from electrical machines in terms of sound power rather than single point pressure measurements (Wang et al., 2004), because the directionality of the acoustic radiation for a 490 Hz excitation is different from that at 1105 Hz. Figure 11.25 shows the mode of vibration at 1105 Hz simulated in ANSYS. The mode at 490 Hz was unfortunately not available. From the figure, it can be observed that the vibration is a combination of a radial and a bending mode. On one hand, the stator expands and contracts radially in anti-phase along the X and Y axis of an imaginary XY plane parallel to the laminations. On the other hand it can be observed that the mode shape changes along the length of the motor. This kind of mode is more easily excited from excitation in the radial direction, which supports the experimental results.

In general, the PWL at 1105 Hz is higher than at 490 Hz. At no load the increment for the direct current excitation is 5 dB and for the quadrature

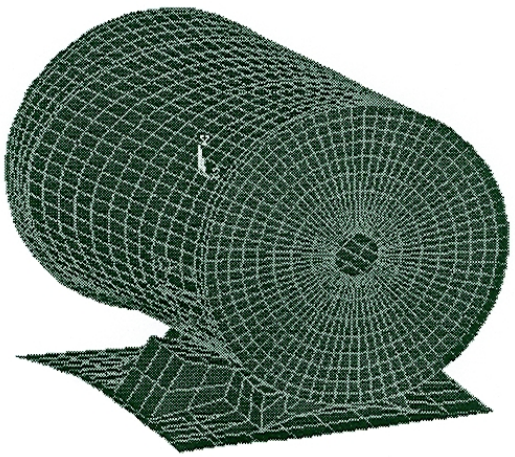

Figure 11.25: Mode of vibration at 1105 Hz predicted in ANSYS. Source (Wang, 1998).

current excitation 2 dB. At load this increment is 0.5 dB for the direct current, and for the quadrature current the response at 490 Hz is 2 dB higher than at 1105 Hz. Finally, it is confirmed that the PWL decreases when the machine is loaded. The decrease at 490 Hz when the direct current is modulated is 9 dB, and 6 dB in the case of the quadrature current excitation. At 1105 Hz this decrease is 13 dB and 9 dB for the direct and quadrature currents respectively.

The reduction in the noise at load must have an electromagnetical origin, since the mechanical and aerodynamic noise components were found to be negligible. The loading modifies the amplitude and phase of the current flowing in the conductors and the slip. This influences in turn the amplitude and the frequency of the exciting airgap force, while the main flux and leakage reactances are modified as a consequence of saturation. Also, the coupling with the load affects the resonance frequencies, and all these factors affect the noise radiation from the machine. Considering that only a part of the changing parameters tends to increase the noise, the other part may increase or decrease it alike, so it cannot be stated in general that loading increases or decreases noise (Timar, 1989). Stephen and Davies (1970) stated that there is not much difference in the sound radiation of small machines at load and no-load, which may be due to the fact that small machines have generally higher resonance frequen-

cies than those in the exciting force, and they are poor radiators due to their small size. Brozek (1973) found an important increase in the noise at load in large machines, which may be explained by the smaller resonance frequencies of the structure and their better radiating capability. Zhu et al. (1999) showed that in a small machine (1.5 Kw) the foot-mounting and shaft-coupling can significantly affect the natural frequencies and consequently the radiated acoustic noise. These two factors increase the stiffness of the machine and hence can reduce the emitted acoustic noise.

11.7 Conclusions

The no load stand still tests show a considerable change in the total sound pressure level at four different positions, indicating that the dynamic eccentricity is an important factor to consider in the test machine. Therefore, an average value of the noise emitted at a certain position is obtained by operating the machine at low speed. This low speed also reduces the influence of the mechanical and aerodynamic noise in the measurements, which are found to be negligible compared to the noise produced by the electromagnetic forces.

The sound pressure measurements reveal that the noise emitted increases with the level of modulation almost linearly. The results from direct and quadrature modulation are closer at 1105 Hz compared to the 490 Hz case, and the level of noise measured at 1105 Hz is greater than at 490 Hz. This is due to the fact that these two frequencies excite different modes of vibration. The directional characteristic of the noise radiation implies that single point sound pressure measurements are not representative of the overall acoustic behaviour of the machine. Therefore, a better way of quantifying the acoustic noise from electrical machines is to measure the sound power. The sound power results determined from sound intensity measurements show that direct modulation produces more noise than quadrature modulation, as well as the decrease in the noise emissions when the machine is loaded.

Although the direct and the quadrature excitations have the same amplitude and frequency, it has been found that the excitation in the radial direction (direct) generates up to 7 dB higher sound power level than the excitation in the tangential direction (quadrature). This is probably due to the radial shape of the modes of vibration, which are much more easily excited by radial than tangential forces.

In general, it has been observed that the noise emissions are considerably

reduced when the machine is loaded (by up to 13 dB). This should be due to the change in the electromagnetic component of the noise, since the mechanical and aerodynamic components were found to be negligible. It is however difficult to generalize these results since many factors influence the noise emissions at load compared to the no load case, which in turn may affect in different ways the noise radiation from different machines.

Chapter 12

Analytical force computation

12.1 Introduction

In this chapter an analytical expression will be deduced for the estimation of the radial air gap magnetic force in the motor used in the experiments. The procedure, which is based in the one presented by Bakhuizen (1973), is extended from a one-phase winding to a three-phase winding distribution, and the slotting effects are also taken into account. The results will serve to check the FEM calculations, which will be used for the noise prediction presented in Chapter 13.

The conductors in the machine are distributed in the slots forming a combined single and double layer winding as shown in Figure 12.1. Each slot contains the side of either one short pitched coil with 88 conductors or two fully pitched coils with 44 conductors each. Thus, the number of conductors in each slot is constant and equal to 88, although each one of the two 44-conductor coils sharing the same slot contributes to the flux in a different pole.

12.2 One phase winding distribution

Figure 12.2 shows the distribution of one phase along a quarter of the stator. Each one of the three-slot groups has a winding distribution as shown in Figure 12.1. A Fourier analysis can be developed on the applied MMF in one quarter of the machine exploiting symmetry. For convenience, a reference magnetic coordinate system is defined with its horizontal axis coinciding with the line of maximum airgap MMF, at an angle ζ with the horizontal axis of the

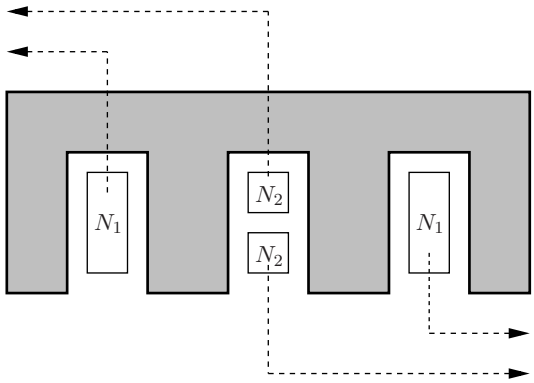

Figure 12.1: Winding distribution in the slots.

machine as shown in the figure. The 10 degrees angle between two slots will be referred to as ξ and the applied MMF in each slot will be considered to be homogeneously distributed along an angle 2ϵ. The absolute value of the infinitesimal applied MMF along one slot will be defined as $\frac{N \cdot i_a}{2\epsilon}$, and the total contribution of one slot to the airgap MMF will be $N \cdot i_a$, where N is the total number of conductors in one slot. With this nomenclature the applied MMF, which will be referred as $F_a(\alpha)$, can be expressed as follows:

$$-\frac{N \cdot i_a}{2\epsilon} \qquad -\zeta - \xi - \epsilon < \alpha < -\zeta - \xi + \epsilon \tag{12.1}$$

$$-\frac{N \cdot i_a}{2\epsilon} \qquad -\zeta - \epsilon < \alpha < -\zeta + \epsilon \tag{12.2}$$

$$-\frac{N \cdot i_a}{2\epsilon} \qquad -\zeta + \xi - \epsilon < \alpha < -\zeta + \xi + \epsilon \tag{12.3}$$

$$\frac{N \cdot i_a}{2\epsilon} \qquad \zeta - \xi - \epsilon < \alpha < \zeta - \xi + \epsilon \tag{12.4}$$

$$\frac{N \cdot i_a}{2\epsilon} \qquad \zeta - \epsilon < \alpha < \zeta + \epsilon \tag{12.5}$$

$$\frac{N \cdot i_a}{2\epsilon} \qquad \zeta + \xi - \epsilon < \alpha < \zeta + \xi + \epsilon \tag{12.6}$$

$$0 \qquad elsewhere \tag{12.7}$$

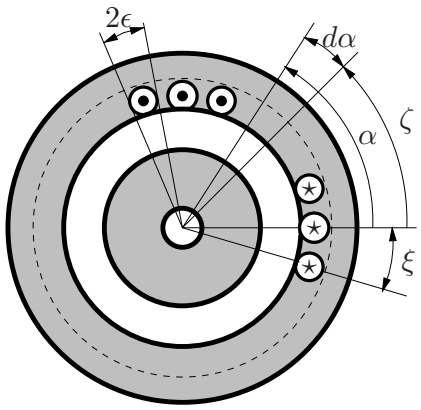

Figure 12.2: One phase winding distribution along one quarter of the machine

In order to examine the harmonic components in the airgap MMF, it is useful to develop the Fourier analysis of equations (12.1) to (12.7), defining F_a as in (12.8),

$$F_a(\alpha) = \sum_{\nu=-\infty}^{\nu=\infty} C_\nu \cdot e^{-jp\nu\alpha} \tag{12.8}$$

where p is the number of pole pairs and ν is the number of the harmonic. From this equation, and for p=2, C_ν is defined as in (12.9).

$$C_\nu = \frac{1}{\pi} \int_{-\frac{\pi}{2}}^{\frac{\pi}{2}} F_a(\alpha) \cdot e^{j2\nu\alpha} d\alpha \tag{12.9}$$

Combining the MMF in (12.1)-(12.7) and (12.9), and after some mathematical transformations, C_ν can be expressed as in (12.10).

$$C_\nu = \frac{N \cdot \vec{i}_a}{\pi} 2j \frac{\sin(2\nu\epsilon)}{2\nu\epsilon} [\sin(2\nu(\zeta+\xi)) + \sin(2\nu(\zeta-\xi)) + \\ + \sin(2\nu\zeta)] \tag{12.10}$$

A so called slot factor $f_{g,2\nu}$ is introduced, which is defined as in (12.11).

$$f_{g,2\nu} = \frac{\sin(2\nu\epsilon)}{2\nu\epsilon} \tag{12.11}$$

This factor can be approximated to '1', considering the small slot opening and a reasonable number of ν harmonics. A closer look into (12.10) shows that the number of slots is multiplied by a factor of three if a concentrated winding is considered, i.e. if ξ is zero. This is reasonable since the winding is distributed in three slots with N conductors each. If the winding was concentrated in one slot instead, the number of conductors would be three times bigger.

The relation between the applied and airgap MMF can be deduced applying Ampere's law to an infinitesimal sector of the machine enclosing a certain applied MMF, as shown in Figure 12.3.

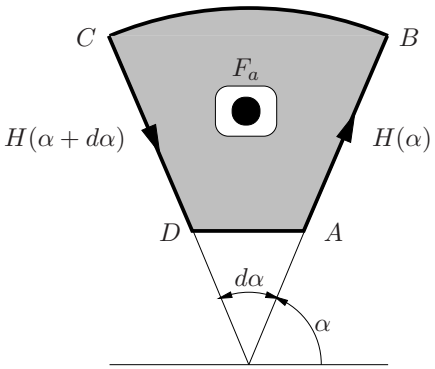

Figure 12.3: Infinitesimal sector of the machine.

The sign of the MMF has been selected to be positive in the outward direction. Considering that the applied MMF is homogeneously distributed within the sector, Ampere's law can be expressed as in (12.12).

$$\oint H dl = F_a(\alpha) d\alpha \tag{12.12}$$

Evaluating the line integral along the path ABCD, and neglecting the tangential components, leads to (12.13) for the radial magnetic field strength H across the airgap g.

$$[H(\alpha) - H(\alpha + d\alpha)] \cdot g = F_a(\alpha) d\alpha \tag{12.13}$$

The second term on the left hand side of this equation can be rewritten

using the first order Taylor expansion in (12.14),

$$f(x) = f(a) + \frac{f'(a)}{1!}(x-a) + ... \tag{12.14}$$

where $f = H$, $a = \alpha$, and $x = \alpha + d\alpha$ in this case. With these modifications (12.15) is obtained.

$$H(\alpha + d\alpha) = H(\alpha) + \frac{\partial H(\alpha)}{\partial \alpha} d\alpha \tag{12.15}$$

Combining this equation with (12.13) leads to (12.16),

$$H(\alpha) = -\frac{1}{g} \int F_a(\alpha) d\alpha \tag{12.16}$$

where $H(\alpha) \cdot g$ corresponds to the airgap MMF, which will be referred to as F_δ. Hence, the relation between the applied and the airgap MMF is (12.17).

$$F_\delta = -\int F_a(\alpha) d\alpha \tag{12.17}$$

Introducing (12.8) into (12.17) yields (12.18) for a four pole machine.

$$F_\delta = -\sum_{\nu=-\infty}^{\nu=\infty} \int C_\nu \cdot e^{-j2\nu\alpha} d\alpha \tag{12.18}$$

Developing the integral gives (12.19).

$$F_\delta = \sum_{\nu=-\infty}^{\nu=\infty} \frac{1}{2j\nu} C_\nu \cdot e^{-j2\nu\alpha} \tag{12.19}$$

Introducing the expression for C_ν from (12.10) into (12.19) yields (12.20).

$$F_\delta = \sum_{\nu=-\infty}^{\nu=\infty} \frac{N \cdot \vec{i}_a}{\pi\nu} f_{g,2v} \cdot e^{-j2\nu\alpha} [\sin(2\nu(\zeta+\xi)) + \sin(2\nu(\zeta-\xi)) + \\ + \sin(2\nu\zeta)] \tag{12.20}$$

This expression is valid for one phase, with $\vec{i}_a$ defined as in (12.21).

$$\vec{i}_a = \hat{i} \cdot e^{j\omega t} \tag{12.21}$$

This represents a current vector rotating with an angular frequency ω. For the case of a concentrated winding, i.e. ξ = 0, the sum of the three sine terms in (12.20) is reduced to $3 \cdot \sin(2\nu\zeta)$. The value of $\sin(2\nu\zeta)$ is equal to zero for all even harmonics. For a given pair of odd harmonics $\pm\nu$, the sum of $\sin(2\nu\zeta)$ will be equal to ± 2. Thus, the amplitude of the airgap MMF for the different harmonics is given by (12.22).

$$\frac{2 \cdot N\hat{i}}{\pi}\frac{3}{|\nu|} \tag{12.22}$$

In this equation $\{|\nu|$ = 1, 3, 5, 7, ...$\}$. The direction of rotation will alternate between two adjacent odd harmonics. Dividing (12.20) by the airgap length g and taking the real part yields the magnetic field strength H. Assuming infinite permeability in the iron, the airgap flux density B_δ is directly obtained multiplying H by μ_0. Figure 12.4 shows B_δ over one half of the motor when a current with an amplitude of 1.82 A (which corresponds to the no load phase current in the real motor) and a frequency of 50 Hz is used.

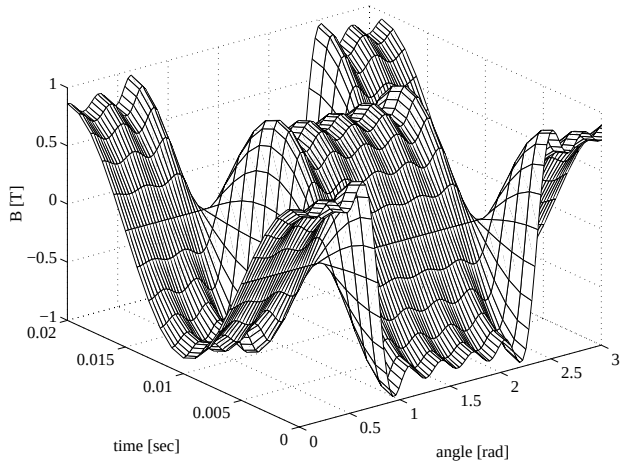

Figure 12.4: Airgap B for the one phase concentrated winding.

In the case of the distributed winding, it can be shown that the sine terms inside the brackets in (12.20) still add zero for all even harmonics, leading to

the expression for the amplitude of the airgap MMF in (12.23).

$$\frac{2 \cdot N\hat{i}}{\pi} \frac{\sin(2\nu(\zeta+\xi)) + \sin(2\nu(\zeta-\xi)) + \sin(2\nu\zeta)}{|\nu|} \tag{12.23}$$

For the odd harmonics, the sum of the sine terms decreases and increases periodically for $\{|\nu| = 1, 3, 5, 7, 9, 11, ...\}$, but the contribution of higher order harmonics is little since $|\nu|$ in the denominator increases a well. This is also true for the concentrated winding, but there the factor introduced from the sine term is constant and equal to 3, whereas in the distributed winding it decreases for the first 9 odd harmonics. Hence, the influence of these harmonics in the distributed winding is less compared to the concentrated winding, as can be appreciated in Figure 12.5. The amplitude of the fundamental airgap MMF decreases when the winding is distributed, although the difference is rather small. For the winding distribution in the test motor, the sine terms in equation 12.23 add 2.968 for $|\nu| = 1$, which represents a negligible decrease of 1.07 % with respect to the concentrated winding.

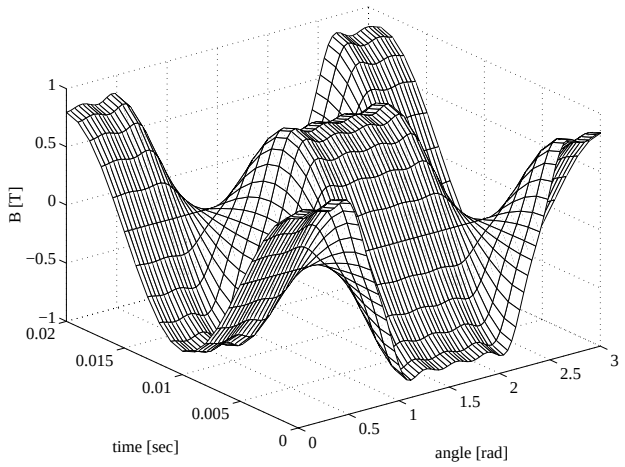

Figure 12.5: Airgap B for the one phase distributed winding.

12.3 Three phase winding distribution

The airgap MMF for one phase can easily be extended for the case of a three phase machine where the current vector has the form in (12.24).

$$\vec{i}_{a,b,c} = \hat{i}\left(1 + e^{j\nu\frac{2\pi}{3}} \cdot e^{-j\frac{2\pi}{3}} + e^{j\nu\frac{4\pi}{3}} \cdot e^{-j\frac{4\pi}{3}}\right) e^{j\omega t} \tag{12.24}$$

In one hand, this expression takes into account the electrical phase difference between the currents from the three phases. This phase difference will be 120 degrees for the fundamental, and a multiple of this number for the corresponding harmonics. On the other hand it considers also the fact that the coils are shifted in space around the stator of the motor by an angle of 120 degrees. Introducing this three phase current into (12.20) and taking the real part, the total airgap MMF in the machine can be written as in (12.25).

$$\begin{aligned} F_\delta = \sum_{\nu=-\infty}^{\nu=\infty} \frac{N\hat{i}}{\pi\nu} f_{g,2\nu}(\sin(2\nu(\zeta+\xi)) + \sin(2\nu(\zeta-\xi)) + \sin(2\nu\zeta)) \cdot \\ \cdot(\cos(\omega t - 2\nu\alpha + \frac{2\pi}{3}(\nu-1)) + \cos(\omega t - 2\nu\alpha + \frac{4\pi}{3}(\nu-1)) + \\ + \cos(\omega t - 2\nu\alpha)) \end{aligned} \tag{12.25}$$

The effect of introducing three phases and distributing the winding around the motor results in a further decrease of the winding harmonics, as shown in Figure 12.6.

12.4 Modelling the slots

So far, a constant airgap g around the motor has been assumed, which should be modified by the Carter factor to take into consideration the higher reluctance in the slot openings. Equation (12.26) has been proposed by Lipo (1996) for the calculation of the Carter factor, based on the slot dimensions.

$$K_c = \frac{\tau_s}{\tau_s - \frac{b_0^2}{(5g+b_0)}} \tag{12.26}$$

In this equation τ_s is the slot pitch, and b_0 corresponds to the slot opening. In the test motor, the 10 degrees angle ξ between two slots, at an inner stator

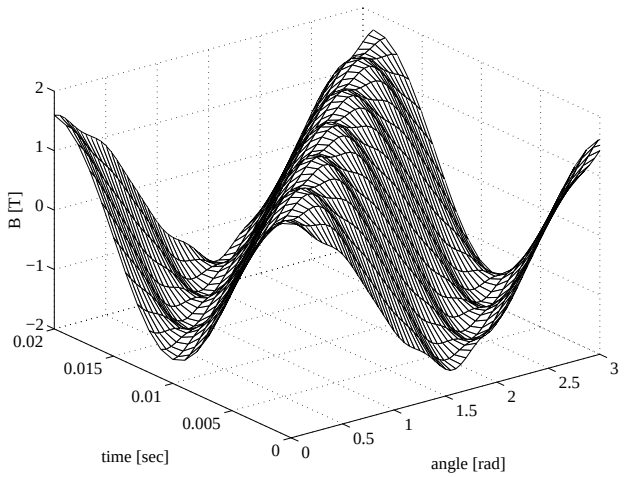

Figure 12.6: Airgap B for the three phase distributed winding.

radius of 47.66 mm gives a length of 8.32 mm. For a slot opening of 2.54 mm and an airgap equal to 0.3 mm the Carter factor becomes 1.2375.

However, it is possible to calculate the slotting harmonics by considering the inverse airgap function between two slots, as shown in Figure 12.7. The value of h_e corresponds to the actual length of the path that the flux follows through the air along one slot opening before penetrating one of the adjacent stator teeth. This value has been estimated based on the work presented by Gerling (1994). A 'magnetically effective slot depth' h_e is defined to be equal to the geometrical slot depth h if the slot opening is greater or equal to double the geometrical slot depth. Otherwise $h_e = \frac{\pi \cdot b_0}{8}$, as it is the case in the test motor. For a geometrical slot depth of 20.085 mm, h_e becomes 0.997. Based on Figure 12.7, the inverse airgap function is expressed as:

$$\hat{g} \quad -\tfrac{\xi}{2} < \alpha < -\epsilon \tag{12.27}$$

$$\check{g} \quad -\epsilon < \alpha < +\epsilon \tag{12.28}$$

$$\hat{g} \quad +\epsilon < \alpha < +\tfrac{\xi}{2} \tag{12.29}$$

Following the same procedure as for the applied MMF, a Fourier expansion

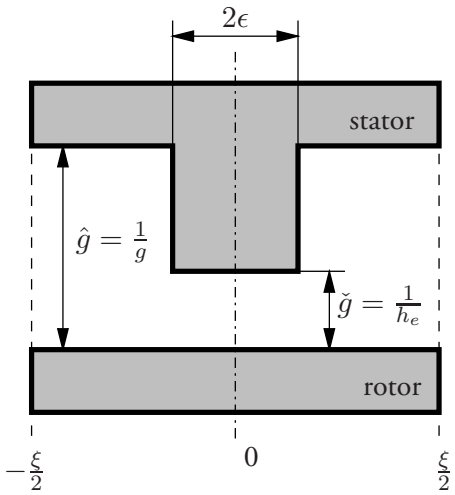

Figure 12.7: Inverse airgap function.

of equations (12.27)-(12.29) leads to (12.30),

$$q(\alpha) = \sum_{n=-\infty}^{n=\infty} C_n e^{-jnN_s\alpha} \tag{12.30}$$

where n is the number of the slot harmonic and N_s is the number of stator slots. From this expression C_n is defined as in (12.31).

$$C_n = \frac{N_s}{2\pi} \int_{-\frac{\pi}{N_s}}^{\frac{\pi}{N_s}} g(\alpha) e^{jnN_s\alpha} \tag{12.31}$$

Developing the integral term a final expression for C_n is given by (12.32), where the new slotting factor has the form in (12.33), and can be approximated to '1'.

$$C_n = \frac{N_s \cdot \epsilon}{\pi} \cdot \frac{\sin(n\epsilon N_s)}{n\epsilon N_s}(\check{g} - \hat{g}) + \hat{g}\frac{\sin(n\pi)}{n\pi} \tag{12.32}$$

$$f_{g,n} = \frac{\sin(n\epsilon N_s)}{n\epsilon N_s} \tag{12.33}$$

Introducing (12.32) into (12.30) and taking the real part yields (12.34).

$$q(\alpha) = \sum_{n=-\infty}^{n=\infty} \left(\frac{N_s \cdot \epsilon}{\pi} f_{g,n}(\breve{g} - \hat{g}) + \hat{g} \frac{\sin(n\pi)}{n\pi} \right) \cos(nN_s\alpha) \quad (12.34)$$

Finally, the radial magnetic field strength including the slotting harmonics is obtained multiplying (12.34) by (12.25), yielding (12.35).

$$\begin{aligned} H(\alpha) = \sum_{\nu=-\infty}^{\nu=\infty} \sum_{n=-\infty}^{n=\infty} & \left(\frac{N_s \cdot \epsilon}{\pi} f_{g,n}(\breve{g} - \hat{g}) + \hat{g} \frac{\sin(n\pi)}{n\pi} \right) \cos(nN_s\alpha) \cdot \\ & \cdot \frac{N \cdot \hat{i}}{\pi\nu} f_{g,2\nu}(\sin(2\nu(\zeta + \xi)) + \sin(2\nu(\zeta - \xi)) + \sin(2\nu\zeta)) \cdot \\ & \cdot (\cos(\omega t - 2\nu\alpha + \frac{2\pi}{3}(\nu - 1)) + \cos(\omega t - 2\nu\alpha + \frac{4\pi}{3}(\nu - 1)) + \\ & + \cos(\omega t - 2\nu\alpha)) \quad (12.35) \end{aligned}$$

The airgap flux density obtained when the slotting effects are included is shown in Figure 12.8.

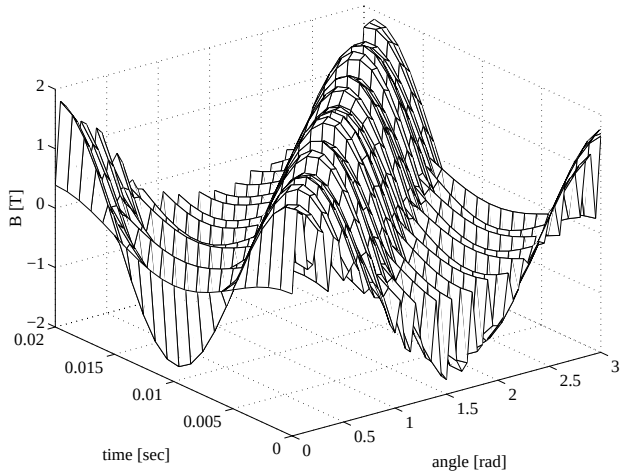

Figure 12.8: Airgap B for the three phase distributed winding with slots.

12.5 FEM validation

It is instructive to use the procedure presented in this chapter to compare the analytical solution to the numerical using the finite element method (FEM). The software used for the calculations is OPERA 2D, version 7.5. Symmetry could be exploited, and Figure 12.9 shows one quarter of the geometry, indicating the rotor, stator and surrounding air. The option of defining air around the stator was preferred rather than imposing the Dirichlet condition in the outer surface of the stator (vector potential equal to zero). Although the number of elements in the model increases, the fact that leakage flux can appear in the surface of the motor under very heavy saturation was taken into consideration. The thickness of the layer of air surrounding the stator was made equal to the radius of the machine.

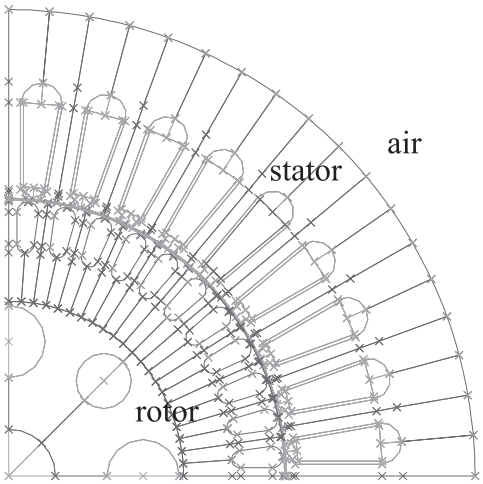

Figure 12.9: Plot of the geometry modelled in OPERA 2D.

Since this model will be also used for transient calculations, where the rotor mesh is rotated with respect to the stator, a new boundary condition needs to be imposed between the stationary and the rotating parts. This was achieved by defining a 'rotating airgap'. In order to obtain a very fine calculation of the airgap forces, five layers of elements were modelled in the airgap of the machine.

Two of them were attached to the rotor mesh, other two to the stator mesh and the rotating airgap was set in-between. In this way, the number of elements in both sides of the boundary condition was optimized, and it was also ensured that the calculation of the forces could be done through the middle of the airgap without crossing any node, since the field there is multivalued. Defining the rotating airgap also had the advantage that the rest of the boundary conditions were set automatically so as to match both the magnetical and mesh properties in any of the solvers available. Figure 12.10 shows the element distribution in the area surrounding the airgap. The mesh was automatically generated using triangular elements, although it could be adapted defining the facets in a proper way and changing the number of subdivisions at the edges.

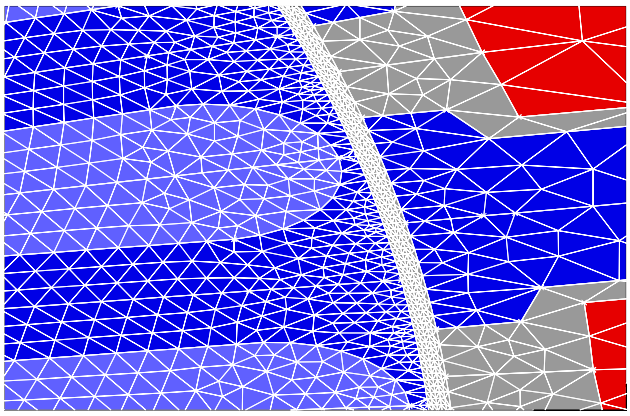

Figure 12.10: Mesh generated in the surroundings of the airgap.

The model was checked using a harmonic analysis at no load and full load. The number of elements, especially in the airgap, the rotor slots and the surrounding regions, was increased until the change in the torque delivered was less than 1%. The total number of elements used in the model corresponding to one quarter of the machine is 8314, comprising 1254 elements distributed along three layers in the airgap, and 86 elements per rotor slot. The full load value obtained was 10% higher than the rated torque specified in the data sheets. The difference could be attributed to an inaccurate BH curve, and/or the fact that the inductance and the resistance in the aluminium end-rings were neglected in the model.

The flux density distribution through the middle of the airgap was calculated performing a magnetostatic solution at no load. Since the analytical solution assumes infinite permeability for the iron, a first calculation was carried out defining a very high linear isotropic permeability for the iron. The results from both FEM and the analytical calculations are shown in Figure 12.11, where a similar behaviour can be observed. It should be remarked that the phases of the curves in this plot have been displaced in order to improve their visual inspection.

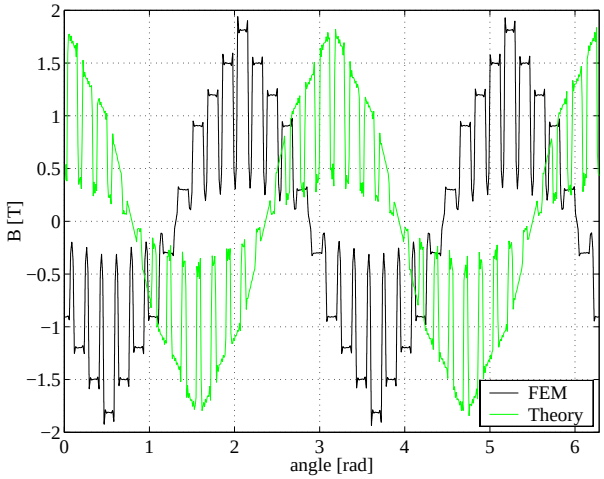

Figure 12.11: Comparison between analytical and FEM flux densities for ideal iron, phase displaced.

When the non-linearities in the iron are considered in the FEM calculation, the airgap flux density drops to a more reasonable level around 1 T and its shape resembles a square wave, as shown in Figure 12.12. Besides, more irregularities appear due to the saturation effects which are more predominant in the tip of the teeth.

The radial stress in the laminated stator stack can be implemented applying Maxwell's stress equation for radial forces, given by (12.36).

$$\sigma_r(\alpha) = \frac{B_\delta^2(\alpha)}{2\mu_0} \tag{12.36}$$

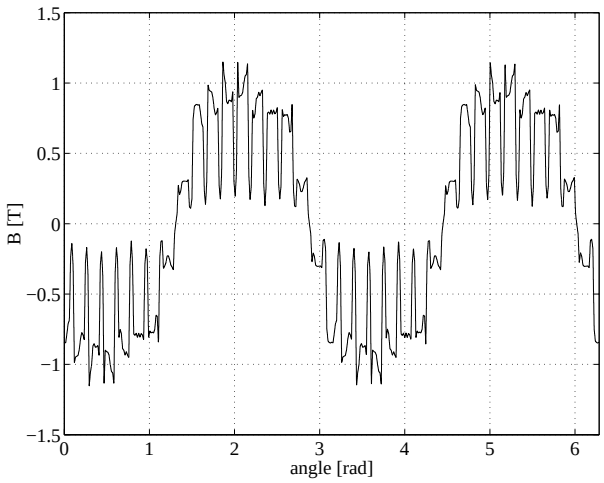

Figure 12.12: FEM solution considering non-linear iron.

The result from the analytical calculation is shown in Figure 12.13, where the slotting effects have not been included in order to make the picture more clear. The stress in the airgap of the machine was also calculated in FEM and the results when using non-linear iron are presented in Figure 12.14.

12.6 Conclusions

An analytical expression has been deduced for the radial airgap forces in the test motor. The method is based in the Fourier analysis of the applied MMF. The expressions have been gradually developed from a one phase concentrated winding to the three phase distributed winding setup in the machine. The slotting effects have been incorporated in the model, developing the Fourier analysis of an inverse airgap function. Although the method assumes ideal iron, it is useful as a check of the results obtained from an ideal finite element model of the machine, and it could be appreciated that the results using both methods showed a good agreement.

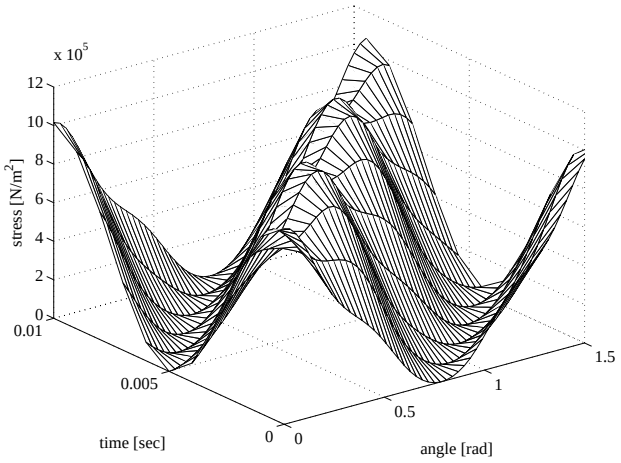

Figure 12.13: Analytical radial Maxwell stress, ideal iron.

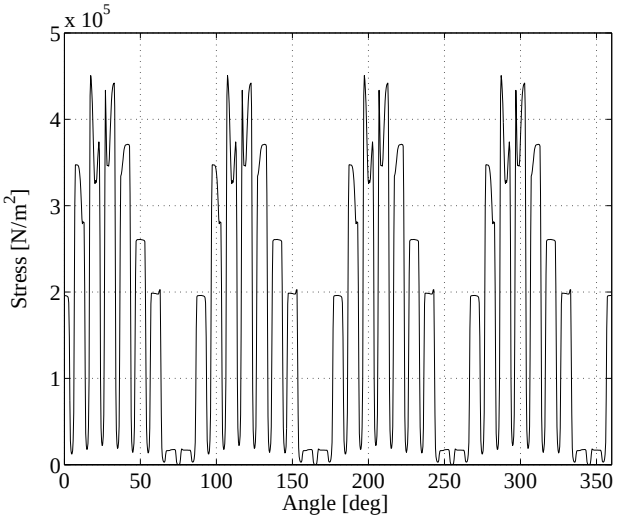

Figure 12.14: FEM Maxwell stress, non-linear iron.

Chapter 13

Acoustic noise prediction

13.1 Introduction

The analytical model presented in Chapter 12 introduced an understanding on how the linear airgap force distribution can be calculated based on the winding distribution in the machine. However, in order to perform an accurate calculation of the electromagnetic airgap forces, both the iron non linearities and the details of the motor geometry must be taken into consideration, and this can be achieved using numerical methods. The mechanical properties of the machine structure also influence the noise emissions, and numerical packages are also available for mechanical and acoustic calculations. The aim of this chapter is to develop a process for the prediction of the sound power radiation in an electrical machine, based on numerical calculations. This would allow implementation of appropriate noise control measures at the design stage.

The noise radiated from electric machinery may be predicted analytically or numerically. In the analytical approach, the motor acoustic behaviour is usually approximated using methods based on spherical or finite-cylindrical acoustic models (Zhu and Howe, 1994). However, analytical methods are insufficient when dealing with complex topologies or taking into account the end-plates. For variable speed operations, it is difficult to calculate in practice the magnitude of the noise peaks, although the frequencies at which they occur can be deduced from the interaction of the harmonics present in the inverter output (Yang, 1981). An algorithm to calculate the lowest limit of noise radiated from a variable speed drive was presented by Timar and Lai (1994), and Timar and Lai (1996).

In the numerical approach, the deterministic method is traditionally used for the noise prediction in induction motors, although statistical approaches appear to be promising, especially for high frequencies and large motors (Wang et al., 2002). The deterministic method has been used by Wang et al. (2004) for the prediction of the sound power from a PWM inverter driven induction motor. However, the influence of the stator slot harmonics on the rotor could not be considered since the finite element package used did not allow currents to be induced in the rotor, which instead had to be estimated (Astfalck et al., 1997). The software used for the electromagnetic calculations presented in this thesis allows currents to be induced in the rotor, and the noise prediction process has been tested using vector control. In the process, the sensitivity of the noise prediction to uncertainty factors such as the damping of the structure and the accuracy of the BH curve has also been assessed.

In the deterministic method, the electromagnetic forces acting on the motor structure are calculated from the input currents (or voltages) using an electromagnetic model based on FEM. The commercial package OPERA 2D/3D version 7.5 was used for this purpose. The vibration characteristics are usually simulated using a structural model also normally based on FEM, and the commercial package used was ANSYS version 5.1. A detailed description of the structural simulations with the motor used in this part of the thesis was presented by Wang (1998), Wang and Lai (1999), and a summary will be included in this chapter. By using the vibration velocities on the motor structure predicted from the structural model, the radiated sound power level can then be calculated using an acoustic model. This model was implemented in another commercial package, SYSNOISE version 5.2, based on the boundary element method (BEM). The main advantage of using BEM is that only the boundary of the problem domain needs to be discretized, i.e. there is no interior or exterior mesh. Although the mathematics involved in BEM are more difficult, the modelling effort is lower compared to FEM and it also presents the advantage of solving both interior (inside the defined model) and exterior (in the surrounding fluid) problems, with different possibilities of fluid-structure interaction (Zhou, 1993). An overview of the prediction process is shown in Figure 13.1. The electromagnetic excitation force was imported into SYSNOISE from OPERA, and the modal information as well as the geometry were taken from ANSYS.

The following sections describe the details of the different finite/boundary element models, and the calculations performed within the structural, electromagnetic and acoustic analyses involved in the process shown in Figure 13.1.

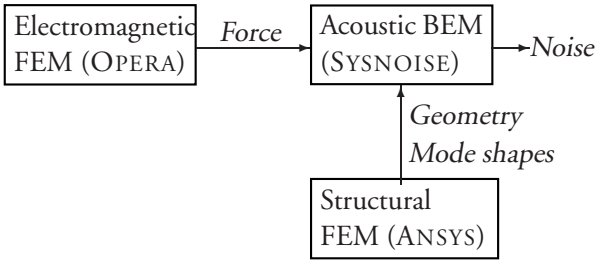

Figure 13.1: Numerical prediction process.

13.2 Structural modal analysis

The purpose of the structural modal analysis is to determine the modes of vibration, which define the vibro-acoustic characteristics of the structure. This is achieved through the so-called *free response synthesis*, which can be performed experimentally or by means of numerical simulations. These two procedures will be described in this section. They were used to determine the characteristics of the test machine by Wang and Lai (1999), and the main results and conclusions from this work will be summarized.

Experimental free response synthesis

Resonance occurs when the dynamic forces in a process excite the natural frequencies in the structure, and a suitable way to identify them is to analyze the frequency response function (FRF) of the system. The FRF is expressed as the ratio of the output vibration (X) to the input force (F) spectra over a defined frequency range (ω).

$$H(\omega) = \frac{X(\omega)}{F(\omega)} \tag{13.1}$$

Vibration can be measured as displacement, velocity or acceleration of the particles in the structure and the FRF will be known as *receptance, mobility* and *inertance* respectively. A resonance is represented in the FRF plot of the system as a peak. Since this excitation force is usually difficult to measure in most

industrial processes, the identification of the natural frequencies of a structure is better done in the laboratory, where the applied force can be selected conveniently. Modal analysis is a common tool used in the laboratory not only to identify the natural frequencies but also the way the structure vibrates at those frequencies (mode shapes) as well as the rate at which the vibrations decay (modal damping). These two components, together with the modal frequency, constitute the *modal parameters* of a structure and they fully characterize the vibration of single degree of freedom (SDOF) models. In fact, each resonance peak can be considered as the response of a SDOF system. Since a FRF consists of a collection of resonance peaks, it is important to understand how these systems can be modelled in the physical, time and frequency domains.

SDOF models

A SDOF model can be described as a combination of a point mass *m*, a massless linear spring with stiffness *k*, and a linear viscous damper *c*, and the constraint that it can move in only one direction (*x*) is assumed. The mathematical model in the time domain when a force f is applied is easily obtained from Newton's second law:

$$m\ddot{x}(t) + c\dot{x}(t) + kx(t) = f(t) \tag{13.2}$$

An analytical model can also be developed in the frequency domain, where the behaviour of each component is expressed mathematically as a function of the frequency of the system: $\frac{1}{k}$ for the spring, $\frac{1}{j\omega c}$ for the damper and $\frac{1}{-\omega^2 m}$ for the mass (Ewins, 1984). At low frequencies the response of the system is dominated by the spring and it is in phase with the excitation. When the frequency increases, the inertial force of the mass becomes more important, until a point is reached where the mass and the spring terms cancel each other. At this frequency, called *undamped natural frequency*, the response is controlled only by the damping term and it lags the excitation by 90 degrees. If the frequency increases even further, the mass term takes control over the system and the response lags the excitation by 180 degrees.

The values of the mass, stiffness and damping used in the analytical model are usually unknown in the real structure. However there is an experimental way of modelling the vibration of a SDOF system, which indirectly leads to these parameters (Brüel & Kjær, 1988). The properties of the system are now defined in terms of the pole location p and the residue R, which are quantities

that can be measured from the FRF plot of the system. The pole location consists of a real part equal to half the -3 dB bandwidth of the FRF peak and an imaginary part which is directly the modal frequency. The peak amplitude of the mode is equal to $\left|\frac{R}{\sigma}\right|$, and this yields the value of the residue since the real part of the pole is the value of the damping σ. The modal frequency is defined as the damped natural frequency ω_d, and (13.3) shows how it is related to the undamped natural frequency ω_0, which in turn is expressed as in (13.4). The damping ratio ζ is also related to these frequencies through (13.5), and the mass is linked to the value of the residue as in (13.6). Knowing the mass, damping and damping ratio, the stiffness is easily obtained from (13.7).

$$\omega_0^2 = \omega_d^2 + \sigma^2 \tag{13.3}$$

$$\omega_0 = \sqrt{k/m} \tag{13.4}$$

$$\omega_d = \omega_0\sqrt{1-\zeta} \tag{13.5}$$

$$R = -j\frac{1}{2m\omega_d} \tag{13.6}$$

$$\zeta = \frac{\sigma}{2\sqrt{k \cdot m}} \tag{13.7}$$

Two of the modal parameters are contained in the pole location itself. The third one, the mode shape, is related to the residue. When a structure is excited with a force, each SDOF experiences a relative modal displacement. The residue of a particular mode is proportional to the product of the modal displacement at the response and excitation SDOF. The combination of the relative displacements of all the SDOF of the structure gives the mode shape for a given frequency.

In practice, the FRF is measured using a dual-channel analyzer, which in turn is connected to a computer where the data is stored for further post-processing. For each mode, the pole location and the residue need to be estimated from this data, but for each FRF measurement the analyzer provides around 800 complex values. With this enormous amount of data the use of a computer is essential, where advanced mathematical algorithms for the estimation are implemented. From the estimated parameters a new analytical FRF curve is obtained, which is superimposed on the measured data so that the operator can evaluate how they fit. This process is known as 'curve fitting'.

Curve fitting

The aim of curve fitting is to extract reliable modal data from the measurements. There are different types of curve fitting techniques that are used depending on the application, and they contain algorithms to reduce the effects of random noise in the measurements and the bias errors, such as any leakage or phase errors, which would cause erroneous parameter estimations. SDOF curve fitters can be used with lightly coupled modes, i.e. when the interaction between different modes is not important. Under these conditions a SDOF behaviour can be assumed around the modal frequencies. The user specifies a band around each mode containing the relevant data that will be used in the curve fitting process. The selection of the band is often a compromise between including as much data as possible and avoid moving far away from the resonance to minimize the effects of nearby modes, as otherwise the assumption of SDOF behaviour would be invalid. When the modes are heavily coupled, multiple degree of freedom (MDOF) curve fitters are used instead. In this case, the operator specifies a region over which the curve fitter will seek the parameters and the number of modes contained in that region. The results using this technique depend to a large extent on the user's skill and experience in specifying the correct number of modes for the model. An example of a plot of the FRF function is presented in Figure 13.2, where the cursors define the band for one of the modes.

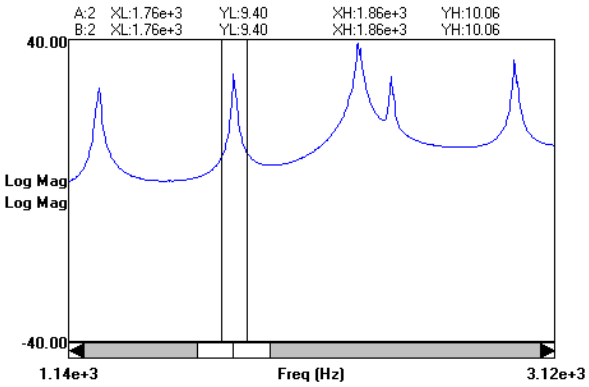

Figure 13.2: Frequency Response Function plot.

After the curve fitting process, each group of the resulting modal parameters is associated with the corresponding mode number. The different modes of vibration contain important information about the inherent dynamic properties of the free structure, i.e. when no forces are acting. The modal analysis of the motor used for the experiments had already been performed by Wang and Lai (1999). It is necessary to describe this process though, since it will provide useful information about how the modal properties that will be used in future calculations have been determined.

The free vibration of the machine structure was achieved using two kinds of excitation: random excitation, provided from a shaker, and impact excitation, using a hammer with a steel tip but without extra mass. The frequency band for the analysis spanned from 0 to 3.2 kHz. The motor was tested resting on the test bench, through four isolators, and also without isolators, suspended together with the support and the base plate by soft rubber bands. In order to examine the contribution to the overall vibration of the different parts of the motor, the response was measured with five different motor configurations: the whole motor structure; without the rotor; without isolators; without rotor and isolators; and finally, without rotor, isolators and end-shields. Only acceleration in the radial direction was measured and the modes of vibration were determined with reasonable accuracy, except perhaps those caused by the isolators.

In order to verify the modal results, the sound power spectra obtained from the machine when driven by three inverters under no load was also determined. It was observed that almost corresponding to each peak in the sound power spectra, a vibration mode was identified when the whole motor or the motor without the rotor was tested, indicating that the modal testing results obtained were reliable. The end-shields had also a great influence on the vibration of the motor, since they impose boundary conditions on the motor casing. Besides, the modes determined without the rotor were similar to those with the rotor, implying that experimental modal testing or numerical modelling may be conducted without the rotor if low-frequency modes are not of interest.

FEM free response synthesis

Any structural model developed using the finite element technique has to be validated using experimental modal tests. While FEM will provide all the modes of vibration, the less significant are likely to be missing in the experimental results. Nevertheless, all the measured modes should correspond to modes calculated

with FEM. Wang and Lai (1999) used the experimental results obtained with the motor to help develop a structural model using the modal analysis solver in ANSYS. In order to investigate the effects of the various substructures on the overall vibration behaviour, six motor models were developed taking into consideration the teeth of the stator, casing, slots on the casing, support and end-shields, as shown in Figure 13.3. It is important to describe these models and the results obtained, in order to justify the selection of one of them for the acoustic calculations presented in this thesis, over the other models.

Each steel lamination in the stator has a density of 7800 kg/m^3, and the Young's modulus was determined to be 13.6 x 10^{10} N/m^2. The total mass of the stator and the windings is 6.6 and 2.88 kg respectively. The material of the stator was first assumed to be isotropic. The element types were Brick eight-node Solid45 and Tetrahedron Solid72 and the boundary conditions of the stator were set to be free at both ends. The effect of the winding was examined first. The windings were taken into account by treating them as an additional mass uniformly distributed in the stator, and this was done by changing the density of the material to 11193 kg/m^3 in model A. It was observed that the windings affect the natural frequencies of the stator very much. Hence, the mass of the windings must be taken into account in developing a structural model with reasonable accuracy.

The effect of the teeth was investigated next. For this purpose, the stator without teeth was considered, model B, which corresponds to the non-teeth region of model A. Both cases with and without windings were also investigated, again by changing the density of the iron material. It was observed that without windings the teeth had a strong influence on the calculated natural frequencies, with variations up to 18%. Also, the natural frequencies with teeth were lower than without teeth, which suggests that the mass of the teeth influences more the results, rather than their stiffness. When the winding was considered, the differences in frequency variations compared to model A were less than 10% in general. The reason for this behaviour is that the total mass of the stator and windings (9.48 kg) is much greater than that of the teeth (2.5 kg) and consequently, the vibration behaviour is dominated by the cylindrical shell, which in this case turns out to be a good approximation of the stator structure when the windings are considered. However, it was indicated that such an approximation might not be valid for other stators, where the different number of teeth and dimensions could lead to a different vibration behaviour of the stator structure.

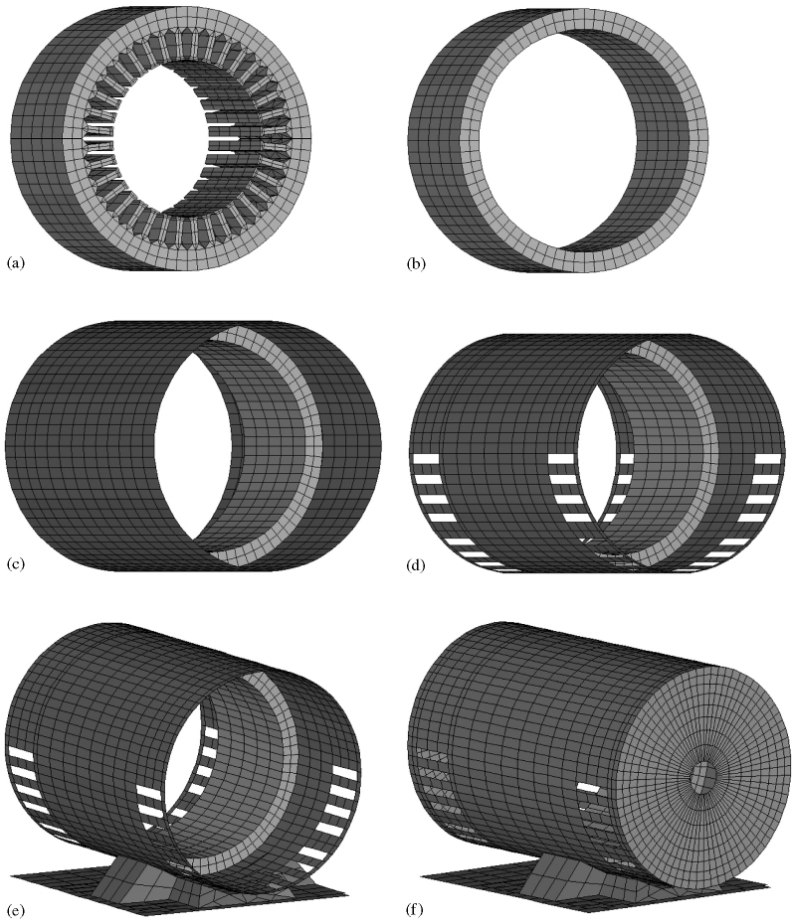

Figure 13.3: Finite element structural models: (a), the actual stator model; (b), a cylindrical shell stator model; (c), a two cylindrical shell model of the motor; (d), a two cylindrical shell model of the motor with slots on the outer casing; (e), a two cylindrical shell model of the motor with slots, the support and the base plate; (f), a two cylindrical shell model of the motor with slots, the support, the base plate and end-shields. Source (Wang and Lai, 1999).

The effect of the casing coupled to the stator and the end-shields was analyzed as well. Previous studies cited in the paper concluded that its effect could be neglected. However, the different physical properties of the material used, as well as the different ratio between the length of the casing and the stator in the test motor, suggested that the effect of the casing might not be negligible in this case. A two cylindrical shell model, which included the mass of the windings in the stator, was developed as model C. The material was first defined as isotropic, but a closer study of the results suggested that the material in the stator should be orthotropic instead. The laminations are compressed in the axial direction and, although the density of the material in the stator remains approximately the same, the stiffness of the stator in the axial direction would not be equal to the one of the stator made in solid material. As it is difficult to determine the pressure between the laminations, a typical value of Young's modulus in the axial direction was chosen, corresponding to 2% of the Young's modulus in the circumferential direction. The results obtained with this modification showed improved agreement with the experimental results. Hence it is essential to consider the material of the stator to be orthotropic. From the results, it could be observed that the vibration modes of the stator and the casing were influenced by the coupling between them. The modes of vibration of the casing were different from those without the coupling, as it would be expected since now the part of the casing attached to the stator is constrained while the rest of the casing is not. The effect of the coupling in the stator was to increase the natural frequencies in the low frequency range, corresponding also to an increase of the stiffness of the stator. At high frequencies the outer casing acts as a mass load to the stator, thus decreasing the natural frequencies. It was concluded therefore that the outer frame of the stator can play an important role in the vibration of small and medium-sized motors, where the mass of the frame is not negligible compared to that of the stator, and this effect would be further emphasized if the dimensions of the two structures are also quite different.

In order to further improve the calculated frequencies, the ventilation slots in the motor casing were included in model D. The reduction in the mass of the casing, and thus the load on the stator, increased the frequencies of the stator modes marginally, while the change in the stiffness of the casing decreased the frequency of its modes substantially, showing a better agreement with the experimental results.

The motor structure could be more accurate if the support and base plate are included, as shown in model E. The inclusion of these parts reduces the

frequencies of the casing due to the increase of its effective mass. The effect of the stator teeth was again examined with this new model, and the results were within 5% compared to the model without teeth. Hence, the teeth of the stator can be neglected in the vibration analysis.

Finally, the end-shields made of aluminium by casting are incorporated in model F. Since their real geometry is rather complicated and the interest is not in their vibration itself but in their influence on the vibration of the casing, an equivalent end-shield with the form of a circular flat plate of the same mass, 0.36 kg, and a thickness of 6 mm was considered. The end-shields are coupled to the casing by coupling the corresponding nodes in all degrees of freedom. From the analysis of the results, most of the vibration modes could be predicted, although the results show more discrepancy than the previous model. This is due to the complicated coupling between the end-shields and the casing, not all the points along the edges of the two structures are coupled and those who are, present different coupling strengths from each other. These details are too complex to consider in the model and nevertheless, the natural frequencies of all the modes identified in the calculations were within 10% of the experimental results, concluding that the model may be acceptable for acoustic prediction. Further studies showed that the details of the motor structure such as slots, support, base plate and end-shields affect the vibration behaviour of the motor very much, so they need to be modelled.

The geometry and modal results obtained from model F are the ones that were used in SYSNOISE for the noise calculations in this chapter.

13.3 Electromagnetic analysis

The purpose of this section is to explain how the electromagnetic models were built and how the airgap forces were calculated and applied to the SYSNOISE model. The cases studied are those corresponding to [d=m, q=0], [d=0, q=m] and [d=0, q=0] in the experiments. Only the harmonic frequency of 490 Hz was considered, and the machine rotated at 70 r.p.m, at no load. The different cases were simulated using the drive system presented in Chapter 10 (Figure 10.12). An example of the three phase currents for direct and quadrature modulation is presented in Figure 13.4. These currents were applied to the coils in the FEM electromagnetic model, where the airgap stress was calculated.

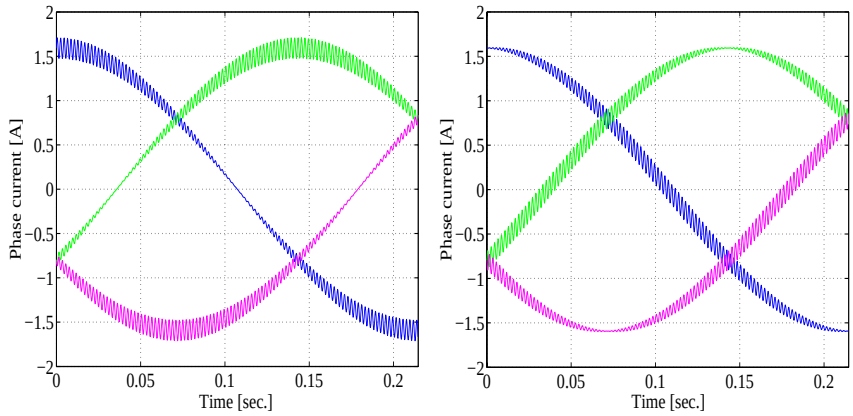

(a) Direct modulation currents (b) Quadrature modulation currents

Figure 13.4: Simulated phase currents for direct and quadrature modulation.

The 3D model

The aim was to simulate the motor with a 3D model in order to take into consideration end-winding effects, and also the influence of skewing in the rotor slots, which contributes to decrease the torque ripple and thus the noise emissions. This model is shown in Figure 13.5, where the modulus of the flux density is plotted at no load. The aluminium in the rotor has been removed from the picture for the sake of clarity. Part of the conductors are visible on the surface of the stator along the extrusion direction, but this is only due to a display problem in the version of OPERA used for the calculations. The number of nodes and elements was 44020 and 32352 respectively.

The solution presented in Figure 13.5 was obtained from a harmonic analysis. In this case the model could only be solved for single a.c. excitation frequencies at a time, and for a given slip. The currents from the SIMULINK model could be uploaded in a transient solver, where the rotor was rotated with a user-defined speed. However, the FE simulations could not be performed, since they failed due to convergence problems in the solver. Besides, although symmetry could be exploited in the extrusion direction, it was not possible to apply it

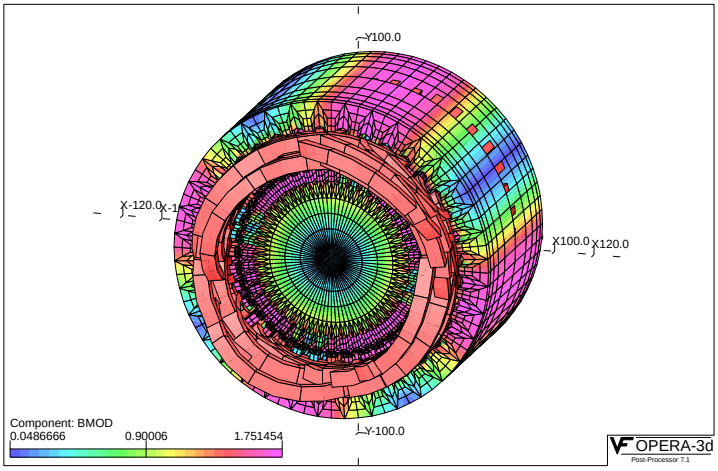

Figure 13.5: 3D FEM model of the test motor.

along the circumferential direction, which increased dramatically the number of elements in the model and hence the computation time. These problems contributed to the transition towards the 2D software.

The 2D model

The 2D model corresponds to that described in Chapter 12. The currents in Figure 13.4 could only be loaded as tables using the transient analysis module. This solver included the effects eddy currents. The airgap forces were calculated at 1952 time steps along one period of the fundamental current, which provided a resolution of 9.3 samples per noise cycle. The fact that the maximum number of output cases per analysis was limited to 99 implied that 20 analyses had to be carried out in order to obtain the results at the 1952 points within one cycle of the fundamental. Each analysis was re-started from the last value in the previous solution. A static analysis was performed before starting to rotate the rotor, in order to reduce starting transients. In fact, no transients were observed in the first fundamental cycle of the current. These results were the same as those at the end of the third cycle, after one rotor turn. Therefore it was concluded that the forces could be extracted already from the first cycle of the fundamental. The calculations were carried out in a PC pentium 1.2 GHz processor equipped

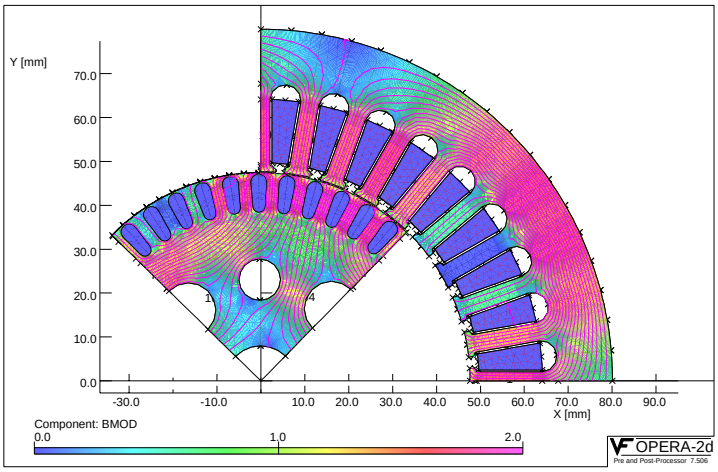

Figure 13.6: Flux density distribution in the 2D FEM model.

with 500 Mb RAM, and the 1952 simulations for each case were completed in 60 hours, including post-processing. A picture showing the flux density in the motor at one position is presented in Figure 13.6.

Force computation

The shell in model F was divided into 72 elements along the circumferential direction and 5 in the longitudinal direction. The forces in the electromagnetic model were calculated at 13 points along each equivalent element in the shell, and the frequency spectrum of the forces in Cartesian components was applied to the nodes located along the inner surface of this shell. The results in the time domain were translated into the frequency domain using the fast Fourier transform function (FFT) in MATLAB. The nature of the 2D force calculation implied that all the nodes along the extrusions in the shell were assigned the same force as their corresponding node in the first layer. The force applied at one node represents the one that should be applied in the middle of the adjacent element. Since there is actually one more layer of nodes than of elements, the nodes around both edges of the cylinder were assigned half of the force that is applied at the inner nodes. The force densities in the airgap were obtained from the electromagnetic FEM simulation, implementing (13.8) and (13.9)

through the middle of the airgap. The values of H_x and H_y correspond to the Cartesian components of the airgap magnetomotive force, B_x and B_y are the flux densities and N_x and N_y are unit length vectors corresponding to the x and y components around the motor. The force densities, F_x and F_y were transformed into force by multiplying with the area of an imaginary element at the airgap, spanned through the same angle as one element in the back core of the shell, and with the same length. In this way, the total force applied is maintained constant, although the force density in the back core is reduced since the area of the elements is increased.

$$F_x = B_x H_n - N_x \frac{H_m}{2} \tag{13.8}$$

$$F_y = B_y H_n - N_y \frac{h_m}{2} \tag{13.9}$$

$$H_n = H_x N_x + H_y N_y \tag{13.10}$$

$$H_m = B_x H_x + B_y H_y \tag{13.11}$$

There are several ways of integrating the force in the electromagnetic model. One extrusion in the acoustic model consists of 72 elements and there are 36 teeth around the stator. Therefore, half of the elements could be assigned the force in the teeth and the other half the force in the slots, alternating between adjacent elements. In practice, part of the force in the sides of the teeth was also applied to the slot element, since the width of the teeth and the slots is not the same. The integration performed in this way was referred to as the *odd function integration*. The other possibility is to do the integration of the forces around groups of half a tooth and half a slot, and vice-versa for the adjacent group, and this was referred to as the *even function integration*. An example of the forces calculated with both methods is presented in Figure 13.7. The odd function integration was used in the simulations since it resembled the force distribution around the airgap of the real machine. However, it could be argued that the gradient of the forces in the back core between adjacent elements would be small and therefore the even function should be used instead. It was observed that the acoustic results obtained using the odd function integration correlated better with the measurements.

Two tables were created for each one of the Cartesian components of the forces that should be applied at each node in the acoustic model. Each table consisted of three columns, the first one specifying the frequency and the second and the third ones specifying the real and imaginary components of the Fourier

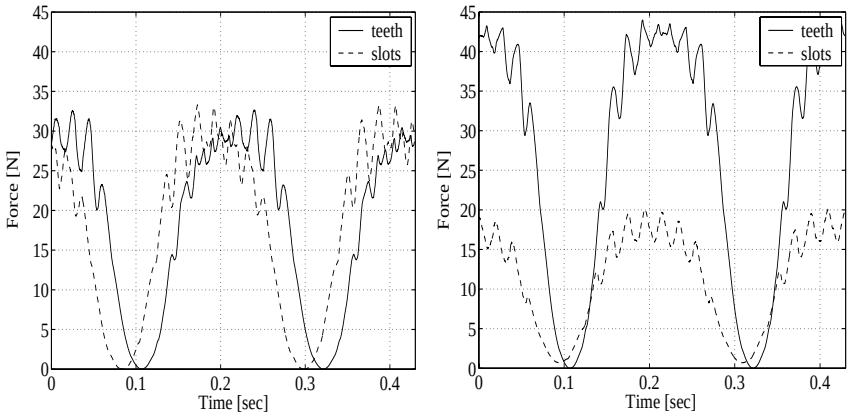

(a) Even integration

(b) Odd integration

Figure 13.7: Force at the teeth and slots for the even and odd integration functions.

transform. The spectrum of the total force was computed using (13.12) in order to compare the applied force for the different cases simulated. This was done by adding the absolute value of the spectrum at the 72 nodes around one layer of elements. The expression for F_N and its components are given in (13.13)-(13.15).

$$F_T = \sum_{N=1}^{72} F_N \tag{13.12}$$

$$F_N = \sqrt{F_{nx}^2 + F_{ny}^2} \tag{13.13}$$

$$F_{nx} = \sqrt{\Re\left(f_{nx}\right)^2 + \Im\left(f_{nx}\right)^2} \tag{13.14}$$

$$F_{ny} = \sqrt{\Re\left(f_{ny}\right)^2 + \Im\left(f_{ny}\right)^2} \tag{13.15}$$

In this way, the values of the total force were calculated when the machine rotated at 70 r.p.m. at no load. Figure 13.8 shows the results of the total force in one extrusion for direct current modulation ([d=m, q=0]) and quadrature current modulation ([d=0, q=m]) with a noise frequency of 490 Hz, as well as the

case with no modulation ([d=0, q=0]). For comparison, the narrow band results were transformed into 1/12 octave bands by linearly adding all the components within each band, see Figure 13.8(d). This plot shows a substantial increase in the total force due to either direct or quadrature current modulation.

Figure 13.6 shows that a considerable amount of iron in the machine is saturated. The flux density reaches 1.75 Tesla in the rotor teeth and 1.6 Tesla in the stator teeth and in the stator back core. It is reasonable to assume that the saturated part of the BH curve at best can be determined experimentally within 10% accuracy. A sensitivity analysis was performed by increasing the saturated part of the BH curve by 10% for the case [d=m, q=0] (see Figure 13.9(a)). It can be seen from Figure 13.9(b) that the total force was increased by up to 25 N at some frequencies around 500 and 1000 Hz.

13.4 Acoustic analysis

The acoustic simulations were performed for a frequency range between 80 Hz and 2250 Hz, in steps of 10 Hz. The sound power results at these frequencies were stored and converted into 1/3 octave bands for comparison with the measurements. The sound power level (PWL) without noise excitation is shown in Figure 13.10(a), and the results when a 490 Hz harmonic is added to the direct or quadrature currents are shown in Figure 13.10(b), and Figure13.10(c), respectively. A structural damping of 0.01 for all the modes was used in these simulations. Another way of comparing the predictions with measurements is to plot the difference in the sound power level between the case when one of the currents is modulated and the case when there is no modulation at all. These results are presented in Figure 13.10(d) and Figure 13.10(e), and a comparison between the direct and the quadrature current modulation is shown in Figure 13.10(f).

In general, from these plots it can be observed that there are some discrepancies below 400 Hz between the simulated and the experimental results. This may be attributed to the rotor not being included in the acoustic model (Wang and Lai, 1999). It should be noted that when no extra noise is added to the currents the sound power level at the 1 kHz, 1.25 kHz and 2 kHz centre frequencies is considerably higher compared to the measurements, see Figure 13.10(a). These levels are maintained when any of the currents is modulated. At the excitation frequency of 490 Hz the difference in the measured PWL between direct and quadrature modulation is 4 dB, whereas this difference reaches 30 dB in

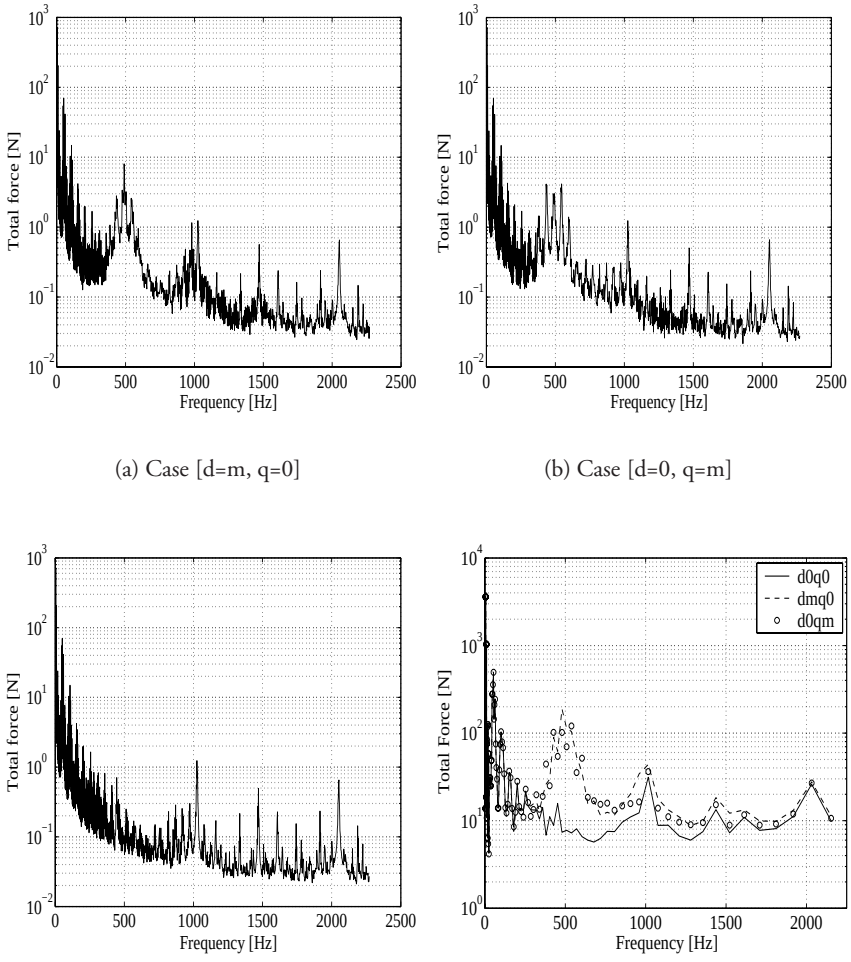

(a) Case [d=m, q=0]

(b) Case [d=0, q=m]

(c) Case [d=0, q=0]

(d) 1/12 octave band comparison

Figure 13.8: Spectrum of the total force for the different simulation cases.

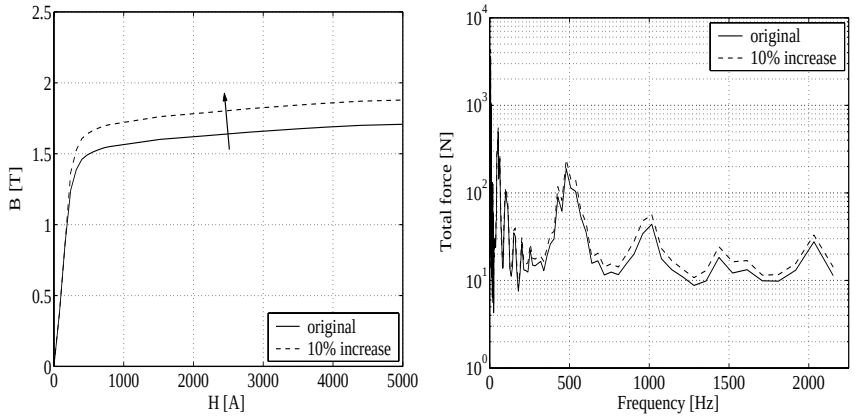

(a) BH curve increase

(b) Force comparison for [d=m, q=0]

Figure 13.9: Effect of a BH curve change in the calculated airgap force.

the simulations, see Figure 13.10(b) and Figure 13.10(c). The difference in the measurements is because the acoustic noise emission is more readily enhanced by radial forces (direct current) than tangential forces (quadrature current).

From the incremental plots, it can be observed that while the general trend is similar for the predictions and measurements, there are some noticeable quantitative differences for the frequency range between 400 Hz and 1 kHz. The agreement between predictions and measurements at higher frequencies (above 1 kHz) is rather promising. This seems to indicate that the acoustic model does not reproduce accurately the behaviour of the experimental motor below 1 kHz, and this was confirmed through a detailed modal analysis. The modes of vibration up to 2 kHz and the part of the motor they are associated with are presented in Table 13.1, both for the simulations and the experiments. It can be appreciated that below 1 kHz only three modes are calculated in the FE simulation for the structural model used in the acoustic simulations, and all of them are associated with the seat. However, the experiments show ten modes of vibration in the same frequency range, associated with the stator, rotor, casing and seat. Also, the mode close to the 490 Hz excitation frequency is related to the seat instead of to the stator/casing as in the experiments. Hence, the re-

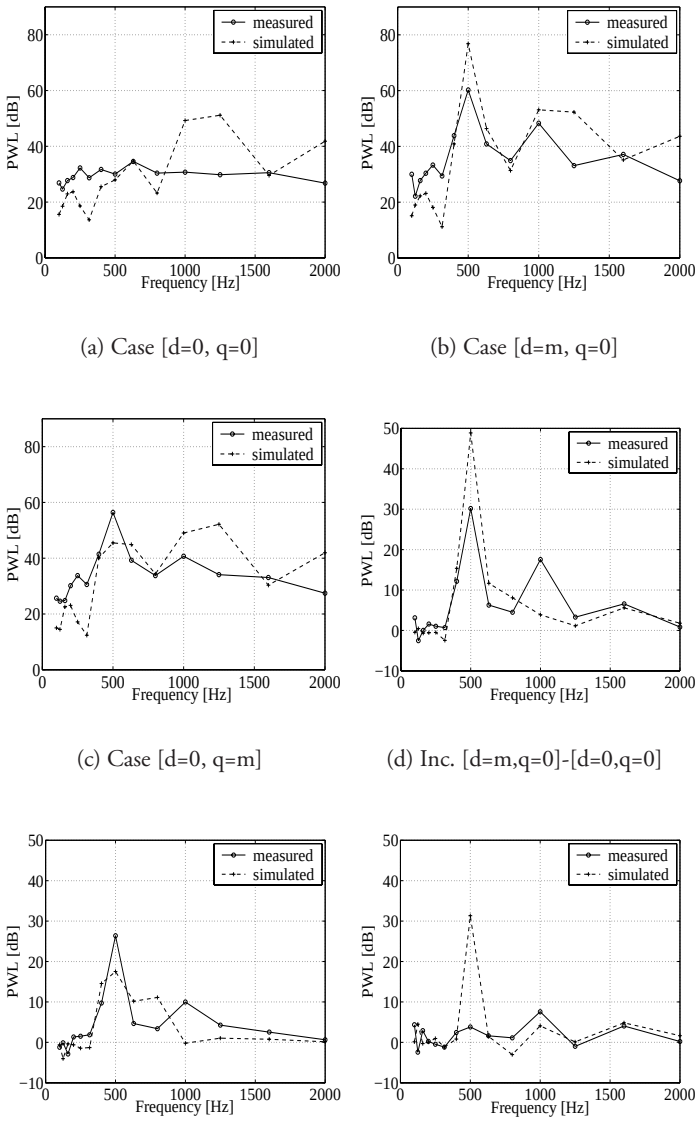

(a) Case [d=0, q=0]

(b) Case [d=m, q=0]

(c) Case [d=0, q=m]

(d) Inc. [d=m,q=0]-[d=0,q=0]

(e) Inc. [d=0,q=m]-[d=0,q=0]

(f) Inc. [d=m,q=0]-[d=0,q=m]

Figure 13.10: Comparison of simulated and experimental acoustic results at 1/3 octave band centre frequencies.

Experiment	**Simulation**	**Experiment**	*Simulation*
294 rotor		1105 stator	1123 stator
	375 seat	1240 seat	1097 seat
392 st/casing		1270 casing	
490 st/casing		1307 casing	
567 seat	485 seat	1393 seat	1353 seat
664 rotor		1480 seat	1559 seat
717 seat	695 seat		1535 casing
770 casing		1655 casing	1572 casing
816 casing		1743 stator	1682 stator
928 rotor		1795 stator	1933 stator
961 casing		1869 casing	1897 casing
1057 stator	1121 stator	1919 casing	

Table 13.1: Comparison between the simulated and the experimental modes of vibration.

sponse of the structure at this frequency would be expected to be quite different from the measured response. Above 1 kHz, there is better agreement between the experimental and the simulated results, not only in the frequencies but also in the part of the motor the modes are associated with, hence the better agreement above 1 kHz between the simulated and measured sound emissions. The peaks observed at 1 kHz, 1.25 kHz and 2 kHz are related to rotor harmonics. In fact, skewing was not included in the 2D electromagnetic model, so the rotor harmonics are not appropriately damped at these frequencies.

The results due to a change in the damping coefficient of the material, from 0.01 to 0.05, are presented in Figure 13.11(a). It can be observed that the sound power level could be reduced by up to 10 dB at 500 Hz, 800 Hz, 1250 Hz and 2000 Hz, whereas the effect is negligible at other centre frequencies. Finally, the results from a change in the properties of the material, by increasing 10% the saturated part of the BH curve, are presented in Figure 13.11(b). It can be observed that the variations in the sound power level are around 3 dB or less up to 2 kHz.

Finally, the sound pressure distribution in the motor and the surroundings obtained from SYSNOISE at 490 Hz is presented in Figure 13.12, for the case with no modulation. The results when the direct and the quadrature cur-

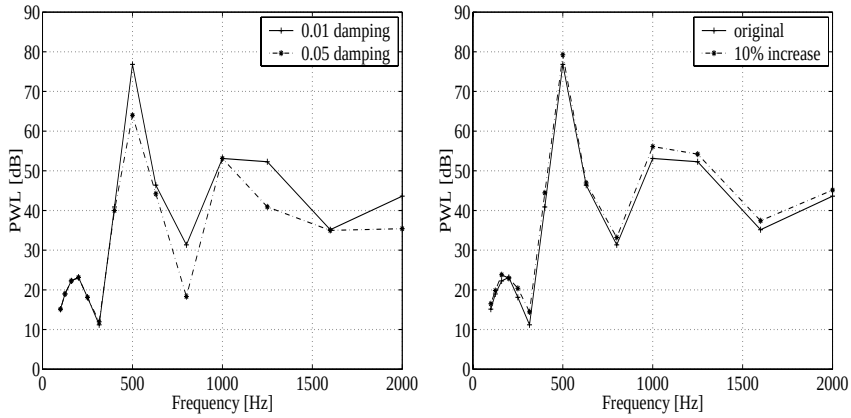

(a) Change in damping

(b) Change in BH curve

Figure 13.11: Effect of a change in the damping and in the BH curve on the sound power level for the case [d=m, q=0].

rents are modulated are presented in Figure 13.13 and Figure 13.14 respectively. These plots actually confirm that at this frequency the vibration of the motor in the acoustic model is associated with the seat instead of with the stator, where no displacement is recorded on the surface of the casing. It should be noted that the scales used for these plots are different since otherwise the cases [d=0, q=0] and [d=0, q=m] can not be distinguished compared to the case [d=m, q=0]. The lower limit of the scales is 35 dB for all the plots, and the upper limit is 40 dB, 85 dB and 70 dB for the cases [d=0, q=0], [d=m, q=0] and [d=0, q=m] respectively.

13.5 Conclusions

The aim of the noise prediction is to be able to model the acoustic radiation from a machine without actually building it, in order to implement appropriate noise control measures at the design stage. The deterministic approach using FEM/BEM has been adopted to predict the noise emissions from a vector controlled induction motor.

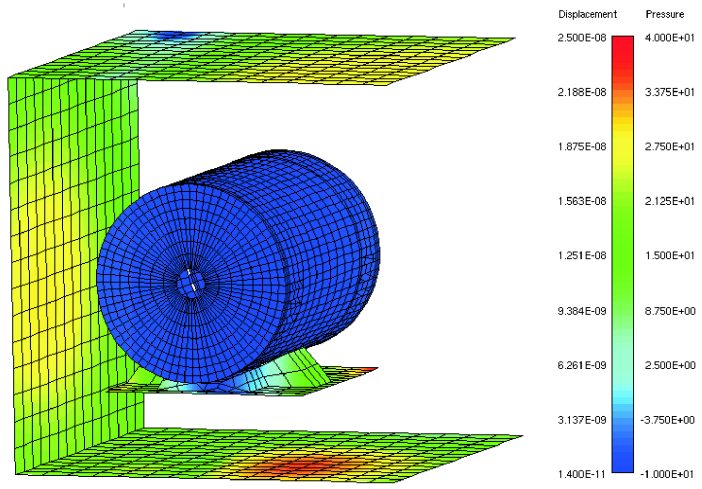

Figure 13.12: SPL distribution at 490 Hz, case [d=0, q=0].

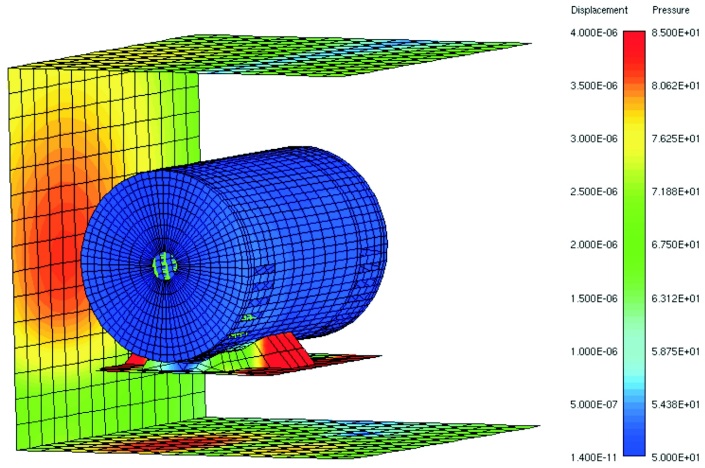

Figure 13.13: SPL distribution at 490 Hz, case [d=m, q=0].

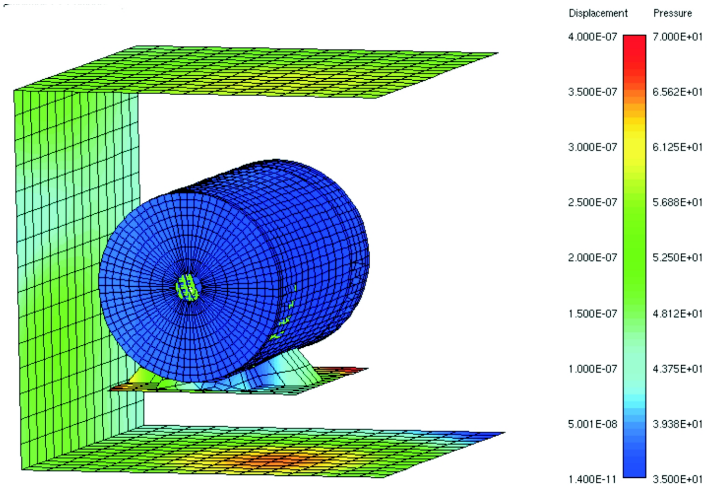

Figure 13.14: SPL distribution at 490 Hz, case [d=0, q=m].

It was shown that the disagreement at low frequencies was due to the inaccuracy in the structural modal model. The number of modes of vibration predicted in ANSYS in this region was considerably less compared to the measurements. Also, these modes were associated with other parts of the machine, specially at the 490 Hz frequency used for the prediction. Including the rotor and perhaps the teeth in the structural model might improve these results. However, the complexity of the model would be considerably increased, especially since it is difficult to assess how the windings constrain the mobility of the teeth.

However, the behaviour of the model resembled that of the machine above 1 kHz, as could be observed from the modal results and the noise prediction. Now the results are affected by the force calculation, since the skewing of the rotor, which minimizes the rotor harmonics, has not been modelled. This could explain why the levels of noise were considerably higher above 1 kHz in the simulations, when the currents were not modulated with extra noise. Skewing could be accurately modelled using a 3D electromagnetic model. However, there are still important limitations in 3D transient FEM calculations, both in complexity and computation time.

The influence of uncertainties in the damping of the structure and the sat-

urated part of the BH curve has also been assessed. Increasing five times the overall damping applied to all the modes did not affect the response at different frequencies in the same way. Basically, some of them remained unchanged whereas others experienced a reduction of 10 dB. Hence, the damping is a critical factor for an accurate noise prediction. However, it is difficult to estimate a priori in electrical machines, due to the particular assembling characteristics of different machines and the modifications introduced by the winding. A change in the material properties corresponding to a 10% increase in the saturated part of the BH curve was associated with a change of 3 dB or less in the acoustic simulations. Therefore, compared to the damping, the inaccuracies in the saturated part of the BH curve have relatively low impact in the noise prediction.

Chapter 14

Acoustic properties of stators with a layer of air gaps

14.1 Introduction

Adjustable-speed drives in industry and commercial buildings embodied as converter fed a.c. induction motor drives have a major drawback in increased magnetic noise. This is due to the strong interaction between the fundamental airgap flux and harmonic components in the voltages and currents from the converter. To deal with this problem, numerous studies have been conducted to investigate possible changes in the converter switching pattern that would reduce these harmonics, or move them to a frequency range where the human ear is less sensitive, as pointed out in Chapter 9. However, not enough effort has been directed towards reducing noise through a change in the structure of the motor. The aim of this chapter is to evaluate the influence that several structural changes in the stator have in the acoustic behaviour of the machine.

Previous work

Andersson and Skarrie (1997) carried out a theoretical study using a structure where a layer of air gaps was introduced around the stator periphery to reduce the noise emission. The goal was to isolate the outer surface of the stator, and therefore the surrounding air, from the vibrations transmitted through the teeth into the core. The air gaps in the new mass-spring-mass system (inner core - air gaps - outer core) were optimized so as to reduce the vibrations of the new structure. A prototype was built and tested, but there was no improvement

in the acoustic behaviour compared to the original structure. However, no in-depth investigation was carried out into why such a structure did nod lead to the desired improvements. The work presented in this chapter provides further insight into understanding the mechanisms of noise production in this novel design solution using combined structural FEM and acoustic BEM simulations. Other structures with different air gap design are also studied, as well as the ideal case where the inner core and the outer core are completely separated by a continuous airgap layer.

14.2 Basic model

The vibrations produced by the airgap forces are transmitted through the teeth into the core, and then into the surrounding air. The teeth can contribute to the vibration of the stator since their stiffness in the tangential direction is less than that in the core. This contribution to the noise production becomes more important if the tangential airgap forces are big enough to induce a tangential movement of the teeth. However, the influence of the radial forces in the teeth is negligible, and the teeth mainly serve as a path for the transmission of this excitation into the core. The simulations in this chapter are only concerned with the transmission of the vibrations from the core into the surrounding air, independent of whether or not the teeth contribute to these vibrations.

The modes of vibration in the machine structure were calculated using ANSYS version 5.1. The core was modelled as a cylinder using Solid45 elements, see Figure 14.1. The laminated nature of the structure was simulated by setting different values for the Young's modulus in the circumferential and in the axial directions, $2.72 \cdot 10^9$ and $1.36 \cdot 10^{11}$ respectively. The element type and the physical properties of the cylinder correspond to those used in the stator of the motor by Wang and Lai (1999), which provided a good correlation between the experimental and numerical modal analysis results. The cylinder had an inner radius of 68 mm, an outer radius of 93 mm and a length of 60 mm, and the number of nodes and elements was 4032 and 3024 respectively. The size of the elements was adapted to achieve good accuracy when the model was used for the acoustic simulations, which required a minimum of six elements per wavelength. The upper frequency for the acoustic analysis was 5 kHz, and thus the maximum length allowed for any of the three dimensions of the elements was 11 mm. In order to meet this specification, the number of divisions along the circumferential and axial directions were 72 and 6, respectively. With this dis-

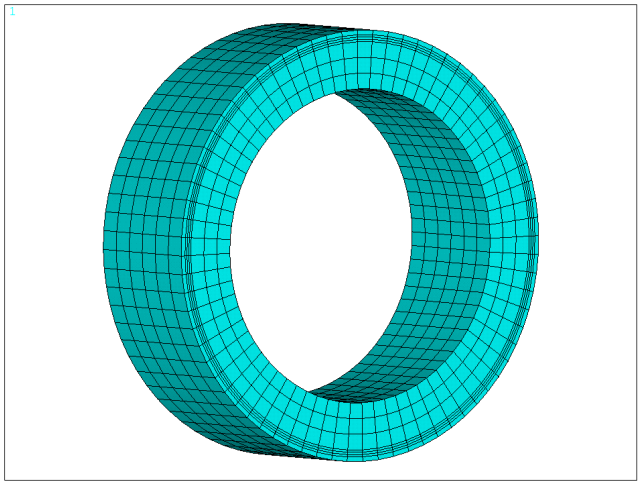

Figure 14.1: Cylindrical model of the core.

tribution, the area of each element in the inner circumference became $2.1 \cdot 10^{-5}$ m^2. In the radial direction, the structure was meshed in a series of layers graded towards the surface of the cylinder (Figure 14.1), where the modifications in the form of air gaps will be introduced.

The modal analysis of the structure was performed using the subspace method in ANSYS, and all the modes of vibration up to 5 kHz were extracted. These modes, together with the geometry, were imported into SYSNOISE. In this package, a finite element (FE) model was used first to calculate the vibration response in the surface of the structure. The magnitude of the applied stress was $5 \cdot 10^4$ N/m^2, which corresponded to a force of 1.05 N at each element located in the inner surface of the cylinder. The components of the applied force at the nodes were set so that the magnitude of the force was the same for all the nodes and the direction pointing outwards in the radial direction. The vibration response was then used to calculate the radiated sound power using a boundary element (BE) model. This model was solved using the BE indirect variational approach (Zhou, 1993).

The mechanical input power in a structure is defined as the product between the force and the vibration velocity at the driving point. In general, this

power is converted into two components: the vibration input power, which in turn is converted into acoustic power depending on the radiation efficiency, and the power dissipated by structural damping. In the following, the vibration input power will be referred to simply as input power. In the BE indirect method, the radiation efficiency is calculated as the ratio of the output power (W_o) to the input power (W_i), which are defined as in (14.2) and (14.1),

$$W_o = \frac{1}{2} \int \frac{p\sigma^*}{-ip\omega} dS \tag{14.1}$$

$$W_i = \rho c \int \bar{v}_n^2 dS \tag{14.2}$$

where ρ is the density of the fluid (air in this case), c is the speed of sound, $\bar{v}_n^2$ is the space average mean-square normal velocity of the surface, S is the area of the radiating surface, $i = \sqrt{-1}$, p is the acoustic pressure, σ^* is the complex conjugate of the single layer potential, and ω is the circular frequency. It should be noted that the radiation efficiency calculated in this way is equivalent to the definition found in the specialized literature (Harris, 1991), which is the ratio of the sound power radiated by the structure to the sound power radiated by a piston (which is large compared with the acoustic wavelength) vibrating with the same space-average mean-square velocity as the structure, see (14.3) . If the spatial velocity is uniform then the behaviour is like in the case of the piston. If the spatial velocity is not uniform, then the behaviour is similar to a piston with a uniform velocity equal to the spatial averaged velocity of the structure.

$$\sigma = \frac{W_o}{\rho c S \bar{v}_n^2} \tag{14.3}$$

Equations (14.2) and (14.1) are evaluated through all the radiating surfaces, and the result for the active sound power is determined over a surface enclosing the source, as it is done experimentally by means of sound intensity measurements. The coupling between the structure and the surrounding fluid was defined as 'weak'. This is true when the fluid is air, since the modes of vibration of the structure are not modified by the surrounding fluid. Nevertheless, simulations were also performed using a 'strong' coupling and the changes in the results were negligible.

The geometry analyzed contains a cavity, and when used to calculate exterior radiation problems, the solution is not unique. This means that there is more than one solution at a given frequency, but it is not possible to know whether the solution has converged to the right answer. The unreal solutions correspond to the resonance frequencies of the cavity and when a solution is obtained for one of these frequencies, the only way of ensuring that the solution converges to a correct answer is to ensure that the sound pressure field inside the cavity does not become too large because of resonance. When using a BE direct method this can be achieved specifying a minimum number of points (known as overdetermination points) inside the cavity, where the sound pressure is constrained to be zero. In this case the solution is 'overdetermined', since there are initially m equations and m unknowns but, by specifying additional points inside the cavity, new constraints are introduced overspecifying the problem. When using a BE indirect method, the treatment to overcome this 'non-uniqueness' problem is to add some impedance (absorption) inside the cavity. However, according to the SYSNOISE manual, impedance elements should not be used inside closed volumes in a BE indirect model which is linked to a structure. In this case, 'singularities' in the response will be due to physically-correct behaviour, the interaction of internal resonances of the volumes through the flexible structure to the exterior. Since all the models in this thesis are simulated by using a BE indirect model which is linked to a structure, the 'non-uniqueness' problem will not be present and no remedy is needed for this phenomenon.

The superposition method was used for the acoustic analysis, and it is based on a linear summation of the contributions from the different modes. Each mode can be represented as a curve with a resonance at a certain frequency. The response at the resonance frequency is dominated by the mode at that frequency. At any other frequency, the response depends on the location of the nearby resonance frequencies and the number of modes involved in the addition. The results obtained from the basic model (Figure 14.1) are compared in the following sections with other models where some changes are introduced in the core structure.

14.3 Zig-zag gap model.

The shape of the zig-zag gap is shown in Figure 14.2, and it resembles the one studied by Andersson and Skarrie (1997). The gaps were distributed in two adjacent layers and shifted in the circumferential direction. These gaps were

located close to the stator surface, at 95% of the outer radius, in order to reduce their interaction with the natural paths followed by the flux. The number of elements in the model was reduced to 2448, while the number of nodes was unchanged.

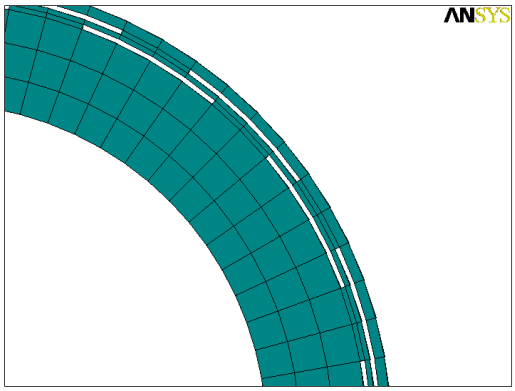

Figure 14.2: Zig-zag gap model.

The fact that some iron material is replaced by air results in a decrease in the weight of the structure, which in turn affects the modal frequencies. Thus two cases were considered. In the first case, the density of the new model was kept the same as the basic model, which implied a reduction in its total weight. In the second case, the density of the new model was increased so that the weight of the basic model was maintained. Figure 14.3 shows a comparison between the total sound power level (PWL) radiated by the three different structures, when a material damping of 0.01 was used. It can be observed that the frequencies of the zig-zag gap model with constant weight have slightly different peak frequencies compared to the case with constant density, but their response is still very similar up to 3 kHz. Above this limit the curve of the constant weight model is slightly shifted towards lower frequencies, as it would be expected since the modal frequencies decrease when the mass of the system is increased.

The acoustic response of the zig-zag gap model is actually worse compared to the basic model. The PWL is increased below 2 kHz. Between 2 kHz and 3 kHz the response is characterised by a sudden change in the slope of the PWL. The radiation efficiency in this region is significantly more accentuated in the zig-zag model, as shown in Figure 14.4. Above 4 kHz the PWL is slightly higher

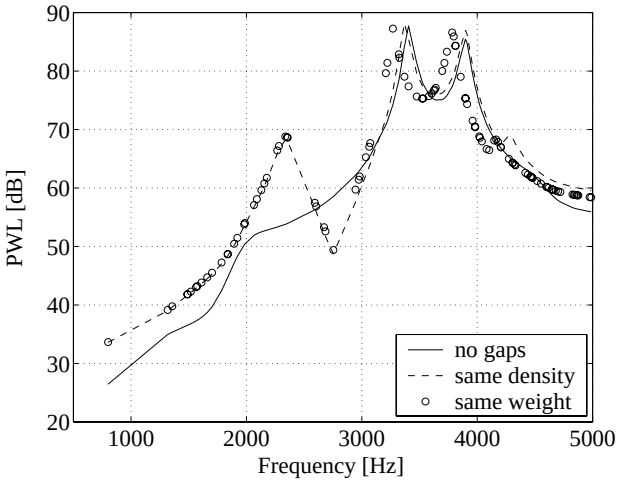

Figure 14.3: PWL of basic and zig-zag gap models, damping 0.01.

than in the basic model, even though the radiation efficiency is considerably lower in the zig-zag model. Although the force applied in the different models is the same, the input power is different (Figure 14.5) because the structures are different. The structure with gaps is less stiff, so it would be expected to have a higher response velocity and therefore higher input power. In general, the increase in the PWL is a result of higher input power and, to a certain extent, higher radiation efficiency in the zig-zag model, as shown in the figures.

The influence of the material damping was tested for the constant weight case. The radiated sound power level for a material damping of 0.001, 0.01 and 0.1 is presented in Figure 14.6. A decrease in the damping implies an increase in the PWL at the resonance frequencies above 3 kHz. When the damping is increased from 0.001 to 0.1, the PWL at the peak frequencies above 3 kHz is reduced by 20-40 dB. This behaviour is explained by the input power being also reduced above 3 kHz due to the lower response velocity of the structure when the damping is increased, as shown in Figure 14.7. The radiation efficiency in this region is also decreased when the damping is increased, as shown in Figure 14.8.

The results for the zig-zag gap structure agree with those for the prototype presented by Andersson and Skarrie (1997), see Figure 14.9. That is, the

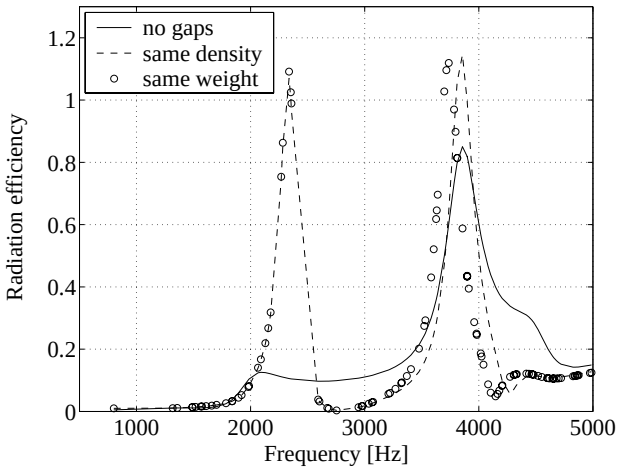

Figure 14.4: Radiation efficiency of basic and zig-zag gap models, damping 0.01.

acoustic response is not improved when the gaps are introduced around the stator, and it is characterized by a shift in the resonance frequencies. However, it should be noted that the results are not directly comparable to the basic model, since the experimental stator included teeth and windings. Its vibrations were also constrained by the casing and the end-plates attached to the stator as in any conventional machine, and the exciting force was also different.

The idea of introducing the gaps in the back of the stator core was based on the assumption that the vibrations are mainly transmitted through iron and that the air barriers would contain these vibrations within the inner part of the core, thus isolating the outer part and also the surrounding air. The unsatisfactory results were initially attributed to the fact that the vibrations could still be transmitted through the thin iron paths located between the two air gap layers. Hence, reducing the amount of these paths would contribute to a better isolation, and this led to the study of a new geometry.

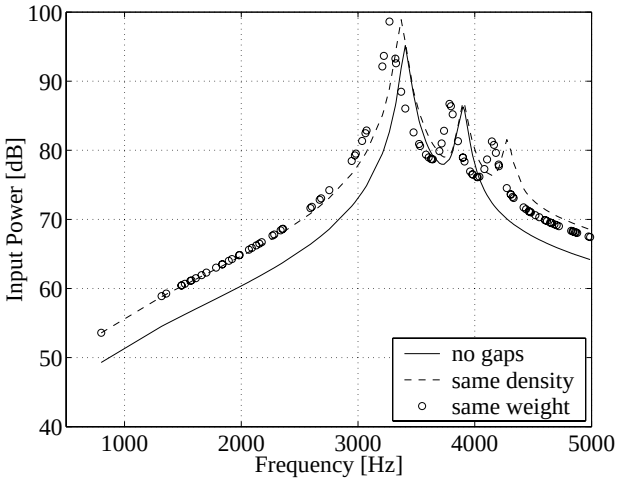

Figure 14.5: Input power of basic and zig-zag gap models, damping 0.01.

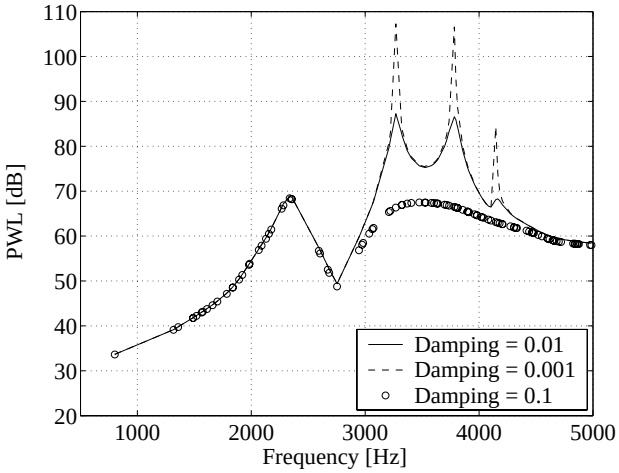

Figure 14.6: PWL of zig-zag gap model with constant weight for different damping coefficients.

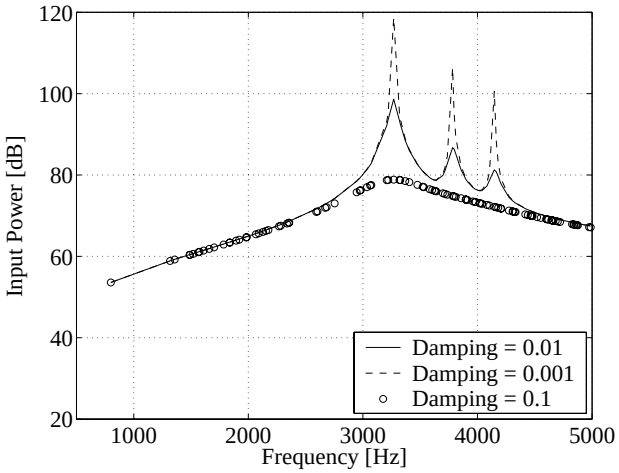

Figure 14.7: Input power of zig-zag gap model with constant weight for different damping coefficients.

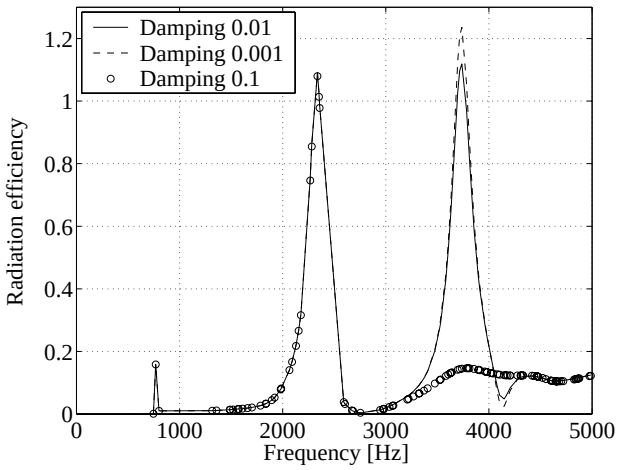

Figure 14.8: Radiation efficiency of zig-zag gap model with constant weight for different damping coefficients.

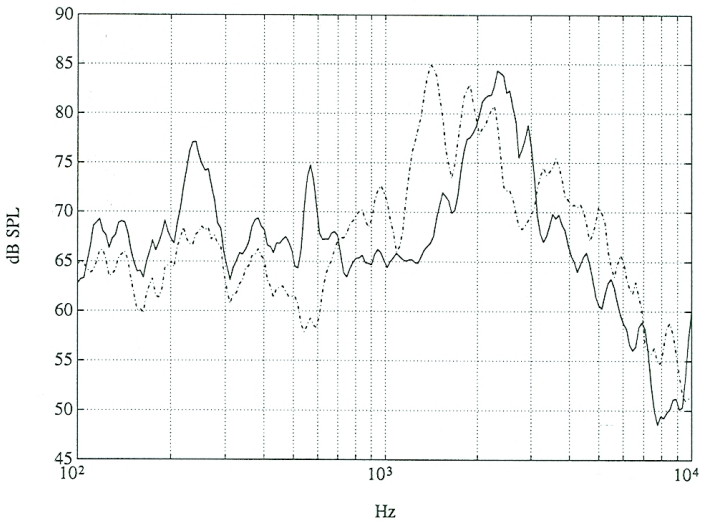

Figure 14.9: Experimental results from Andersson and Skarrie (1997). The continuous line corresponds to the prototype without air gap layers, and the dashed-dotted line to the prototype with air gap layers.

14.4 Four gap model

This model was built by replacing the iron with air between the gaps and between the two air gap layers in the zig-zag gap structure. Only four small areas of connection remained between the inner and outer parts of the core, as shown in Figure 14.10. The number of nodes and elements decreased to 3136 and 1800 respectively. A comparison between the PWL obtained from the new structure and the basic model is shown in Figure 14.11. Within the same frequency range, there are seven peak frequencies for the PWL in the four gap model compared with only two in the basic model. For the four gap model, the peak frequencies below 2.5 kHz are lower for the constant weight case compared with the constant density case, because of its heavier mass. The radiation efficiencies for the four gap model are considerably higher than those of the basic and zig-zag gap models for frequencies above 2.5 kHz, as shown in Figure 14.12. The input power, however, is considerably lower than the radiated acoustic power at peak frequencies above 2.5 kHz, as shown in Figure 14.13.

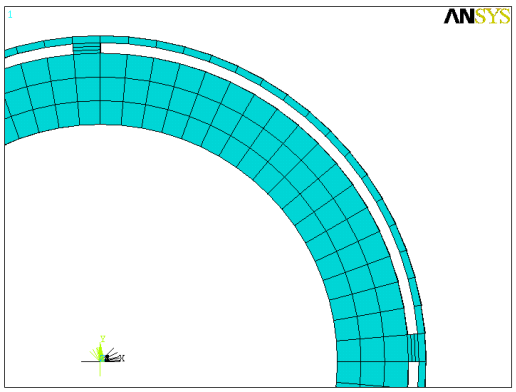

Figure 14.10: Four gap model.

The influence of a change in the damping of the structure was also studied and the results are presented in Figure 14.14. The response below 2.5 kHz at the peak frequencies is considerably reduced as the damping is increased. This behaviour is explained by the lower input power below 2.5 kHz when the damping is increased, as shown in Figure 14.15. The radiation efficiency, shown in Figure 14.16, is very similar for the three cases, except around 2 kHz, where it increases with the material damping.

The reduction in the number of iron paths between the inner and the outer core in the four gap model does not yield a reduction in the radiated sound power level. Actually, the acoustic behaviour of the structure is worsened, mainly due to the increase in the number of resonance frequencies within the same frequency range. A theoretical study where there are no connections between the inner and the outer parts of the core would determine the maximum achievable level of isolation.

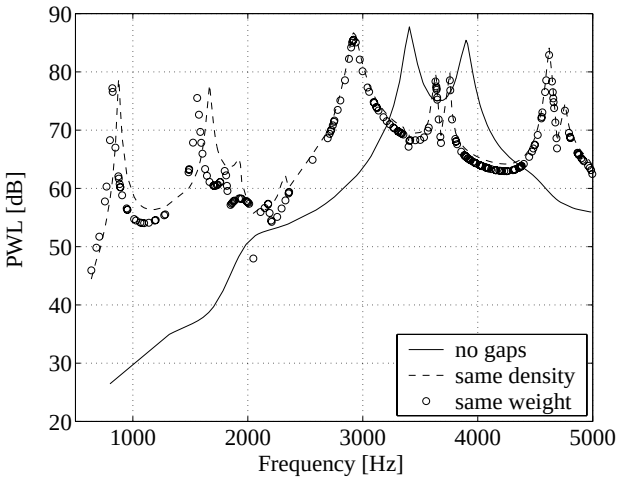

Figure 14.11: PWL of basic and four gap models, damping 0.01.

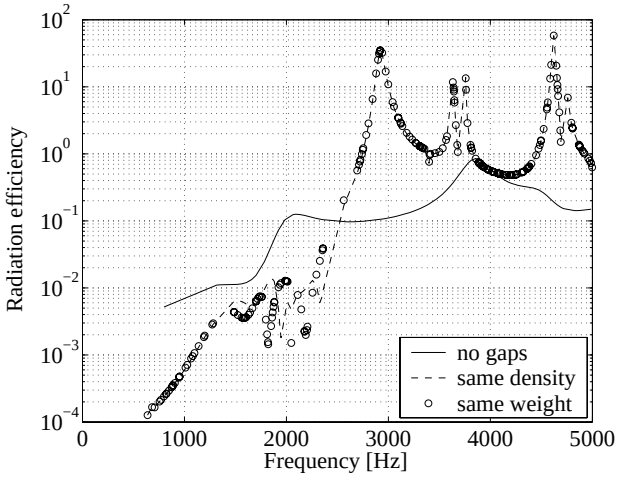

Figure 14.12: Radiation efficiency of basic and four gap models, damping 0.01.

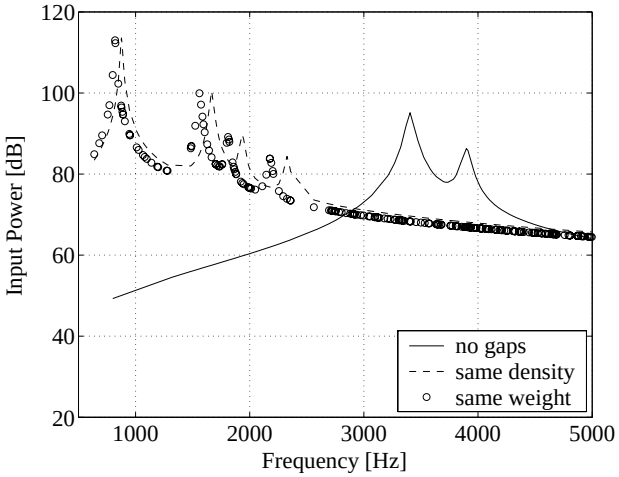

Figure 14.13: Input power of basic and four gap models, damping 0.01.

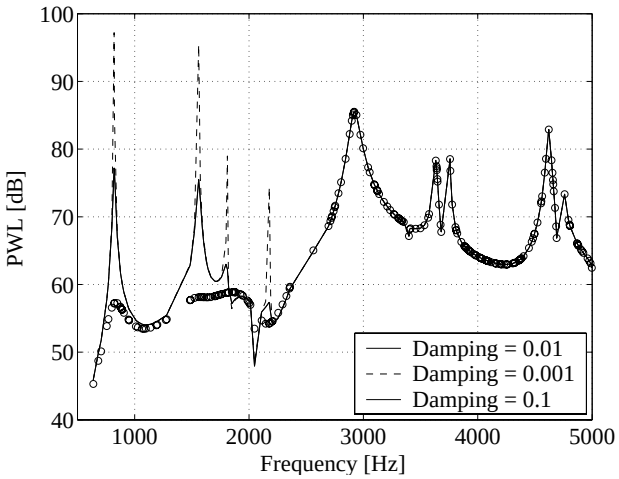

Figure 14.14: PWL of four gap model with constant weight for different damping coefficients.

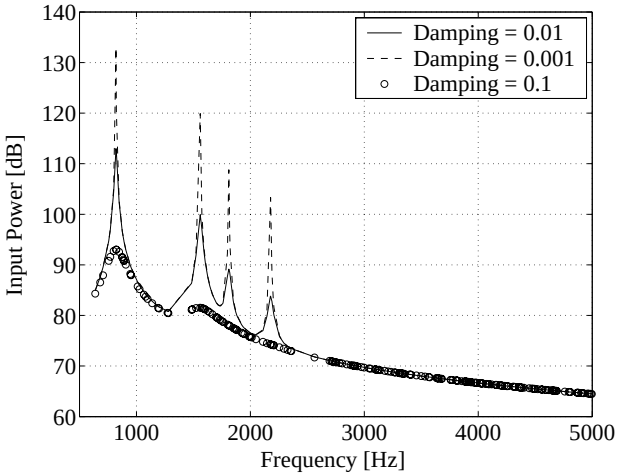

Figure 14.15: Input power of four gap model with constant weight for different damping coefficients.

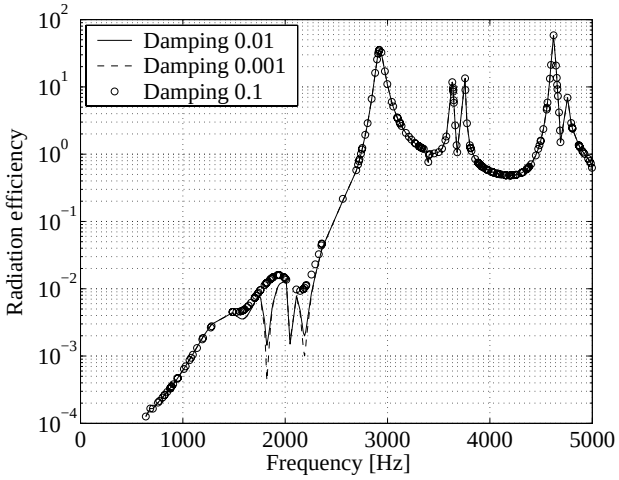

Figure 14.16: Radiation efficiency of four gap model with constant weight for different damping coefficients.

14.5 Ideal gap model

The ideal model was built with a continuous airgap separating completely the inner and outer parts of the core, forming two separate rings, as shown in Figure 14.17. The number of nodes and elements was 3528 and 2160 respectively. This increase in the number of elements compared with the four gap model is because one of the thin layers close to the surface was not replaced by air. Although there is no physical connection between the two rings, their vibration modes were calculated by ANSYS. It should be noted that in the BE acoustic model using SYSNOISE, the link between the inner and outer rings is still provided by the air, through which the vibrations are transmitted. Both cases where the fluid-structure interaction was defined as 'weak' and 'strong' were simulated, and the change in the results was negligible. This is reasonable since the load imposed by the air on the structure is not big enough to change its modes of vibration.

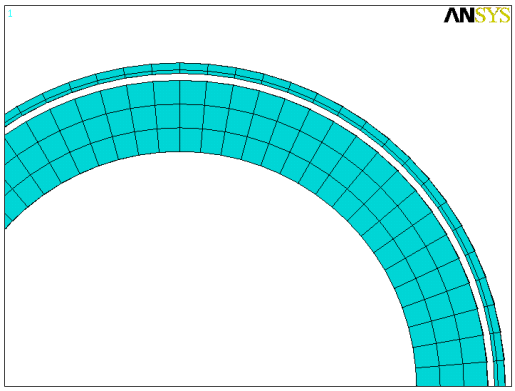

Figure 14.17: Ideal gap model.

Since the difference in the previous models between the constant weight and constant density simulations is small, only the structure with the same weight as the basic model was simulated. The result is shown in Figure 14.18. The overall PWL is still higher compared to the basic model, mainly in the region between 2 kHz and 3 kHz. The peak PWL occurs around 2.7 kHz, and at this frequency the radiation efficiency of the ideal model is considerably more pronounced, as shown in Figure 14.19.

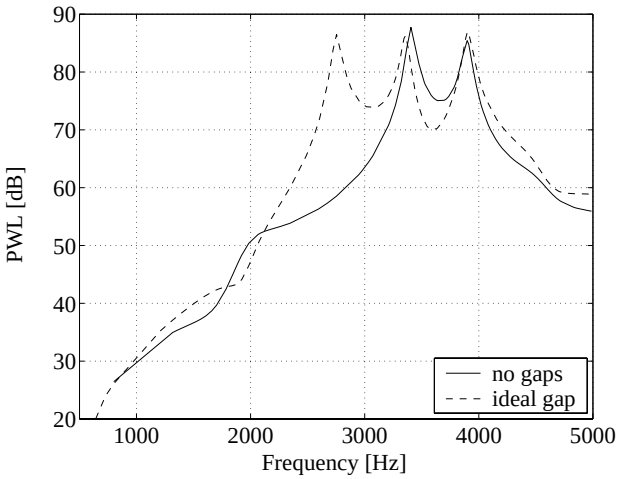

Figure 14.18: PWL of ideal gap and basic models, damping 0.01.

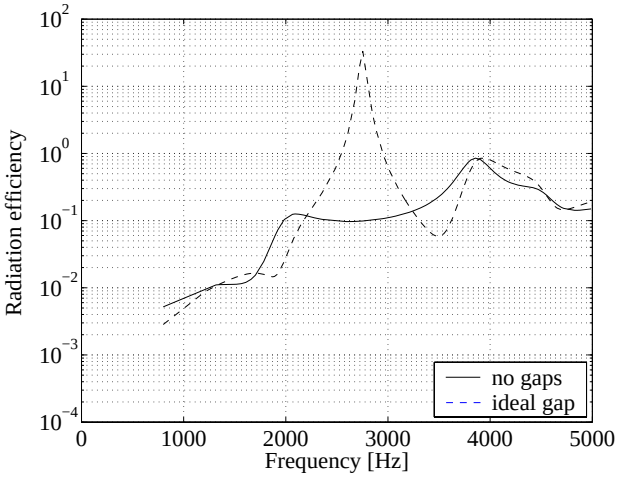

Figure 14.19: Radiation efficiency of ideal gap and basic models, damping 0.01.

To investigate the difference in the noise radiation between 2 kHz and 3 kHz, the modal characteristics of the ideal gap model and the basic model were compared in that region. The basic model has three modal frequencies, at 2176 Hz, 2357 Hz and 2753 Hz. The modes of the two rings in the ideal model were calculated separately in ANSYS. The inner ring has exactly the same three modes of vibration as the basic model, but the frequencies were slightly higher (2246 Hz, 2357 Hz and 2846 Hz), as it would be expected since the mass of the structure is decreased. Hence, the inner ring and the basic model can be considered to be acoustically equivalent between 2 kHz and 3 kHz. The outer ring has 9 vibration modes in this region. Furthermore, it was observed that the modes of vibration calculated for the inner ring and the outer ring separately coincided with all the modes of vibration calculated in ANSYS for the ideal gap model.

Table I shows a comparison of the sound power levels calculated at the modal frequencies for the basic and the ideal gap models. The values with the superscript '*' in the ideal gap model correspond to the modes associated with the inner ring. The value with the superscript '**' corresponds to a modal frequency present in both the inner and the outer rings. The remaining modes calculated for the ideal gap model are associated with the outer ring. From Table I, it is clear that the outer ring is excited, and also that it is responsible for the higher PWL of the ideal model compared to the basic model. The sound emitted at the frequencies corresponding to the inner ring modes is higher compared to the same modes in the basic model. This is due to the influence of the nearby outer ring modes. Also, it should be noted that the peak PWL response occurs at 2721 Hz, which is associated with the vibration mode of the outer ring.

The results from the simulations indicate that not only the iron but also the air are the media conducting the vibrations from the inner part to the outer part of the core. Even if the transmission coefficient through the air is lower compared to the iron, the fact that the stiffness in the outer part of the cylinder is considerably decreased by removing iron material is a key factor in the acoustical behaviour of the new structures. On one hand the outer core introduces more modal frequencies within the same frequency range. On the other hand, the outer core is also more easily deformed, which makes it more sensitive to the vibrations transmitted from the inner core. This behaviour can be seen in Figures 14.20, 14.21 and 14.22, which show some of the vibration modes calculated in ANSYS for the different structures. It is illustrated how the degree of

Table 14.1: Modal frequencies for the basic and ideal gap models

Basic model	Ideal gap model
	2076 Hz: 50.7 dB
2176 Hz: 52.9 dB	2246 Hz: 56.7 dB*
	2278 Hz: 57.7 dB
	2336 Hz: 59.7 dB
2357 Hz: 53.9 dB	2357 Hz: 60.4 dB**
	2604 Hz: 71.9 dB
	2675 Hz: 78.0 dB
	2721 Hz: 83.7 dB
	2805 Hz: 82.1 dB
	2842 Hz: 72.9 dB
2753 Hz: 58.5 dB	2846 Hz: 79.0 dB*

deformation experienced in the outer part of the core is more accentuated than in the inner part, and this contributes to the radiation of noise, which explains the unsatisfactory results obtained from the models where the surrounding air gaps are introduced.

14.6 Conclusions

In this chapter the effect of some structural changes in the stator of an electrical machine with the aim of reducing the noise emissions has been discussed. The structural change consisted of introducing some air gaps around the periphery of the stator to control the transmission path for the vibrations. Various geometries for the air gaps have been investigated, together with the ideal case, where the outer core is not physically connected through iron with the inner core. Results indicate that the idea of introducing air gaps in the periphery of the stator core does not reduce the noise emissions. Replacing some iron by air reduces the stiffness in this area and makes the structure more sensitive to vibration excitation. However, it has also been shown that increasing the damping

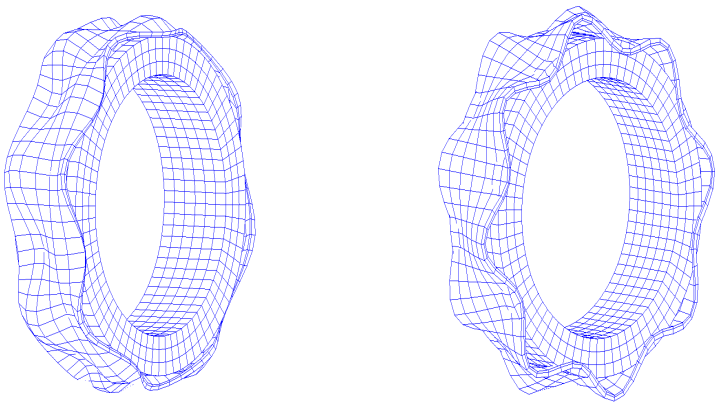

(a) Mode 81, 3397 Hz (b) Mode 89, 3546 Hz

Figure 14.20: Modes of vibration in the ideal model.

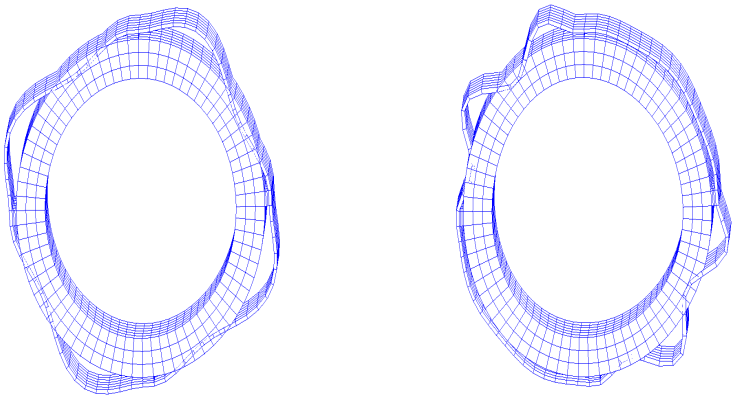

(a) Mode 6, 848 Hz (b) Mode 58, 2918 Hz

Figure 14.21: Modes of vibration in the four gaps model.

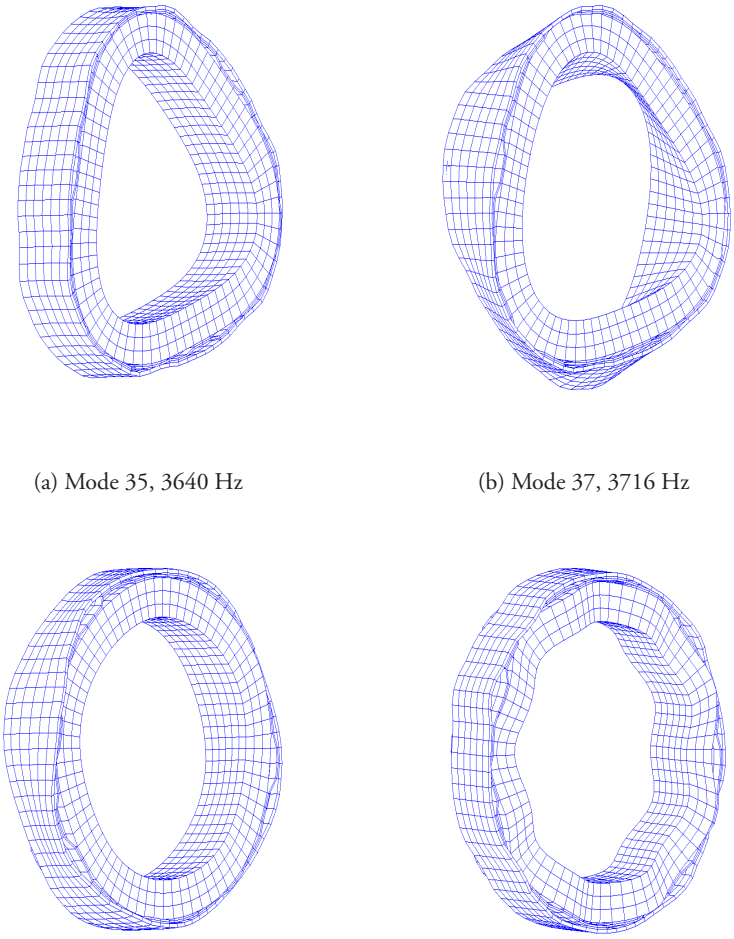

(a) Mode 35, 3640 Hz

(b) Mode 37, 3716 Hz

(c) Mode 68, 4618 Hz

(d) Mode 69, 4659 Hz

Figure 14.22: Modes of vibration in the zig-zag gap model.

of the material decreases the noise emissions. An increase in the damping could be achieved by filling the slots with additional materials, preferably with high thermal and magnetic conductivity.

Chapter 15

Conclusions

This second part of the thesis deals with topics related to the acoustic noise radiated from vector controlled induction motor drives, the noise prediction in an electrical machine, and structural changes in the stator to reduce the noise emissions. First, a summary of the obtained results is given. Second, some topics for future research regarding experimental and numerical studies of the acoustic noise in electrical machines are provided.

15.1 Summary of results

Noise from vector controlled drives

The acoustic noise emissions from a vector controlled induction motor drive have been analyzed. Vector control provides faster transient response compared to conventional v/f drives, and this is achieved with an efficient decoupling of the currents controlling the flux and the torque in the machine. Measurements were carried out when the direct and the quadrature currents were modulated with high frequency noise signals, exciting the structure with radial and tangential forces.

The directional behaviour of the noise radiation from electrical machines implies that the most proper way of quantifying their acoustic noise emissions is to measure the sound power. Results from sound intensity measurements indicated that direct modulation produced up to 7 dB more sound power than quadrature modulation. This is likely due to the radial/bending modal shape of the excited mode of vibration, which is more easily excited by radial than

tangential forces.

When the machine was loaded, it was observed that the overall sound power emissions decreased by up to 13 dB. This should be due to a change in the electromagnetic component of the noise, since the mechanical and aerodynamic components were found to be negligible. It is however difficult to generalize these results for other machines, since the factors influencing the noise emissions at load could affect in different ways the noise radiation from one machine to another.

Noise prediction

A method for the prediction of the sound radiation from an electrical machine has been analyzed, based on the combination of structural and electromagnetic finite element models, together with an acoustic boundary element model. It was found that the level of agreement between the noise calculations and the measurements was sensitive to a few factors. From the structural point of view, it is mandatory to calculate properly the modes of vibration in the structural analysis over the whole frequency range of interest, to ensure a proper correlation with the real machine. It was observed that a change in the damping influenced the response at some frequencies considerably, while at others the behaviour remained basically unchanged. From the electromagnetical point of view, using a two-dimensional model for the induction machine implies that the skewing of the rotor bars cannot be precisely modelled. If skewing is not modelled at all, the rotor harmonics are not damped, which in turn affects the force calculations. Finally, a change in the material magnetic properties, consisting of a 10% increase in the flux density along the saturated part of the BH curve, produced an increase of 3 dB or less in the simulated acoustic response.

Stator structural changes

A layer of air gaps of different geometries was introduced around the periphery of the stator core, in order to interfere with the path for the vibrations and reduce the noise emissions. The idea was tested by means of finite and boundary element models. It was observed that the stiffness around the gap area is decreased due to the material removal. This makes the structure more sensitive to vibration excitation, and it actually radiates more noise than the original model without air gaps. These results agree with earlier experimental tests with a machine built using a similar concept.

15.2 Future work

Concerning the experiments, other modal frequencies could be tested in order to assess if the direct and the quadrature current modulation affect differently the noise emissions. Regarding the acoustic noise prediction, the FEM modal analysis referred in this thesis needs to be improved below 1 kHz for a better agreement with the real machine. The prediction process could also be tested at higher frequencies, for example at 1105 Hz, where the predicted and measured modes of vibration show a better agreement than at 490 Hz. However, if the sampling frequency in the electromagnetic calculations is maintained, then the number of simulations at higher frequencies is considerably increased. Furthermore, for a more accurate force calculation the airgap forces should be extracted from a three-dimensional FE electromagnetic model, in order to take into account the influence of skewing and end-windings. This would however also increase dramatically the computation time.

The results from Chapter 14 indicated that an increase in the damping of the material resulted in a decrease of the noise emissions. New ways of increasing homogeneously the damping in the stator structure could be investigated. In principle, iron powder cores would present a higher damping factor in the radial and circumferential directions compared to a similar axially laminated structure, due to the distributed insulation around the iron particles. However, the damping in the axial direction is probably higher in the laminated core, due to the thicker layer of insulation between the laminations. Nevertheless, the study of the acoustic properties of iron-powder structures is needed, in order to assess the acoustic characteristics of machines built from this material compared to their laminated counterparts.

Bibliography

Andersson, C., Skarrie, H. (1997). *Mekanisk ljudreducering i en asynkronmaskin*. MSc Thesis, Dept of Industrial Electrical Engineering and Automation, Lund University, Sweden. (In Swedish).

Alaküla, M. (2002). *Power electronic control*. Dept of Industrial Electrical Engineering and Automation, Lund University, Sweden.

Astfalck, A., Pulle, D.W.J., Lai, J.C.S. (1997). Prediction of transient stator force distribution of inverter driven induction motors. *Proceedings of AUPEC/EECON'97, The University of New South Wales*, vol. 1, pp. 1-6, Australia.

Bakhuizen, A.J.C. (1973). *A contribution to the development of stepping motors.* PhD Thesis, Eindhoven Technical University, The Netherlands.

Belkhayat, D., Roger, D., Brudny, J.F. (1997). Active reduction of magnetic noise in asynchronous machines controlled by stator current harmonics. *Proceedings of IEE International Conference in Electrical Machines and Drives*, pp. 400-405, London, UK.

Belmans, R., Verdyck, D., Geysen, W., Findlay, R.D. (1991). Electromechanical analysis of the audible noise of an inverter-fed squirrel-cage induction motor. *IEEE Transactions on Industry Applications*, vol. 27, no. 3, pp. 539-544.

Belmans, R., Hameyer, K. (1998). Impact of inverter supply and numerical calculation techniques in audible noise problems. *International seminar on vibrations and acoustic noise of electric machinery*, pp. 9-23. Béthune, France.

Bologniani, S., Di Bella, A., Zigliotto, M. (1999). Random modulation and acoustic noise reduction in IM drives: a case study. *Proceedings of IEE International Conference on Electrical Machines and Drives*, pp. 137-141, Canterbury, UK.

Brozek, R. (1973). No-load to full-load airborne noise level change on high-speed polyphase induction motors. *IEEE Transactions on Industry Applications*, IA-9, 2, pp. 180-184.

Brüel & Kjær (1986). *Sound Intensity booklet*.

Brüel & Kjær (1988). *Structural testing. Part 2: Modal analysis and simulation*.

Chang, S.C., Yacamini, R. (1996). Experimental study of the vibrational behaviour of machine stators. *IEE Proceedings on Electric Power Applications*, vol. 143, no. 3, pp. 242-250.

Chau, K.T., Jiang, S.Z., Chan, C.C. (2000). Reduction of current ripple and acoustic noise in dual-inverter pole-changing induction motor drives. *Record of the 31th Annual IEEE Power Electronics Specialists Conference*, vol. 1, pp. 67-72.

Cho, D.H., Kim, K.J. (1998). Modelling of electromagnetic excitation forces of small induction motor for vibration and noise analysis. *IEE Proceedings on Electric Power Applications*, vol. 145, no. 3, pp. 199-205.

Covic, G.A., Boys, J.T. (1998). Noise quieting with random PWM AC drives. *IEE Proceedings on Electric Power Applications*, vol. 145, no. 1, pp. 1-10.

Delaere K., Hameyer K., Belmans, R. (1998). Static eccentricity as a cause for audible noise of induction motors. *Proceedings of International Conference on Electrical Machines*, vol. 1, pp. 502-506, Istanbul, Turkey.

Ewins, D.J. (1984). *Modal testing: theory and practice*. Research Studies Press Ltd.

Fahy, F.J. (1995). *Sound Intensity*. E & FN Spon, London, UK.

Garcia-Otero, S., Devaney, M. (1994). Minimization of acoustic noise in variable speed induction motors using a modified PWM drive. *IEEE Transactions on Industry Applications*, vol. 30, no. 1, pp. 111-115.

Garvey, S.D., Glew, G.N. (1999). Magnetostrictive excitation of vibration in machines - a modal approach. *Proceedings of IEE International Conference on Electrical Machines and Drives*, pp. 169-173, Canterbury, UK.

Garvey, S.D., Le Flem, G.D. (1999). Tangential forces matter. *Proceedings of IEE International Conference on Electrical Machines and Drives*, pp. 174-178, Canterbury, UK.

Gerling, D. (1994). The audible noise of induction machines compared for different methods of calculating the air-gap field. *Proceedings of International Conference on Electrical Machines*, vol. 3, pp. 409-414, Paris, France.

Habetler, T.G., Deepakraj, M.D. (1991). Acoustic noise reduction in sinusoidal PWM drives using a randomly modulated carrier. *IEEE Transactions on Power Electronics*, vol. 6, no. 3, pp. 356-363.

Hadj Amor, A., Timar P.L., Poloujadoff M. (1995). Induction squirrel cage machine design with minimization of electromagnetic noise. *IEEE Transactions on Energy Conversion*, vol. 10, no. 4, pp. 681-687.

Harris, C.M. (1991). *Handbook of acoustical measurements and noise control*. 3rd edition, McGraw-Hill, USA.

Holmes, D.G. (1997). *A generalized approach to the modulation and control of hard switched converters*. PhD Thesis, Dept of Electrical and Computer Systems Engineering, Monash University, Australia.

Hubert, A., Friedrich, G. (2002). Influence of power converter on induction motor acoustic noise: interaction between control strategy and mechanical structure. *IEE Proceedings on Electric Power Applications*, vol. 149, no. 2, pp. 93-100.

Hupe, R., Kennel, R. (1989). Increase of power and reduction of noise and current ripple of inverter fed induction machines. *Proceedings of European Conference on Power Electronics and Applications*, pp. 47-50, Aachen, Germany.

Ishibashi, F., Noda, S., Mochizuki, M. (1998). Numerical simulation of electromagnetic vibration of small induction motors. *IEE Proceedings on Electric Power Applications*, vol. 145, no. 6, pp. 528-534.

ISO 9614-2 (1996). Acoustics - Determination of sound power levels of noise sources using sound intensity - Part 2: Measurement by scanning.

Jahns, T.M., Owen, E.L. (2001). AC adjustable-speed drives at the millenium: How did we get there? *IEEE Transactions on Power Electronics*, vol. 16, no. 1, pp. 17-25.

Kobayashi, T., Tajima, F., Ito, M., Shibukawa, S. (1997). Effects of slot combination on acoustic noise from induction motors. *IEEE Transactions on Magnetics*, vol. 33, no. 2, pp. 2101-2104.

Krause, P.C. (1986). *Analysis of Electric Machinery*. McGraw-Hill.

Lipo, T.A. (1996). *Introduction to AC machine design*. WisPERC UW, Madison Wisconsin, USA.

Lo, W.C., Chan, C.C., Zhu, Z.Q., Xu, L., Howe, D., Chau, K.T. (2000). Acoustic noise radiated by PWM-controlled induction machine drives. *IEEE Transactions on Industrial Electronics*, vol. 47, no. 4, pp. 880-889.

Låftman, L. (1997). The contribution to noise in an induction machine, fed from a pulse width modulated inverter. *Proceedings of European Conference on Power Electronics and Applications*, vol. 2, pp. 2483-2489, Trondheim, Norway.

Maliti, K.C. (2000). *Modelling and analysis of magnetic noise in squirrel-cage induction motors*. PhD Thesis, Dept of Electric Power Engineering, Electrical Machines and Power Electronics, Royal Institute of Technology, Sweden.

Norton, M.P. (1989). *Fundamentals of noise and vibration analysis for engineers*. Cambridge University Press, UK.

Novotny, D.W., Lipo, T.A. (1996). *Vector control and dynamics of AC drives*. Oxford Science Publications, Wisconsin, USA.

Ramesohl, I., Kaehler, C., Henneberger, G. (1999). Influencing factors on acoustical simulations including manufacturing tolerances and numerical strategies. *Proceedings of IEE International Conference on Electrical Machines and Drives*, pp. 142-146, Canterbury, UK.

Stemmler, H., Eilinger, T. (1994). Spectral analysis of the sinusoidal PWM with variable switching frequency for noise reduction in inverter-fed induction motors. *Record of the 25th Annual IEEE Power Electronics Specialists Conference*, vol. 1, pp. 269-277.

Stephen, D.D., Davies, R.J. (1970). Discussion on acoustic noise and vibration of rotating electrical machines. *IEE Proceedings*, vol. 117, no. 1, pp. 127-129.

Timar, P.L. (1989). *Noise and vibration of electrical machines*. Elsevier Science Publishers, Amsterdam, The Netherlands.

Timar, P.L., Lai, J.C.S. (1994). Acoustic noise of electromagnetic origin in an ideal frequency converter driven induction motor. *IEE Proceedings -B on Electric Power Applications*, vol. 141, no. 6, pp. 341-346.

Timar, P.L., Lai, J.C.S. (1996). Analysis of the effects of time harmonics on the radiated sound power of induction motors. *Proceedings of Internoise 96*, Book 1, pp. 445-448, Liverpool, UK.

Vandevelde, L., Melkebeek, J.A.A. (1994). Theoretical and experimental study of radial forces in relation to magnetic noise of induction motors. *Proceedings of International Conference on Electrical Machines*, vol. 3, pp. 419-424, Paris, France.

Vandevelde, L., Melkebeek, J.A.A. (1997). Calculation of radial magnetic forces for the analysis of noise and vibrations of squirrel-cage induction motors. *Proceedings of IEE International Conference in Electrical Machines and Drives*, pp. 86-90, London, UK.

Vas, P. (1990). *Vector control of AC machines*. Oxford University Press, UK.

Verma, S.P., Balan, A. (1998). Experimental investigations on the stators of electrical machines in relation to vibration and noise problems. *IEE Proceedings on Electric Power Applications*, vol. 145, no. 5, pp. 455-461.

Wang, C. (1998). *Vibro-acoustic analysis of inverter driven induction motors*. PhD Thesis, School of Aerospace and Mechanical Engineering, University College, The University of New South Wales, Australia.

Wang, C., Lai, J.C.S. (1999). Vibration analysis of an induction motor. *Journal of Sound and Vibration*, 224(4), pp. 733-756.

Wang, C., Lai, J.C.S., Astfalck, A. (2004). Sound power radiated from an inverter driven induction motor II: numerical analysis. *IEE Proceedings on Electric Power Applications*, vol. 151, no. 3, pp. 341-348.

Wang, C., Lai, J.C.S., Pulle, D.W.J. (2002). Prediction of acoustic noise from variable speed induction motors: deterministic versus statistical approaches. *IEEE Transactions on Industry Applications*, vol. 38, no 4, pp. 1037-1044.

Xu, L., Zhu, Z.Q., Howe, D. (2000). Acoustic noise radiated from direct torque controlled induction motor drives. *IEEE Proceedings on Electric Power Applications*, vol. 147, no. 6, pp. 491-496.

Yang, S.J. (1981). *Low noise electrical machines*. Oxford University Press, New York, USA.

Zhou, P. (1993). *Numerical analysis of electromagnetic fields*. Springer-Verlag, New York, USA.

Zhu, Z.Q., Howe, D. (1994). Improved methods for prediction of electromagnetic noise radiated by electrical machines. *IEE Proceedings on Electric Power Applications*, vol. 141, no. 2, pp. 109-120.

Zhu, Z.Q., Xu, L., Howe, D. (1997). Acoustic noise radiated by nominally identical induction machines fed from sinusoidal and non-sinusoidal power supplies. *Proceedings of European Conference on Power Electronics and Applications*, vol. 2, pp. 2489-2494, Trondheim, Norway.

Zhu, Z.Q., Xu, L., Howe, D. (1999). Influence of mounting and coupling on the natural frequencies and acoustic noise radiated by a PWM controlled induction machine. *Proceedings of IEE International Conference on Electrical Machines and Drives*, pp. 164-168, Canterbury, UK.

Åstrom, K.J., Wittenmark, B. (1997). *Computer controlled systems: theory and design*. 3rd edition, Pentrice Hall, Inc., NJ, USA.

Appendix E

Current controllers

E.1 Controller for the direct current

Predictive dead beat control assumes that the reference value for one signal (denoted in the following by the superscript '*') set at one discrete time t_k is achieved by the actual value of the signal with one sampling time delay, i.e. at time t_{k+1}. For the voltage signal this implies that $u^*_{sd}(t_k) = \overline{u}_{sd}(t_{k+1})$. The average voltage at time t_{k+1} can be expressed as a moving average filter of the form in (E.1).

$$\overline{u}_{sd}(t_{k+1}) = \frac{1}{T_s} \int_{t_k}^{t_{k+1}} u_{sd}(\tau) d\tau \tag{E.1}$$

Introducing (10.8) from Chapter 10 into this equivalence and multiplying by the sampling time T_s leads to (E.2).

$$T_s u^*_{sd}(t_k) = R_s T_s \frac{1}{T_s} \int_{t_k}^{t_{k+1}} i_{sd}(\tau) d\tau + \psi_s(t_{k+1}) - \psi_s(t_k) \tag{E.2}$$

In this equation the derivative of the flux has been approximated using a forward Euler approximation (Åstrom and Wittenmark, 1997). The average value of the current within one sampling interval is denoted by $\overline{i}_{sd}(t_{k+1})$, following the same equivalence as for the voltage in (E.1). Assuming that the current varies linearly within one sampling interval, it can be approximated as

in (E.3).

$$\bar{i}_{sd}(t_{k+1}) \simeq \frac{i_{sd}(t_{k+1}) + i_{sd}(t_k)}{2} \tag{E.3}$$

If the leakage inductance is neglected, the flux is expressed as $\psi_s \simeq i_{sd} L_M$. For dead beat control $i_{sd}(t_{k+1}) = i^*_{sd}(t_k)$ and introducing these changes into (E.2) yields (E.4).

$$T_s u^*_{sd}(t_k) = \frac{R_s T_s}{2} \left[i^*_{sd}(t_k) + i_{sd}(t_k) \right] + i^*_{sd}(t_k) - i_{sd}(t_k) \tag{E.4}$$

This expression can be transformed using (E.5), which leads to (E.6).

$$\frac{R_s T_s}{2} = R_s T_s - \frac{R_s T_s}{2} \tag{E.5}$$

$$T_s u^*_{sd}(t_k) = R_s T_s i_{sd}(t_k) + \left(L_M + \frac{R_s T_s}{2} \right) \left[i^*_{sd}(t_k) - i_{sd}(t_k) \right] \tag{E.6}$$

Assuming dead beat control, the current at one point in time t_k can be written as the sum of all the set point changes up to the time t_{k-1}, as in (E.7).

$$i_{sd}(t_k) = \sum_{j=0}^{j=k-1} \left[i^*_{sd}(t_j) - i_{sd}(t_j) \right] \tag{E.7}$$

and the final expression for the direct current controller takes the form in (E.8).

$$\begin{aligned} T_s u^*_{sd}(t_k) \quad = \quad & R_s T_s \sum_{j=0}^{j=k-1} \left[i^*_{sd}(t_j) - i_{sd}(t_j) \right] + \\ & + \left(L_M + \frac{R_s T_s}{2} \right) \left[i^*_{sd}(t_k) - i_{sd}(t_k) \right] \end{aligned} \tag{E.8}$$

E.2 Controller for the quadrature current

Equation (10.9) for the quadrature current can be transformed into (E.9) using the equivalence that the synchronous speed ω_s is the sum of both the slip and rotor electrical frequencies, ω_{sl} and ω_m respectively.

$$u_{sq} = R_s i_{sq} + \omega_{sl} \psi_s + \omega_m \psi_s \tag{E.9}$$

In order to deduce an expression for the slip frequency, it is helpful to consider the rotor equation, which in stationary coordinates takes the form in (E.10).

$$-j\omega_m\vec{\psi}_R^{\alpha\beta} + \vec{i}_R^{\alpha\beta}R_R + \frac{d\vec{\psi}_R^{\alpha\beta}}{dt} = 0 \tag{E.10}$$

This equation is translated into the synchronous dq reference frame yielding (E.11), where the rotor flux and current in synchronous coordinates are given by (E.12) and (E.13) respectively.

$$\frac{d\vec{\psi}_R^{dq}}{dt} + j(\omega_s - \omega_m)\vec{\psi}_R^{dq} + \vec{i}_R^{dq}R_R = 0 \tag{E.11}$$

$$\vec{\psi}_R^{dq} = \vec{\psi}_s^{dq} - \vec{i}_s^{dq}L_\sigma \tag{E.12}$$

$$\vec{i}_R^{dq} = \frac{\vec{\psi}_R^{dq}}{L_M} - \vec{i}_s^{dq} \tag{E.13}$$

The rotor current can be expressed in terms of stator variables substituting (E.12) into (E.13), and introducing the equivalence $L_s = L_M + L_\sigma$, where L_s is the stator inductance, L_M is the magnetizing inductance and L_σ is the combined leakage inductance from the stator and the rotor in the four parameter model, and (E.14) is obtained.

$$\vec{i}_R^{dq} = \frac{\vec{\psi}_s^{dq}}{L_M} - \frac{L_s}{L_M}\vec{i}_s^{dq} \tag{E.14}$$

Introducing (E.12) and (E.14) into (E.11) yields (E.15).

$$\begin{aligned}&\frac{d\vec{\psi}_s^{dq}}{dt} - L_\sigma\frac{d\vec{i}_s^{dq}}{dt} + j\omega_{sl}\left(\vec{\psi}_s^{dq} - \vec{i}_s^{dq}L_\sigma\right) + \\ &+\frac{R_R}{L_M}\vec{\psi}_s^{dq} - \frac{R_R L_s}{L_M}\vec{i}_s^{dq} = 0\end{aligned} \tag{E.15}$$

This expression can be divided into a real and an imaginary part, still considering that $\psi_{sq} = 0$ for the reference system selected, as in (E.16) and (E.17) respectively.

$$\frac{d\psi_s}{dt} - L_\sigma\frac{di_{sd}}{dt} + \omega_{sl}i_{sq}L_\sigma + \frac{R_R}{L_M}\psi_s - \frac{R_R L_s}{L_M}i_{sd} = 0 \tag{E.16}$$

$$-L_\sigma \frac{di_{sq}}{dt} + \omega_{sl}\left(\psi_s - L_\sigma i_{sd}\right) - \frac{R_R L_s}{L_M} i_{sq} = 0 \tag{E.17}$$

From (E.17) the slip frequency is obtained, assuming that $\psi_s - L_\sigma i_{sd} \simeq \psi_s$ since the leakage flux can be neglected compared to the linkage flux in the machine, giving (E.18).

$$\omega_{sl} = \frac{\frac{R_R L_s}{L_M} i_{sq} + L_\sigma \frac{di_{sq}}{dt}}{\psi_s} \tag{E.18}$$

Substituting (E.18) into (E.9) leads to (E.19).

$$u_{sq} = \left(R_s + \frac{R_R L_s}{L_M}\right) i_{sq} + L_\sigma \frac{di_{sq}}{dt} + \omega_m \psi_s \tag{E.19}$$

In the same way as for the direct voltage, $u^*_{sq}(t_k) = \overline{u}_{sq}(t_{k+1})$ where the quadrature voltage is averaged using a moving average filter of the form shown in (E.1). Introducing (E.19) in the expression for the moving average filter and multiplying by the sampling time T_s yields (E.20).

$$\begin{aligned} T_s u^*_{sq}(t_k) = \left(R_s + \frac{R_R L_s}{L_M}\right) T_s \frac{1}{T_s} \int_{t_k}^{t_{k+1}} i_{sq}(\tau) d\tau + \\ + L_\sigma [i_{sq}(t_{k+1}) - i_{sq}(t_k)] + T_s \frac{1}{T_s} \int_{t_k}^{t_{k+1}} \omega_m(\tau) \psi_s(\tau) d\tau \end{aligned} \tag{E.20}$$

In this equation the derivative of the current has been approximated with a forward difference, using Euler's method. The integral of the quadrature current divided by the sampling time becomes $\overline{i}_{sq}(t_{k+1})$ which can be approximated as in (E.3) for the direct current. The approximation in (E.21) is applied to the speed dependent term.

$$\frac{1}{T_s} \int_{t_k}^{t_{k+1}} \omega_m(\tau) \psi_s(\tau) d\tau \simeq \omega_m(t_k) \psi_s(t_k) \tag{E.21}$$

If the main flux and the speed change, they do it slowly and these components can be assumed to be constant during one sampling period. Assuming

dead beat control for the quadrature current leads to (E.22).

$$i_{sq}(t_k) = \sum_{j=0}^{j=k-1} \left[i^*_{sq}(t_j) - i_{sq}(t_j) \right] \tag{E.22}$$

Taking into consideration all these assumptions, (E.20) can be rewritten as in (E.23).

$$\begin{aligned} T_s u^*_{sq}(t_k) = \left(R_s + \frac{R_R L_s}{L_M} \right) T_s \sum_{j=0}^{j=k-1} \left[i^*_{sq}(t_j) - i_{sq}(t_j) \right] + \\ + \left[L_\sigma + \left(R_s + \frac{R_R L_s}{L_M} \right) \frac{T_s}{2} \right] \left[i^*_{sq}(t_k) - i_{sq}(t_k) \right] + \\ + \omega_m(t_k) \psi_s(t_k) T_s \end{aligned} \tag{E.23}$$

Appendix F

Acoustic terminology

In acoustics it is important to distinguish between sound pressure and sound power. Sound power relates to the rate at which a sound source radiates energy, i.e. energy per unit time. A noise source radiating a certain amount of sound power will produce a change in the sound pressure depending on the surrounding environment. This concept can be better understood by considering its analogy with a heater placed in a room. The heater radiates a certain amount of heat into the room (sound power), but the actual temperature (sound pressure) will depend on the dimensions of the room, materials, other heat sources, insulation, distance from the heat source, etc. Sound pressure is therefore the physical quantity that is perceived by the ear. The unit of pressure is Pascal (Pa), and 1 Pascal is equivalent to 1 N/m^2. The human ear is sensitive to a range of frequencies from 20 Hz to 20 kHz and a range of acoustic pressure from the threshold of hearing of 20 μPa to the threshold of pain of 200 Pa (Norton, 1989). Owing to the wide range of pressure (10 million times) that causes the sensation of hearing, a logarithmic scale is used to express the sound pressure level (SPL, L_p) in decibels (dB). The SPL is defined by (F.1), where p is the root-mean-square sound pressure in Pa and p_0 is the reference sound pressure, which is 20 μPa for air.

$$L_p = \log_{10}\left(\frac{p}{p_0}\right)^2 \tag{F.1}$$

In general, for noise due to a composite of sounds with different frequencies,

the total sound pressure level is given by (F.2).

$$L_p = \log_{10} \sum_{i=1}^{n} 10^{0.1 L_{pi}} \tag{F.2}$$

The amount of noise produced by a machine cannot be necessarily quantified by measuring the sound pressure. The sound power has to be determined instead, which is a better descriptor of the noise producing capacity of a sound source. The sound power level (PWL, L_W) of a source is defined in dB by (F.3), where W_0 is the reference power, which is 10^{-12} W for air.

$$L_W = \log_{10} \frac{W}{W_0} \tag{F.3}$$

Related to the sound power is the concept of sound intensity, which is the sound power in watts per unit area in m^2, and is defined as the average rate of energy flow through a unit area normal to the direction of propagation, as given by (F.4), where $\vec{u}$ is the particle velocity. The instantaneous sound intensity, $p\vec{u}$, is a vector quantity whose magnitude and direction at any point in space may vary with time. Note also that energy travelling back and forth does not contribute to the averaged intensity, and thus there will be some net intensity flow only if there is a net energy flow through the area considered.

$$\vec{I} = \frac{1}{T} \int_0^T p\vec{u} dt \tag{F.4}$$

The sound intensity level, L_I, of a source is defined in dB by (F.5), where I_0 is the reference intensity which is 10^{-12} W/m^2 for air.

$$L_I = \log_{10} \frac{I}{I_0} \tag{F.5}$$

The sound pressure or sound intensity levels can be displayed and stored in a spectrum analyzer for further post-processing. Frequency analyzers may be based on either constant bandwidth or proportional bandwidth devices. The constant bandwidth device is basically a tunable narrow-band filter with constant bandwidth $\Delta f = f_u - f_l$, where f_l and f_u are the lower and upper half-power frequencies. The proportional bandwidth device consists of a series

of relatively broadband filters such that the ratio f_u/f_l is constant. The centre frequency f_c of a proportional bandwidth filter is calculated as in (F.6). The most common proportional bandwidth filters are in the form that satisfies that f_u/f_l = 2^x, where x=1 for octave band filters and x=1/3 for 1/3-octave band filters.

$$f_c = \sqrt{f_l f_u} \tag{F.6}$$

In order to reflect the response of the ear to different frequencies, a weighting function (known as A-weighting function) approximating an inverted 40-phon loudness contour is usually applied to the measured sound pressure level and the result is expressed as dB(A). There are other weighting functions, as shown in Figure F.1. The B and C functions approximate the human response at loudness levels of 70 phon and 90 phon respectively while D is a standarized function for use in aircraft noise measurements. The A-weighting scale is the most widely used since it best approximates the human response. Below 1 kHz and over 6 kHz the A-scale is negative, representing a reduction in the sound level in order to compensate for the human ear poorer sensitivity in the lower and higher frequency ranges.

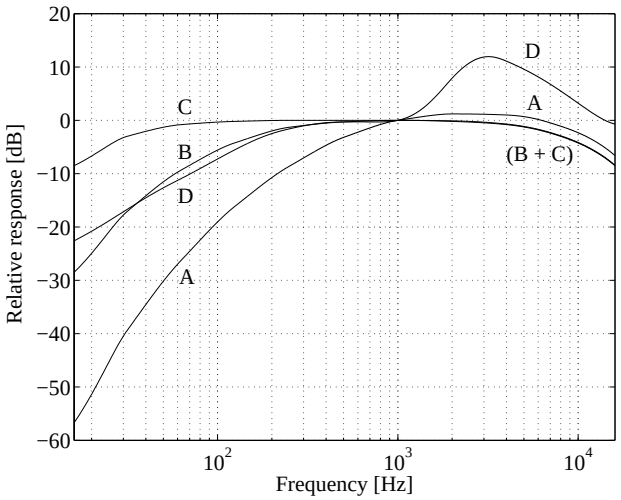

Figure F.1: The frequency weighting functions (Harris, 1991).

Sound measurement techniques

Sound power can be related to sound pressure only under carefully controlled conditions, where special assumptions are made about the sound field. The 'free field' describes sound propagation in idealized free space where there are no reflections. These conditions are held in open air far from the ground or in an anechoic room, where all the sound striking the walls is absorbed. In a free field the intensity I is related to the root-mean-square pressure p by (F.7), where c is the speed of sound.

$$I = \frac{p^2}{\rho c} \tag{F.7}$$

Introducing this equation into (F.5) leads to (F.1), implying that in a free field the sound intensity level is equal to the sound pressure level. Hence, the sound power of a source can be determined by measuring the averaged sound pressure level over a hypothetical surface enclosing the sound source in an anechoic room, and is given by (F.8), where $\overline{L_p}$ is the averaged surface sound pressure level in dB and S is the area of the test surface in m^2.

$$L_W = \overline{L_p} + \log_{10} S \tag{F.8}$$

In a 'diffuse field' sound is reflected so many times that it travels in all directions with equal magnitude and probability, and this field is approximated in a reverberant room. In a diffuse field, the relation between the intensity and the pressure is given by (F.9).

$$I = \frac{p^2}{4\rho c} \tag{F.9}$$

The sound power level of a source can be determined by measuring the average sound pressure level inside a reverberation room. It can be calculated from (F.10), where T is the reverberation time of the room in seconds, V is the volume of the room in m^3, S is the total surface of the room in m^2 and λ is the wavelength at the centre frequency of the frequency band in meters.

$$L_W = Lp - \log_{10} T + \log_{10} V + \log_{10}\left(1 + \frac{S\lambda}{8V}\right) \tag{F.10}$$

Appendix G

No load sound intensity measurements

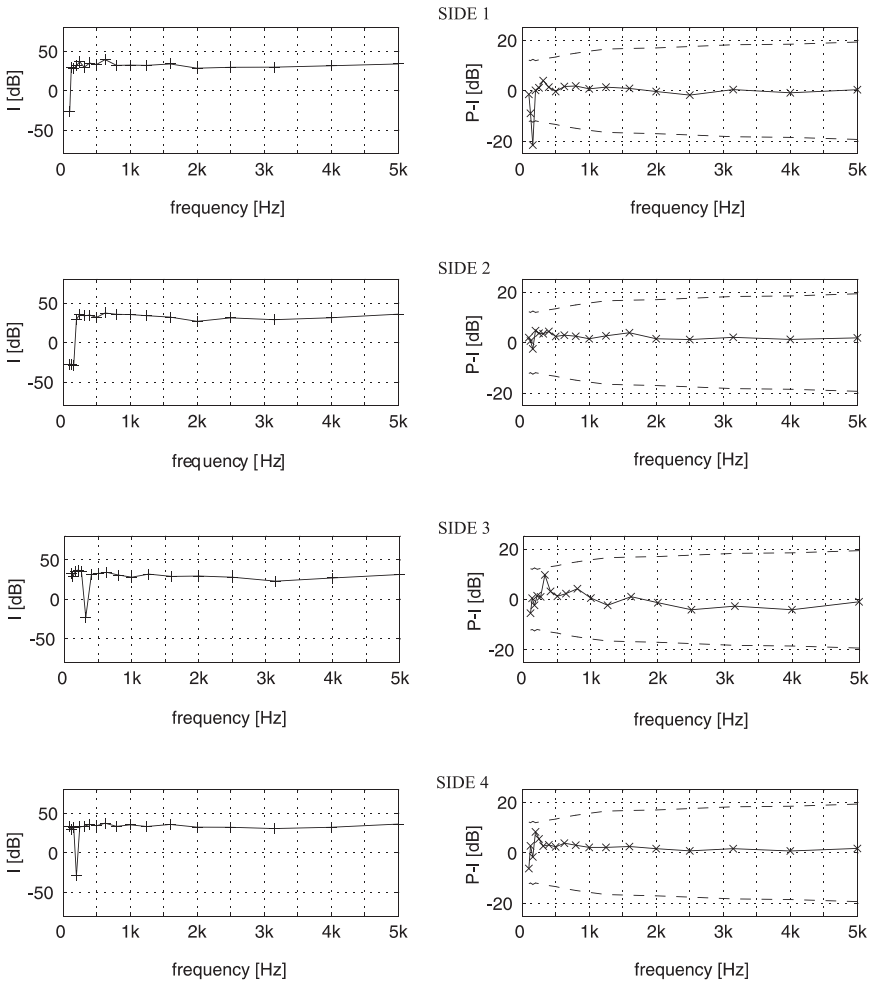

Figure G.1: Measured sound intensity and residual index over the four free sides of the frame, case [d=0, q=0].

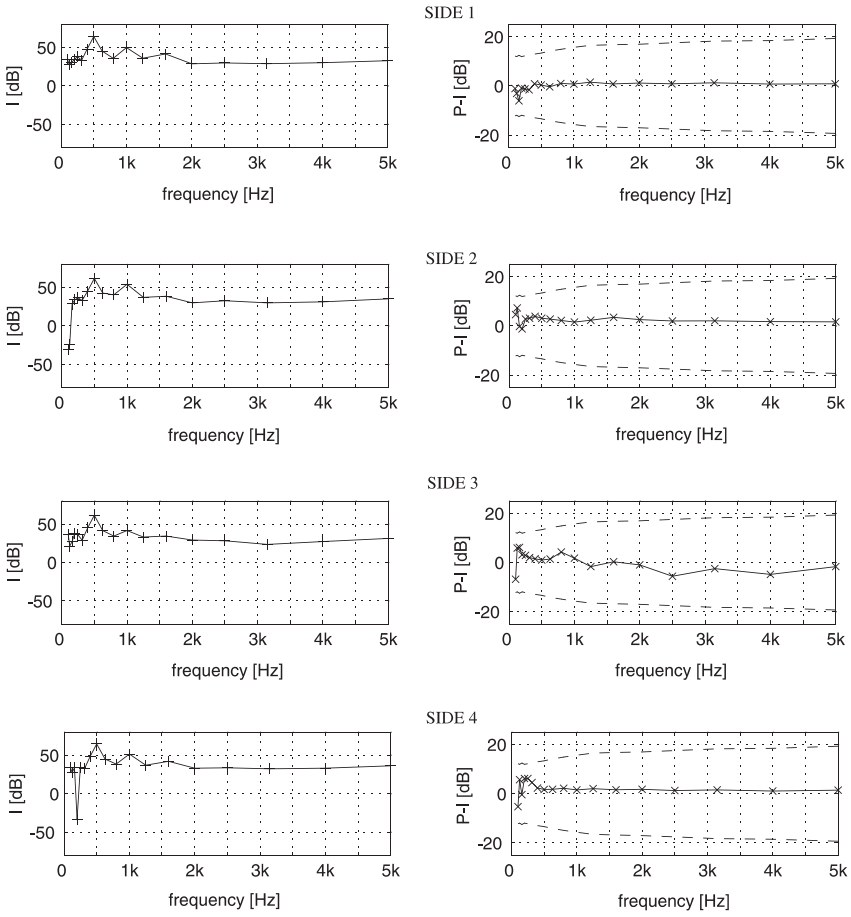

Figure G.2: Measured sound intensity and residual index over the four free sides of the frame, case [d=m, q=0], f=490 Hz.

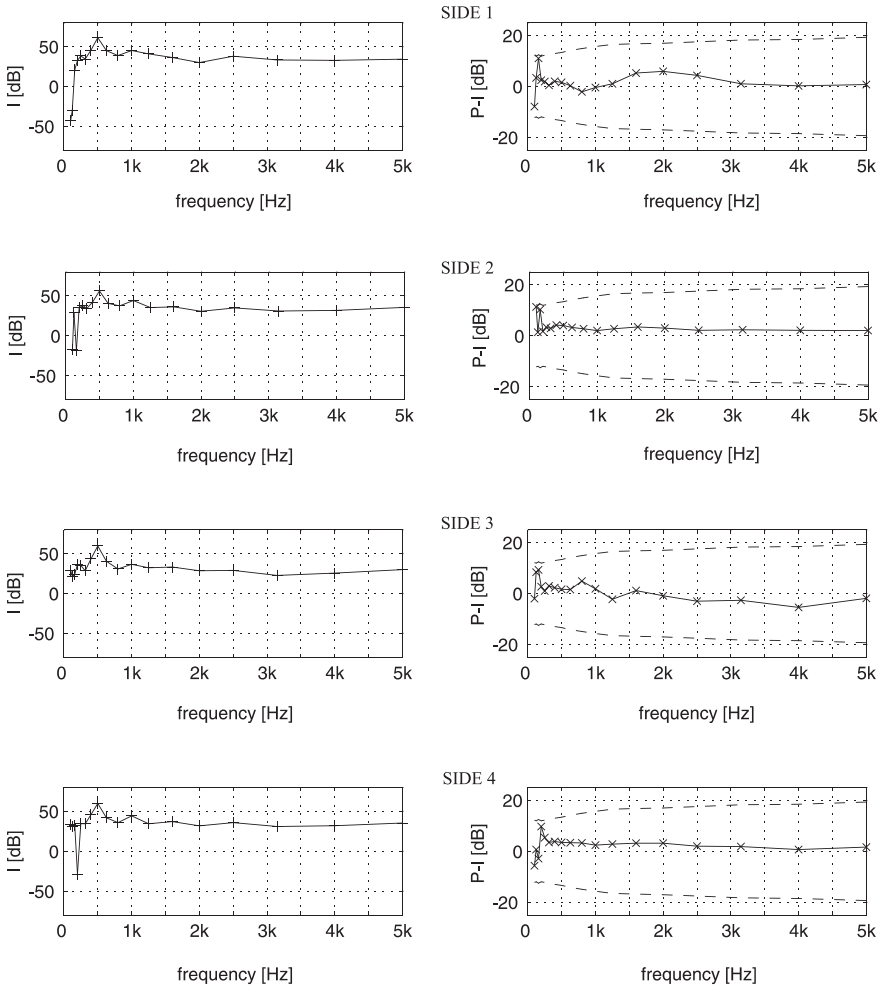

Figure G.3: Measured sound intensity and residual index over the four free sides of the frame, case [d=0, q=m], f=490 Hz.

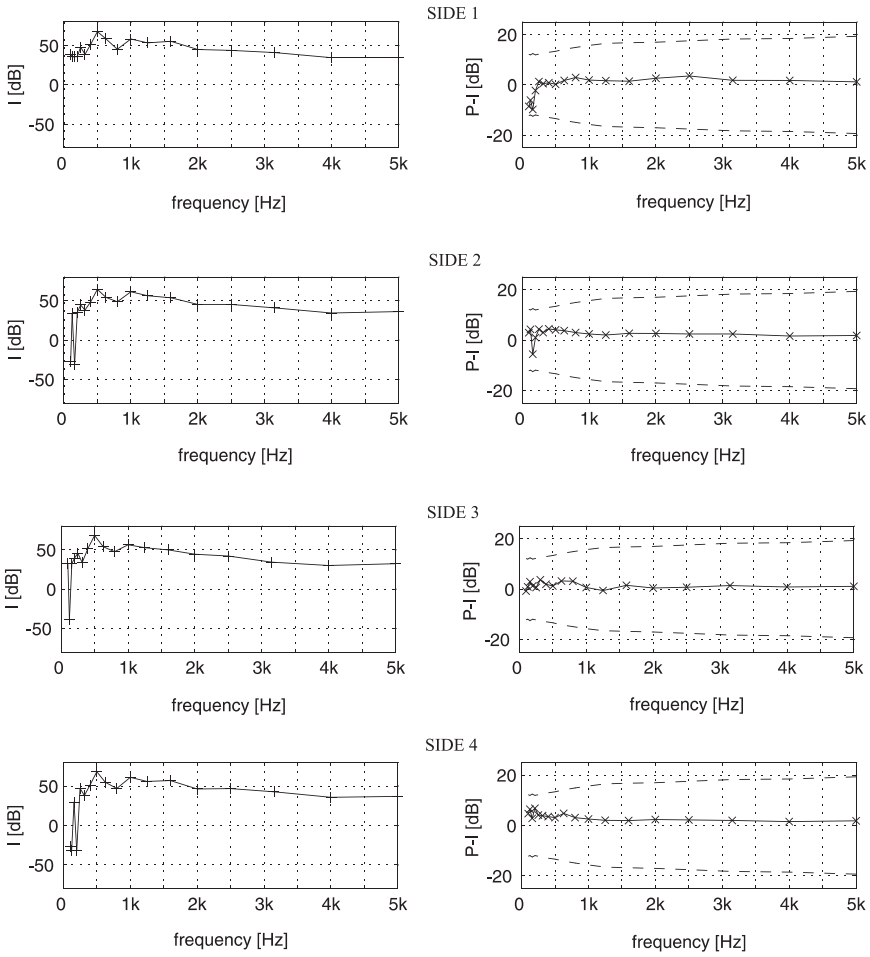

Figure G.4: Measured sound intensity and residual index over the four free sides of the frame, case [d=m, q=0], f=1105 Hz.

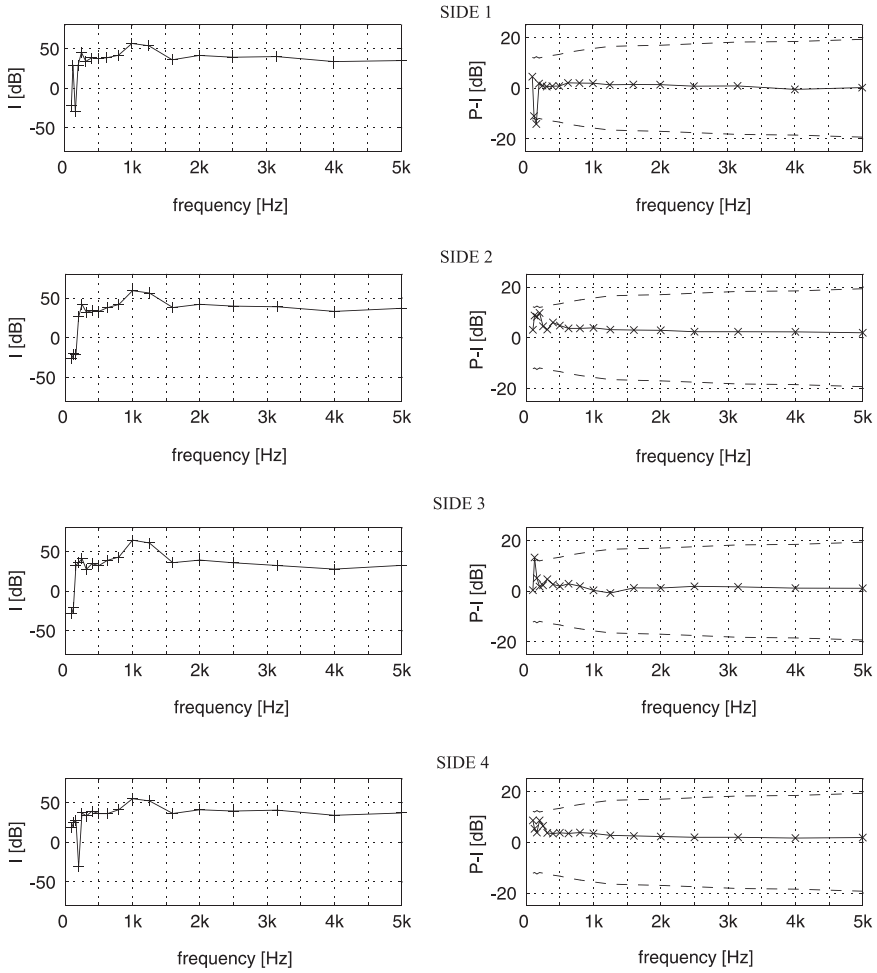

Figure G.5: Measured sound intensity and residual index over the four free sides of the frame, case [d=0, q=m], f=1105 Hz.

Appendix H

Load sound intensity measurements

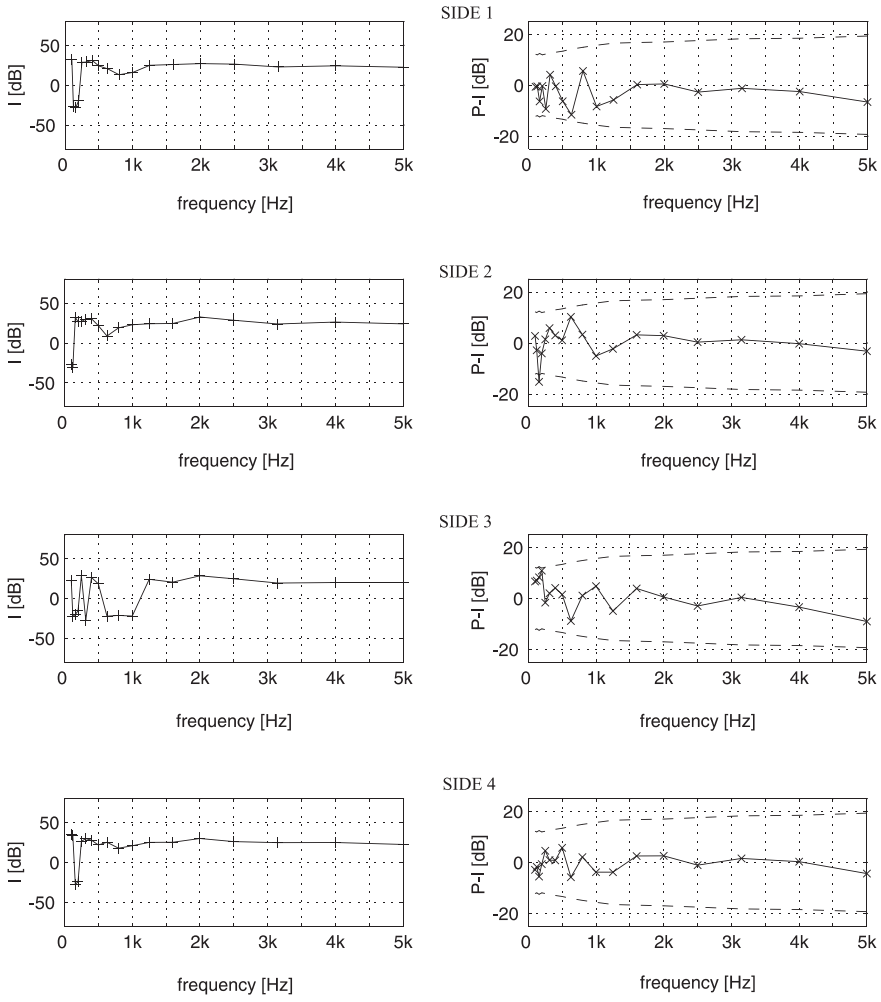

Figure H.1: Measured sound intensity and residual index over the four free sides of the frame, case [d=0, q=0].

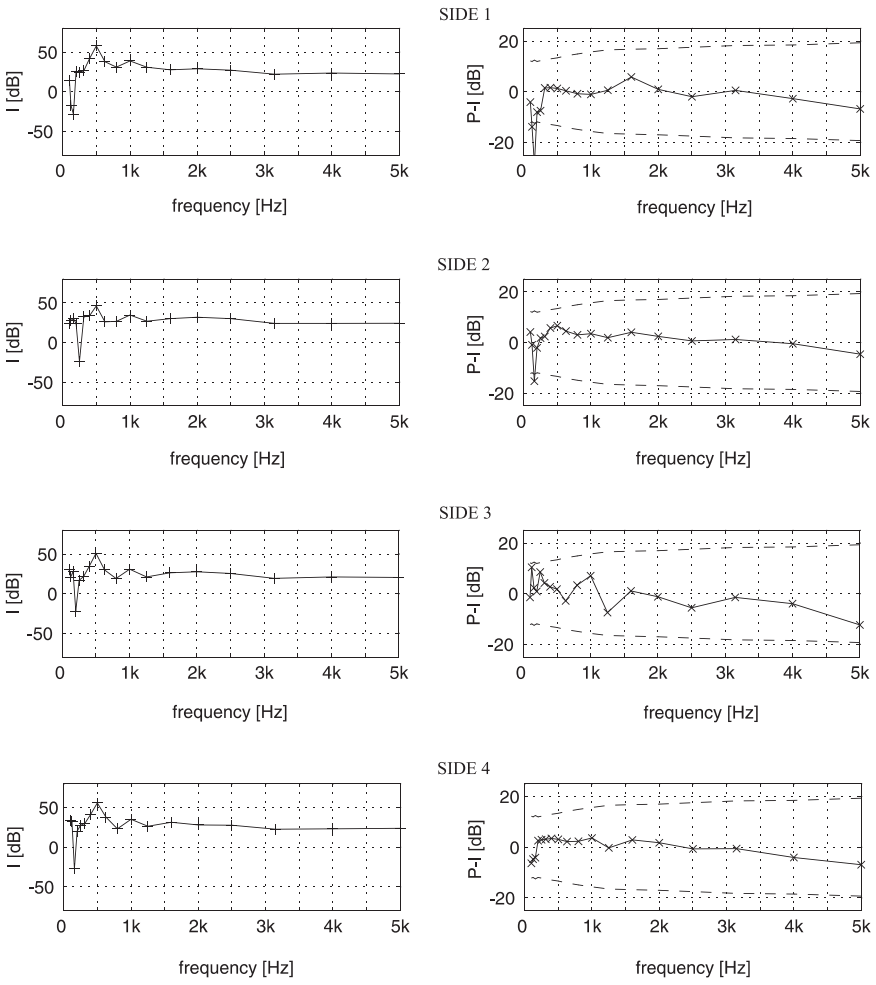

Figure H.2: Measured sound intensity and residual index over the four free sides of the frame, case [d=m, q=0], f=490 Hz.

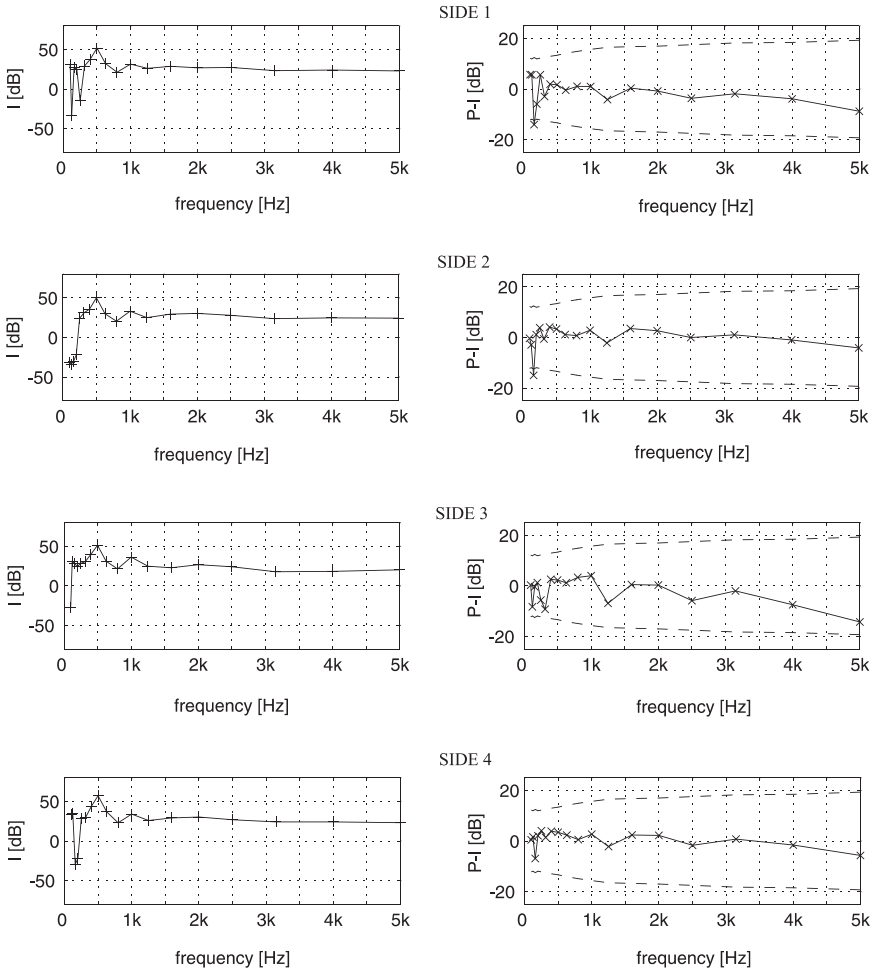

Figure H.3: Measured sound intensity and residual index over the four free sides of the frame, case [d=0, q=m], f=490 Hz.

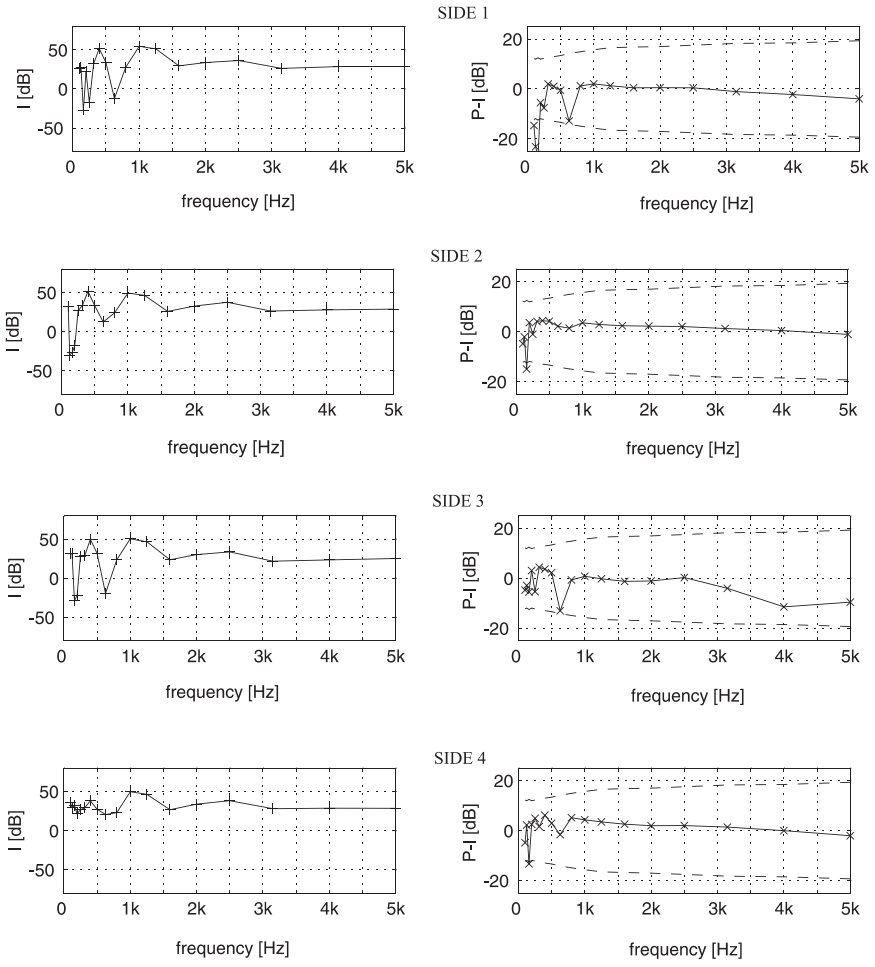

Figure H.4: Measured sound intensity and residual index over the four free sides of the frame, case [d=m, q=0], f=1105 Hz.

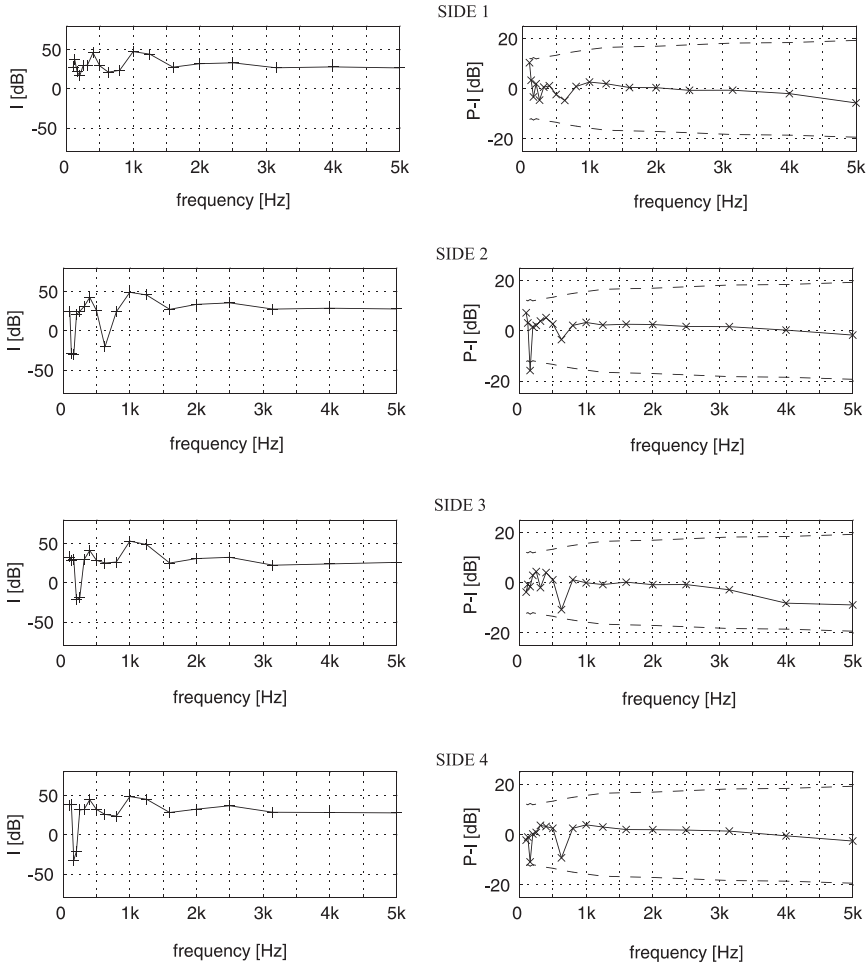

Figure H.5: Measured sound intensity and residual index over the four free sides of the frame, case [d=0, q=m], f=1105 Hz.